



**HAL**  
open science

# Spectroscopic studies of cerium and Ytterbium-based Kondo systems

Bodry Tegomo Chiogo

► **To cite this version:**

| Bodry Tegomo Chiogo. Spectroscopic studies of cerium and Ytterbium-based Kondo systems. Physics  
| [physics]. Université de Lorraine, 2022. English. NNT : 2022LORR0193 . tel-04127388

**HAL Id: tel-04127388**

**<https://hal.univ-lorraine.fr/tel-04127388>**

Submitted on 13 Jun 2023

**HAL** is a multi-disciplinary open access archive for the deposit and dissemination of scientific research documents, whether they are published or not. The documents may come from teaching and research institutions in France or abroad, or from public or private research centers.

L'archive ouverte pluridisciplinaire **HAL**, est destinée au dépôt et à la diffusion de documents scientifiques de niveau recherche, publiés ou non, émanant des établissements d'enseignement et de recherche français ou étrangers, des laboratoires publics ou privés.



**UNIVERSITÉ  
DE LORRAINE**

**BIBLIOTHÈQUES  
UNIVERSITAIRES**

## AVERTISSEMENT

Ce document est le fruit d'un long travail approuvé par le jury de soutenance et mis à disposition de l'ensemble de la communauté universitaire élargie.

Il est soumis à la propriété intellectuelle de l'auteur. Ceci implique une obligation de citation et de référencement lors de l'utilisation de ce document.

D'autre part, toute contrefaçon, plagiat, reproduction illicite encourt une poursuite pénale.

Contact bibliothèque : [ddoc-theses-contact@univ-lorraine.fr](mailto:ddoc-theses-contact@univ-lorraine.fr)  
*(Cette adresse ne permet pas de contacter les auteurs)*

## LIENS

Code de la Propriété Intellectuelle. articles L 122. 4

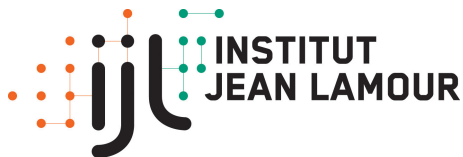
Code de la Propriété Intellectuelle. articles L 335.2- L 335.10

[http://www.cfcopies.com/V2/leg/leg\\_droi.php](http://www.cfcopies.com/V2/leg/leg_droi.php)

<http://www.culture.gouv.fr/culture/infos-pratiques/droits/protection.htm>



UNIVERSITÉ  
DE LORRAINE



INSTITUT  
JEAN LAMOUR

C2MP



# THÈSE

présentée pour l'obtention du titre de

DOCTEUR DE L'UNIVERSITÉ DE LORRAINE

en Physique

par

Bodry TEGOMO CHIOGO

---

## SPECTROSCOPIC STUDIES OF CERIUM AND YTTERBIUM-BASED KONDO SYSTEMS

---

Soutenue publiquement le 16 décembre 2022  
à Nancy, devant le jury composé de :

Rapporteurs :

O. ISNARD      Professeur, Université Grenoble Alpes - Institut Néel  
S. BURDIN      Maître de Conférences HDR, LOMA, Université de Bordeaux

Examineurs :

A. JUHIN      Directrice de recherche CNRS, Sorbonne Université  
E. GAUDRY      Professeur, Université de Lorraine (Président du jury)  
A. NICOLAOU      Chercheur, Synchrotron Soleil  
D. MALTERRE      Professeur, Université de Lorraine (Directeur)

Invité :

A. CHAINANI      Chercheur, Synchrotron Taiwan (Co-directeur)

*Institut Jean Lamour - UMR 7198 - CNRS  
Université de Lorraine - Pôle M4 : matière, matériaux, métallurgie, mécanique*



# Remerciements

Un physicien ne travaille jamais seul! Les études de cette thèse n'auraient pas pu être réalisées sans l'énorme effort de nombreuses personnes. Avant de nous plonger dans ce manuscrit je souhaiterais exprimer ma gratitude envers tous ceux qui ont contribué aux projets et m'ont soutenu tout au long de mon doctorat. Je tiens tout d'abord à remercier les membres du jury, ses rapporteurs Olivier Isnard et Sébastien Burdin ainsi que ses trois examinateurs Amélie Juhin, Emilie Gaudry et Alessandro Nicolaou pour avoir accepté de lire et d'évaluer ce mémoire. Un remerciement particulier à Amélie, grâce à toi nous avons découvert le très précieux programme Quany et son interface graphique Crispy qui ont été largement utilisés dans le cadre de cette thèse.

Mes plus profonds remerciements vont à mon directeur de thèse Daniel Malterre qui m'a accepté pour ce projet thèse très intéressant sur les systèmes Kondo à base de cérium et d'ytterbium. Daniel, tu étais toujours présent dès que j'en éprouvais le besoin, et cela tout au long de ma thèse. Ton bureau était toujours ouvert lorsque j'avais des questions ou des problèmes, et même les questions banales, tu y répondais patiemment. Je te remercie d'avoir partagé toutes ces connaissances sur la physique, ton expertise, ton sens de la rigueur et du détail, ainsi que l'atmosphère de travail toujours positive pendant toutes ces années. Il était fascinant d'apprendre de toi comment des problèmes physiques complexes peuvent être abordés en combinant expériences et théorie. Je garde de super souvenirs de nos campagnes de mesures à Soleil sur les lignes Ode et Sextants.

Merci beaucoup Ashish Chainani, tes nombreux conseils m'ont été très précieux. Merci pour tous ces moments partagés au synchrotron de Taiwan et aussi lors de nos dernières mesures au synchrotron Soleil. Travailler avec toi au cours de ces dernières années a considérablement accru mon désir de travailler dans le domaine de la spectroscopie à haute énergie et plus particulièrement la spectroscopie RIXS. J'espère sincèrement pouvoir continuer à collaborer avec Daniel et toi pendant mon postdoc au centre Helmholtz de Berlin.

Je remercie également les membres permanents de l'équipe Surface, Spectroscopies et Modélisations avec qui j'ai eu du plaisir à travailler. Merci Luc, j'ai beaucoup aimé travailler avec toi, merci pour toutes ces connaissances sur l'environnement ultra-vide, l'instrumentation et la cryogénie. Merci Bertrand pour toutes les discussions passionnantes sur microscopie à effet tunnel. Merci Yannick pour l'initiation à la technique de photomémission et pour ces bons moments sur la ligne Cassiopee au synchrotron Soleil. Merci Calvin pour ton aide précieuse pendant les mesures au synchrotron Soleil. Je te souhaite plein de réussite pour la suite de ta thèse.

Toutes les expériences n'auraient bien sûr pas été possibles sans les échantillons de haute qualité fournis par les chimistes de l'équipe 103 de l'institut Jean Lamour. Un grand merci à Thomas Mazet, Leopold Diop et Thierry Schweitzer.

Je souhaite également remercier tous mes amis en particulier mes promotionnaires de master Danny, Daniel et Nadine. Je vous souhaite beaucoup de succès pour vos thèses.

Enfin, mes remerciements les plus chaleureux vont à mes parents, à mon frère Dimitri et à ma fiancée Marlise, qui m'ont beaucoup soutenu et pris soin de moi dans le monde extérieur à la physique.

# Résumé

Au début des années 80, les composés à base de cérium et d'ytterbium ont suscité un vif intérêt car ils présentent à basse température des propriétés magnétiques, électroniques et thermodynamiques fascinantes et très intéressantes telles que l'effet Kondo, fermions lourds, valence intermédiaire, la supraconductivité non conventionnelle et les ondes de densité de charge. Ces propriétés sont dues aux interactions électron-électron très fortes des états  $f$  et à l'hybridation des états  $f$  avec les électrons de conduction.

Ce manuscrit est divisé en deux parties présentant des résultats expérimentaux et des simulations. Dans la première partie, nous étudions le matériau fortement corrélé YbPd. YbPd a une structure de type CsCl, c'est l'un des premiers composés intermétallique à base d'ytterbium présentant à la fois un comportement de valence intermédiaire et un ordre magnétique, et a été intensivement étudié dans le passé. Il présente une transition de phase antiferromagnétique à  $T_N = 1.9$  K et une onde de densité de charge incommensurable à  $T_1 = 130$  K. A  $T_2 = 105$  K, cette onde de densité de charge incommensurable se transforme en une onde de densité de charge commensurable. Lorsque la température diminue, la structure cubique avec un site Yb unique se transforme en une symétrie tétragonale à 130 K avec deux sites Yb différents. En dessous de 105 K, le site magnétique  $\text{Yb}^{3+}$  et nonmagnétique  $\text{Yb}^{2.6+}$  sont disposés alternativement le long de l'axe  $c$ , ce qui signifie un ordre de valence. Cet ordre de valence dans le composé YbPd est très intrigant car il présente une résistivité électrique métallique à partir de  $T_1$  et jusqu'à basse température. De plus, les mesures de pression ont révélé un autre phénomène inhabituel. En effet, alors que dans les autres composés d'Yb, la pression stabilise souvent l'ordre magnétique, dans l'YbPd, la température de transition magnétique  $T_N = 1.9$  K diminue avec l'augmentation de la pression, et l'ordre antiferromagnétique est supprimé à 2 GPa. Simultanément, l'onde de densité de charge commensurable est également supprimé à 2 GPa et l'onde de densité de charge incommensurable est supprimé à 5 GPa. Afin d'étudier l'origine de l'onde de densité de charge dans le composé YbPd, nous étudions la dépendance en température des valences des deux sites Yb à travers la température de transition. Deux techniques expérimentales sont utilisées pour déterminer l'évolution de la valence en fonction de la température : La spectroscopie de photoémission dans le domaine des rayons X mous ( $h\nu \leq 1500$  eV) et durs ( $h\nu = 5-10$  KeV), et la spectroscopie d'absorption des rayons X. La spectroscopie de photoémission est une technique courante pour étudier les effets d'hybridation dans les terres rares, et leur structure électronique en général. Cependant, dans le domaine d'énergie des rayons x mous, les effets de surface sont connus pour avoir de l'importance, de sorte que l'occupation des états  $4f$  dans les composé d'ytterbium à la surface peut être surestimée par rapport à celle du volume. L'utilisation de rayons X durs garantit une profondeur de pénétration et un libre parcours moyen suffisamment grand, et s'est avérée très précise pour déterminer les informations sur la structure électronique dans le volume dont la valence de l'ytterbium.

Les spectres HAXPES de l'YbPd dans la phase cubique au seuil 3d de l'Yb 3d, mesurés avec un faisceau incident polarisé linéairement d'énergie  $h\nu = 6500$  eV, présentent deux structures correspondant aux états finals  $4f^{14}$  ( $\text{Yb}^{2+}$ ) et  $4f^{13}$  ( $\text{Yb}^{3+}$ ). La présence de ces

deux états finals est une signature du caractère de valence intermédiaire de l'ytterbium dans la phase cubique. La dépendance en température des spectres Yb-3d par HAXPES révèle un comportement singulier de l'YbPd. En effet, suivant le mécanisme de Kondo, avec l'augmentation de la température, une diminution du poids spectral de  $\text{Yb}^{2+}$  transféré à  $\text{Yb}^{3+}$  est attendue avec une augmentation continue de l'occupation des états  $4f$ ,  $n_f$  à travers la température de Kondo,  $T_K$  pour les systèmes avec une température de Kondo relativement élevée ( $T_K \leq 100$  K). Pour les systèmes à réseau Kondo ( $n_f \approx 1$ ), un faible changement est observé dans les spectres alors que, les spectres sont indépendants de la température dans la gamme inférieure à 300 K pour les systèmes à valence fortement mixte ( $T_K \geq 1000$  K) tels que  $\text{YbAl}_2$  qui présente une valence d'environ 2,2 ( $T_K = 2500$  K). Cependant, l'évolution de la valence de Yb avec la température dans le composé YbPd présente deux régimes: elle augmente progressivement lorsque la température augmente de 20 K à 135 K alors qu'elle est constante de 135 K à 200 K. La dépendance en température de la valence est donc observée uniquement dans la phase tétragonale ( $T \leq 135$  K), ce qui indique qu'elle ne provient pas du mécanisme Kondo mais plutôt de l'onde de densité de charge. Une analyse quantitative détaillée des spectres HAXPES au seuil 3d de l'Yb et de bande de valence pour quantifier la l'occupation des états  $4f$ ,  $n_f$  (la valence  $v = 2 + n_f$ ) ainsi que la force d'hybridation nécessite des simulations avec un modèle approprié.

Les résultats expérimentaux de ces différentes spectroscopies sur des terres rares notamment les composés de Ce, d'Yb et de La présentent des spectres très complexes caractérisés par la présence des effets de multiplet et des satellites mal compris. Plusieurs théories ont été proposées pour expliquer les résultats de ces différentes spectroscopies. Kotani et Toyozawa ont formulé une première explication qualitative de ces spectres expérimentaux de composés à base de La en utilisant le modèle à une impureté d'Anderson et en tenant compte de l'interaction entre les états  $4f$  et le trou de coeur créé lors des différents processus. En tenant compte de la grande dégénérescence des états  $4f$ , Gunnarsson et Schönhammer ont étendu la théorie de Kotani et Toyozawa pour étudier les spectres au seuil 3d des composés de cérium à valence intermédiaire. Cependant, l'approche GS nécessite un effort considérable de calcul numérique, ce qui a souvent conduit les expérimentateurs à ajuster leurs données spectroscopiques avec des approches phénoménologiques.

Dans le cadre de ce travail de thèse, nous avons développé une approche simplifiée fondée sur l'approche GS. Nous avons développé un code pour décrire les spectres de photoémission au seuil  $3d$  et de bande de valence des composés d'Yb. Ce qui est nouveau dans notre calcul est que nous prenons explicitement en compte la dégénérescence totale des états  $4f$  (1 état pour la configuration  $f^0$ , 14 états pour la configuration  $f^1$  et 91 états pour  $f^2$ ). De plus, contrairement à l'approche GS, qui décrit uniquement les spectres à  $T = 0$  K, cette approche simplifiée permet de décrire qualitativement la dépendance de la température des spectres de photoémission. Nous utilisons cette nouvelle approche pour analyser quantitativement les spectres HAXPES du composé YbPd au seuil  $3d$  de l'Yb. Comme nous l'avons mentionné plus haut, la dépendance en température des spectres de photoémission n'est pas due à une population thermique des premiers états excités selon le scénario de Kondo mais semble liée au mécanisme de CDW. Nous avons donc simulé les différents spectres dans l'état fondamental en faisant varier uniquement le paramètre d'hybridation. Dans la phase cubique, le

site unique d'Yb correspond à une valence moyenne de  $v_{av} = 2,84$  ( $n_f = 0,84$ ). Dans la phase tétragonale, la valence du site magnétique Yb<sub>1</sub> diminue de  $v_1 = 2,98$  à 20 K à 2,84 à 135 K, tandis que celle du site à forte valence intermédiaire Yb<sub>2</sub> augmente de  $v_2 = 2,6$  à 2,84. En suivant la loi phénoménologique d'échelle de puissance entre la température de Kondo  $T_K$  et l'occupation des trous  $f$  récemment établie, nous avons déterminé la température de Kondo de l'unique site cristallographique Yb dans la phase cubique et celle des sites Yb<sub>1</sub> et Yb<sub>2</sub>. Ensuite, nous introduisons l'énergie électronique gagnée par le mécanisme de Kondo. Nous obtenons un bon accord entre cette quantité et le champ moyen du gap de Bardeen-Cooper-Schrieffer qui est considéré comme un paramètre d'ordre valide du CDW. Nous conjecturons donc que l'effet Kondo est probablement la force motrice de la transition CDW observée dans le composé YbPd.

Dans la deuxième partie de ce manuscrit, nous étudions les échelles de basse et haute énergie dans les systèmes Kondo à base de cérium, qui sont cruciales pour une compréhension précise de leurs propriétés électroniques. La photoémission de la bande de Valence, la photoémission inverse, la spectroscopie d'absorption des rayons x, la spectroscopie de photoémission résonante et spectroscopie de photoémission inverse résonante sont des techniques spectroscopiques puissantes qui ont été largement utilisées ces dernières décennies pour étudier le mécanisme de Kondo dans les composés du cérium. Ces techniques donnent accès à toutes les différentes échelles d'énergie d'intérêt : les échelles de haute énergie qui sont liées aux excitations de charge (interaction coulombienne  $U_{ff}$  et l'énergie des états  $f$  localisés  $\epsilon_f$ ), et les échelles de basse énergie liées aux excitations de spin (l'énergie de Kondo) et aux excitations de champ cristallin. Alors que les techniques thermodynamiques permettent d'accéder uniquement aux échelles de basse énergie (énergies de Kondo et de champ cristallin), les spectroscopies électroniques permettent d'accéder aux échelles de basse et de haute énergie. Cependant, ces spectroscopies sont sensibles à la surface et les effets de surface peuvent obscurcir les résultats. La diffusion résonante inélastique des rayons X (RIXS) est une technique tout photon qui est très efficace pour étudier les excitations élémentaires dans une grande variété de systèmes fortement corrélés tels que les composés du cérium. Le RIXS possède un certain nombre de propriétés uniques par rapport aux autres techniques spectroscopiques. La technique RIXS est spécifique à l'élément et à l'orbitale, ce qui est particulièrement important lorsque l'on souhaite se concentrer sur une excitation spécifique telle que les excitations  $dd$  ou  $ff$  sur un matériau donné. Sa sensibilité au volume nous permet d'éviter les contributions supplémentaires dans les spectres dues à la surface. Son caractère résonnant nous permet de renforcer le signal  $4f$ . Par exemple, la caractéristique spectrale du XAS au seuil M<sub>5</sub> du cérium associée à la contribution  $f^0$  dans l'état fondamental a un poids spectral très faible dans les composés à faible température de Kondo, alors que la caractéristique correspondante dans les spectres RIXS présente une intensité importante. De plus, le RIXS correspond à un processus optique de second ordre avec des transitions d'absorption et d'émission. Chacune d'entre elles est régie par les règles de sélection dipolaire. Cependant,



le processus RIXS total ne suit pas ces règles. Typiquement, la technique RIXS donne accès aux excitations  $f\bar{f}$  contrairement à l'absorption des rayons X.

Dans cette deuxième partie, nous étudions premièrement le système Kondo ferromagnétique CeAgSb<sub>2</sub>. C'est un composé de fermions lourds faiblement hybridés avec une température Kondo d'environ 10-20 K. En utilisant la spectroscopie RIXS au seuil M<sub>5</sub> du cérium, nous étudions les excitations de charge  $f^1 \rightarrow f^2$  et  $f^1 \rightarrow f^0$  ainsi que l'excitation spin-orbite. Nous mettons également en évidence la suppression totale de l'état final  $f^0$  du RIXS et du pic élastique, ce qui nous permet de déterminer la symétrie  $^1S_0$  de l'état fondamental. Afin d'analyser quantitativement les spectres et de déterminer les différents paramètres tel que l'occupation de l'état  $f$ , nous calculons les spectres XAS et RIXS en utilisant un modèle d'impureté d'Anderson simplifié combiné à la théorie des multiplets en utilisant le code QUANTY. En effet, le SIAM permet de reproduire les énergies relatives des structures de perte de spin et de charge, tandis que la théorie des multiplets permet de reproduire la forme correcte des spectres et, plus important encore, la dépendance des spectres vis-à-vis de la polarisation. Outre les structures d'énergie de perte, les spectres RIXS présentent des structures de type fluorescence qui présentent une forte dépendance avec température, similaire à la dépendance en température de la résonance Kondo observée en spectroscopie de photoémission inverse. Par conséquent, l'intensité de fluorescence donne accès au degré de délocalisation des états  $4f$  donné par le poids de la configuration  $f^0$  dans l'état fondamental.

Enfin, nous étudions comment les spectres RIXS évoluent avec la température Kondo  $T_K$  dans trois matériaux Kondo à base de Ce : un composé Ce de type  $\gamma$  ( CeSi<sub>2</sub>,  $T_K \sim 50$  K), un composé Ce de type  $\alpha$  ( CeNi<sub>2</sub>,  $T_K > 500$  K) et un composé  $T_K$  intermédiaire ( CePd<sub>3</sub>,  $T_K \sim 150$  K). Nous avons mesuré l'alliage Ce<sub>0,93</sub>Sc<sub>0,07</sub> à travers la transition  $\gamma$ - $\alpha$ . Le poids spectral RIXS de la structure  $f^0$  ainsi que la structure de type fluorescence présentent une diminution rapide à travers la transition  $\gamma$ - $\alpha$  et une hystérésis en fonction de la température qui ressemblent beaucoup à la boucle d'aimantation. Ceci nous permet de conjecturer que la structure de type fluorescence est corrélée au poids de la configuration  $f^0$  dans l'état fondamental et reflète l'échelle de Kondo.

# Contents

<b>1</b>	<b>General Introduction</b>	<b>10</b>
1.1	Physics of Ce and Yb-based compounds . . . . .	10
1.1.1	Kondo effect . . . . .	10
1.1.2	Heavy fermions: Kondo lattice and RKKY interaction . . . . .	11
1.1.3	Intermediate valence systems . . . . .	12
1.1.4	High-energy spectroscopies of Kondo systems . . . . .	15
<b>I</b>	<b>YbPd</b>	<b>17</b>
<b>2</b>	<b>Interplay between Kondo behavior and charge density wave in YbPd</b>	<b>18</b>
2.1	Introduction . . . . .	18
2.2	Summary of the known properties of YbPd . . . . .	19
2.3	High energy spectroscopic properties of YbPd . . . . .	21
2.3.1	Yb-3d and Pd-3d core level HAXPES . . . . .	21
2.3.2	Yb 4f valence band spectra . . . . .	24
2.3.3	Photon energy dependence of the valence band: surface contribution and cross-section effect . . . . .	25
2.4	Temperature dependence of the 4f occupancy across the CDW transitions in YbPd compound . . . . .	26
2.4.1	Temperature dependence of the Yb-3d, Pd-3d core level, and valence band HAXPES spectra . . . . .	26
2.4.2	Temperature dependence of the valence band HAXPES spectra . . . . .	28
2.5	Simulations . . . . .	29
2.5.1	The Gunnarsson and Schönhammer approach, and the Imer-Wuilloud toy model . . . . .	29
2.5.2	Simple approximation scheme of Gunnarsson and Schönhammer model: Case of Yb compounds . . . . .	34
2.5.3	Description of the model . . . . .	34
2.5.4	3d core-level photoemission . . . . .	36

2.5.5	Phenomenological reproduction of the complex line shape due to multiplet effects: $3d^9 4f^{13}$ photoemission final states . . . . .	37
2.5.6	Calculation of the Yb core level: Final states effect and influence of the different parameters . . . . .	38
2.5.7	Temperature dependence . . . . .	41
2.5.8	4f valence band . . . . .	43
2.5.9	Phenomenological simulation of the complex line shape due to multiplet effects: $(\underline{f}^2) f^{12}$ final states in the valence band . . . . .	44
2.6	Quantitative analysis of the experimental HAXPES spectra of YbPd . . . . .	45
2.6.1	Yb 3d core level . . . . .	45
2.6.2	4f Valence band . . . . .	49
2.7	Dual Kondo effect charge ordering . . . . .	49
2.7.1	Zero thermal expansion . . . . .	54
2.7.2	Temperature dependence of the valence band soft PES spectra . . . . .	55
2.8	Yb $L_3$ X-ray absorption spectroscopy . . . . .	56
2.8.1	Yb $L_3$ X-ray absorption spectroscopy, Temperature dependence . . . . .	59
2.8.2	Pressure-induced anomalous valence fluctuation in YbPd . . . . .	59
2.9	conclusion . . . . .	61
	Bibliography . . . . .	62

## **II Spin-charge excitations in cerium compounds studied by Resonant inelastic X-ray scattering** **69**

<b>3</b>	<b>RIXS to probe the properties of Ce Kondo systems</b>	<b>70</b>
3.1	Introduction . . . . .	70
3.2	RIXS review on cerium compounds . . . . .	71
3.2.1	Scattering process and outstanding features of RIXS . . . . .	71
3.2.2	Theoretical description of RIXS . . . . .	73
3.3	Relevant energy scales probed by Ce- $M_5$ RIXS . . . . .	75
3.3.1	First evidence of the charge transfer excitations . . . . .	75
3.3.2	Spin-orbit and crystal field excitations . . . . .	79
3.3.3	Fluorescence emission . . . . .	81
3.4	Experimental Aspects . . . . .	84
3.4.1	RIXS at AERHA spectrometer at synchrotron SOLEIL . . . . .	84
3.4.2	Sample surface . . . . .	87
3.5	XAS and RIXS simulation . . . . .	88
3.5.1	Atomic full multiplet theory . . . . .	88
3.5.2	Full multiplet configuration interaction . . . . .	92
3.5.3	XAS and RIXS spectral functions . . . . .	94
3.5.4	RIXS spectra for a trivalent system: CeF <sub>3</sub> . . . . .	96
3.5.5	RIXS spectra for an intermediate-valent system . . . . .	98
3.5.6	Polarization dependence: Discussion . . . . .	101

3.5.7	Importance of the $f^2/f^3$ configuration in the initial/intermediate state	104
3.5.8	Influence of the different parameters	105
3.6	RIXS insights into CeAgSb <sub>2</sub> Kondo system	107
3.6.1	Properties of CeAgSb <sub>2</sub>	107
3.6.2	Charge transfer excitations	108
3.6.3	Low energy excitations	111
3.6.4	Temperature dependence of the fluorescence-like structure	112
3.7	RIXS in typical low- $T_K$ and high- $T_K$ Kondo systems	115
3.7.1	Overview of the RIXS results	116
3.7.2	Understanding the Ce $M_5$ -edge RIXS in Ce compounds: the Ce-Sc alloy	121
3.7.3	Oxidation effect	125
3.7.4	A direct investigation of $\gamma$ - $\alpha$ phase transition by Ce $M_5$ -edge RIXS	126
3.8	Conclusion	129
	Bibliography	131
<b>4</b>	<b>General conclusions and outlook</b>	<b>139</b>

# General Introduction

## 1.1 Physics of Ce and Yb-based compounds

### 1.1.1 Kondo effect

It is well-known that a large number of Ce and Yb materials exhibit the Kondo effect with characteristic electrical, magnetic and thermodynamical properties. The Kondo effect results from the introduction of a localized magnetic moment in metals and is usually referred to as an impurity embedded in a quantum sea of mobile conduction electrons. Such a magnetic impurity might be expected to survive in the metallic host with a susceptibility characterized by a Curie-Weiss law  $\chi(T) = \frac{M^2}{T+\theta}$ , where  $M$  is the magnetic moment of the impurity,  $T$  is the temperature and  $\theta$  is a constant. Surprisingly, in certain conditions this impurity strongly affects the conduction electrons of the host metal and exhibits a Pauli-type susceptibility  $\chi(T) = \text{cste}$  at low temperatures. Such an anomalous behavior has been evidenced in materials with a low concentration of magnetic  $3d$  transition metals substituted in non-magnetic metal hosts, e.g Mn and Fe in Au, Cu, or Ag, and also in the  $4f$  dilute rare earth compounds such as  $\text{Ce}_x\text{La}_{1-x}\text{Cu}_6$ . Such an impurity gives an anomalous contribution not only to the magnetic susceptibility but also to the transport properties such as specific heat and resistivity. Historically, the earliest manifestation of the effect of the magnetic impurity was identified by De Haas et al [1, 2] when they observed a minimum (see Figure 1.1) at low temperature in the electrical resistivity of a gold wire with a small number of impurities. It was very surprising since in most metals the resistivity is dominated by a constant impurity contribution at low temperatures and by increasing temperature the resistivity monotonically increases, where it is dominated by the inelastic scattering due to phonons. The first theoretical explanation of this effect was made 30 years later by J. Kondo [3] by using a third-order perturbation theory in the coupling  $J\rho$ , where  $J$  is the antiferromagnetic exchange and  $\rho$  is the density of states at the Fermi level. He showed that the antiferromagnetic interaction between the localized magnetic impurity and the conduction electrons leads to a  $\log(\frac{1}{T})$  dependence of the resistivity which increases with decreasing temperature. This Kondo picture can be described

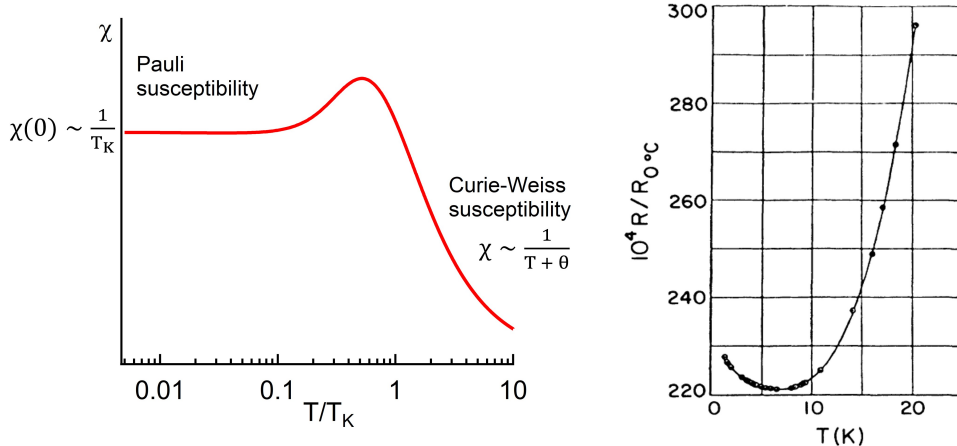


Figure 1.1: Susceptibility in Kondo system calculated with the Zwignagle Zevin Fulde approach: local moments are free at high temperature but are screened at low temperature by the spin of conduction electrons. Resistivity minimum in a gold metal (Au) with a residual magnetic metal impurities, taken from [1, 2].

by the so-called Kondo Hamiltonian:

$$H_K = \sum_{k,\sigma} \epsilon_k c_{k\sigma}^+ c_{k\sigma} - 2J\vec{S} \cdot \vec{s}(0), \quad (1.1)$$

and the Kondo temperature scale which governs the thermodynamic properties at low energy is given by:

$$T_K = D \exp \frac{-1}{J\rho}, \quad (1.2)$$

Here,  $J$  ( $< 0$ ) is the antiferromagnetic exchange interaction constant,  $c_{k\sigma}$  ( $c_{k\sigma}^+$ ) the creation (destruction) operator of a conduction electron,  $\vec{s}(0)$  is the spin of the conduction electron at the impurity site and  $\vec{S}$  is the spin impurity.

### 1.1.2 Heavy fermions: Kondo lattice and RKKY interaction

At the beginning of the 1970s, considerable efforts were devoted to the experimental and theoretical study of dilute and concentrated alloys with rare earth and actinides elements such as cerium, ytterbium, and uranium. The large interest in these systems received a strong impetus with the discovery of a new class of materials by Andres et al. in 1975 [4]. They measured the specific heat and resistivity of the  $\text{CeAl}_3$  compound and found that the low-temperature specific heat term  $C = \gamma T$  ( $\gamma = 1620 \text{ mJ mole}/K^2$ ) was 1000 times larger than that of normal metals. This means that, in this system, the effective mass was strongly enhanced compared to the free electron mass and therefore, the system was called "heavy fermion material". In order to explain the origin of this huge mass renormalization, S. Doniach [5] suggested that heavy fermion materials could be theoretically described as a Kondo lattice where, at each

site, the local moment is "quenched" by the conduction electrons via an antiferromagnetic interaction  $J$ . He thus proposed the so-called Kondo lattice Hamiltonian:

$$H_K = \sum_{k,\sigma} \epsilon_k c_{k\sigma}^\dagger c_{k\sigma} - 2J \sum_i \vec{S}_i \cdot \vec{s}_i, \quad (1.3)$$

where  $i$  is the lattice index,  $S_i$  and  $s_i$  are, respectively, the spin of the impurity and the conduction electron at each site  $i$ . While the on-site Kondo effect leads to a nonmagnetic ground state, the coupling between the localized moment and the conduction electron leads to an order effect that favors a magnetically ordered ground state, usually antiferromagnetic. This is due to the so-called Ruderman-Kittel-Kasuya-Yoshida (RKKY) interaction. The RKKY interaction is an inter-site interaction where  $f$  electrons couple with each other via the conduction electrons, and the Hamiltonian is given by:

$$H_{RKKY} = J_{RKKY} \vec{s}_i \cdot \vec{s}_j \quad (1.4)$$

The sharp discontinuity in the occupancies at the Fermi surface produces slowly decaying Friedel oscillations in the RKKY interaction given by :

$$J_{RKKY} = -D(E_F)J^2 \cos\left(\frac{k_F r}{r^3}\right), \quad (1.5)$$

where  $r$  is the distance from the impurity,  $k_F$  is the Fermi wave vector, and  $D(E_F)$  is the density of states at the Fermi energy. So, depending on the distance between impurities, the RKKY interaction oscillates in sign. The characteristic temperature of the RKKY interaction is approximate as  $T_{RKKY} = D(E_F)J^2$ . The oscillatory nature of this magnetic interaction favors the development of either antiferromagnetism for  $J_{RKKY} < 0$  or ferromagnetism for  $J_{RKKY} > 0$ .

The competition between RKKY and Kondo effects leads to an original set of magnetic and electronic properties at low temperatures. These properties may be tuned through control parameters such as chemical doping, pressure, or magnetic field. When  $J$  is small, the RKKY interaction is the dominating effect, and the systems exhibit a magnetically ordered ground state (usually antiferromagnetic). When  $J$  is large, the Kondo effect becomes dominant, and the system exhibits a heavy fermion behavior. Between the two regimes, there is a quantum critical point. The Doniach schematic phase diagram [5] shows various possible ground states as a function of  $T$  and  $J$ , which can be tuned by pressure or chemical doping as presented in Figure 1.2.

### 1.1.3 Intermediate valence systems

The single impurity Anderson model has been introduced in 1961 by P. W. Anderson [7] to describe the appearance of a localized magnetic moment in metals. Historically introduced for the magnetic moment of 3d metal transitions, it can be applied in the framework of rare earth compounds such as cerium and ytterbium. For rare earth compounds, the 4f orbital is

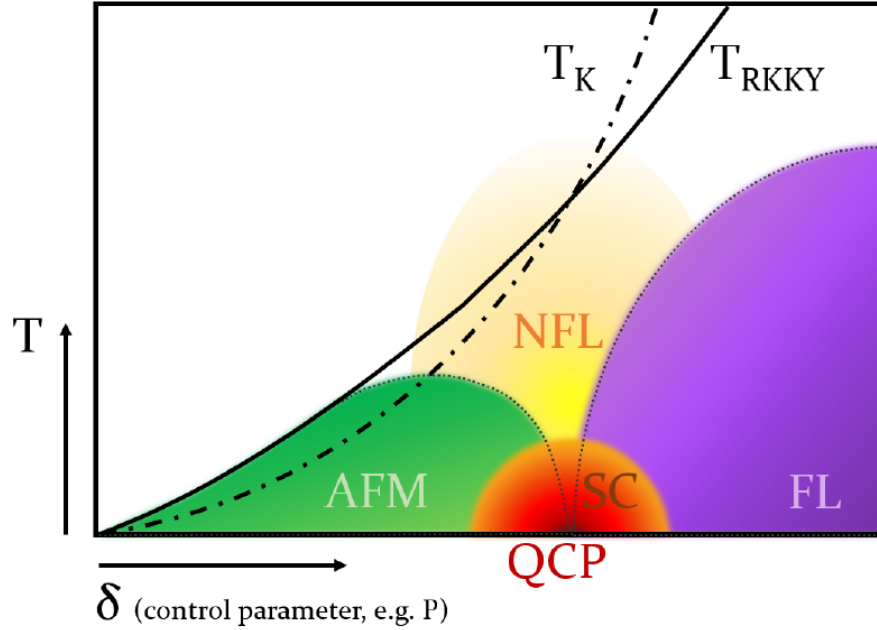


Figure 1.2: Doniach Diagram. For  $T_{RKKY} \gg T_K$  an antiferromagnetic ground state forms (localized regime), whereas for  $T_{RKKY} \ll T_K$  a paramagnetic Fermi liquid phase develops (delocalized regime). At the boundary of the two phases, a quantum critical point can arise. Redrawn from Ref [5, 6].

even more localized than the 3d orbital and yields a localized magnetic moment. The single impurity Anderson Hamiltonian can be written as:

$$H = \sum_k \epsilon_k a_k^\dagger a_k + \sum_m \epsilon_f a_{f,m}^\dagger a_{f,m} + \sum_{mm'} U_{ff} n_m n_{m'} + \sum_{k,m} V_{k,m} (a_k^\dagger a_{f,m} + a_{f,m}^\dagger a_k), \quad (1.6)$$

where the first term describes the conduction electrons, the second term is the energy of the  $f$  states, the third term is the Coulomb repulsion between two  $f$  states and the fourth term is the hybridization between the conduction electrons and the  $f$  states. Creation and annihilation operators of an  $f$  electron (conduction electron) are denoted  $a_{f,m}^\dagger$  ( $a_k^\dagger$ ) and  $a_{f,m}$  ( $a_k$ ), respectively. When the 4f states are not coupled with the conduction electrons ( $V = 0$ ), the eigenstates of the Hamiltonian correspond to the configurations  $f^n$  which depend only on the parameters  $\epsilon_f$  and  $U_{ff}$ . In the case of cerium, the Coulomb repulsion is very strong and we are limited to three configurations:  $f^0$  with energy 0, the 14 degenerate states  $f^1$  with energy  $\epsilon_f$  and the 91 degenerate states of the  $f^2$  configuration with energy  $2\epsilon_f + U_{ff}$ . Each state has respectively zero, one, and two holes in the conduction band. Since  $\epsilon_f < 0 < 2\epsilon_f + U$  for cerium, the ground state is given by the  $f^1$  configuration and the first and second excited states are respectively given by the  $f^0$  and  $f^2$  configurations. When a weak hybridization is turned on, the degeneracy of the ground state is lifted and a singlet state is stabilized which gets separated from the first excited state by a characteristic energy scale  $K_B T_K$  where  $T_K$





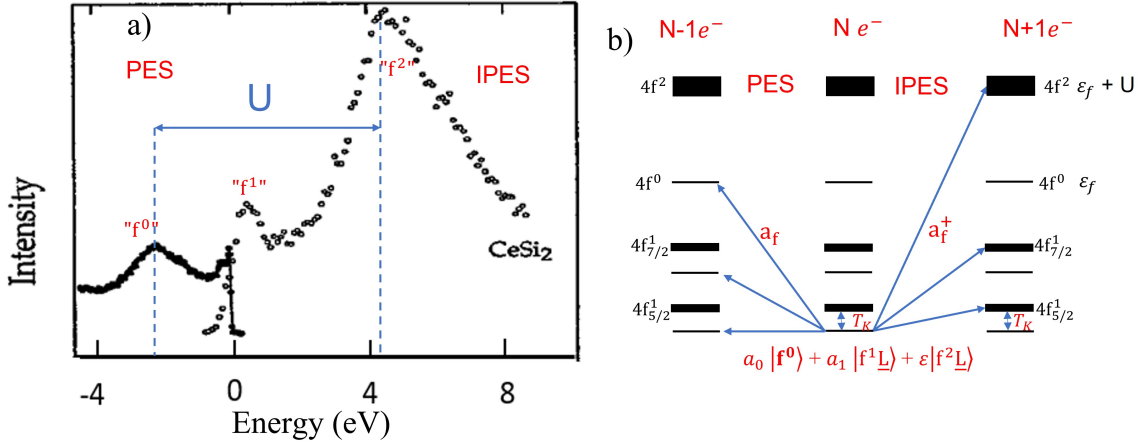


Figure 1.4: (a) Superposition of a photoemission spectrum and an inverse photoemission spectrum for the  $\text{CeSi}_2$  compound, taken from [8]. (b) Schematic representation of the energy levels for systems with  $N-1$ ,  $N$ , and  $N+1$  electrons and the associated transition probabilities.

Fermi liquid regime with heavy quasiparticles at low temperature and a localized moment regime at high temperature. So, the Anderson Hamiltonian has an emergent low energy scale (the Kondo energy  $K_B T_K$ ) corresponding to the spin-excitation which governs the properties at low temperature, and high energy scales ( $\epsilon_f$  and  $U_{ff}$ ) corresponding to charge excitations.

### 1.1.4 High-energy spectroscopies of Kondo systems

In the last two decades, there have been a large number of high-energy spectroscopies measurements such as core-level x-ray photoemission (XPS), valence band photoemission, inverse photoemission spectroscopy, and x-ray absorption (XAS) devoted to rare earth compounds, and especially to cerium and ytterbium compounds. These measurements allow us to determine the occupation of the  $f$  level, the high energy scale, as well as the low energy of the Kondo scale, which are crucial for a good understanding of the exotic properties of such systems. In figure 1.4a, we show a typical photoemission and inverse photoemission spectra of the  $\text{CeSi}_2$  compound. Figure 1.4b shows a schematic representation of the initial state and the different final states with  $(N-1)$  and  $(N+1)$  electrons. The arrows indicate the transitions which are allowed at  $T = 0$  K, from the intermediate valence ground state to the different final states. The photoemission spectrum is dominated by a broad structure at about  $\epsilon_f = -2$  eV corresponding to the  $f^0$  final state, and two sharp peaks appear at the Fermi level and at  $-0.3$  eV. The inverse photemission spectrum exhibits a prominent structure at about  $U_{ff} + \epsilon_f = 4$  eV corresponding to the  $f^2$  final state. Moreover, the spectrum exhibits the Kondo resonance (the transition from the ground state to the low lying excited magnetic states) just above the Fermi level. Therefore, unlike the thermodynamic properties which reflect only the low-energy scale, spectroscopic measurements are also sensitive to the high-energy scale ( $f^1 \rightarrow f^0$  and  $f^2 \rightarrow f^1$ ) charge excitations that dress the heavy quasiparticles.

X-ray absorption spectroscopies at  $L_{2,3}$  and  $M_{4,5}$  of rare earth compounds are powerful techniques to study the valence of Kondo and intermediate valence systems as a function of pressure, composition, and temperature. High-resolution photoemission spectroscopy can reveal the existence of the Kondo energy in a direct way by investigating the thermal excitations of the system. Recently, the strong development of resonant inelastic x-ray scattering has opened the possibilities for studying the crystal electric field and to determine the valence and Kondo scale with very high accuracy. In this thesis, we use a variety of spectroscopic techniques to study the electronic structure of Yb and Ce compounds.

**Part I**

**YbPd**

# Interplay between Kondo behavior and charge density wave in YbPd

## 2.1 Introduction

The strongly correlated YbPd material is a unique Yb compound exhibiting both an intermediate valence behavior and a charge density wave (CDW). It crystallizes in the cubic CsCl structure at room temperature and exhibits an antiferromagnetic phase transition at  $T_N = 1.9$  K. It undergoes an incommensurate CDW at  $T_1 = 130$  K. At  $T_2 = 105$  K, the incommensurate CDW turns into a commensurate CDW. With decreasing temperature, the cubic structure with a unique Yb site is transformed into a tetragonal symmetry at 130 K with two different Yb sites. Below 105 K, magnetic  $Yb^{3+}$  and nonmagnetic  $Yb^{2.6+}$  are arranged alternatively along the c axis, which means valence order. The valence order in YbPd is very intriguing since YbPd shows metallic electrical resistivity from above  $T_1$  and down to low temperature. Hence, many studies have been devoted to the manifestation of the magnetic ordering in the intermediate valence YbPd compound and to the origin of the CDW transition.

In this chapter, we will investigate the electronic structure of YbPd by means of high-energy spectroscopy techniques combined with a simplified single impurity Anderson model (SIAM) calculations. The chapter is organized as follows: First, we will give a general introduction to the material properties in section 1. In section 2, we report the Yb-3d core level and valence band of YbPd by means of hard x-ray and soft x-ray photoemission spectroscopy. In section 3, we will focus on the temperature dependence of Yb-3d<sub>5/2</sub> core level and valence band spectra. In section 4 we will present the new approach we introduced in the framework of the SIAM to quantitatively analyze the core level and valence band spectra. In section 5, we will apply this approach to simulate the spectroscopic data of YbPd. Then in section 6, we will discuss the link between the valence evolution provided by the spectroscopic techniques and the CDW transition and, how the dual Kondo effect provides a driving mechanism of the charge ordering in the YbPd compound.

## 2.2 Summary of the known properties of YbPd

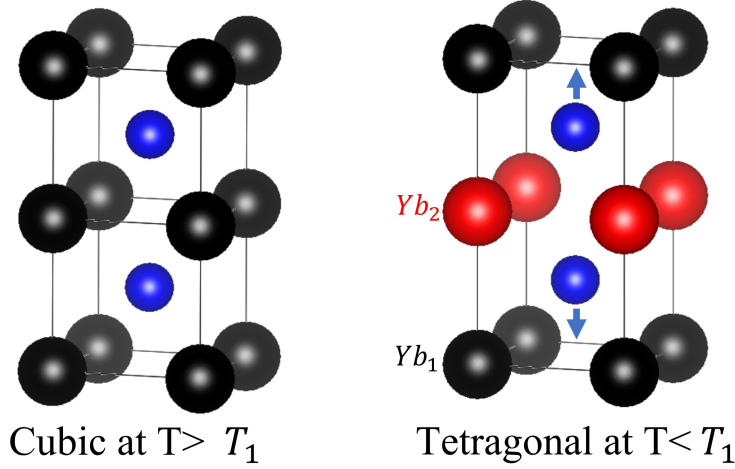


Figure 2.1: Crystal structure of YbPd below  $T_1 = 130$  K (tetragonal phase) and above  $T_1$  (cubic phase). Only one Yb site in the cubic phase and 2 in the tetragonal phase, redrawn from Ref [9].

YbPd is an intermediate valence compound that crystallizes into the CsCl-type structure (see Figure 2.1). In the middle of the 1980s, this compound attracted considerable interest, because both magnetic ordering and intermediate valence were observed. This behavior was not very common. In fact, at that time all the intermediate intermetallic Yb compounds were found to be non-magnetic until the unexpected discovery of the magnetic ordering in five compounds:  $YbBe_{13}$ ,  $Yb_3Pd_4$ ,  $YbIr_2$ ,  $YbPt$  and  $Yb_3Pt_4$ .

In the early 80's, R. Pott et al. [10] performed a number of different macroscopic technique measurements on YbPd such as specific heat, resistivity and magnetic susceptibility. They found that YbPd undergoes four main phase transitions, at  $T_1 = 130$  K,  $T_2 = 105$  K,  $T_3 = 1.9$  K and  $T_4 = 0.5$  K. Its intermediate valence character has been evidenced by XAS at Yb  $L_3$  edge ( $\nu = 2.88$ ) [10] as well as soft x-ray photoemission spectroscopy ( $\nu = 2.75$ ) [11]. The temperature dependence of the difference of the specific heat of YbPd and LuPd is shown in Figure 2.2a with one anomaly at  $T_3$  and 2 unusual sharp peaks at  $T_1$  and  $T_2$ . Figure 2.2b presents the temperature dependence of the resistivity measured at ambient pressure by R. Pott et al. The resistivity decreases upon cooling, drops at  $T_1$  and  $T_2$ , and remains metallic down to 40 mK [10]. They concluded that the transition at  $T_4$  is due to the magnetic ordering and those at  $T_1$  and  $T_2$  should be due to structural transitions.

Hasegawa et al.[12] performed Raman scattering experiments at low temperature and they evidenced a structural distortion from the CsCl structure. However, they surprisingly concluded that the crystal symmetry of YbPd at low temperature is neither cubic nor tetragonal. On the other hand, P. Bonville et al. [13] also reported that the cubic structure at room temperature with the cell parameter  $3.4443 \pm 0.001$  Å changes to a tetragonal structure at low

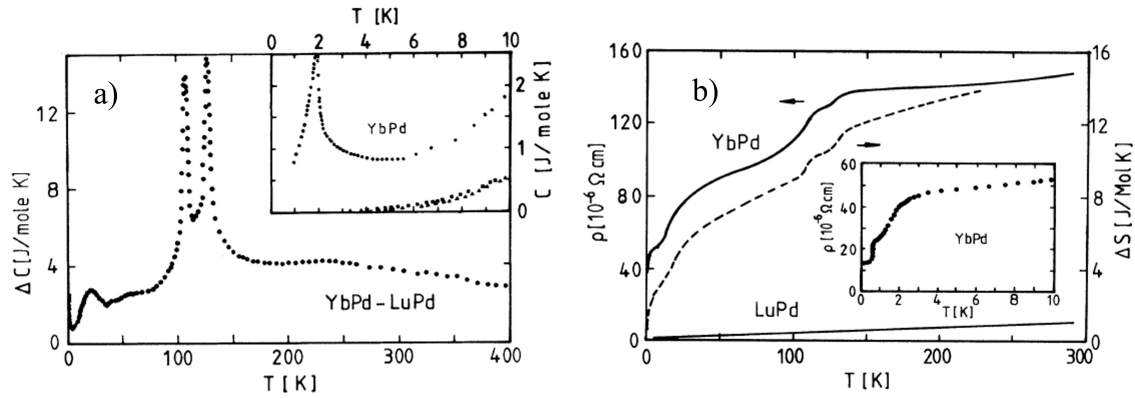


Figure 2.2: Temperature dependence of the specific heat (a) with two sharp transitions at  $T_1$  and  $T_2$ . Temperature dependence of the resistivity (b) with 2 drops at respectively  $T_1 = 130$  K and  $T_2 = 105$  K. Taken from Ref [10]

temperature with a ratio of  $c/a = 1.007$ , but with no detailed explanation. They also found from magnetic susceptibility that the magnetic ordering occurs in fact at  $T_3 = 1.9$  K and not at  $T_4 = 0.5$  K as suggested by R. Pott et al. Interestingly, P. Bonville et al. performed  $^{170}\text{Yb}$  Mössbauer absorption measurements at 4.2 K and revealed the existence of 2 kinds of Yb in the YbPd compound, one of which is magnetic and the other one is nonmagnetic in essentially equal proportions. Therefore, it is now accepted that the structural phase transitions at  $T_1 = 130$  K and  $T_1 = 105$  K are associated with a valence ordering characterized by one  $\text{Yb}^{3+}$  type of ions which order magnetically and the other one with intermediate valence type of Yb ions [13, 14, 15].

Recently, X-ray diffraction measurements [9] on YbPd single crystals confirmed that the highly symmetrical cubic phase deforms into a tetragonal phase below  $T_1 = 130$  K. Moreover, it was found that the Pd atoms are displaced by  $0.11 \text{ \AA}$  and no displacement was found for Yb ones. This Pd atom displacement along the c direction induces the distortion into a tetragonal structure below  $T_1$  resulting in a twofold structure with two inequivalent Yb-sites as shown in Figure 2.1: one Yb site with a short interatomic distance to Pd atoms and other Yb site with a long interatomic distance to Pd atoms respectively labeled  $\text{Yb}_1$  and  $\text{Yb}_2$ . Owing to the ionic radius of  $\text{Yb}^{3+}$  ( $f^{13}$ ) which is smaller than that of  $\text{Yb}^{2+}$  ( $f^{14}$ ),  $\text{Yb}_1$ -site is expected to have larger valence than  $\text{Yb}_2$ -site. A quantitative analysis of this valence ordering has been performed by R. Takahashi et al.[9] by using Yb  $L_3$  absorption edge energy and they found that the unique crystallographic Yb-site in the cubic phase has an average valence of  $v = 2.8$  and in the tetragonal phase, the valences of  $\text{Yb}_1$ -site and  $\text{Yb}_2$ -site are respectively  $v_1 = 3$  and  $v_2 = 2.6$ . Very recently, M. Shiga et al. [16] performed point contact spectroscopy on YbPd and estimated that the Kondo temperature of  $\text{Yb}_1$ -site ( $v_1 = 3$ ) is  $\sim 30$  K while that of the  $\text{Yb}_2$ -site ( $v_2 = 2.6$ ) is  $\sim 800$  K.

X-ray diffraction measurements [9] revealed that YbPd undergoes an incommensurate CDW at  $T_1 = 130$  K characterized by the wave vector  $(\pm 0.07 \pm 0.07 \ 1/2)$  with an alternating

arrangement of a larger valence ( $v_2 = 2.6$ ) and a smaller valence ( $v_1 = 3$ ) sites. At  $T_2 = 105$  K, the incommensurate structure turns into a commensurate structure characterized by the wave vector  $(0\ 0\ 1/2)$ .

In terms of structural changes, the valence ordering transitions observed in YbPd are similar to that of  $\text{Yb}_4\text{As}_3$  [17], but in which the charge ordering is accompanied by a distortion from the cubic to the trigonal phase. The distortion in  $\text{Yb}_4\text{As}_3$  results in inequivalent Yb-sites arrayed along the [111] direction in the fraction of 1/4 for  $\text{Yb}^{3+}$  and 3/4 for  $\text{Yb}^{2+}$  yielding an average valence of  $v = 2.25$ . However, in contrast to the classical charge ordering systems  $\text{Yb}_4\text{As}_3$  which shows a sudden increase in the resistivity at the charge-ordering temperature ( $T_{CO} = 290$  K), the electrical resistivity of YbPd decreases in all temperature ranges.

Pressure measurements revealed another unusual phenomenon of the YbPd compound. Indeed, while in other Yb compounds the pressure often stabilizes the magnetic ordering in YbPd, the magnetic transition temperature  $T_3$  decreases with increasing pressure, and the antiferromagnetic ordering is suppressed at 2 GPa [14]. Simultaneously, the commensurate CDW is also suppressed at 2 GPa and the incommensurate CDW is suppressed at 5 GPa [18].

## 2.3 High energy spectroscopic properties of YbPd

### 2.3.1 Yb-3d and Pd-3d core level HAXPES

For the purely divalent metallic Yb compounds, the Yb 3d core-level spectrum exhibits two set of features corresponding to the spin-orbit split  $3d_{5/2}$  and  $3d_{3/2}$  states. Similarly, two spin-orbit features structured by the multiplet effects are observed in the 3d core-level spectra of purely trivalent compounds such as  $\text{Yb}_2\text{O}_3$ . An example of early measurements of the  $3d_{5/2}$  core levels in  $\text{Yb}_2\text{O}_3$  and Yb metal with a monochromatized Si  $\text{K}\alpha$  source (1739.9 eV) are shown in Figure 2.3 [19]. Figure 2.4 shows the Yb 3d core level HAXPES of YbPd at  $T = 200$  K, the spectrum has been measured with a linearly polarized incident beam of incident photon energy  $h\nu = 6500$  eV. The Yb 3d core-level spectrum is split into two regions  $3d_{5/2}$  between 1515-1540 eV and  $3d_{3/2}$  between 1560-1590 eV due to the spin-orbit interaction. The spectra exhibit two single peaks at 1520 eV and 1567 eV which are attributed to  $4f^{14}3d_{5/2}^9$  ( $\text{Yb}^{2+}$ ) and  $4f^{14}3d_{3/2}^9$  ( $\text{Yb}^{2+}$ ) final states, respectively. The structures at 1524-1536 eV (12 multiplets) and at 1527-1584 eV (7 multiplets) correspond to  $4f^{13}3d_{5/2}^9$  ( $\text{Yb}^{3+}$ ) and  $4f^{13}3d_{5/2}^9$  ( $\text{Yb}^{3+}$ ) final states, respectively. The two broad structures at 1545 eV and 1591 eV are due to plasmons. Therefore, the presence of  $\text{Yb}^{3+}$  ( $4f^{13}$ ) and  $\text{Yb}^{2+}$  ( $4f^{14}$ ) in the same spectra is a signature of the intermediate valence character of the single ytterbium site in the cubic phase ( $T \geq 130$  K). Indeed, the  $f^{13}$  and  $f^{14}$  configurations are close in energy, and a non-zero hybridization yields a hybridized ground state with a non-integer 4f electron occupation number  $n_f$ . The  $f^{12}$  configuration lies at very high energy in the initial state, therefore its contribution is negligible. In the final state of the 3d photoemission process in Yb compounds, the core hole strongly interacts with the f-hole via the Coulomb interaction and leads to a reordering in the energies of the different configurations in the final state. The



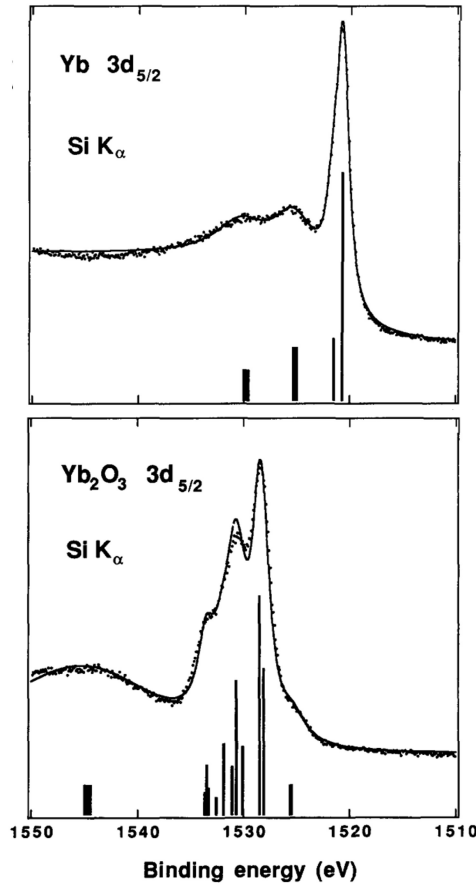


Figure 2.3: (a) Experimental Yb- $3d_{5/2}$  core level spectrum of Yb metal. The high intensity feature at 1520 eV corresponds to a  $3d^{10} \rightarrow 3d^9$  excitation while the peak around 1530 eV is related to a plasmon interaction. (b) Experimental Yb- $3d_{5/2}$  core level spectrum of  $Yb_2O_3$  with a structured feature around 1530 eV due to the multiplet effect and the structure at 1545 eV correspond to a plasmon interaction.

energies of the  $d^9 f^{13}$  and  $d^9 f^{14}$  configuration are respectively pulled down by the amount  $13U_{fc}$  and  $14U_{fc}$ , with  $U_{fc}$  denoting the interaction term between the f electrons and the 3d core hole which is attractive since the core hole is positively charged (see section 2.5 for detailed explanations). It has been shown that  $U_{fc}$  is about -10 eV for typical Yb compounds [20]. In the following, the Yb- $3d_{5/2}$  spectra will be investigated to obtain information about the hybridization and the Yb valence in YbPd.

Figure 2.5 shows the Pd 3d core level HAXPES spectrum of YbPd at  $T = 200$  K. The spectrum presents two single peaks which are Pd- $3d_{5/2}$  and Pd- $3d_{3/2}$  spin-orbit features. We performed a numerical fitting to accurately determined the binding energy of the spin-orbit features as well as their line shape. For this purpose, we used Lorentzian line shape after subtracting a Shirley background. The fitting result shown in Table 2.1 gives the binding energy of 336.1 eV and 341.4 eV for Pd- $3d_{5/2}$  and Pd- $3d_{3/2}$  respectively. The Pd- $3d_{5/2}$  and

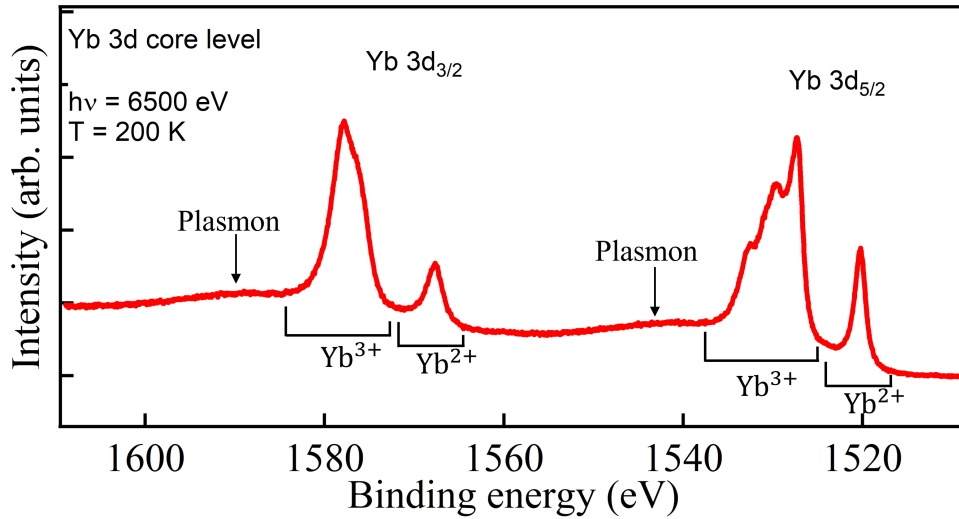


Figure 2.4: HAXPES spectra of Yb 3d core level in YbPd. Each spin-orbit manifold separated by about 48 eV is split into  $Yb^{2+}$  and  $Yb^{3+}$  characters which reflects the intermediate valence character of the Yb atom.

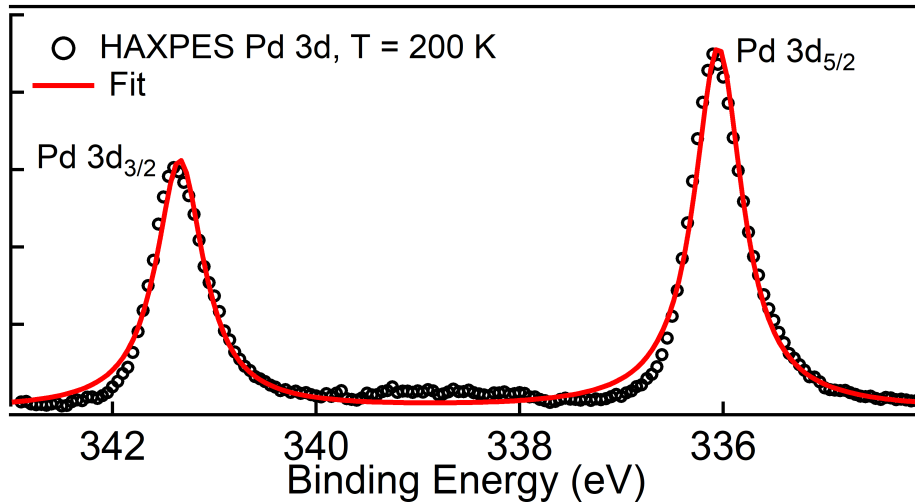


Figure 2.5: The Pd-3d core-level HAXPES spectrum of YbPd measured at  $T = 200$  K with an incident photon energy  $h\nu = 6500$  eV.

Pd- $3d_{3/2}$  binding energies are  $\sim 1$  eV higher than in pure metal. Moreover, the Pd peaks are symmetric as compared to the pure metal which are asymmetric with a factor  $\alpha = 0.2$ [21]. This is consistent with the fact that the Pd 4d band is completely filled as we will present just below given that the asymmetry factor is proportional to the density of states at the Fermi level.

Spin-orbit component	BE (eV)	width (eV)
Pd- $3d_{3/2}$	341.4	0.26
Pd- $3d_{5/2}$	336.1	0.26

Table 2.1: The fit parameters for the Pd 3d core-level spectrum

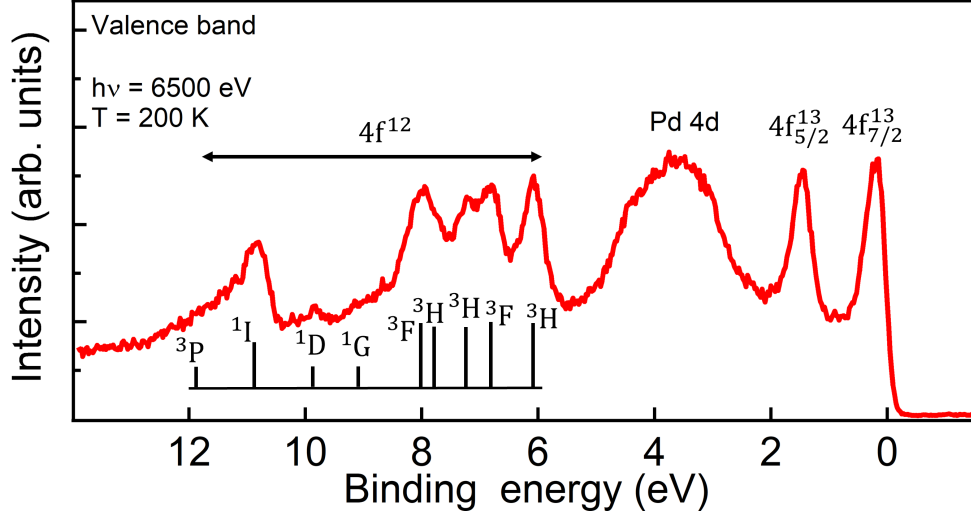


Figure 2.6: HAXPES valence band spectra of YbPd measured at  $T = 200$  K with 6500 eV of incident photon energy.

### 2.3.2 Yb 4f valence band spectra

Owing to the intermediate valence character of the ground state, the photoemission spectroscopy gives rise to both  $f^{13} \rightarrow f^{12}$  and  $f^{14} \rightarrow f^{13}$  transitions. Figure 2.6 shows the HAXPES valence band spectrum of YbPd measured at  $T = 200$  K. The spectrum exhibits a peak just below the Fermi level corresponding to Yb- $4f_{7/2}^{13}$  final states and its spin-orbit replicate Yb- $4f_{5/2}^{13}$  is at 1.3 eV. The broad prominent structure at 4 eV corresponds to the Pd-4d band which is completely filled. This is confirmed by the soft x-ray photoemission spectroscopy measured at 171 eV and 50 eV (see figure 2.7). The multiplet structures between 5 and 12 eV correspond to Yb- $4f^{12}$  final states. According to the LS coupling, the strong 4f-4f electron interaction leads to the splitting of the  $f^{12}$  configuration into seven multiplet states  $^1S$ ,  $^3P$ ,  $^1D$ ,  $^3F$ ,  $^1G$ ,  $^3H$  and  $^1I$ , where  $^3H$  corresponds to the lowest energy state following Hund's rules. In Figure 2.6, the distinct peaks between 6 eV and 8 eV are related to  $^3H$ ,  $^3F$  which are split into five peaks due to the spin-orbit coupling ( $^3H_6$ ,  $^3H_5$ ,  $^3H_4$ ,  $^3F_4$  and  $^3F_5$ ). The structures between 12 eV and 10 eV are associated with  $^1D$ ,  $^1I$ , and  $^3P$  final states.  $^3P$  states are also split into 3 different multiplets ( $^3P_0$ ,  $^3P_1$  and  $^3P_2$ ) but the experimental resolution is not enough to resolve the corresponding structures.

### 2.3.3 Photon energy dependence of the valence band: surface contribution and cross-section effect

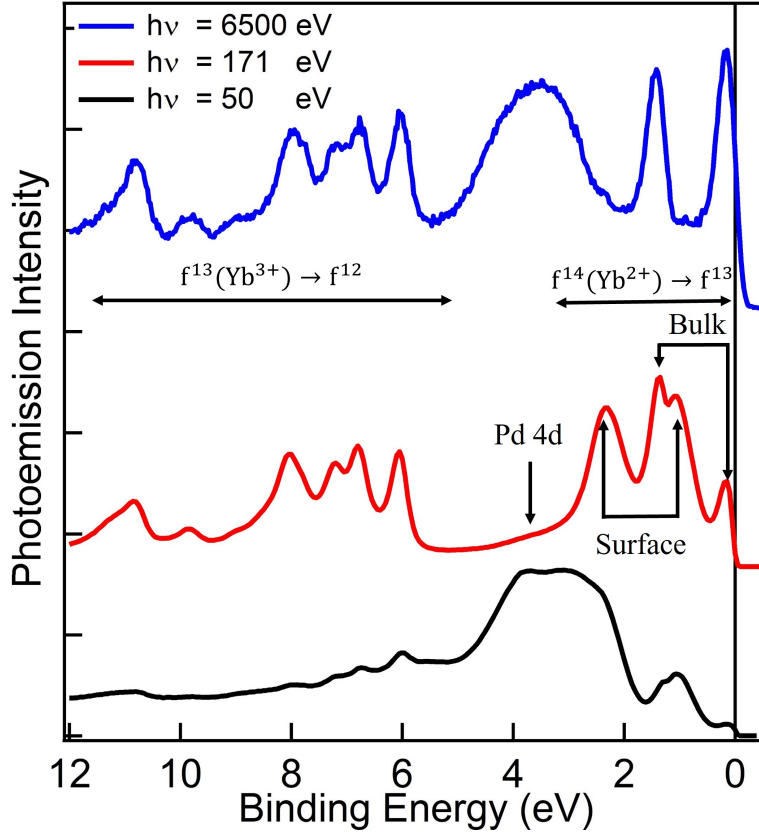


Figure 2.7: HAXPES valence band spectra of YbPd measured with 6500 eV, 171 eV and 50 eV of incident photon energy.

The different surface sensitivity of soft and hard x-ray photoemission spectroscopy has important effects on ytterbium compounds. Indeed, while the bulk contribution is usually intermediate valent, it has been theoretically [22] demonstrated and confirmed experimentally [23] that the divalent configuration  $4f^{14}$  is stabilized at the surface. Moreover, the relative intensities of the 4f structure are strongly photon energy dependent. Therefore, the spectral shape of the 4f states is strongly affected depending on subtle experimental conditions as well as the incident photon energy. To emphasize this surface sensitivity as well as the cross-section effect on the YbPd compound, we carried out the valence-band photoemission spectroscopy with three different incident photon energies:  $h\nu = 50$  eV, 171 eV and 6500 eV (see Figure 2.7). The spectrum at 6500 eV exhibits 2 structures near the Fermi-energy reflecting the bulk contribution and associated with  $f_{7/2}^{13}$  and  $f_{5/2}^{13}$  as explained above. The spectrum at 171 eV shows in addition to the structures at  $E \approx 0$  and 1.3 eV, two broad structures at  $E \approx 1.1$  and 2.3 eV which represent the surface contribution of the Yb 4f states. One can

see that the surface contribution at  $h\nu = 6500$  eV is negligible compared to that measured at 171 eV. This is due to the significant increase of the inelastic mean free path in the HAXPES region.

The shape of the valence band spectrum is also strongly dependent on the cross-section of Yb 4f and Pd 4d states. At 171 eV, we are close to the Cooper minimum of the Pd-4d band and therefore the intensity of the Pd structure is strongly reduced and appears just as a shoulder in the spectrum. At 50 eV of incident photon energy, the spectrum is dominated by the Pd 4d band due to the strong increases in its cross-section [24]. It should be noted that Pd 4d states are well below the Fermi level reflecting that the 4d band is completely filled.

## 2.4 Temperature dependence of the 4f occupancy across the CDW transitions in YbPd compound

### 2.4.1 Temperature dependence of the Yb-3d, Pd-3d core level, and valence band HAXPES spectra

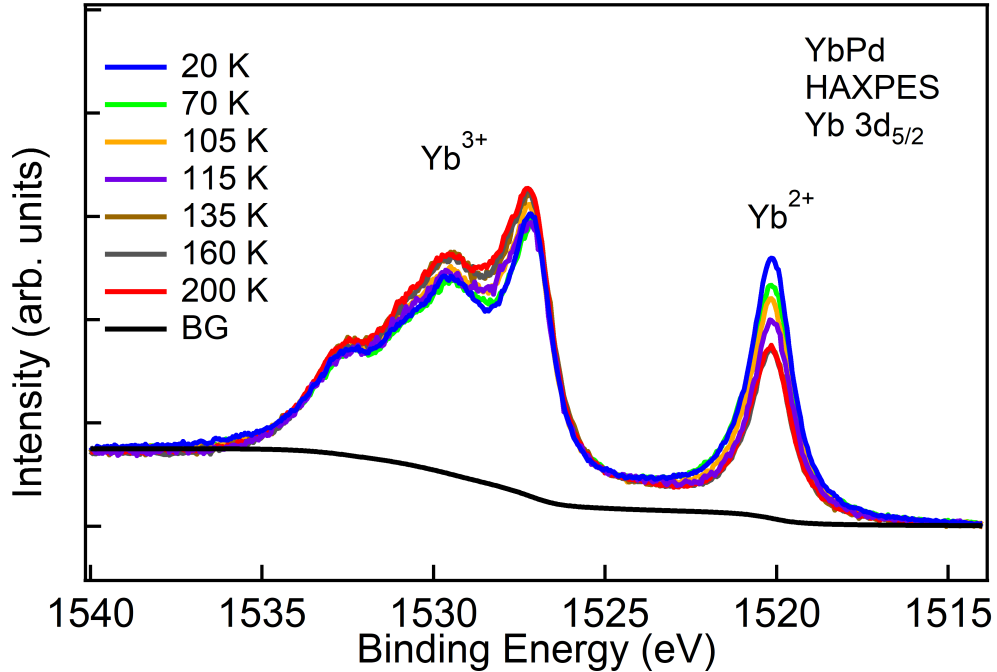


Figure 2.8: Experimental temperature dependence Yb- $3d_{5/2}$  of the core level HAXPES of YbPd between 20K and 200 K. The solid black line is the Shirley background subtracted to estimate the Yb- $3d_{5/2}$ -spectral weight. The spectra exhibit a temperature dependence below the CDW transition but are temperature independent above  $T_1 = 130$  K.

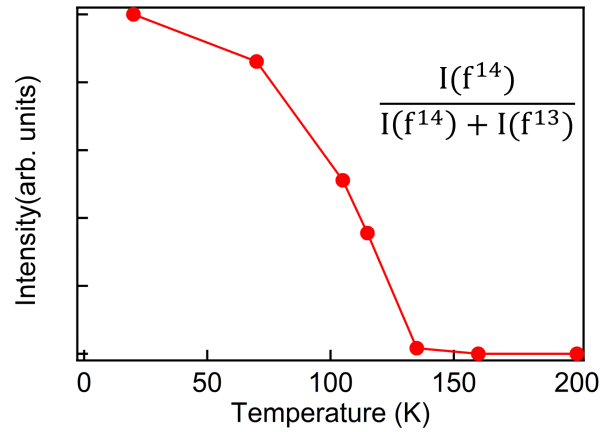


Figure 2.9: (a) Temperature dependence of the integrated intensities of the  $f^{14}$  to the  $f^{13}$  structure.

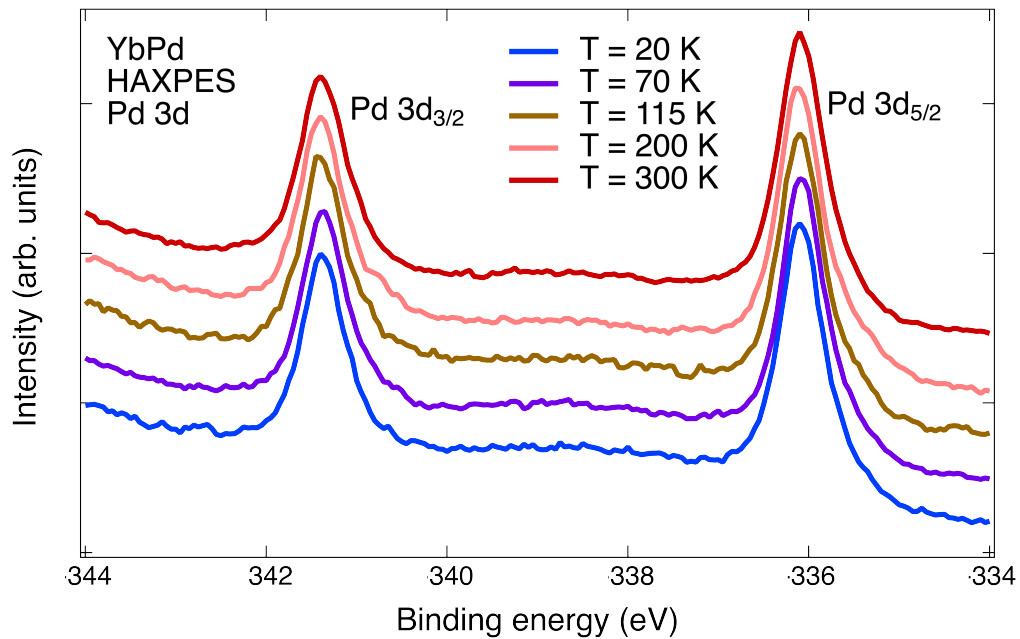


Figure 2.10: Temperature dependence of the Pd-3d core levels taking at different temperatures in the CDW phase ( $T = 20$  K,  $70$  K and  $115$  K) and in the cubic phase ( $T = 200$  K and  $300$  K).

The large mean free path of HAXPES makes this technique very powerful and accurate to determine the valence in Yb compounds. In order to study how the valence in YbPd changes across the CDW transition, we performed temperature-dependent HAXPES measurements. The temperature dependence of Yb- $3d_{5/2}$  spectra shown in Figure 2.8 exhibits 2 different

regimes: with increasing temperature from  $T = 20$  K to 135 K,  $\text{Yb}^{2+}$  spectral weight decreases and is transferred to  $\text{Yb}^{3+}$  suggesting an evolution of the average valence, whereas from  $T = 135$  K to 200 K the spectra are nearly temperature independent. This behavior is illustrated in Figure 2.9 where we report the temperature dependence of the relative integrated intensities of the  $\text{Yb}^{2+}$  to the  $\text{Yb}^{3+}$  structures. Interestingly, this temperature dependence is only observed in the CDW phase. The fact that the spectra are temperature independent above 135 K indicates that the temperature dependence observed below 135 K is due to the CDW and not the Kondo mechanism. Therefore, this temperature dependence is very unusual and does not resemble those of other Yb compounds reported in the literature [25, 26, 27, 28]. In the typical CDW materials such as transition-metal dichalcogenides, 1T-TaSe<sub>2</sub> and 1T-TaS<sub>2</sub> [29, 30], the XPS spectra exhibit a core level splitting and a change in the width of the Ta-4f features of up to 0.2 eV and 0.1 eV respectively. Therefore, the temperature independence of the energy peak positions of  $\text{Yb}^{2+}$  and  $\text{Yb}^{3+}$  features as well as their widths reveal an unusual behavior of the CDW transition in YbPd. This might be due to the fact that  $\text{Yb}^{3+}$  states are dominated by the multiplet effect which significantly broaden the structure ( $\sim 10$  eV), while for the  $\text{Yb}^{2+}$  ( $f^{14}$ ) states, the 4f level is completely filled and as a result, it is insensitive to any modification in shape and peak position. This unusual behavior is also evidenced via the temperature dependence of the Pd-3d core levels presented in Figure 2.10. The spectral shapes as well as the binding energies of Pd-3d<sub>5/2</sub> and Pd-3d<sub>3/2</sub> structures do not show any change with temperature.

One, therefore, needs to look for a mechanism that could explain the temperature dependence observed in the Yb 3d core level HAXPES of the YbPd compound. The fact that Yb 3d core-level photoemission spectra exhibit a temperature dependence only below 135 K indicates that there is a link with the CDW phase. In the CDW phase, the Pd atoms get continuously displaced, leading to a continuous increase of the  $\text{Yb}_1$ -Pd interatomic distances and a continuous decrease of the  $\text{Yb}_2$ -Pd interatomic distance with decreasing temperature. Hence, the ionic radius of the nearly trivalent  $\text{Yb}_1$ -site continuously decreases with decreasing temperature (the valence decreases), conversely the ionic radius of the intermediate valence  $\text{Yb}_2$ -site increases (the valence increases).

## 2.4.2 Temperature dependence of the valence band HAXPES spectra

Figure 2.11 shows the HAXPES valence band spectra of YbPd measured in the cubic phase ( $T = 200$  K) and in the CDW phase ( $T = 115$  K and 20 K). Unfortunately, spectra at only 3 temperatures have been recorded. Clear temperature dependence is observed in the  $\text{Yb}^{2+}$  and  $\text{Yb}^{3+}$  4f region while the Pd 4d state is almost temperature independent and no energy shift is observed. Furthermore, it should be noticed that the energy separation of the  $\text{Yb}^{2+}$  and  $\text{Yb}^{3+}$  structures given by  $\epsilon_f + U_{ff}$  is almost unchanged through the CDW transition.

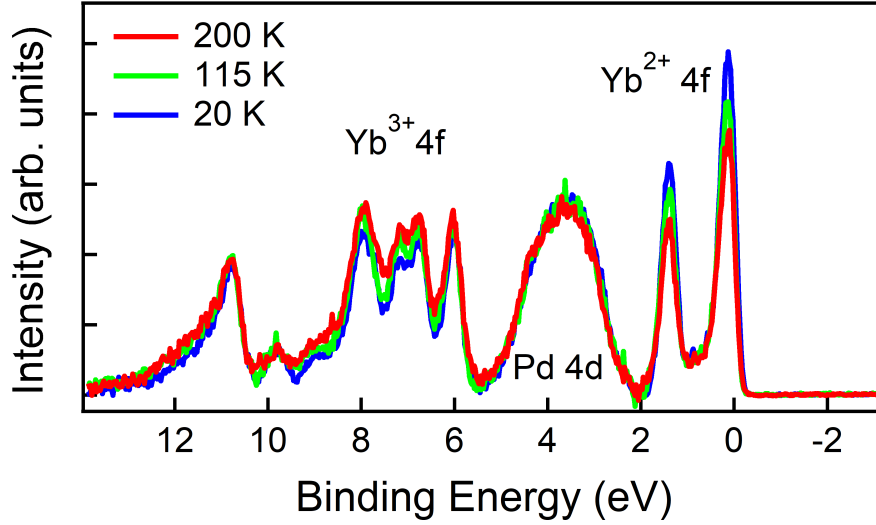


Figure 2.11: valence band temperature dependence

## 2.5 Simulations

### 2.5.1 The Gunnarsson and Schönhammer approach, and the Imer-Wuilloud toy model

When performing high-energy spectroscopy like core level photoemission on rare earth compounds and especially Ce and Yb compounds, the spectra are complex due to the presence of satellites with large intensities. The core hole strongly interacts with the valence band electron in the final state. By using a simplified version of the SIAM, Kotani and Toyozawa [31] proposed a new mechanism for La metal where the core hole potential can be either screened by the conduction electrons near the Fermi level or by a charge transfer electron from the conduction band states to the f states. Owing to the strongly localized character of the f states, this latter is more efficient.

In the early '80s, Gunnarsson and Schönhammer [32, 33, 34] extended the theory of Kotani and Toyozawa to study the core level (XPS and XAS at the  $M_{4,5}$  edges) spectra of cerium mixed-valence compounds by taking into account the large degeneracy of the 4f states ( $N_f = 14$  or  $N_f = 6$  if we take into account the spin-orbit splitting) as well as the Coulomb interaction ( $U_{ff}$ ). In order to take into account the core hole potential, the SIAM Hamiltonian is modified as follows in the final state:

$$\begin{aligned}
 H = & \sum_k \epsilon_k a_k^\dagger a_k + \sum_m \epsilon_f a_{m,\sigma}^\dagger a_{m,\sigma} + \sum_{mm'} U_{ff} n_m n_{m'} + \\
 & \sum_m V_{k,m} (a_k^\dagger a_{m,\sigma} + a_{m,\sigma}^\dagger a_k) + \epsilon_c - U_{fc} \sum_i a_{fi}^\dagger a_{fi},
 \end{aligned} \tag{2.1}$$



where  $\epsilon_c$  is the core level binding energy. GS assumed a semielliptical shape to represent the conduction band states given by:

$$f(\epsilon) = 2V^2[B^2 - (\epsilon - B)^2]^{1/2}/B^2, \quad (2.2)$$

with the hybridization strength  $\Delta = 2V^2/B$  defined as the average of  $f(\epsilon)$  over the occupied part of the conduction states. They calculated the ground state of the SIAM Hamiltonian variationally by using the  $\frac{1}{N_f}$  expansion method on a systematic basis represented in Figure 2.12 and calculated the spectroscopic properties. The states in the first, second and third row correspond to the basis states expanded by one order to  $N_f^0$ ,  $N_f^{-1}$  and  $N_f^{-2}$ , respectively. However, the orbital degeneracy of cerium ( $N_f = 14$ ) is sufficiently high and the lowest order approximation is enough to provide a satisfactory description of the core level spectra. Therefore the band electron-hole states can be neglected (second and third row in figure 2.12). Since the Coulomb interaction of the 4f state is very large, the basis state to diagonalize the Anderson Hamiltonian can be limited to 3 configurations: the  $|A\rangle = \prod_{i=1}^{N_f} a_{ki}^+ |0\rangle$  configurations where all the conduction electrons below the Fermi level are occupied and the f shell is empty, the  $|B\rangle$  configurations which contain one f-electron and one hole in the conduction band and the  $|C\rangle$  configuration with 2 holes in the conduction band.

$$|B\rangle = \frac{1}{\sqrt{N_f}} \sum_i a_{fi}^+ a_{ki} |A\rangle,$$

$$|C\rangle = \frac{1}{\sqrt{N_f(N_f - 1)}} \sum_{i,j} a_{fi}^+ a_{k_1i} a_{fj}^+ a_{k_2j} |A\rangle,$$

$|A\rangle$  is a singlet state and  $|B\rangle$  and  $|C\rangle$  are built to be singlet. In figure 2.12 we show an example of a calculated spectrum with a hybridization  $\Delta = 0.1$  eV ( $n_f = 0.83$ ) compared to the experimental Ce 3d XPS spectrum of *CeRu<sub>2</sub>* [35]. For many cerium compounds, the GS approach has been successfully applied to describe Ce  $M_{4,5}$ -edge XAS, core level, and valence band photoemission spectra. Most importantly, the same set of parameters consistently describe the XAS, core-level and VB PES for a compound [36, 37]. Contrary to thermodynamic and transport measurements which predicted a 4f occupancy (the valence) between 0 and 1 ( $3 \leq v \leq 4$ ) and hybridization of order  $\Delta \sim 0.01$  eV, the GS approach provides more reliable values for the hybridization which can be larger by 1 order of magnitude and show that  $n_f$  (the valence  $v$ ) can be in the range 0.7 to 1 ( $3 \leq v \leq 3.3$ ).

However, the GS approach requires considerable numerical computation effort which often led experimentalists to fit their spectroscopic data with phenomenological approaches. Following the GS model, a simplified version with a zero conduction bandwidth was introduced by Imer and Wuilloud [38]. The numerical effort of this approach is strongly reduced and is nearly trivial. As a result, it has been widely and successfully used to describe the core level spectra of cerium compounds [39, 40, 41, 42, 43, 44]. IW approach does not take into account the degeneracy of the 4f states and the basis which allows to qualitatively describe the spectra is limited to 3 singlet states: the configurations  $|f^0\rangle$ ,  $|f^1\bar{L}\rangle$  and  $|f^2\bar{L}^2\rangle$  with energy 0,  $\epsilon_f$  and  $2\epsilon_f + U_{ff}$ . In cerium compound, the typical values of these parameters are

$\epsilon_f \approx -1.7, -2$  eV and  $U_{ff} \approx 6-7$  eV. So, when the hybridization is zero, the ground state is given by the  $|f^1\rangle$  configuration and the second and third excited states are respectively given by the configurations  $|f^0\rangle$  and  $|f^2\underline{L}^2\rangle$  (see Figure 2.13a). In this basis the Anderson matrix Hamiltonian of the initial state ( $H_i$ ) is given by:

$$H_i = \begin{pmatrix} 0 & \Delta & 0 \\ \Delta & \epsilon_f & \Delta \\ 0 & \Delta & 2\epsilon_f + U_{ff} \end{pmatrix}, \quad (2.3)$$

where the diagonal terms represent the energies of the different configurations. Due to the off-diagonal hybridization, the eigenstates of the Hamiltonian are admixtures of the three different configurations. Then the initial ground state can be expressed as

$$|GS\rangle = a_0|f^0\rangle + a_1|f^1\underline{L}\rangle + a_2|f^2\underline{L}^2\rangle, \quad (2.4)$$

where  $|a_0|^2$ ,  $|a_1|^2$  and  $|a_2|^2$  respectively correspond to the weight of the  $f^0$ ,  $f^1$  and  $f^2$  configurations. The ground state is dominated by the  $f^1$  configuration ( $a_1 > a_0$  and  $a_1 \gg a_2$ ) and the 4f occupation is given by  $n_f = |a_1|^2 + 2|a_2|^2$ , which is non-integer and decreases on increasing the hybridization strength. In the final state, the presence of a core hole leads to a reordering in the energies of the configurations due to the strong attractive Coulomb interaction between the core hole and f electrons. The  $f^0$  energy remains unchanged while the  $f^1$  and  $f^2$  configurations are respectively pulled down by  $U_{fc}$  and  $2U_{fc}$ . The final state configurations in presence of a core-hole (in the limit of zero hybridization) are shown in Figure 2.13a. The lowest state in energy is given by the  $f^2$  configuration in which the core hole is well screened by the f electrons. The first excited state is given by the  $f^1$  configuration that nearly overlaps with the  $f^2$  configuration while the  $f^0$  configuration is well separated by about 11 eV from the  $f^1$  configuration. In the final state, the matrix Hamiltonian  $H_f$  is given by :

$$H_f = \begin{pmatrix} 0 & \Delta & 0 \\ \Delta & \epsilon_f + U_{fc} & \Delta \\ 0 & \Delta & 2\epsilon_f + U_{ff} + 2U_{fc} \end{pmatrix}. \quad (2.5)$$

The off-diagonal terms lead to a sizable mixture of the  $f^1$  and  $f^2$  configurations since they are close in energy contrary to the  $f^0$  configuration, which are well separated from the  $f^1$  configuration and nearly remain a pure configuration. Therefore, the lowest state in energy is dominated by the  $f^2$  configuration, the first excited state is dominated by the  $f^1$  configuration and the last excited state is nearly a purely  $f^0$  configuration. The photoemission spectrum corresponds to the transitions from the ground state to all final states. Therefore, three structures are expected as shown in Figure 2.13b with their intensity reflecting the hybridized character in both the initial and final states of the photoemission process. Indeed, the intensity of the  $f^0$  structure depends on the mixing between the  $f^0$  and  $f^1$  configurations in the ground state while the intensity of the  $f^2$  structure depends both on the mixing between the  $f^0$  and  $f^1$  configurations in the initial state and the mixing between  $f^1$  and  $f^2$  configurations in the final state. It should be noted that owing to the 3d spin-orbit coupling which split

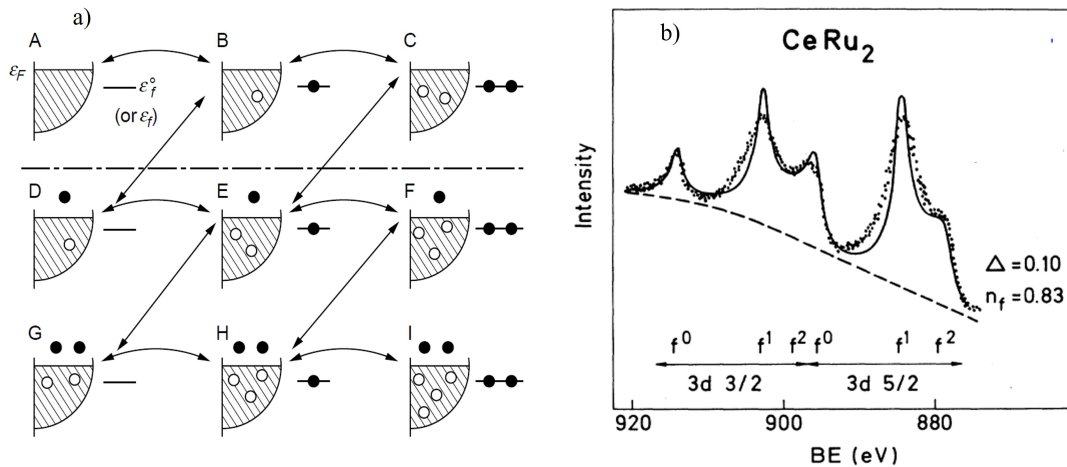


Figure 2.12: (a) Schematic representation of the basis state in the GS approach. The hatched semi-elliptical form represents the conduction bands states and the horizontal bar represents the 4f shell. (b) Comparison between experimental Ce 3d XPS spectra of  $CeRu_2$  and calculated spectra with GS approach [35].

the  $3d_{5/2}$  and  $3d_{3/2}$  by about 18 eV, the photoemission spectra exhibit 6 structures, three for each spin-orbit feature (see Figure 2.12b)

This toy model allows to qualitatively reproduce the main features in the core-level spectra. However, it has drawbacks compared to the original approach by Gunnarsson and Schönhammer, especially regarding the low-energy excitations reflected by the Kondo peak in valence band PES. Indeed, it is no longer possible to extract reliable values for the Kondo temperature since the approach only takes into account three singlet states. Moreover, it is not possible to satisfactorily describe both photoemission and inverse photoemission spectra with the same set of parameters ( $\Delta$ ,  $\epsilon_f$ , and  $U_{ff}$ ).

IW mentioned that this model can be adapted and used to describe the spectra of other 4f elements in the beginning and the ending of the rare earth series if the multiplet effects are discarded. However, such an adaptation to the Yb core-level photoemission has not been developed to date. This might be due to the fact that cerium compounds have been studied much more than Yb compounds, mainly because the binding energy of Yb 3d levels was larger (about 1576.3 eV for  $3d_{3/2}$  and 1527.8 eV for  $3d_{5/2}$ ) than the photon energy of Al  $K\alpha$  ( $h\nu = 1486.6$  eV) and Mg  $K\alpha$  ( $h\nu = 1253.6$  eV) used in laboratory measurements. Thanks to the development of synchrotron radiation sources with high brilliance and hard x-ray energy, a large number of photoemission spectroscopy measurements have been performed on Yb 3d levels of Yb compounds in the last few years.

As a free atom, Yb is characterized by a divalent  $[Xe]5d^06s^24f^{14}$  configuration, where divalent refers to the number of valence electrons. In a solid, Yb atoms can also be found in the trivalent  $[Xe]5d^16s^24f^{13}$  configuration which is close in energy to the divalent configuration and gives rise to an intermediate valent behavior via the hybridization between f

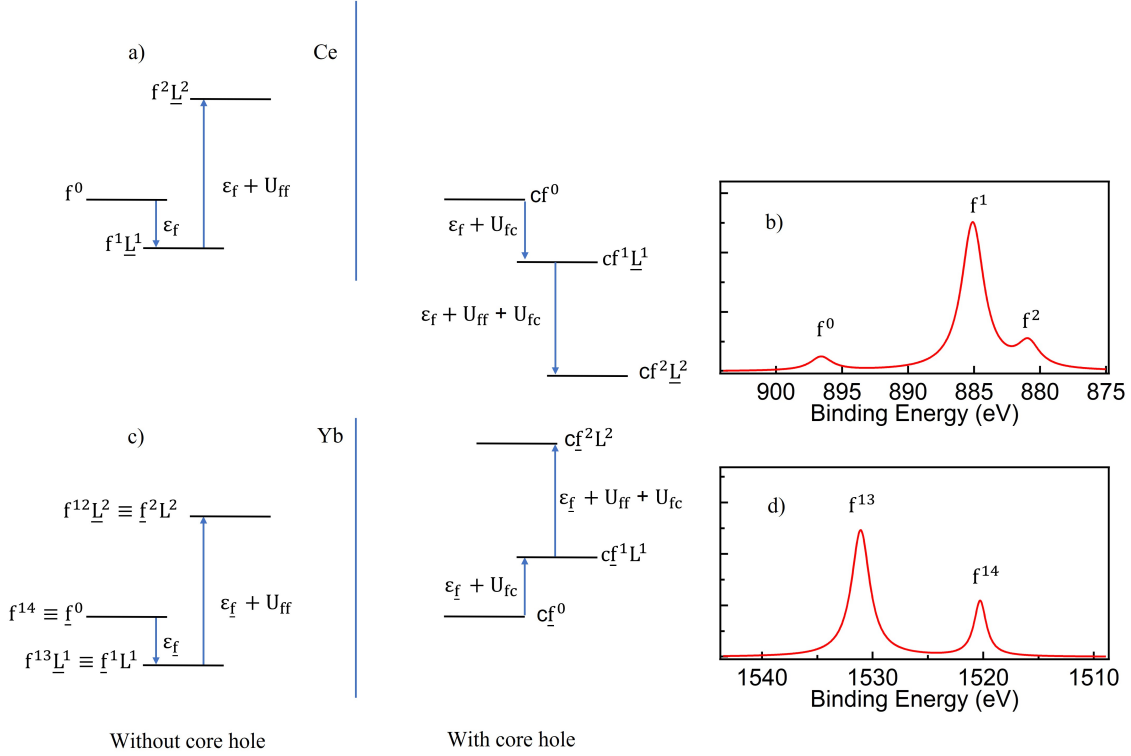


Figure 2.13: Schematic representation of the energies of the different configurations of Ce atom (a) in the electron picture and Yb atom (c) in the hole picture with and without a core hole. Configurations are labeled according to the number of f-holes or electrons.  $\underline{L}$  and  $L$  respectively denote a hole and an electron in the conduction band states. (b) Ce and (d) Yb core-level spectra with respectively three and two structures corresponding to the final states in presence of a core hole.

and conduction electrons. We can describe the core level spectra of Yb compounds by exploiting the electron-hole symmetry of the Anderson Hamiltonian. Electron-hole symmetry consists of taking into account the presence of a hole instead of an electron in the 4f shell. For instance, the  $f^1$  configuration where one f electron is added with respect to the empty  $f^0$  configuration is similar to the  $f^{13}$  configuration where one f electron is removed from the filled  $f^{14}$  configuration (a hole is created in the 4f shell). So,  $f^{13}$  is equivalent to  $\underline{f}^1$  configuration with  $\underline{f}$  denoting a hole in the 4f shell. Similarly,  $f^{14}$  and  $f^{12}$  configurations are equivalent to  $\underline{f}^0$  and  $\underline{f}^2$  configurations respectively. Electron-hole symmetry transformation of the Anderson Hamiltonian is obtained by replacing the destruction (creation) operator for f states by a creation (annihilation) operator of f-holes  $a_{m,\sigma} \rightarrow \underline{f}_{m,\sigma}^+$  ( $a_{m,\sigma}^+ \rightarrow \underline{f}_{m,\sigma}$ ). The f electron energy  $\epsilon_f$  in the Anderson Hamiltonian is thus changed as  $\epsilon_f = -\epsilon_f - 13U_{ff}$  whereas the coulomb repulsion remains unchanged ( $U_{ff} = U_{\underline{f}\underline{f}}$ ). Similarly, in the Hamiltonian of the final state, the core-hole interaction  $U_{fc}$  is changed to  $U_{\underline{f}c} = -U_{fc}$ . So, the  $f^{14}$ ,  $f^{13}$  and  $f^{12}$  configurations with energy  $14\epsilon_f + 91U_{ff}$ ,  $13\epsilon_f + 78U_{ff}$  and  $12\epsilon_f + 66U_{ff}$  respectively are

equivalent to the hole representation: the  $\underline{f}^0$ ,  $\underline{f}^1$  and  $\underline{f}^2$  configurations with energy 0,  $\epsilon_{\underline{f}}$  and  $2\epsilon_{\underline{f}} + U_{ff}$  respectively. In the final state, the  $\underline{f}^1$  and  $\underline{f}^2$  configurations are respectively pulled up by  $U_{fc}$  and  $2U_{fc}$  (see Figure 2.13) and the 4f hole occupation is given by  $n_{\underline{f}} = 14 - n_f$ . An example of a calculated core-level spectrum of Yb compounds is shown in figure 2.13d. Contrary to cerium compounds, we have a repulsive core-hole interaction in the final state ( $U_{fc} > 0$ ) and therefore the spectrum exhibits two structures corresponding to  $\underline{f}^{14}$  and  $\underline{f}^{13}$  final states separated by about 10 eV.

To quantitatively analyze core level spectra of Yb compounds and determine the valence, it is sometimes assumed that the effect of the final states is smaller than in Ce. Therefore, the SIAM in the framework of the GS approach [45] is sometimes omitted and it is assumed that the relative weight of the spectral structures  $Yb^{2+}$  ( $\underline{f}^{14}$ ) and  $Yb^{3+}$  ( $\underline{f}^{13}$ ) directly yield access to the 4f hole occupancy:

$$\frac{I(\underline{f}^{13})}{I(\underline{f}^{13}) + I(\underline{f}^{14})} \approx n_{\underline{f}}. \quad (2.6)$$

As we will present in more detail in the next section, this is a crude approximation and a mixing of the final state configuration requires a SIAM calculation to determine the 4f hole occupancy from Yb 3d core-level photoemission.

## 2.5.2 Simple approximation scheme of Gunnarsson and Schönhammer model: Case of Yb compounds

### 2.5.3 Description of the model

We have developed a simplified approach following the GS approach initially introduced to describe the core level (XPS and XAS) and valence band spectra of Ce and La compounds. We developed a code to describe XPS and valence band spectra of Yb compounds. What is new in our calculation is that we explicitly take into account the total degeneracy of the 4f states. The basis states are given by:

$$|\underline{f}^0\rangle = \prod_{i=1}^{N_f} a_{ki}^+ |0\rangle,$$

$$|\underline{f}^1, i\rangle = a_{fi}^+ a_{ki} | \underline{f}^0 \rangle,$$

$$|\underline{f}^2, ij\rangle = a_{fi}^+ a_{ki} a_{fj}^+ a_{kj} | \underline{f}^0 \rangle, \quad (i > j, i \neq j)$$

where  $i$  and  $j$  run from 1 to  $N_f$ .  $a_{ki}^+$  ( $a_{ki}$ ), and  $a_{fi}^+$  ( $a_{fi}$ ) are the electron creation (annihilation) operators in the conduction band (zero bandwidth) and 4f states respectively. So, the dimension of the basis used to diagonalize the Hamiltonian is  $1 + N_f + N_f(N_f - 1)/2$ , which includes 1 state of configuration  $\underline{f}^0$ ,  $N_f$  states of configuration  $\underline{f}^1$  and  $N_f(N_f - 1)/2$  states of configuration  $\underline{f}^2$ . Further, we include the 4f spin-orbit splitting  $\Delta_{so}$  which has a negligible

effect in the core level spectra but it is crucial for describing the valence band spectra. In this basis, the matrix elements of the Hamiltonian are given by:

- for the 106 diagonal elements

$$\langle \underline{f}^0 | H | \underline{f}^0 \rangle = 0$$

$$\langle \underline{f}_{7/2}^1, i | H | \underline{f}_{7/2}^1, i \rangle = \epsilon_{\underline{f}}$$

$$\langle \underline{f}_{5/2}^1, i | H | \underline{f}_{5/2}^1, i \rangle = \epsilon_{\underline{f}} + \Delta_{so}$$

$$\langle \underline{f}^2, ij | H | \underline{f}^2, ij \rangle = 2\epsilon_{\underline{f}} + U_{ff}$$

- for the 392 nonzero off diagonal elements

$$\langle \underline{f}_{5/2}^1, i | H | \underline{f}^0 \rangle = \langle \underline{f}_{7/2}^1, i | H | \underline{f}^0 \rangle = V$$

$$\langle \underline{f}^2, ij | H | \underline{f}_{5/2}^1, i \rangle = \langle \underline{f}^2, ij | H | \underline{f}_{7/2}^1, i \rangle = V$$

$$\langle \underline{f}^2, ij | H | \underline{f}_{5/2}^1, j \rangle = \langle \underline{f}^2, ij | H | \underline{f}_{7/2}^1, j \rangle = V$$

$$\left( \begin{array}{cccccccccccc} 0 & V & V & V & V & \dots & V & 0 & \dots & \dots & \dots & 0 \\ V & \epsilon_{\underline{f}} & 0 & 0 & 0 & 0 & 0 & 0 & V & \dots & 0 & 0 \\ V & 0 & \epsilon_{\underline{f}} & 0 & 0 & 0 & 0 & 0 & 0 & V & \dots & 0 \\ \\ V & 0 & 0 & \ddots & 0 & 0 & 0 & 0 & \dots & V & 0 & V \\ V & 0 & 0 & 0 & \epsilon_{\underline{f}} + \Delta_{so} & V & 0 & 0 & \dots & V & \dots & 0 \\ \vdots & 0 & 0 & \vdots & \vdots & \vdots & \ddots & \vdots & \ddots & \ddots & V & 0 \\ V & 0 & 0 & 0 & 0 & 0 & \epsilon_{\underline{f}} + \Delta_{so} & 0 & \dots & \dots & 0 & V \\ \\ 0 & 0 & 0 & 0 & 0 & \vdots & 0 & 2\epsilon_{\underline{f}} + U_{ff} & 0 & 0 & \dots & 0 \\ 0 & V & 0 & \vdots & \dots & \ddots & \dots & 0 & \ddots & \vdots & \ddots & \vdots \\ \vdots & \vdots & V & V & V & \ddots & \dots & 0 & 0 & 2\epsilon_{\underline{f}} + U_{ff} & 0 & 0 \\ \vdots & 0 & \vdots & 0 & \dots & V & 0 & 0 & \dots & \ddots & 2\epsilon_{\underline{f}} + U_{ff} & 0 \\ 0 & 0 & 0 & V & 0 & 0 & V & 0 & 0 & \dots & \dots & 2\epsilon_{\underline{f}} + U_{ff} \end{array} \right) \quad (2.7)$$

A direct diagonalization allows us to obtain the ground state which can be written in terms of a quantum mechanical mixture of the different configurations as:

$$|GS\rangle = a^0 |\underline{f}^0\rangle + a_{7/2}^1 \sum_{i=1}^8 |\underline{f}_{7/2}^1, i\rangle + a_{5/2}^1 \sum_{i=9}^{14} |\underline{f}_{5/2}^1, i\rangle + \sum_{i>j} a_{ij}^2 |\underline{f}^2, ij\rangle. \quad (2.8)$$

The number of f-holes in the ground state is given by :

$$n_{\underline{f}} = w_1 + 2w_2, \text{ with } w_1 = 8(a_{7/2}^1)^2 + 6(a_{5/2}^1)^2 \text{ and } w_2 = 2 \sum_{i>j} (a_{ij}^2)^2, \quad (2.9)$$

where  $w_1$  and  $w_2$  represent the weights of the  $\underline{f}^1$  and  $\underline{f}^2$  configurations. The first excited states are nearly pure  $\underline{f}_{7/2}^1$  states, and the second excited state is a singlet mixture of all the different configurations but dominated by the  $\underline{f}^0$  configurations. The hybridized singlet and  $\underline{f}_{5/2}^1$  spin-orbit states correspond to the third and fourth excited states respectively, and the last excited states correspond to the  $\underline{f}^2$  configuration (see Figure 2.14). Let us note that in cerium compounds the ground state is given by the  $\underline{f}_{5/2}^1$  configuration with the  $\underline{f}_{7/2}^1$  configuration located at 0.28 eV so that  $|\Delta_{so}| < |\epsilon_f|$  whereas in Yb compounds the ground state is the  $\underline{f}_{7/2}^1$  configuration and  $|\Delta_{so}| > |\epsilon_f|$  ( $\Delta_{so} \sim 1.28$  eV).

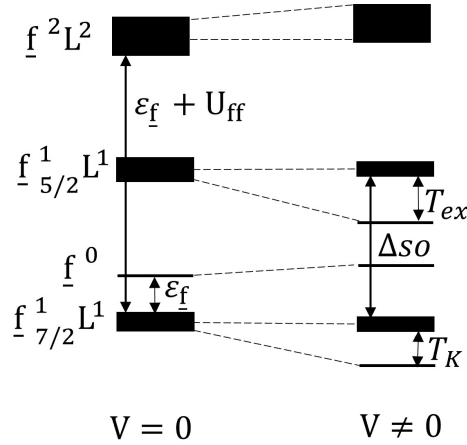


Figure 2.14: Total energy spectrum of the ytterbium states. The atomic levels ( $V = 0$ ) are displaced in energy by the hybridization.

### 2.5.4 3d core-level photoemission

In the 3d photoemission process, the spectral intensity of PES at zero temperature is given by:

$$I(E) = \sum_f \left| \langle \Psi_f | a_c | GS \rangle \right|^2 \left[ \frac{\Gamma/\pi}{\Gamma^2 + (E - E_f + E_G)^2} \right], \quad (2.10)$$

where  $a_c$  represents the annihilation operator of core electron,  $|GS\rangle$  is the ground state (with energy  $E_G$ ) and  $|\Psi_f\rangle$  is a final state (with energy  $E_f$ ).  $\Gamma$  is the broadening to take into account the core hole lifetime and the instrumental resolution (the energy resolution for the HAXPES measurements was about 0.25 eV).

For the 3d photoemission final states, we do need to account of the core-hole, so the basis states can be written as:  $|c\underline{f}^0\rangle = a_c|\underline{f}^0\rangle$ ,  $|c\underline{f}^2, ij\rangle = a_c|\underline{f}^2, ij\rangle$ ,  $|c\underline{f}^1, i\rangle = a_c|\underline{f}^1, i\rangle$ , where  $c$  denotes the presence of a core hole in the final state. The diagonal elements of the final state Hamiltonian is defined as :

$$\langle c\underline{f}^0 | H | c\underline{f}^0 \rangle = \epsilon_c$$

$$\begin{aligned}\langle c_{\underline{f}_{7/2}}^1, i | H | c_{\underline{f}_{7/2}}^1, i \rangle &= \epsilon_{\underline{f}} + U_{\underline{f}c} + \epsilon_c \\ \langle c_{\underline{f}_{5/2}}^1, i | H | c_{\underline{f}_{5/2}}^1, i \rangle &= \epsilon_{\underline{f}} + \Delta_{so} + U_{\underline{f}c} + \epsilon_c \\ \langle c_{\underline{f}}^2, ij | H | c_{\underline{f}}^2, ij \rangle &= 2\epsilon_{\underline{f}} + U_{\underline{f}f} + 2U_{\underline{f}c} + \epsilon_c\end{aligned}$$

Here,  $\epsilon_c$  is defined as the energy of the core level. We assume that the off-diagonal matrix elements are the same as for the initial state. The diagonalization of the corresponding Hamiltonian gives the final states which are expressed as:

$$|\Psi_f^m\rangle = c^{0,m} |c_{\underline{f}}^0\rangle + c_{7/2}^{1,m} \sum_{i=1}^8 |c_{\underline{f}_{7/2}}^1, i\rangle + c_{5/2}^1 \sum_{i=9}^{14} |c_{\underline{f}_{5/2}}^1, i\rangle + \sum_{i>j} c_{ij}^{2,m} |c_{\underline{f}}^2, ij\rangle, \quad (2.11)$$

where  $m$  runs over all the final 106 states.

## 2.5.5 Phenomenological reproduction of the complex line shape due to multiplet effects: $3d^9 4f^{13}$ photoemission final states

Using only the single parameters for the Coulomb interaction between f electrons and the interaction between the core hole and the f electron is very suited to describe the  $3d^9 4f^{13}$  and  $3d^9 4f^{14}$  final state configuration in the photoemission spectra, but it is impossible to reproduce the complex line shapes of the  $Yb^{3+}$  final state which is due to the multiplet effect.

In rare-earth compounds and especially ytterbium, the strongly localized character of the 4f shell leads to a complex line shape of the core level and valence band photoemission spectra. Let's describe these complex line shapes by studying the spectra of purely divalent and trivalent Yb compounds such as Yb metal and  $Yb_2O_3$ . For Yb metal, Yb ion is 2+ and has a  $f^{14}$  configuration. The 3d photoemission final state corresponds to  $3d^9 4f^{14}$  configuration, which is split by the 3d spin-orbit coupling into  $3d_{5/2}^9 4f^{14}$  and  $3d_{3/2}^9 4f^{14}$  states separated by about 50 eV. Yb ions in  $Yb_2O_3$  is 3+ and has therefore a  $f^{13}$  configuration which is split by the 4f spin-orbit interaction into 8 states with  $J = 7/2$  and 6 states with  $J = 5/2$ . The final state of 3d photoemission has a  $3d^9 4f^{13}$  configuration with  $10 \times 14 = 140$  states. The strong interaction between the core hole and the f-hole lifts the degeneracy of this electronic configuration and leads to 10 multiplet states in the LS coupling including 5 spin singlets ( $S = 0$ ) and 5 spin triplets ( $S = 1$ ):  $^1S, ^1P, ^1D, ^1F, ^1G, ^1H, ^3S, ^3P, ^3D, ^3F, ^3G, ^3H$ . Therefore, the 3d-photoemission spectra correspond to the transition from the ground state to all the multiplets in the final state. In figure 2.15, we show on the left side the initial state  $3d^9 4f_{5/2}^{13}$  and the transitions within the final state multiplets. On the right side of Figure 2.15, we show the calculated multiplet structure of  $3d^9 4f^{13}$  for the 3d spin-orbit level  $J = 5/2$ . All the multiplet states are not resolved and the spectrum exhibits 4 main structures centered around 1350 eV.

In order to phenomenologically reproduce the complex line shape of  $Yb^{3+}$  final state with our present approach, we have regrouped the 10 multiplets into 4 different states namely  $\psi_1$ ,



$\psi_2$ ,  $\psi_3$  and  $\psi_4$  by introducing 4 different energy levels  $E(cf)_1$  (4 times degenerate),  $E(cf)_2$  (2 times degenerate),  $E(cf)_3$  (1 time degenerate) and  $E(cf)_4$  (1 time degenerate) (see Figure 2.15 right panel). These 4 different energy levels have been introduced in the  $cf_{7/2}^1$  final states in our Hamiltonian. The calculated spectra with this simplified approach exhibit 4 structures close to  $\epsilon_f + E(cf)_1$ ,  $\epsilon_f + E(cf)_2$ ,  $\epsilon_f + E(cf)_3$  and  $\epsilon_f + E(cf)_4$ . In order to check the validity of our approach, we carried out atomic full-multiplet calculations to reproduce the line shape of the  $Yb3d_{5/2}$  core level spectrum. The values of the Slater integrals F and G, as well as the spin-orbit coupling  $\zeta$ , are taken from the Crispy [46](the graphic interface of the Quanty code). These values are then reduced to 95% to account for the screening of the electron-electron interaction in solids. The parameters of the  $3d^{10}4f^{13}$  and  $3d^94f^{13}$  configurations in units of eV are respectively given by:  $(F_{ff}^2, F_{ff}^4, F_{ff}^6, \zeta_f) = (16.84, 10.56, 7.6, 0.37)$  and  $(F_{df}^2, F_{df}^4, F_{df}^6, G_{df}^1, G_{df}^3, G_{df}^5, \zeta_d) = (11.68, 5.55, 8.62, 5.06, 3.5, 19.39)$ . The calculated spectrum is then convoluted with a Lorentzian function (FWHM = 0.2 eV) to account for the core-hole lifetime. As shown in figure 2.15, our simplified calculation is in nice agreement with the full multiplet calculation using the Quanty code [47, 48].

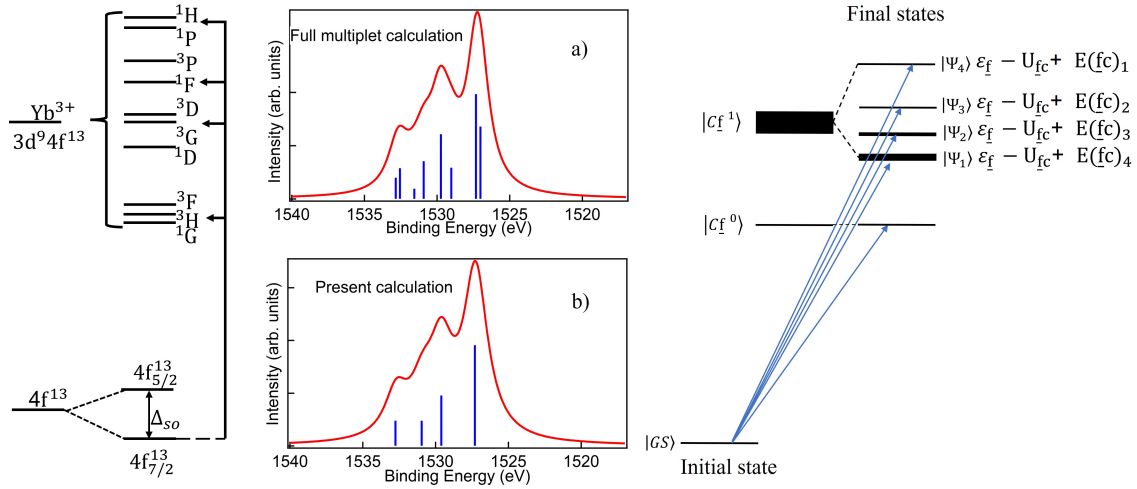


Figure 2.15: (a) Calculated spectrum with the parameters:  $E(cf)_1 = 2.5$  eV,  $E(cf)_2 = 0.4$  eV,  $E(cf)_3 = -0.6$  eV,  $E(cf)_4 = -2.95$  eV. (b) Full multiplet calculation using the Quanty code. The line diagrams indicate the spectral weight of the final states in both cases.

## 2.5.6 Calculation of the Yb core level: Final states effect and influence of the different parameters

- **Final states effect** By neglecting the hybridization in the final states, the intensity of  $Yb^{3+}$  ( $f^{13}$ ) and  $Yb^{2+}$  ( $f^{14}$ ) final states in Yb 3d PES would be respectively proportional to the weight of  $f^1$  and  $f^0$  configurations in the initial ground state and therefore we would

have:

$$\frac{I(f^{14})}{I(f^{14}) + I(f^{13})} = 1 - n_{\underline{f}}, \text{ with valence } v = 2 + n_{\underline{f}}. \quad (2.12)$$

In Figure 2.16, we illustrate the relative intensity of  $Yb^{2+}$  structure plotted as a function of the hybridization. For comparison, we also show the evolution of  $1 - n_{\underline{f}}$ , the weight of the  $f^0$  configuration in the ground state. There is a deviation that is small but not negligible, especially for strongly intermediate valences (large hybridization). Therefore, the estimation of the valence by the relative intensities of  $Yb^{2+}$  and  $Yb^{3+}$  final states is underestimated. For instance, with a hybridization,  $\Delta = 110$  meV an estimation of the valence from the relative intensity of  $Yb^{2+}$  structure would give a valence  $v = 2.61$  whereas a ground state valence would correspond to a value of 2.65.

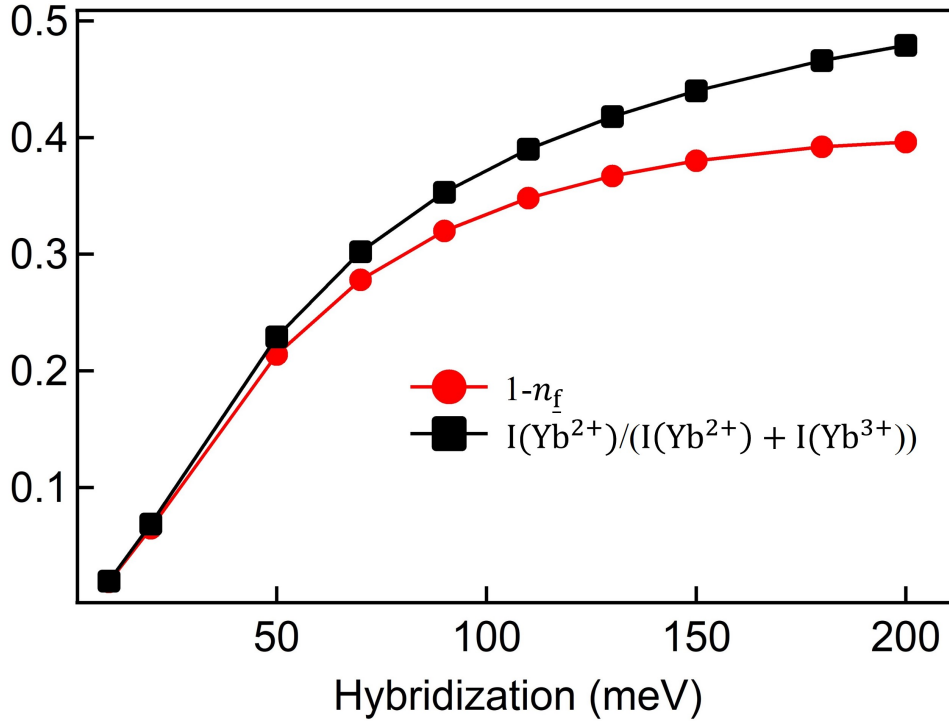


Figure 2.16: Relative integrated intensity of  $f^{14}$  to  $f^{13}$  structures compared to the 4f occupation in the ground state  $1 - n_{\underline{f}}$ .

**- Hybridization dependence** As we have mentioned above, the weights  $w_0$  and  $w_1$  of the configurations  $f^0$  and  $f^1$  in the ground state are in general not directly proportional to the relative intensities of their corresponding PES structure due to the mixing of the configurations in the final states of the process. Let's calculate the XPS spectra as a function of the configuration weights in the ground state. The weights  $w_0$  and  $w_1$  are varied either by shifting the f-energy level with respect to the Fermi level or by increasing hybridization strength from

the trivalent configuration ( $\Delta = 0$ ). The values of Coulomb interaction between f-holes  $U_{ff}$  and the Coulomb interaction between the core hole and f-hole  $U_{fc}$  are also necessary. This later is estimated by using the separation between the center of barycenter of the  $3d_{5/2}^9 4f^{13}$  and the  $3d_{5/2}^9 4f^{14}$  XPS final states which is in general of the order of 10 – 11 eV [20, 49]. From the valence band XPS,  $U_{ff}$  has been found to be about 7 eV [50].

Figure 2.17a presents the hybridization dependence of the calculated 3d photoemission spectra with all the other parameters kept constant. When the hybridization between the f states and the conduction band states is zero, the spectrum only exhibits  $Yb^{3+}$  final state reflecting the purely trivalent character of the initial ground state. By switching on the hybridization, an additional structure appears at 1520 eV of binding energy corresponding to  $Yb^{2+}$  final state and reflecting the mixed character of the ground state. The mixing of the different configurations becomes more important with increasing hybridization strength, leading to the increase of the  $f^0$  weight in the ground state. At the same time, the  $f^0$  weight ( $Yb^{2+}$ ) also increases in the final state. Therefore, the increase of the hybridization leads to the increase of  $Yb^{2+}$  intensity and decreases the hole number  $n_f$ . It is worth noting that there is no structure corresponding to  $3d_{5/2}^9 4f^{12}$  final states. It is due to the fact that  $f^2$  states lie at very high energy and their contribution to the initial ground state is negligible. The parameters and the weight of each configuration in the ground state are reported in table 1. It should be noted that the intensity ratio of the  $Yb^{2+}$  and  $Yb^{3+}$  final states track the  $f^0$  weight in the ground state but does not give  $w_0$  exactly. This is well illustrated in Figure 2.16.

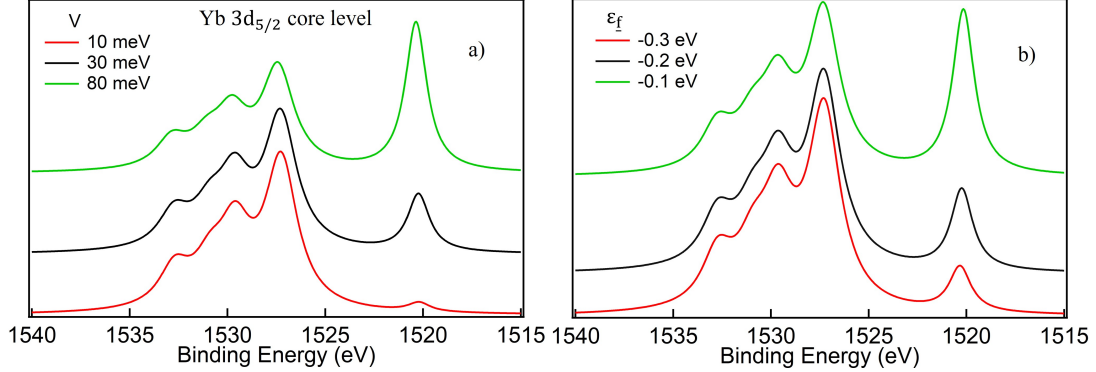


Figure 2.17: Calculated Yb  $3d_{5/2}$  core level spectra as a function of the hybridization  $\Delta$  between the f states and the conduction band states (a) and the energy of the f-hole  $\epsilon_f$  (b).

**- f-hole energy dependence** The relative intensities of  $Yb^{2+}$  and  $Yb^{3+}$  final states are also strongly sensitive to the f energy hole which has been found to be not less than 0.4 eV with respect to the Fermi level. Figure 2.17b shows the evolution of the Yb 3d core level and valence band spectra with the energy of the f state and keeping all the other parameters constant. With decreasing  $|\epsilon_f|$  the energy separation between  $f^0$  and  $f^1$  configurations decreases leading to an increase in the mixing in the initial ground state. Therefore, similar to the hy-

V (meV)	$U_{ff}$ (eV)	$U_{fc}$ (eV)	$\epsilon_f$ (eV)	$n_f$	$w_0$	$w_1$
10	7	11	-0.2	0.98	0.02	0.98
30	7	11	-0.2	0.88	0.12	0.88
80	7	11	-0.2	0.7	0.3	0.7

Table 2.2: Table showing the parameters used for the hybridization (V) dependence of the Yb core level and 4f valence band spectra

bridization dependence, when the energy of the f state decreases  $\epsilon_f$ , the mixing between the f states and the conduction band states is enhanced, and the weight of the  $f^0$  configuration increases leading to the increases of the intensity of  $Yb^{2+}$  structure. The parameters and the weight of each configuration in the ground state are reported in table 2.

V (meV)	$U_{ff}$ (eV)	$U_{fc}$ (eV)	$\epsilon_f$ (eV)	$n_f$	$w_0$	$w_1$
30	7	11	-0.1	0.93	0.06	0.94
30	7	11	-0.2	0.88	0.12	0.88
30	7	11	-0.3	0.75	0.25	0.75

Table 2.3: Table showing the parameters used for the f-hole energy ( $\epsilon_f$ ) dependence of the Yb core level and 4f valence band spectra

## 2.5.7 Temperature dependence

One of the advantages of the approach we have introduced is that, in addition to the singlet ground state, we also have the first excited magnetic states located at energy  $T_K$  above the ground state. Therefore, we can qualitatively describe the temperature dependence of the photoemission spectra in contrast to the GS approach, which only describes the spectra at  $T = 0$  K. Let's illustrate this temperature dependence in the infinite  $U_{ff}$  limit. When the hybridization between f and conduction electrons is zero, the ground state is given by the  $f^{13}$  configuration  $N_f$ -fold degenerate (by discarding the 4f spin-orbit). By turning on the hybridization, the degeneracy of the ground state is lifted and a non-magnetic Kondo singlet ground state is composed of a linear combination of the different electronic configurations mainly  $f^{13}$  and  $f^{14}$  is stabilized. This ground state is separated from the  $N_f - 1$  first excited magnetic states by the Kondo temperature  $T_K$ . This later plays the role of a characteristic energy scale and allows us to qualitatively understand the temperature dependence of the Yb core-level photoemission spectra. In the 3d photoemission process at  $T = 0$ , only the hybridized ground state is occupied and the final states corresponding to  $Yb^{2+}$  ( $f^{14}$ ) and  $Yb^{3+}$  ( $f^{13}$ ) are reached (see Figure 2.18a). Two structures are observed (see Figure 2.18b) reflecting the mixing valence character. With increasing temperature, the first excited states which are purely composed of the magnetic  $f^{13}$  states are progressively populated. They are essentially coupled to the  $Yb^{3+}$  ( $f^{13}$ ) final states, and, only one structure is observed reflecting the trivalent character of the first excited state. Therefore, with increasing the temperature,

a decrease of the  $Yb^{2+}$  spectral weight transferred to  $Yb^{3+}$  is expected with a continuous dependence of  $n_f$  through  $T_K$  for systems with relatively high Kondo temperature ( $T_K \leq 100$  K). For Kondo lattice systems ( $n_f \approx 1$ ), a small change is observed in the spectra whereas, the spectra are temperature independent in the range below 300 K for strongly mixed-valence systems ( $T_K \geq 1000$  K) such as  $YbAl_2$  which presents a valence of about 2.2 ( $T_K = 2500$  K) [51].

Figure 2.18b illustrates the calculated spectra  $I_{GS}(E)$  and  $I_{ex}(E)$  for the initial ground state and for the purely  $f^{13}$  initial state, respectively. At finite-temperature, the spectral weight intensity is given by:

$$I_T(E) = P_{GS}(T)I_{GS}(E) + P_{ex}(T)I_{ex}(E) \quad (2.13)$$

$$P_{GS}(T) = \frac{1}{1 + 7e^{-\beta T_K}} \text{ and } P_{ex}(T) = \frac{7e^{-\beta T_K}}{1 + 7e^{-\beta T_K}} \quad (2.14)$$

where  $P_{GS}$  and  $P_{ex}$  correspond to the thermal population of the ground and first excited state in the initial state according to the Boltzmann statistics with  $\beta = (K_B T)^{-1}$ . In Figure 2.19, we show the calculated Yb core level spectra at various temperature in the range below 300 K for a nearly trivalent configuration ( $n_f = 0.98$ ,  $T_K \sim 5$  K) an intermediate valence configuration ( $n_f = 0.9$ ,  $T_K \sim 100$  K) and a strongly intermediate valence configuration ( $n_f = 0.53$ ,  $T_K \sim 1000$  K). As mentioned above, there is no significant change in the spectra for  $T_K \sim 5$  K and  $T_K \sim 1000$  K while a sizable temperature dependence is observed for  $T_K \sim 100$  K. This is a very crude calculation but it describes qualitatively the temperature dependence.

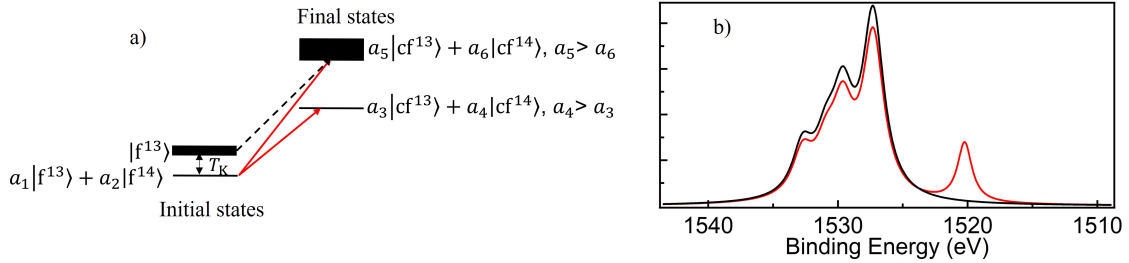


Figure 2.18: (a) Schematic energy diagram of a Yb impurity in the initial and final states of Yb photoemission. The thin and bold lines in the initial states represent hybridized  $f^{13}$ - $f^{14}$  states and the multiplet of the excited states  $f^{13}$ ,  $4f$  spin-orbit excitation are omitted for clarity. The bold line in the final states represents the multiplet states  $3d^9 4f^{13}$ . (b) calculated spectra of the initial ground state (red line) and the first excited magnetic states (black line).

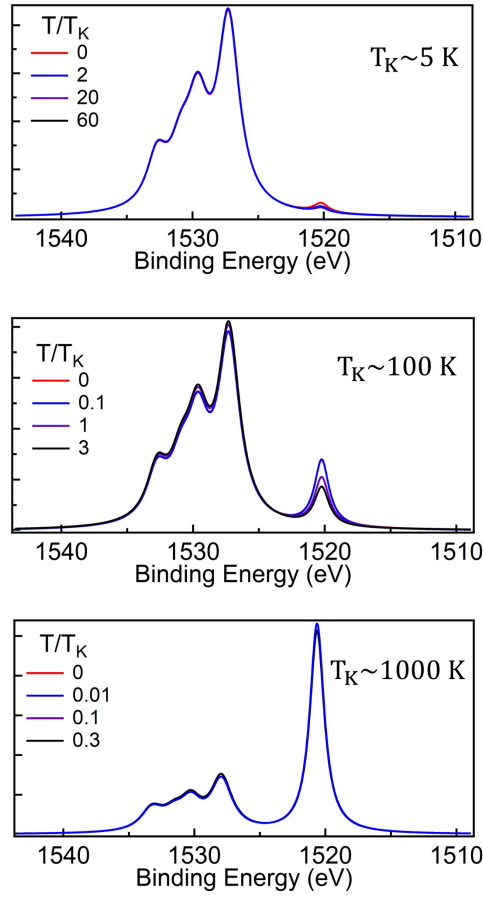


Figure 2.19: Calculated temperature dependence of Yb core level spectra below 300 K for a low  $T_K \sim 5$  K, intermediate  $T_K \sim 100$  K and high  $T_K \sim 1000$  K systems.

### 2.5.8 4f valence band

We have developed another code applying to the valence band photoemission spectroscopy. As in the core level calculation, we use a SIAM with zero bandwidth to simulate the valence band contribution of Yb. The spectral intensity is calculated by :

$$I(E) = \sum_f \left( \sum_i \left| \langle \Psi_f | a_{fi} | GS \rangle \right|^2 \right) \left[ \frac{\Gamma/\pi}{\Gamma^2 + (E - E_G + E_f)^2} \right] \quad (2.15)$$

where  $a_{fi}$  represents the annihilation operator for  $f$  states. The valence band photoemission spectra show the coexistence of the  $f^{12}$  and  $f^{13}$  final states separated in energy by  $\Delta E = U_{ff} + \epsilon_f$ . The basis state of the valence band photoemission final states is the same as the initial states (only one electron less in the conduction band).

## 2.5.9 Phenomenological simulation of the complex line shape due to multiplet effects: $(f^2) f^{12}$ final states in the valence band

Final states	$^3H$	$^3F$	$^3H$	$^3H$	$^3F$	$^3F$	$^1G$	$^3D$	$^1I$	$^3P$	$^3P$	$^3P$	$^1S$
J	6	4	5	4	3	2	4	2	6	0	1	2	0
Energie (eV)	0.000	0.696	1.015	1.552	1.774	1.849	2.625	3.45	4.3	4.393	4.475	4.71	9.84
Intensity	3.113	2.217	1.375	0.937	0.875	0.838	0.219	0.75	1.761	0.16	0.375	0.287	0.09

Table 2.4:  $f^{13} \rightarrow f^{12}$  photoemission intensity in the intermediate coupling taken from Ref [52]. The different final states are characterized by the main contribution given by the angular momentum L.

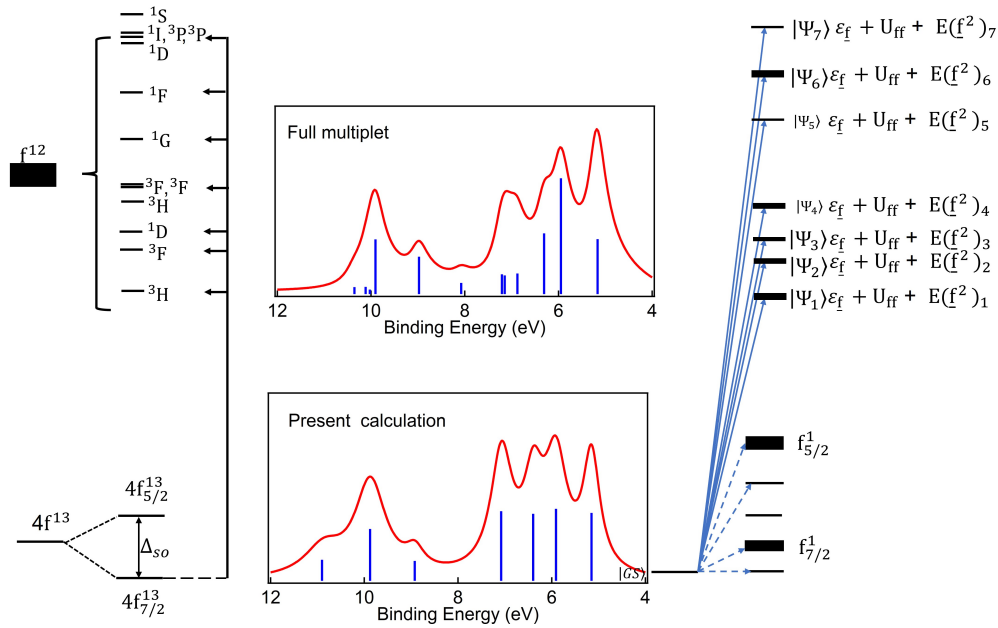


Figure 2.20: (a) Calculated spectra with the parameters:  $E(f^{12})_1 = -1.32$  eV ( $g = 17$ ),  $E(f^{12})_2 = -0.56$  eV ( $g = 14$ ),  $E(f^{12})_3 = -0.06$  eV ( $g = 10$ ),  $E(f^{12})_4 = 0.6$  eV ( $g = 31$ ),  $E(f^{12})_5 = 2.45$  eV ( $g = 4$ ),  $E(f^{12})_6 = 3.4$  eV ( $g = 12$ ) and  $E(f^{12})_7 = 4.4$  ( $g = 3$ ) eV. (b) Full multiplet calculation from table 2.4. The line diagrams indicate the spectral weight of the final states in both cases.

The 4f-valence band photoemission spectra of rare-earth compounds are dominated by the multiplet effects owing to the strong electron-electron interaction as well as the spin-orbit coupling in the final state.

As shown above, seven main structures are usually observed in the  $(f^2) f^{12}$  final states of the 4f valence band spectra. We phenomenologically reproduce such multiplet effects by introducing 7 different energy levels with degeneracy  $g$  in the  $f^2$  configuration :  $E(f^{12})_1 = -1.32$  eV ( $g = 17$ ),  $E(f^{12})_2 = -0.56$  eV ( $g = 14$ ),  $E(f^{12})_3 = -0.06$  eV ( $g = 10$ ),  $E(f^{12})_4 =$

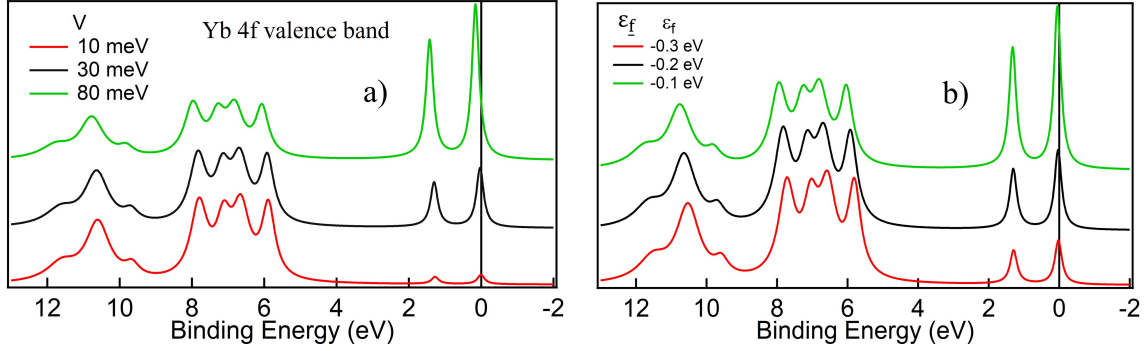


Figure 2.21: 4f valence band photoemission spectra as a function of the hybridization  $\Delta$  between the f states and the conduction band states and the energy of the f-hole  $\epsilon_f$ .

0.6 eV ( $g = 31$ ),  $E(f^{12})_5 = 2.45$  eV ( $g = 4$ ),  $E(f^{12})_1 = 3.4$  eV ( $g = 12$ ) and  $E(f^{12})_3 = 4.4$  ( $g = 3$ ) eV. Figure 2.20 shows a satisfactory agreement between the present calculation (for a trivalent configuration) and the full multiplet calculation. The intensities and energies (see Table 2.4) of the  $(\underline{f}^2) 4f^{12}$  multiplets calculated in the intermediate coupling were taken from [52].

**- Hybridization and f-hole energy dependence** Regarding the valence band photoemission spectra, the intensities of the  $(\underline{f}^2) f^{12}$  and  $(\underline{f}^1) f^{13}$  final states, respectively depend on the weight of the  $\underline{f}^1$  ( $Yb^{3+}$ ) and  $\underline{f}^0$  ( $Yb^{2+}$ ) configurations in the initial state. The energy separation between  $(\underline{f}^1)$  and  $(\underline{f}^2)$  final states is about  $\epsilon_f + U_{ff}$ . As shown in Figure 2.21, the increase of the hybridization leads to a systematic decrease of the  $Yb^{3+}$  spectral weight, which is transferred to  $Yb^{2+}$ . Moreover, there is also a slight shift in the different structures of energy. Similar to Yb 3d core-level spectra, the increase of  $Yb^{2+}$  spectral weight is due to the increases in the weight of  $\underline{f}^0$  configuration in the ground state. As mentioned in the previous section, the hybridization between  $\underline{f}^0$ , and  $\underline{f}^1$  configurations in the initial and final states is enhanced when  $|\epsilon_f|$  decreases. Therefore, when  $|\epsilon_f|$  decreases, the intensities of the  $\underline{f}^2$  final states decrease while that of  $\underline{f}^1$  increases.

## 2.6 Quantitative analysis of the experimental HAXPES spectra of YbPd

### 2.6.1 Yb 3d core level

In the previous section, we adapted the GS approach to describe the Yb 3d core-level photoemission on Yb compounds. We introduced 4 different energy levels to describe the complex line shape of the  $Yb^{3+}$  structure due to the multiplet effects (the  $Yb^{2+}$  configuration consists of one single peak). The set of parameters  $(\Delta, \epsilon_f, \Delta_{so}, U_{ff}, U_{fc})$  allows us to determine the



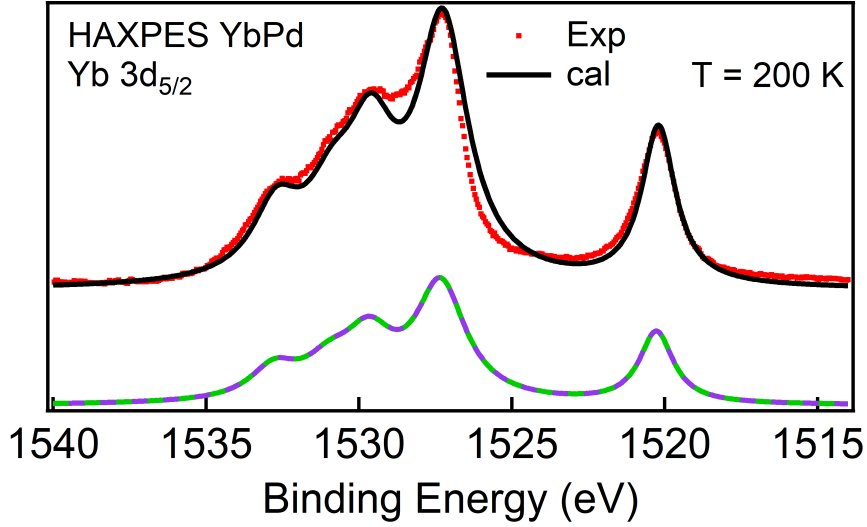


Figure 2.22: Comparison of the experimental spectra at  $T = 200$  K with the simulated spectra. There is only one site in the cubic phase ( $T > 130$  K). Green lines and purple lines represent the calculated spectra of the  $Yb_1$  site and  $Yb_2$  site, respectively.

energy separation and the intensities of the different contributions. Furthermore, the systematic evolution of  $Yb^{2+}$  and  $Yb^{3+}$  spectral features was confirmed by changing only  $\epsilon_f$  or  $\Delta$  and keeping all the other parameters constant. More importantly, we show that owing to the final state effects, the relative  $Yb^{2+}$  spectral weight is larger than  $1 - n_f$  and underestimates the valence. We will use the approach presented in the previous section to quantitatively analyze the Yb core level spectra of YbPd in this section.

As we have mentioned above, the temperature dependence of the photoemission spectra is not due to a thermal population of the first excited states following the Kondo scenario but seems related to the CDW mechanism. Therefore, we simulate the different spectra in the ground state by varying the hybridization strength  $\Delta$ . For the high temperature range ( $T = 200$  K, 165 K and 135 K) we could simulate the experimental spectra as shown in Figure 2.22 with the following parameters  $\epsilon_f = -0.2$  eV,  $U_{ff} = 7$  eV,  $\Delta_{so} = 1.27$  eV and  $\Delta = 38$  meV. The resulting spectra for the single Yb site correspond to an average valence of  $v_{av} = 2.84$  ( $n_f = 0.84$ ).

The presence of two Yb sites of different valences complicate the spectra analysis at low temperatures. Indeed the CDW transitions occur with the distortion due to the Pd atom displacement along the  $c$  direction leading to a valence ordering with one magnetic (nearly trivalent) and another nonmagnetic (strongly intermediate valent) Yb state in equal quantities. In the CDW phase, the Yb-Pd interatomic distances increase for one site and decrease for the other. Therefore, there is one site with reduced hybridization, whereas the hybridization increases for the other one resulting in the observed valence ordering. Each experimental spectrum in the CDW phase is thus composed of two contributions of equal weight. The con-

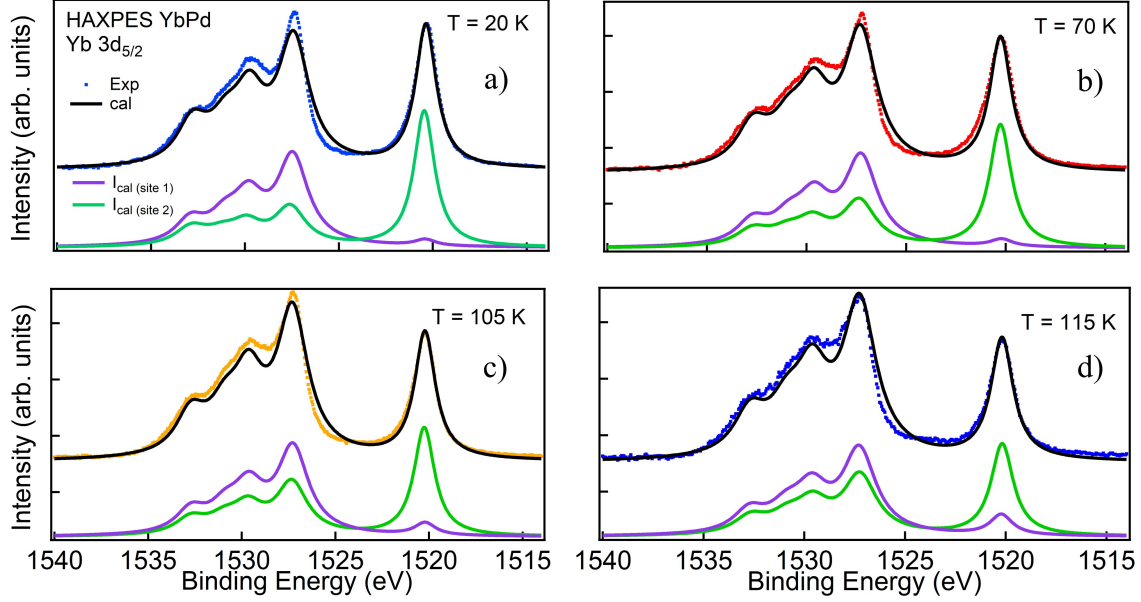


Figure 2.23: Comparison of the experimental Yb  $3d_{5/2}$  core level photoemission spectra with the calculated spectra (solid lines) at (a)  $T = 70$  K, (b)  $T = 105$  K and (c)  $T = 115$  K. Dotted lines and dashed lines represent the calculated spectra of the  $Yb_1$  site and  $Yb_2$  site, respectively.

tribution from the  $Yb_1$ -site should be mainly composed of the  $Yb^{3+}$  structure. Since it is nearly trivalent and, thus, requires a small hybridization  $\Delta_1$ . Since the RKKY interaction should be stronger than the Kondo effect to give rise to a magnetic ordering at low temperature, a very small  $T_K$  is expected for this site. The contribution for the intermediate valent  $Yb_2$ -site with a hybridization  $\Delta_2$  is then calculated so that the sum of the two contributions matches the experimental spectrum.

The calculated spectra for the  $Yb_1$ -site and  $Yb_2$ -site at  $T = 20$  K are shown in Figure 2.23. For  $T = 20$  K, we assume that valence of the nearly trivalent  $Yb_1$  site is  $v_1 = 2.98$  and calculate the spectra with hybridization  $\Delta_1 = 11$  meV. Then, we calculate the spectra of site 2 so that the sum of the spectra of the 2 sites matches with the experimental spectra. We found a nice agreement with  $\Delta_2 = 260$  meV ( $v_2 = 2.6$ ) leading to an average valency of  $v_{av} = 2.79$ . This latter is consistent with the values reported in the literature ( $v_{av} = 2.8$  estimated from Yb- $L_3$  XAS [10] and  $v_{av} = 2.75$  estimated from soft X-ray valence band photoemission spectroscopy [11]).

For the intermediate temperature  $T = 70$  K, 105 K, and 115 K, we calculate the spectra of  $Yb_1$ -site and  $Yb_2$ -site, ensuring that the increase in the valence of the site-1 is compensated by the decrease in the valence of the site-2. For this purpose, we use the following equation:

$$\frac{(n_f)_{Yb_2,T} - (n_f)_{Yb_2,HT}}{(n_f)_{Yb_2,LT} - (n_f)_{Yb_2,HT}} = \frac{(n_f)_{Yb_1,HT} - (n_f)_{Yb_1,T}}{(n_f)_{Yb_1,HT} - (n_f)_{Yb_1,LT}} \quad (2.16)$$

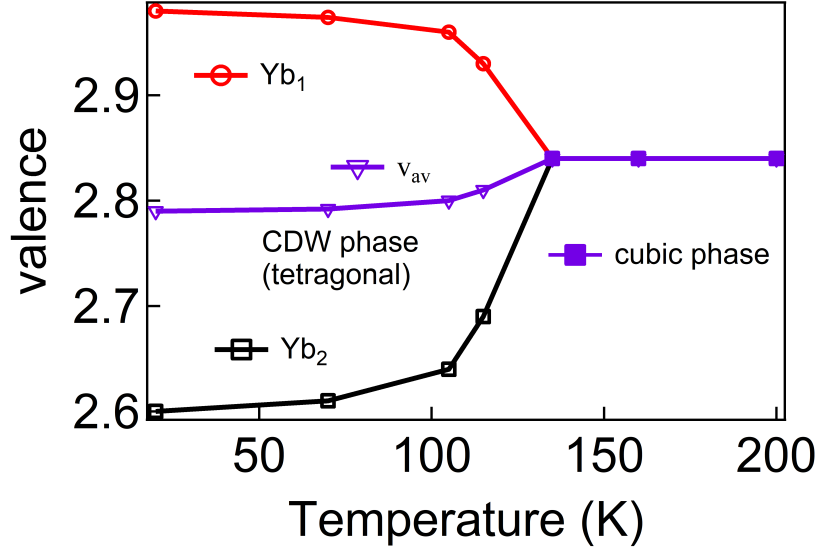


Figure 2.24: Temperature dependence of valence of  $Yb_1$  and  $Yb_2$  site. Below the CDW transition at  $T_1 = 130$  K, the two different Yb sites exhibit T-dependent valencies, whereas above  $T_1$  the valency of the unique Yb site is constant up to 200 K.

The spectra corresponding to site-1 and site-2 at 70 K, 105 K, and 115 K are respectively shown in Figure 2.23b, c, and d. The calculated average spectra are in nice agreement with the experimental ones. The hybridization parameters as well as the obtained valences are given in Table 2.5.

$T(K)$	$n_{f1}$	$n_{f2}$	$T_K^1$ (K)	$T_K^2$ (K)	$\Delta_1$ (meV)	$\Delta_2$ (meV)
20	0.98	0.6	8	718	260	11
70	0.97	0.61	12	690	176	12
105	0.96	0.64	23	611	120	16
115	0.93	0.69	53	490	85	21
135	0.84		181		38	

Table 2.5: Table showing the number of Yb holes in the ground state, the estimated Kondo temperatures for the two sites in the CDW T-phase and the single Yb site in the high-T cubic phase

The temperature dependence of  $Yb_1$  and  $Yb_2$  valence are shown in Figure 2.24. Below the CDW transition at  $T_1$ , the valence of  $Yb_1$ -site increases, and conversely, the valence of  $Yb_2$ -site decreases, whereas above  $T_1$  the valence of the unique Yb site is temperature independent up to 200 K. The corresponding average valence slightly increases from  $v_{av} = 2.79$  at  $T = 20$  K to  $v_{av} = 2.84$  at  $T = 200$  K which is consistent with early measurements [10].

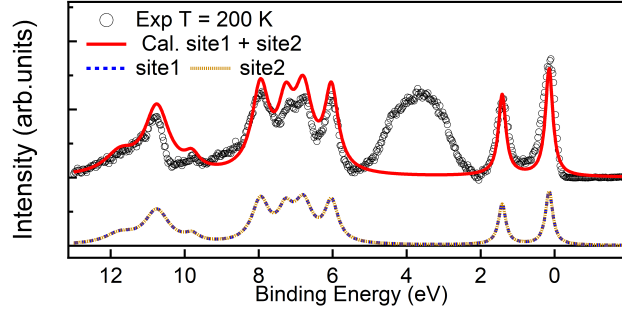


Figure 2.25: Comparison of the experimental 4f valence band spectra spectra at  $T = 200$  K with the simulated spectra. The simulated spectra are composed of two contributions for the two Yb-sites, which are equivalent in the cubic phase.

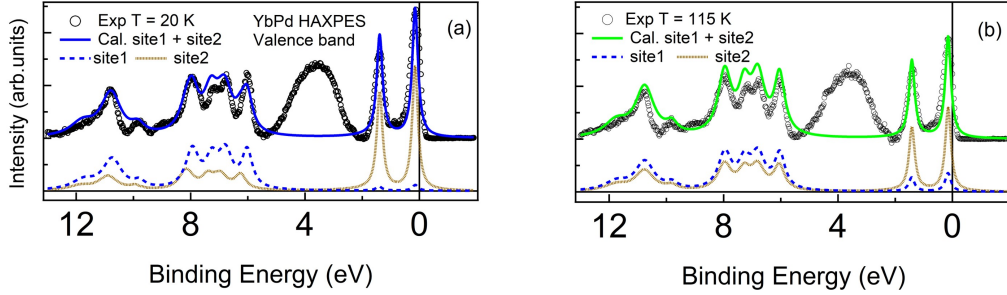


Figure 2.26: Experimental valence band spectra at  $T = 20$  K and 115 K compared with the SIAM calculations for describing the 4f valence changes across the CDW transition.

## 2.6.2 4f Valence band

We have also simulated the 4f valence photoemission of YbPd by using the same parameters ( $\Delta$ ,  $\epsilon_f$  and  $U_{ff}$ ) determined for Yb-3d photoemission spectra (see Table 2.5). As shown in Figure 2.25 we obtain a satisfactory agreement between experimental and calculated spectra of the single Yb site at  $T = 200$  K. The calculated 4f valence band spectra for site-1 and site-2 in the CDW phase are shown in Figure 2.26. The calculated spectra are also in satisfactory agreement with the experimental ones.

## 2.7 Dual Kondo effect charge ordering

Instability of the electron density in metals, even for weakly interacting electrons, often leads to original collective properties at low temperatures [53]. A famous example is the charge density wave transition historically observed for the first time in quasi one-dimensional systems. A considerable amount of experimental as well as theoretical work has been done in the

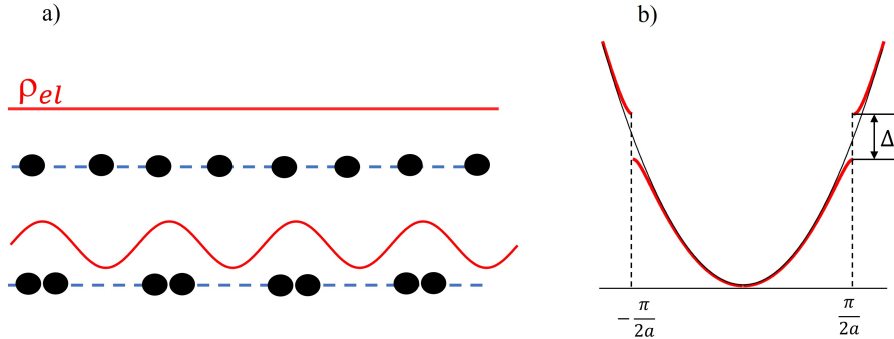


Figure 2.27: (a) one-dimensional chain with a lattice constant  $a$ . The chain is unstable and spontaneously dimerized to get a gap above. (b) Free electron band states in the CDW phase (black line) with a gap opening at  $\pm \pi/2a$  leading to a metal-insulator transition.

last few decades in relation to the CDW mechanism [53, 54]. However, there is still an intense debate on its origin partly because it is highly material-dependent. In this section, we will qualitatively illustrate the CDW origin in the case of a one-dimensional metal. Figure 2.27a shows a one-dimensional chain with one electron per atomic site (half-filled). The corresponding nearly free electron energy is shown in Figure 2.27b, which is filled up to the Fermi level  $E_f$ , with the Fermi wave number given by  $k_F = \pm\pi/2a$ . As pointed out by Peierls in 1930, an electronic disturbance with the wave vector  $q = 2k_F$  gives rise to the displacement of the atoms and changes the atomic periodicity of the chain to  $2a$ , which is more stable. The new Brillouin zone will coincide with the Fermi wave vectors, and a gap  $\Delta$  will open, i.e. the system will gain some electronic energy  $E_{elect.} \sim -u$ , in this process. However, the lattice distortion cost and elastic energy,  $E_{elast.} \sim u^2$ , where  $u$  is the lattice distortion. Therefore the system always gains more energy than it loses, and the dimerized arrangement is more energetically favorable, characterized by a periodic modulation of the charge density and a metal-insulator transition. In the mean-field theory of the CDW formation, the CDW-gap is characterized by the following relation [53] (weak coupling limit)

$$2\Delta = 3.52K_B T_C, \quad (2.17)$$

which is similar to the well-known BCS relation between the critical temperature and the zero-temperature gap in superconductivity theory [55]. The temperature dependence of the CDW-gap is the same as the temperature dependence given by the BCS theory. This latter can be numerically resolved by an analytical approximation given by

$$\Delta(T) = \Delta(0) \tanh \left( \beta \sqrt{\frac{T_c}{T} - 1} \right), \quad (2.18)$$

where  $\Delta(T)$  is the temperature dependent gap,  $\Delta(0)$  is the gap at  $T = 0$ ,  $T_C$  is the ordering temperature and  $\beta$  is a constant dimensionless. Equation 2.18 is known to fit accurately with experimental superconducting gap measurements [56]. In order to check if materials exhibit a CDW-order, the temperature dependence of the gap measured by Angle-resolved photoemission spectroscopy and the intensities of the superlattice structure measured by x-ray diffraction are usually compared with Equation 2.18 and a satisfactory agreement is observed in many materials. One typical example is the monolayer 1T-TaSe<sub>2</sub>, which exhibits a CDW-order at  $T_{CDW} \sim 530$  K [57].

In the last few years, theoretical studies have shown that strong electron-electron correlation can lead to a CDW formation. Indeed, a CDW-order has been theoretically predicted at quarter-filling in a one-dimensional Kondo lattice with strong on-site Kondo coupling  $J$  [58, 59]. Interestingly, it has also been predicted in a recent study that the Kondo effect could be the driving force of a CDW in a two-dimensional metal, by using a cellular dynamical mean-field theory (CDMFT) and variational Monte Carlo calculations [60]. However, in spite of these theoretical predictions, there is no experimental evidence of CDW induced by the Kondo mechanism to date.

As discussed in the introduction, the Kondo model predicts that the temperature dependence of the hole number occupancy  $n_f$  (valence  $v = 3 - n_f$ ) increases with increasing temperature and exhibits a universal scaling law as a function of  $T/T_K$  [61]. Following a simple approximation of the Anderson impurity with a large degeneracy  $N_f$ , Gunnarsson and Schönhammer [32] established that the hole number occupancy can be given by:

$$(1 - n_f) \approx \frac{\pi T_K}{N_f \Gamma}, \quad (2.19)$$

where  $\Gamma = \pi N(E_F)|V|^2$  is the hybridization bandwidth,  $N(E_F)$  the density of states of the conduction electron at the Fermi level, and  $V$  the hybridization strength.  $T_K$  exponentially depends on  $\Gamma$  and is expressed in the asymmetric Anderson model by [62]

$$K_B T_K = U \sqrt{\frac{\Gamma}{2U}} \exp \left[ -\frac{\pi |\epsilon_f| |\epsilon_f + U|}{2U\Gamma} \right] \quad (2.20)$$

In the Kondo regime  $\Gamma \ll U$ , the dependence of  $T_K$  is exponentially dominated by  $\Gamma$ . A linear relation of  $\log(1 - n_f)$  and  $\log(T_K)$  with  $n_f$  is expected for both quantities. From  $1 - n_f$  measured from Resonant inelastic x-ray emission spectroscopy (RXES) at Yb  $L_3$  edge and  $T_K$  determined by thermodynamic measurements, a phenomenological power law dependence has been established very recently [63]:

$$(1 - n_h) \approx \alpha (T_K)^n \text{ with } \alpha = 1/200 \text{ and } n = 2/3. \quad (2.21)$$

In Kondo lattice systems, HAXPES measurements of the 4f hole occupancy in the ground state  $n_f$  have been shown to be very accurate [64] and can thus provide a much more reliable estimate of the Kondo temperature  $T_K$ . By using the power scaling law (Equation 2.21), we determined the Kondo temperature of the unique crystallographic Yb site in the cubic phase  $T_K^{cub} = 184$  K ( $n_f = 0.84$ ). At  $T = 20$  K, we determined the Kondo temperature of Yb<sub>1</sub>-site

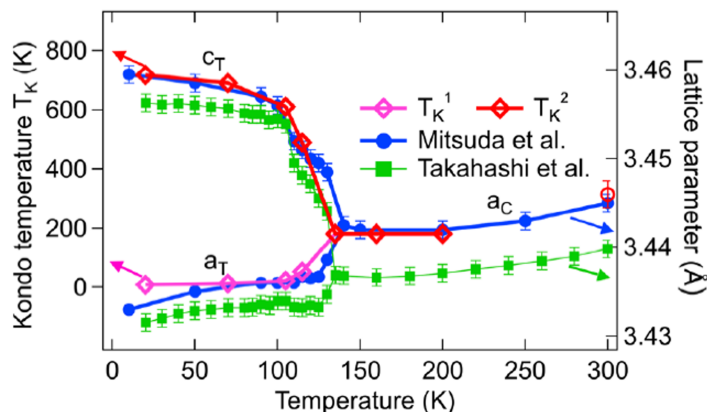


Figure 2.28: Temperature dependence of the lattice parameters and the dual Kondo temperature. Lattice parameters extracted from the papers of Mitsuda et al. [65] and Takahashi et al. [9]

$T_K^1 = 8$  K ( $n_f = 0.98$ ) and  $Yb_2$ -site  $T_K^2 = 718$  K ( $n_f = 0.6$ ). These estimated values are consistent with those obtained recently by point contact spectroscopy ( $T_K^1 \sim 30$  K and  $T_K^2 \sim 800$  K). The Kondo temperature in the CDW phase at  $T = 70$  K, 105 K, and 115 K are determined similarly, and the corresponding values are given in Table 2.5. In Figure 2.28, we show the evolution of  $T_K^1$  and  $T_K^2$  for all measured temperatures. Upon increasing temperature, we observe that  $T_K^1$  ( $T_K^2$ ) gradually decreases (increases) up to  $T = 130$  K (in the CDW phase) and remains constant in the cubic phase. Figure 2.28 also shows the temperature-dependence of the lattice parameter values  $a$ ,  $b$  and  $c$  of YbPd reported in the literature. In the cubic phase, the  $a, b, c = a_C$  values slightly decrease on cooling. At  $T = 130$  K,  $c = c_T$  value abruptly increases, whereas  $a = b = a_T$  decreases. Moreover, at  $T = 105$  K,  $c = c_T$  suddenly expands while  $a = b = a_T$  does not show any significant change on reducing temperature.

The overlaid plot of the temperature dependence of the lattice parameter values and the dual Kondo temperatures in the CDW phase show that  $T_K^1$  and  $T_K^2$  follow  $a_T$  and  $c_T$ , respectively, upon decreasing temperature. It indicates that the Kondo coupling to the lattice parameters could be the dominant contribution to the CDW transition and suggests a CDW order parameter related to the Kondo temperature.

What is the driving force of the CDW transitions in YbPd? We recall that a charge density wave is a mechanism that results from the competition between elastic energy lost due to the distortion of the lattice and the electronic energy gain. As discussed above, this is usually due to the nesting of the Fermi surface, which opens a gap and leads to a metal-insulator transition. However, YbPd is a 3D compound that remains metallic down to 40 mK. Moreover, the nesting of the Fermi surface is unlikely. Therefore, we need to look at another mechanism that can provide an electronic energy gain to compensate for the cost of elastic energy. Since the Kondo energy represents the electronic energy gained by the formation of the singlet state,

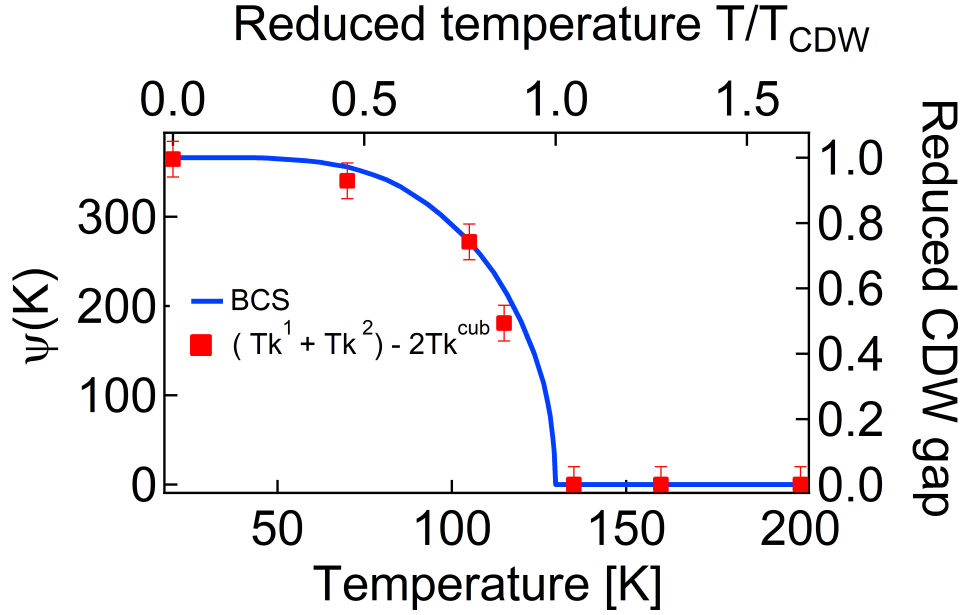


Figure 2.29: Temperature dependence of the total electronic energy gain due to the Kondo mechanism  $\Psi(T)$ .

we introduce the quantity :

$$\Psi(T) = T_K^1 + T_K^2 - 2T_K^{cub}, \quad (2.22)$$

which represents the total electronic energy gain in the CDW phase with respect to the cubic phase. We compared the temperature dependence of  $\Psi(T)$  with the temperature dependence of mean-field Bardeen-Cooper-Schrieffer gap  $\Delta(T)$  [55] (Equation 2.18) which is considered a valid CDW order parameter as mentioned above. We used the following parameters  $\Delta(0) = 365$  K,  $\beta = 1.8$  and  $T_C = 130$  K and obtained a nice agreement between both quantities as illustrated in Figure 2.29. Therefore, we propose that the dual Kondo effect is likely the driving force of the CDW transition observed in the YbPd.



### 2.7.1 Zero thermal expansion

Despite many studies on YbPd, its thermal expansion has not been discussed to date. From the lattice parameter values reported in the literature, we calculated the unit cell volume  $V = a_T \times b_T \times c_T$  of YbPd as a function of temperature in the range below 300 K as presented in Figure 2.30. In the cubic phase (above 135 K), the volume exhibits a small positive thermal expansion, while in the temperature range of 20 - 135 K, the volume remains essentially unchanged, indicating a zero thermal expansion in the CDW phase. The fact that the temperature dependence of the dual Kondo temperatures  $T_K^1$  and  $T_K^2$  follow the lattice parameters and the ZTE appears only in the CDW phase allows us to conjecture that the Kondo coupling is the driving force of the ZTE. Normally, materials expand upon heating. Therefore, in order to get a ZTE, a negative thermal expansion mechanism is required. Typical examples of materials exhibiting NTE are insulating oxides [66, 67, 68] such as  $CuScO_2$ ,  $Y_2W_3O_{12}$  and  $ZrW_2O_8$ . In these latter materials, it was shown that the presence of a M-O-M' (or O-M-O') (M and O denote a metal and oxygen atom, respectively) linkage leads to a transverse vibration of the central atom O (or M) perpendicular to the M-O-M' (or O-M-O') linkage resulting in a decrease of the linkage length. Similar ZTE has also been reported for the square-net compounds  $RE_4MGe_8$  [69] in which a mechanism involving a square-pyramidal configuration of the M-atom positioned below or above a Ge square net was considered as the driving force of the ZTE. Indeed, this geometrical configuration also allows a transverse vibration of the M-atom perpendicular to the Ge-square net. Given that YbPd structure involves Yb square nets with a square pyramidal arrangement of Pd atoms which gets displaced along the c axis, we can consider that a mechanism involving a transverse vibration of the Pd atoms is possible in YbPd.

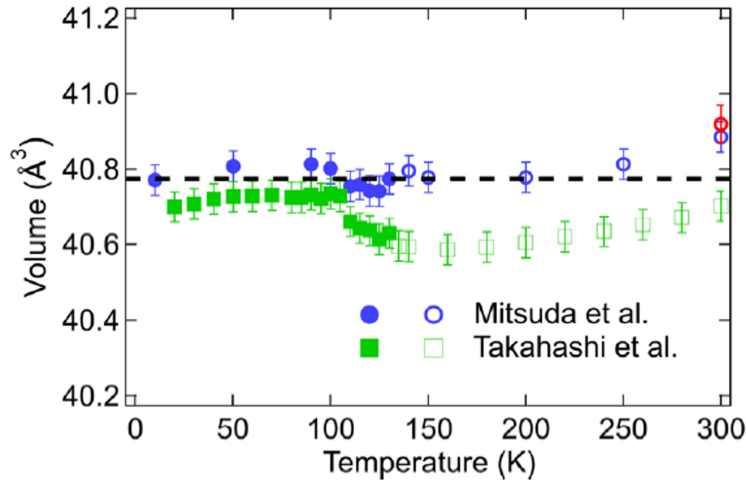


Figure 2.30: Temperature dependence of the unit-cell volume.

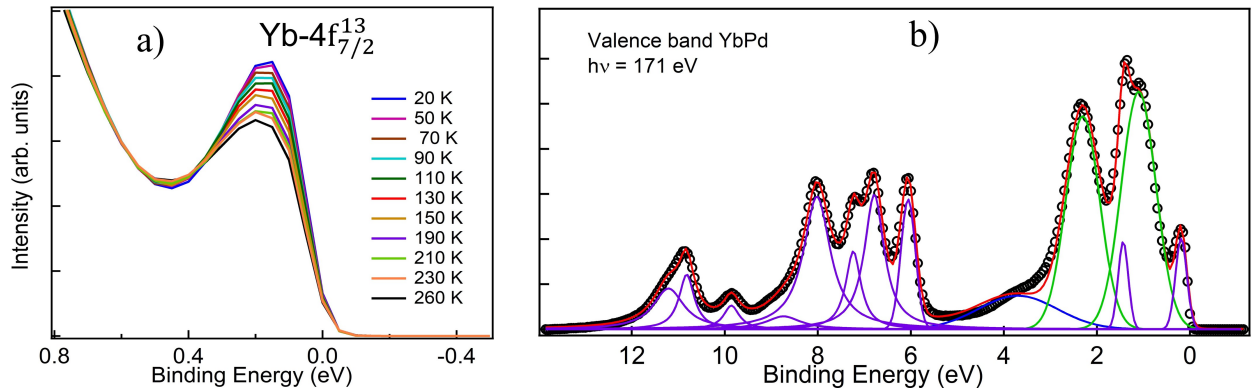


Figure 2.31: (a) Temperature dependence of the Kondo resonance measured with a photon energy  $h\nu = 171$  eV. (b) Example of curve fitting of the photoemission spectrum of YbPd at 260 K and  $h\nu = 171$  eV after subtracting a background. The purple, green and blue lines respectively represent the Yb-4f bulk, Yb-4f surface and Pd-4d contributions.

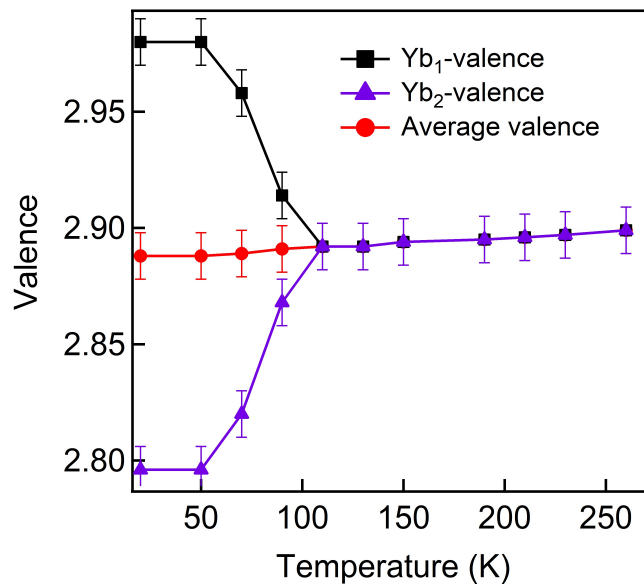


Figure 2.32: Temperature dependence of the average valence of YbPd (red line). The black and purple lines show the calculated temperature dependence of the intermediate-valent and nearly trivalent Yb-site in the cubic CDW phase.

## 2.7.2 Temperature dependence of the valence band soft PES spectra

The temperature dependence of the soft x-ray valence band spectra is sometimes perturbed by the instability of the surface valence towards  $Yb^{2+}$  [45, 70, 71]. Therefore, we focussed on the temperature dependence of the Kondo resonance in the vicinity of the Fermi level (BE =

0) which reflects the bulk excitations. The temperature dependence of the resonance is shown in Figure 2.31a. With increasing temperature from 20 to 260 K, the intensity of the Kondo resonance Yb- $4f_{7/2}$  decreases slightly and continuously, reflecting a small temperature dependence of the average valence across the CDW transition. We evaluated the valence from the intensity ratio of the  $Yb^{2+}$  and  $Yb^{3+}$  4f derived structures ( $4f^{13}$  and  $4f^{12}$  photoemission final states). For this purpose, we have performed numerical fitting of the spectra to extract the bulk contributions from the  $Yb^{2+}$  photoemission region as well as the Pd-4d band contribution (see Figure 2.31b). The Yb average valence  $v_{av} = 3 - I(Yb^{2+}) / (I(Yb^{2+}) + I(Yb^{3+}))$  slightly increases from  $v_{av} = 2.89$  at  $T = 20$  K to  $v_{av} = 2.90$  at  $T = 260$  K. As discussed in the previous section, this temperature dependence is not due to the thermal population of the first excited states following the Kondo scenario but to the continuous Pd atoms displacement leading to a continuous decrease (increase) of the valence of  $Yb_1$ -site ( $Yb_1$ -site) with increasing temperature. Figure 2.32 shows the calculated temperature dependence valences of the  $Yb_1$  and  $Yb_2$  sites in the tetragonal CDW phase by using equation 2.16. However, it should be noted that the valence determined is overestimated by the surface contributions.

## 2.8 Yb $L_3$ X-ray absorption spectroscopy

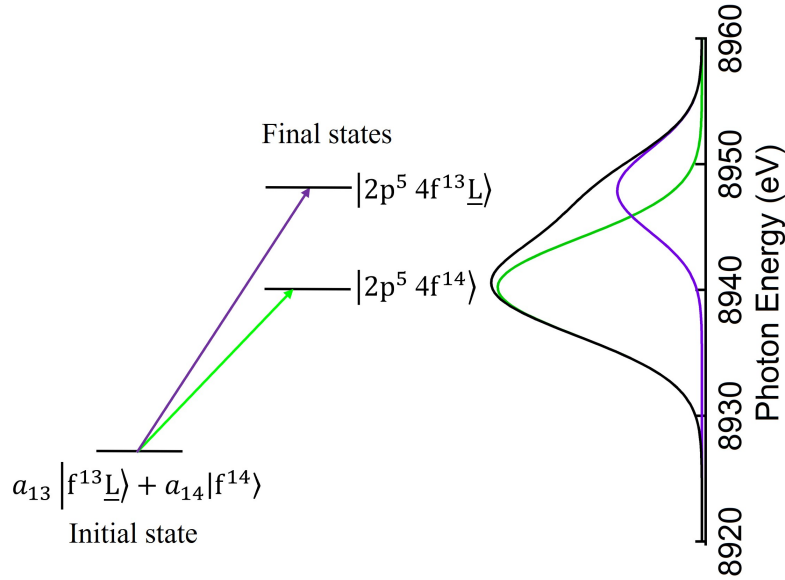


Figure 2.33: Yb  $L_3$ -edge XAS process in mixed-valent Yb compounds represented by a linear combination of  $Yb^{3+}$  and  $Yb^{2+}$  contributions configurations. Green and purple arrows indicate the transitions from the ground state to the two final states. Illustration of Yb  $L_3$ -edge XAS spectrum with two structures.

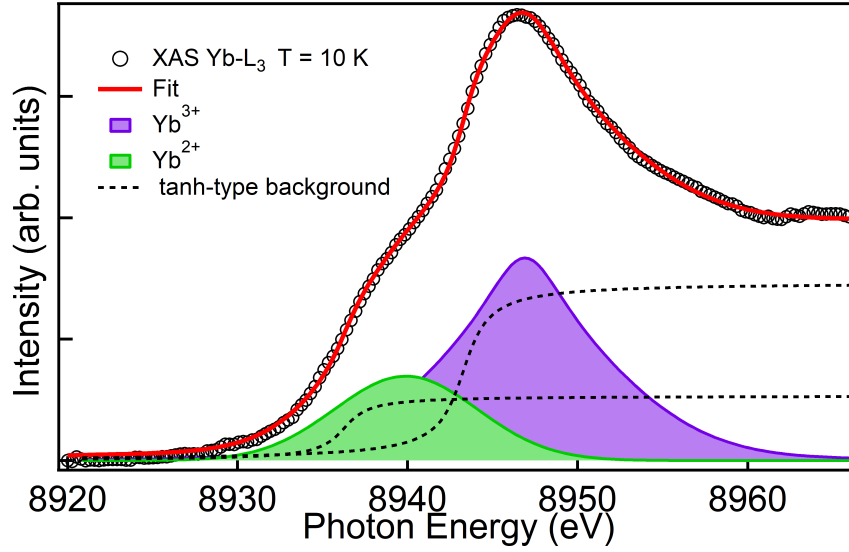


Figure 2.34: Result of fit analysis of Yb  $L_3$ -edge XAS spectrum of YbPd at  $T = 10$  K and  $P = 0$  GPa. the red line shows the phenomenological fit by taking into account the different contributions ( $Yb^{3+}$  and  $Yb^{2+}$ ) and the background (tanh-type).

X-ray absorption spectroscopy at Yb  $L_3$ -edge is a powerful means of probing the mixed-valent character of Yb compounds which has been widely used in the last few decades. It is a bulk-sensitive technique and does not require ultra-high vacuum measurements, which is necessary for photoemission and inverse photoemission spectroscopy. Moreover, it is possible to perform XAS measurements under extreme conditions by applying pressure. However, it is impossible to quantitatively analyze the Yb  $L_3$ -edge XAS spectra within the SIAM since the 5d states, which are not well localized, are involved in the XAS final state. Therefore, a phenomenological approach is used by experimentalists to analyze the spectra. The hybrid ground state is expressed as  $|GS\rangle = a_{14}|4f^{14}\rangle + a_{13}|4f^{13}\underline{L}\rangle$ . In the Yb  $L_3$  XAS process, a  $P_{3/2}$  core electron is excited to the 5d conduction band above the Fermi level. There are two different final states, namely  $2p^54f^{14}$  and  $2p^54f^{13}\underline{L}$  configurations, which are well separated ( $\Delta E \sim 10$  eV) due to the strong core-hole interaction. Therefore, the mixing between the two configurations becomes small and can be neglected and their intensities are assumed to be proportional to  $|a_{13}|^2$  and  $|a_{14}|^2$ , which corresponds to the weight of the two configurations in the ground state. Therefore, the intensities of the two final states can allow us to determine the average valence of the system. However, the experimental shapes of the spectra corresponding to these two contributions are usually different. Indeed, In addition to the transition to the localized 5d states, there are also transitions to the continuum (delocalized states) which contribute to the spectrum. Therefore, it is necessary to take into account two spectra for each configuration of the ground state. These latter are phenomenologically described by the sum of two functions. The transition to the localized states (the white line) is described by a Heaviside function which is convoluted by a Lorentzian or Voigt function to

account for the core-hole lifetime. The transitions to the continuum states are described by an arctangent function. So, the experimental line shape of the two spectral components can be fitted by [72]:

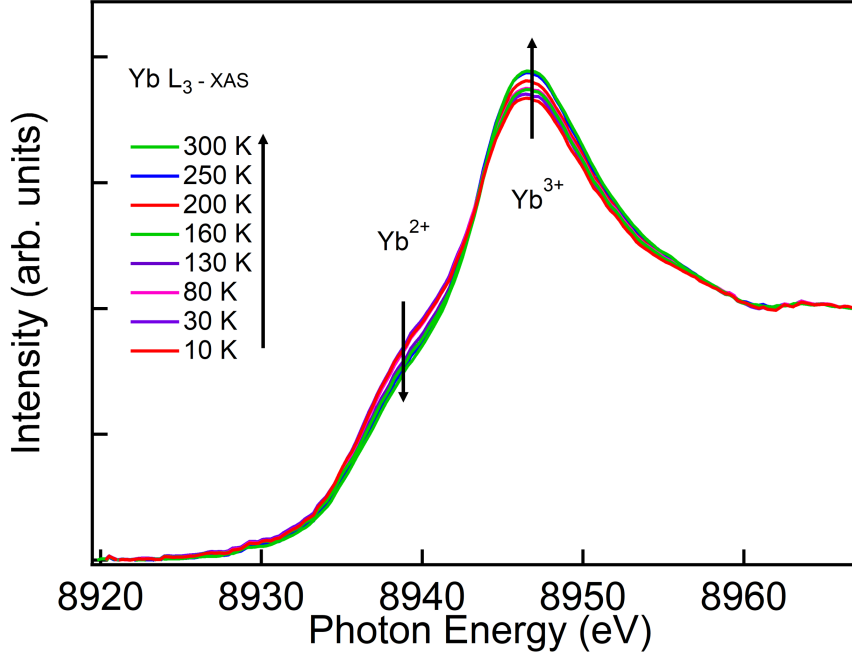


Figure 2.35: Temperature dependence of the Yb- $L_3$ -edge XAS spectra at  $P=0$  Gpa.  $Yb^{2+}$  spectral weight decreases with temperature while  $Yb^{3+}$  spectral weight increases

$$F_{3+}(E) = (1-a_0) \frac{a_1}{(E-E^3)^2 + a_2^2} + a_0 \frac{a_1}{2} \exp \left[ - \left( \frac{E-E^3}{a_2} \right)^2 \right] + n_f \left[ \frac{1}{2} + \frac{1}{\pi} \arctan \frac{E-E^3-\delta}{\Gamma/2} \right] \quad (2.23)$$

$$F_{2+}(E) = (1-b_0) \frac{b_1}{(E-E^2)^2 + b_2^2} + b_0 \frac{b_1}{2} \exp \left[ - \left( \frac{E-E^2}{b_2} \right)^2 \right] + (1-n_f) \left[ \frac{1}{2} + \frac{1}{\pi} \arctan \frac{E-E^2-\delta}{\Gamma/2} \right] \quad (2.24)$$

where  $E$ ,  $E^2$  and  $E^3$  are respectively the incident photon energy, the peak positions of the  $2p^5 4f^{14}$  and  $2p^5 4f^{13} \underline{L}$  final states corresponding to  $Yb^{3+}$  and  $Yb^{2+}$ .  $a_2$ ,  $b_2$  and  $\Gamma$  stand for the core-hole lifetime.  $\delta$  is a shift of the continuum states, and  $n_f$  corresponds to the f states occupation. The asymmetry of the  $Yb^{2+}$  and  $Yb^{3+}$  structures can be accounted for by using the sum of Gaussian and Lorentzian functions with different widths. The average valence is then estimated from the curve fitting by  $v_{av} = 2 + I(Yb^{3+}) / (I(Yb^{2+}) + I(Yb^{3+}))$ , where  $I(Yb^{2+})$  and  $I(Yb^{3+})$  are the intensities of the  $Yb^{2+}$  and  $Yb^{3+}$  peaks. In Figure 2.34, we shown an example of fitting of the Yb  $L_3$ -edge XAS spectrum of YbPd at low temperature

( $T = 10$  K) and ambient pressure ( $P = 0$  GPa), which gives an average valence of  $v_{av} = 2.73 \pm 0.02$ .

### 2.8.1 Yb $L_3$ X-ray absorption spectroscopy, Temperature dependence

Figure 2.35 shows the temperature dependence of Yb  $L_3$ -edge XAS spectra of YbPd at  $P = 0$  GPa. With increasing temperature, the spectral weight of  $Yb^{2+}$  is transferred to  $Yb^{3+}$ , and the average valence slightly increases from 2.73 at 10 K to 2.81 at 300 K. These values are lower than those obtained from Yb-3d hard-Xray photoemission measurements ( $v_{av} = 2.8$  at 20 K and 2.84 at 200 K) but the evolutions of the valence with the temperature are similar from the two techniques. As discussed in the previous sections, the temperature dependence of the average valence in the CDW phase is due to the Pd atom displacement that leads to two different Yb crystallographic sites.

### 2.8.2 Pressure-induced anomalous valence fluctuation in YbPd

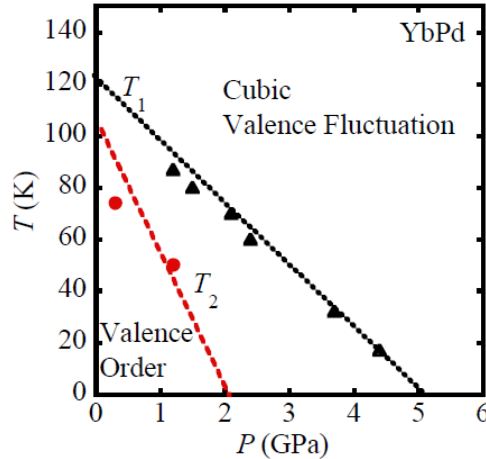


Figure 2.36: Temperature-Pressure phase diagram of YbPd determined by high pressure X-ray diffraction measurements, taken from [18].

In many intermediate-valent Yb compounds, the magnetic ordering is stabilized under high pressures due to the small ionic radius of  $Yb^{3+}$  relative to  $Yb^{2+}$  [73, 74, 75, 76]. However, X-ray diffraction and transport measurements have shown that the antiferromagnetic transition temperature  $T_N$  of YbPd decreases with pressure and is suppressed at  $P \approx 2$  GPa. To the best of our knowledge, only YbNiSn and YbRh<sub>2</sub>Si<sub>2</sub> exhibit such an anomalous evolution of the magnetic ordering with pressure [77, 78]. Indeed, YbNiSn orders ferromagnetically below 5.5 K. The Curie temperature increases with a pressure up to a maximum at about 2 GPa and then decreases. This maximum has been interpreted as the result of the

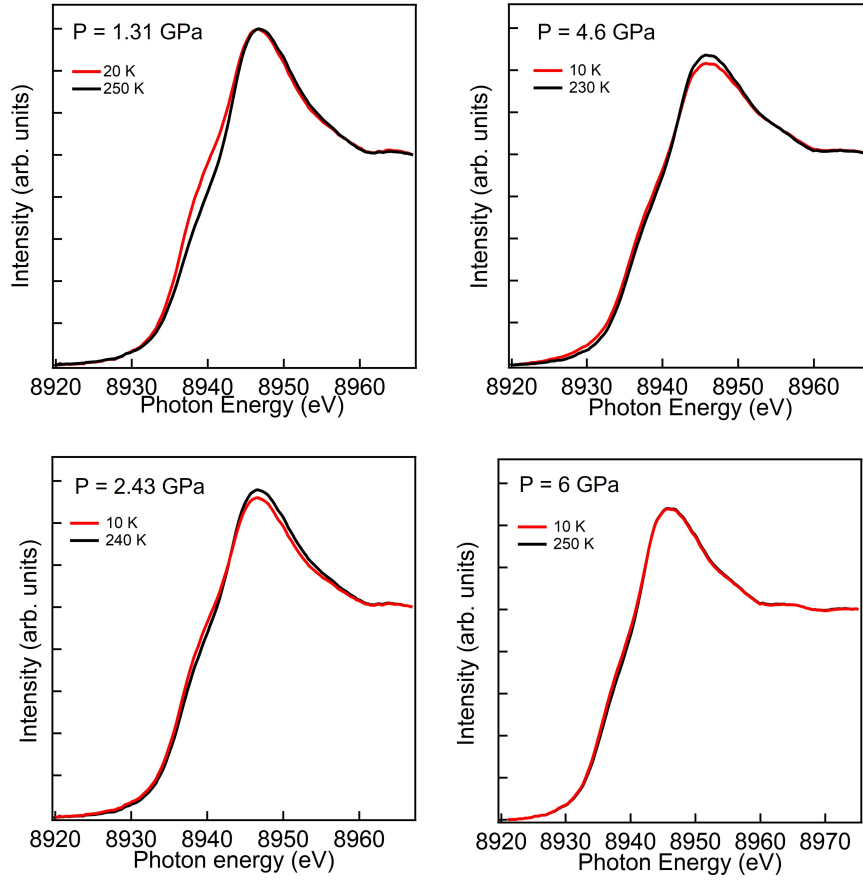


Figure 2.37: Yb  $L_3$ -edge XAS spectra of YbPd at selected pressure and temperature.

competition between the Kondo effect and the RKKY interactions. This negative pressure dependence in YbPd is likely related to the valence ordering. X-ray diffraction measurements have shown that the temperature transition of the incommensurate and commensurate charge density wave decrease with increasing pressure and vanishes respectively at  $P = 5$  GPa, and 2 GPa (see figure 2.36). In order to study how the Yb-valence changes in YbPd, and its interplay with the evolution of the CDW temperature transition, we measured the temperature dependence of Yb  $L_3$ -edge XAS spectra of YbPd at various pressures as shown in Figure 2.37 ( $P = 1.43$  GPa, 2.43 GPa, 3.5 GPa, and 6 GPa). With increasing pressure, the spectral weight transfer from  $Yb^{2+}$  to  $Yb^{3+}$  becomes weaker and nearly temperature-independent at  $P = 6$  GPa. Moreover, as shown in Figure 2.38, the average valence decreases with pressure, with a minimum at  $P \approx 2.43$  GPa, and then increases up to 2.7 at 20 GPa. This behavior is unique in YbPd. Indeed, in most ytterbium compounds, the average valence monotonically increases with pressure leading to a crossover from a nonmagnetic to an antiferromagnetic ground state.

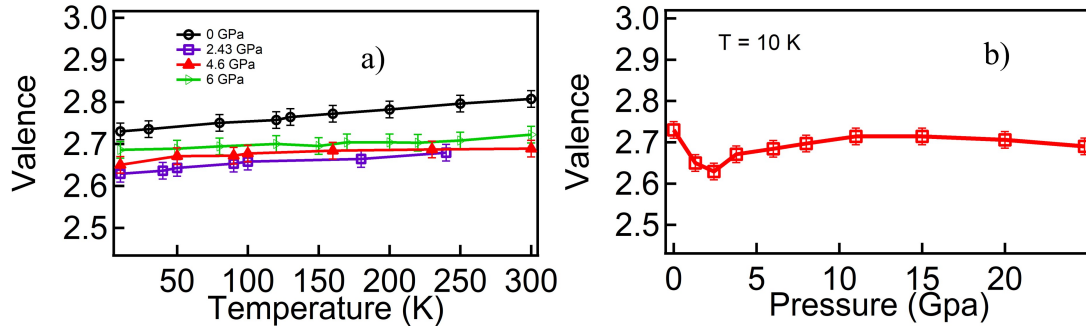


Figure 2.38: Pressure dependence of the average valence of YbPd.

## 2.9 conclusion

We have investigated the electronic structure of YbPd using soft and high x-ray photoemission spectroscopies. The measured Yb-3d core-level and 4f-valence band spectra revealed the intermediate valence character of the Yb atom. We also investigated the Pd-3d core levels and Pd-4d valence band states. The bulk-sensitive Yb 3d HAXPES core level photoemission reveals a clear temperature-dependent intermediate valence of two ytterbium sites in the CDW phase and a temperature-independent intermediate valence of the single crystallographic ytterbium site in the cubic phase. We have developed an approach from the GS model by considering the total degeneracy of the 4f states to describe the core-level and valence band spectra of a Yb compound. From a quantitative analysis of the spectra with this approach, we have successfully extracted the temperature dependence of the 4f hole occupancy, which clearly evidenced an evolution of the single Yb site in the cubic phase to a charge-disproportionated intermediate valence in the CDW phase. We introduced an order parameter given by the Kondo mechanism, and its temperature dependence is in nice agreement with the BCS prediction. The temperature dependence of the dual Kondo temperatures nicely follows the evolution of the lattice parameters in the CDW phase, thus showing an interplay between the Kondo effect and the structural changes giving rise to the zero thermal expansion in the CDW phase.



## Bibliography

- [1] W. De Haas and G. Van Den Berg, “The electrical resistance of gold and silver at low temperatures,” *Physica*, vol. 3, no. 6, pp. 440–449, 1936.
- [2] W. de Haas, J. de Boer, and G. van den Berg, “The electrical resistance of gold, copper and lead at low temperatures,” *Physica*, vol. 1, p. 1115, 1934.
- [3] J. Kondo, “Resistance Minimum in Dilute Magnetic Alloys,” *Progress of Theoretical Physics*, vol. 32, pp. 37–49, 07 1964.
- [4] K. Andres, J. E. Graebner, and H. R. Ott, “ $4f$ -virtual-bound-state formation in  $\text{CeAl}_3$  at low temperatures,” *Phys. Rev. Lett.*, vol. 35, pp. 1779–1782, 1975.
- [5] S. Doniach, “The Kondo lattice and weak antiferromagnetism,” *Physica B+C*, vol. 91, pp. 231–234, 1977.
- [6] D. Aoki, W. Knafo, and I. Sheikin, “Heavy fermions in a high magnetic field,” *Comptes Rendus Physique*, vol. 14, no. 1, pp. 53–77, 2013. *Physics in High Magnetic Fields / Physique en champ magnétique intense*.
- [7] P. W. Anderson., “Localized magnetic states in metals,” *Phys. Rev. B*, vol. **93**, p. 165134, 2016.
- [8] D. Malterre, M. Grioni, P. Weibel, B. Dardel, and Y. Baer, “Correlation between the kondo temperature and the photoemission spectral function in the  $\text{CeSi}_x$  ( $1.2 \leq x \leq 2$ ) system,” *Phys. Rev. B*, vol. 48, pp. 10599–10601, 1993.
- [9] R. Takahashi, T. Honda, A. Miyake, T. Kagayama, K. Shimizu, T. Ebihara, T. Kimura, and Y. Wakabayashi, “Valence ordering in the intermediate-valence magnet  $\text{YbPd}$ ,” *Phys. Rev. B*, vol. 88, p. 054109, 2013.
- [10] R. Pott, W. Boksich, G. Leson, B. Politt, H. Schmidt, A. Freimuth, K. Keulerz, J. Langen, G. Neumann, F. Oster, J. Röhrler, U. Walter, P. Weidner, and D. Wohlleben, “Magnetic order and other phase transitions in mixed-valent  $\text{YbPd}$ ,” *Phys. Rev. Lett.*, vol. 54, pp. 481–484, 1985.
- [11] M. Domke, C. Laubschat, E. V. Sampathkumaran, M. Prietsch, T. Mandel, G. Kaindl, and H. U. Middelmann, “Bulk and surface valence in  $\text{YbPd}_x$  compounds,” *Phys. Rev. B*, vol. 32, pp. 8002–8006, 1985.
- [12] T. Hasegawa, N. Ogita, M. Sugishima, A. Mitsuda, H. Wada, and M. Udagawa, “Low temperature phase of  $\text{YbPd}$  investigated by raman scattering,” *Journal of Physics: Conference Series*, vol. 273, p. 012030, 2011.
- [13] P. Bonville, J. Hammann, J. A. Hodges, P. Imbert, and G. J. Jéhanho, “Magnetic and nonmagnetic charge states in  $\text{YbPd}$ ,” *Phys. Rev. Lett.*, vol. 57, pp. 2733–2736, 1986.

- [14] M. Sugishima, K. Yamada, A. Mitsuda, H. Wada, K. Matsubayashi, Y. Uwatoko, K. Suga, and K. Kindo, “Effects of magnetic field and pressure on the intermediate valence state of YbPd,” *Journal of Physics: Condensed Matter*, vol. 22, no. 37, p. 375601, 2010.
- [15] Y. Tokiwa, S. Grüheit, H. S. Jeevan, C. Stingl, and P. Gegenwart, “Low-temperature antiferromagnetic ordering in the heavy-fermion metal YbPd,” *Journal of Physics: Conference Series*, vol. 273, p. 012062, 2011.
- [16] M. Shiga, K. Okimura, H. Takata, A. Mitsuda, I. Maruyama, H. Wada, Y. Inagaki, and T. Kawae, “Observation of kondo resonance in valence-ordered YbPd,” *Phys. Rev. B*, vol. 100, p. 245117, 2019.
- [17] U. Staub, B. D. Patterson, C. Schulze-Briese, F. Fauth, M. Shi, L. Soderholm, G. B. M. Vaughan, and A. Ochiai, “Direct observation of 1-dimensional charge order below the first-order "metal-insulator" transition in Yb<sub>4</sub>As<sub>3</sub>,” *Europhysics Letters (EPL)*, vol. 53, no. 1, pp. 72–78, 2001.
- [18] K. Oyama, K. Tanabe, A. Mitsuda, H. Wada, N. Hirao, S. I. Kawaguchi, Y. Ohishi, J. Gouchi, and Y. Uwatoko, “Pressure-induced cubic valence fluctuating ground state in YbPd,” *JPS Conf. Proc.*, vol. 30, p. 011141, 2019.
- [19] F. Patthey and W.-D. Schneider, “A monochromatized Si  $k\alpha$  X-ray source and its test on Yb 3d core levels,” *Journal of Electron Spectroscopy and Related Phenomena*, vol. 81, no. 1, pp. 47–53, 1996.
- [20] L. Degiorgi, T. Greber, F. Hulliger, R. Monnier, L. Schlapbach, and B. T. Thole, “Core level photoemission spectra of heavy lanthanides: YbP,” *Europhysics Letters (EPL)*, vol. 4, no. 6, pp. 755–759, 1987.
- [21] S. Hüfner, G. Wertheim, and J. Wernick, “Xps core line asymmetries in metals,” *Solid State Communications*, vol. 17, no. 4, pp. 417–422, 1975.
- [22] B. Johansson, “Valence state at the surface of rare-earth metals,” *Phys. Rev. B*, vol. 19, pp. 6615–6619, Jun 1979.
- [23] G. K. Wertheim, J. H. Wernick, and G. Crecelius, “Surface effects on valence in rare-earth intermetallic compounds,” *Phys. Rev. B*, vol. 18, pp. 875–879, 1978.
- [24] J. Yeh and I. Lindau, “Atomic subshell photoionization cross sections and asymmetry parameters:  $1 \leq Z \leq 103$ ,” *Atomic Data and Nuclear Data Tables*, vol. 32, no. 1, pp. 1–155, 1985.
- [25] L. Moreschini, C. Dallera, J. J. Joyce, J. L. Sarrao, E. D. Bauer, V. Fritsch, S. Bobev, E. Carpena, S. Huotari, G. Vankó, G. Monaco, P. Lacovig, G. Panaccione, A. Fondacaro, G. Paolicelli, P. Torelli, and M. Grioni, “Comparison of bulk-sensitive spectroscopic probes of Yb valence in Kondo systems,” *Phys. Rev. B*, vol. 75, p. 035113, 2007.

- [26] A. Rousuli, S. Nakamura, H. Sato, T. Ueda, Y. Matsumoto, S. Ohara, E. Schwier, T. Nagasaki, K. Mimura, H. Anzai, K. Ichiki, S. Ueda, K. Shimada, H. Namatame, and M. Taniguchi, “Photoemission study of the electronic structure of the kondo lattices  $\text{Yb}_2\text{Pt}_6\text{X}_{15}$  ( $\text{X} = \text{Al}, \text{Ga}$ ),” *Phys. Rev. B*, vol. 96, p. 045117, 2017.
- [27] Y. Utsumi, H. Sato, S. Ohara, T. Yamashita, K. Mimura, S. Motonami, K. Shimada, S. Ueda, K. Kobayashi, H. Yamaoka, N. Tsujii, N. Hiraoka, H. Namatame, and M. Taniguchi, “Electronic structure of Kondo lattice compounds  $\text{YbNi}_3\text{X}_9$  ( $\text{X} = \text{Al}, \text{Ga}$ ) studied by hard x-ray spectroscopy,” *Phys. Rev. B*, vol. 86, p. 115114, 2012.
- [28] H. Yamaoka, P. Thunström, N. Tsujii, I. Jarrige, K. Shimada, M. Arita, H. Iwasawa, H. Hayashi, J. Jiang, H. Namatame, M. Taniguchi, N. Hiraoka, H. Ishii, K. D. Tsuei, M. Giovannini, and E. Bauer, “Electronic structure and the valence state of  $\text{Yb}_2\text{Pd}_2\text{Sn}$  and  $\text{YbPd}_2\text{Sn}$  studied by photoelectron and resonant x-ray emission spectroscopies,” *Phys. Rev. B*, vol. 86, p. 085137, 2012.
- [29] H. P. Hughes and R. A. Pollak, “Charge density waves in layered metals observed by x-ray photoemission,” *The Philosophical Magazine: A Journal of Theoretical Experimental and Applied Physics*, vol. 34, no. 6, pp. 1025–1046, 1976.
- [30] D. Wolverson, B. Smith, E. Da Como, C. Sayers, G. Wan, L. Pasquali, and M. Cattelan, “First-principles estimation of core level shifts for hf, ta, w, and re,” *The Journal of Physical Chemistry C*, vol. 126, no. 21, pp. 9135–9142, 2022.
- [31] A. Kotani and Y. Toyozawa, “Photoelectron spectra of core electrons in metals with an incomplete shell,” *Journal of the Physical Society of Japan*, vol. 37, no. 4, pp. 912–919, 1974.
- [32] O. Gunnarsson and K. Schönhammer, “Electron spectroscopies for Ce compounds in the impurity model,” *Phys. Rev. B*, vol. 28, pp. 4315–4341, 1983.
- [33] O. Gunnarsson and K. Schönhammer, “Double occupancy of the f orbital in the anderson model for Ce compounds,” *Phys. Rev. B*, vol. 31, pp. 4815–4834, 1985.
- [34] O. Gunnarsson and K. Schönhammer, “Photoemission from Ce compounds: Exact model calculation in the limit of large degeneracy,” *Phys. Rev. Lett.*, vol. 50, pp. 604–607, 1983.
- [35] O. Gunnarsson, K. Schönhammer, J. C. Fuggle, F. U. Hillebrecht, J. M. Esteva, R. C. Karnatak, and B. Hillebrand, “Occupancy and hybridization of the f level in Ce compounds,” *Phys. Rev. B*, vol. 28, pp. 7330–7333, 1983.
- [36] J. C. Fuggle, F. U. Hillebrecht, Z. Zołnierak, R. Lässer, C. Freiburg, O. Gunnarsson, and K. Schönhammer, “Electronic structure of Ce and its intermetallic compounds,” *Phys. Rev. B*, vol. 27, pp. 7330–7341, 1983.

- [37] J. Allen, S. Oh, O. Gunnarsson, K. Schönhammer, M. Maple, M. Torikachvili, and I. Lindau, “Electronic structure of cerium and light rare-earth intermetallics,” *Advances in Physics*, vol. 35, no. 3, pp. 275–316, 1986.
- [38] J. Imer and E. Wuilloud, “A simple model calculation for XPS, BIS and EELS 4f-excitations in Ce and La compounds,” *Zeit. Phys. B Condensed Matter*, vol. 66, p. 153, 1987.
- [39] C. Laubschat, E. Weschke, C. Holtz, M. Domke, O. Strebel, and G. Kaindl, “Surface-electronic structure of  $\alpha$ -like Ce compounds,” *Phys. Rev. Lett.*, vol. 65, pp. 1639–1642, 1990.
- [40] E. Weschke, C. Laubschat, R. Ecker, A. Höhr, M. Domke, G. Kaindl, L. Severin, and B. Johansson, “Bandlike character of 4f electrons in CeRh<sub>3</sub>,” *Phys. Rev. Lett.*, vol. 69, pp. 1792–1795, 1992.
- [41] F. Strigari, M. Sundermann, Y. Muro, K. Yutani, T. Takabatake, K.-D. Tsuei, Y. Liao, A. Tanaka, P. Thalmeier, M. Haverkort, L. Tjeng, and A. Severing, “Quantitative study of valence and configuration interaction parameters of the kondo semiconductors cem2al10 (m=ru, os and fe) by means of bulk-sensitive hard x-ray photoelectron spectroscopy,” *Journal of Electron Spectroscopy and Related Phenomena*, vol. 199, pp. 56–63, 2015.
- [42] M. Sundermann, F. Strigari, T. Willers, J. Weinen, Y. Liao, K.-D. Tsuei, N. Hiraoka, H. Ishii, H. Yamaoka, J. Mizuki, Y. Zekko, E. Bauer, J. Sarrao, J. Thompson, P. Lejay, Y. Muro, K. Yutani, T. Takabatake, A. Tanaka, N. Hollmann, L. Tjeng, and A. Severing, “Quantitative study of the f occupation in cemin5 and other cerium compounds with hard x-rays,” *Journal of Electron Spectroscopy and Related Phenomena*, vol. 209, pp. 1–8, 2016.
- [43] Y. Shimura, A. Wörl, M. Sundermann, S. Tsuda, D. T. Adroja, A. Bhattacharyya, A. M. Strydom, A. D. Hillier, F. L. Pratt, A. Gloskovskii, A. Severing, T. Onimaru, P. Gegenwart, and T. Takabatake, “Antiferromagnetic correlations in strongly valence fluctuating CeIrSn,” *Phys. Rev. Lett.*, vol. 126, p. 217202, 2021.
- [44] S. Datta, R. P. Pandeya, A. B. Dey, A. Gloskovskii, C. Schlueter, T. Peixoto, A. Singh, A. Thamizhavel, and K. Maiti, “Giant spectral renormalization and complex hybridization physics in the kondo lattice system CeCuSb<sub>2</sub>,” *Phys. Rev. B*, vol. 105, p. 205128, 2022.
- [45] K. Kummer, Y. Kucherenko, S. Danzenbächer, C. Krellner, C. Geibel, M. G. Holder, L. V. Bekenov, T. Muro, Y. Kato, T. Kinoshita, S. Huotari, L. Simonelli, S. L. Molodtsov, C. Laubschat, and D. V. Vyalikh, “Intermediate valence in yb compounds probed by 4f photoemission and resonant inelastic x-ray scattering,” *Phys. Rev. B*, vol. 84, p. 245114, 2011.

- [46] M. Retegan, “Crispy: v0.7.3,” 2019.
- [47] M. W. Haverkort, M. Zwierzycki, and O. K. Andersen, “Multiplet ligand-field theory using wannier orbitals,” *Phys. Rev. B*, vol. 85, p. 165113, 2012.
- [48] Y. Lu, M. Höppner, O. Gunnarsson, and M. W. Haverkort, “Efficient real-frequency solver for dynamical mean-field theory,” *Phys. Rev. B*, vol. 90, p. 085102, 2014.
- [49] J.-S. Chung, E.-J. Cho, and S.-J. Oh, “3d core-level photoemission spectra of inter-metallic Yb compounds,” *Phys. Rev. B*, vol. 41, pp. 5524–5528, 1990.
- [50] R. Monnier, L. Degiorgi, and D. D. Koelling, “Towards a self-consistent determination of the mixing parameters in the anderson model: An application to the 4f-excitation spectra of YbP,” *Phys. Rev. Lett.*, vol. 56, pp. 2744–2747, 1986.
- [51] M. Matsunami, A. Chainani, M. Taguchi, R. Eguchi, Y. Takata, M. Oura, M. Yabashi, K. Tamasaku, Y. Nishino, T. Ishikawa, M. Kosaka, and S. Shin, “Photoemission evidence for valence fluctuations and kondo resonance in  $\text{YbAl}_2$ ,” *Journal of the Physical Society of Japan*, vol. 81, no. 7, p. 073702, 2012.
- [52] F. Gerken, “Calculated photoemission spectra of the 4f states in the rare-earth metals,” *Journal of Physics F: Metal Physics*, vol. 13, pp. 703–713, mar 1983.
- [53] G. Grüner, “Density waves in solids 1st ed.,” *CRC Press.*, 1994.
- [54] X. Zhu, J. Guo, J. Zhang, and E. W. Plummer, “Misconceptions associated with the origin of charge density waves,” *Advances in Physics: X*, vol. 2, no. 3, pp. 622–640, 2017.
- [55] J. Bardeen, L. N. Cooper, and J. R. Schrieffer, “Theory of superconductivity,” *Phys. Rev.*, vol. 108, pp. 1175–1204, 1957.
- [56] K. Senapati, B. M. G., and Z. H. Barber, “Spin-filter Josephson junctions,” *Nature Materials*, vol. 10, pp. 849–852, 2011.
- [57] Y. Nakata, K. Sugawara, A. Chainani, H. Oka, C. Bao, S. Zhou, C.-M. Chuang, P.-Y. and. Cheng, T. Kawakami, Y. Saruta, T. Fukumura, S. Zhou, T. Takahashi, and T. Sato, “Robust charge-density wave strengthened by electron correlations in monolayer 1T- $\text{TaSe}_2$  and 1T- $\text{NbSe}_2$ ,” *Nature Communications*, vol. 12, no. 5873, 2021.
- [58] J. E. Hirsch, “Strong-coupling expansion for a Kondo-lattice model,” *Phys. Rev. B*, vol. 30, pp. 5383–5385, 1984.
- [59] R. Peters, S. Hoshino, N. Kawakami, J. Otsuki, and Y. Kuramoto, “Charge order in Kondo lattice systems,” *Phys. Rev. B*, vol. 87, p. 165133, 2013.
- [60] T. Misawa, J. Yoshitake, and Y. Motome, “Charge order in a two-dimensional Kondo lattice model,” *Phys. Rev. Lett.*, vol. 110, p. 246401, 2013.

- [61] N. B. D.L. Cox and J. Wilkins, “Self-consistent large-n expansion for normal-state properties of dilute magnetic alloys,” *Phys. Rev. B*, vol. **36**, p. 2036, 1987.
- [62] A. Hewson, “The Kondo problem to heavy fermions,” *Cambridge Univ. Press*, vol. , p. 153, 1993.
- [63] K. Kummer, C. Geibel, C. Krellner, G. Zwircknagl, C. Laubschat, N. B. Brookes, and D. V. Vyalikh, “Similar temperature scale for valence changes in Kondo lattices with different kondo temperatures,” *Nat Commun*, vol. 9, p. 2011, 2018.
- [64] H. Sato, K. Shimada, M. Arita, K. Hiraoka, K. Kojima, Y. Takeda, K. Yoshikawa, M. Sawada, M. Nakatake, H. Namatame, M. Taniguchi, Y. Takata, E. Ikenaga, S. Shin, K. Kobayashi, K. Tamasaku, Y. Nishino, D. Miwa, M. Yabashi, and T. Ishikawa, “Valence transition of YbInCu<sub>4</sub> observed in hard x-ray photoemission spectra,” *Phys. Rev. Lett.*, vol. 93, p. 246404, 2004.
- [65] A. Mitsuda, M. Sugishima, T. Hasegawa, S. Tsutsui, M. Isobe, Y. Ueda, M. Udagawa, and H. Wada, “Origins of phase transitions in valence fluctuating YbPd,” *Journal of the Physical Society of Japan*, vol. 82, no. 8, p. 084712, 2013.
- [66] P. Forster and A. Sleight, “Negative thermal expansion in Y<sub>2</sub>W<sub>3</sub>O<sub>12</sub>,” *International Journal of Inorganic Materials*, vol. 1, no. 2, pp. 123–127, 1999.
- [67] J. Li, A. Yokochi, T. G. Amos, and A. W. Sleight, “Strong Negative Thermal Expansion along the O-Cu-O Linkage in CuScO<sub>2</sub>,” *Chemistry of Materials*, vol. 14, no. 6, pp. 2602–2606, 2002.
- [68] T. A. Mary, J. S. O. Evans, T. Vogt, and A. W. Sleight, “Negative Thermal Expansion from 0.3 to 1050 Kelvin in ZrW<sub>2</sub>O<sub>8</sub>,” *Science*, vol. 272, no. 5258, pp. 90–92, 1996.
- [69] S. C. Peter, M. Chondroudi, C. D. Malliakas, M. Balasubramanian, and M. G. Kanatzidis, “Anomalous Thermal Expansion in the Square-net Compounds RE<sub>4</sub>TGe<sub>8</sub> (RE = Yb, Gd; T = Cr-Ni, Ag),” *Journal of the American Chemical Society*, vol. 133, no. 35, pp. 13840–13843, 2011. PMID: 21819065.
- [70] L. H. Tjeng, S.-J. Oh, E.-J. Cho, H.-J. Lin, C. T. Chen, G.-H. Gweon, J.-H. Park, J. W. Allen, T. Suzuki, M. S. Makivić, and D. L. Cox, “Temperature dependence of the kondo resonance in YbAl<sub>3</sub>,” *Phys. Rev. Lett.*, vol. 71, pp. 1419–1422, 1993.
- [71] A. Generalov, D. A. Sokolov, A. Chikina, Y. Kucherenko, V. N. Antonov, L. V. Bekenov, S. Patil, A. D. Huxley, J. W. Allen, K. Matho, K. Kummer, D. V. Vyalikh, and C. Laubschat, “Insight into the temperature dependent properties of the ferromagnetic kondo lattice YbNi<sub>3</sub>,” *Phys. Rev. B*, vol. 95, p. 184433, 2017.
- [72] J. Röhler, “L<sub>III</sub>-absorption on valence fluctuating materials,” *Journal of Magnetism and Magnetic Materials*, vol. 47-48, pp. 175–180, 1985.

- [73] H. Yamaoka, I. Jarrige, N. Tsujii, J.-F. Lin, N. Hiraoka, H. Ishii, and K.-D. Tsuei, “Temperature and pressure-induced valence transitions in  $\text{YbNi}_2\text{Ge}_2$  and  $\text{YbPd}_2\text{Si}_2$ ,” *Phys. Rev. B*, vol. 82, p. 035111, 2010.
- [74] A. Fernandez-Pañella, V. Balédent, D. Braithwaite, L. Paolasini, R. Verbeni, G. Lapertot, and J.-P. Rueff, “Valence instability of  $\text{YbCu}_2\text{Si}_2$  through its magnetic quantum critical point,” *Phys. Rev. B*, vol. 86, p. 125104, 2012.
- [75] H. Sato, H. Yamaoka, Y. Utsumi, H. Nagata, M. A. Avila, R. A. Ribeiro, K. Umeo, T. Takabatake, Y. Zekko, J. Mizuki, J.-F. Lin, N. Hiraoka, H. Ishii, K.-D. Tsuei, H. Namatame, and M. Taniguchi, “Pressure-induced valence change of  $\text{YbNiGe}_3$  investigated by resonant x-ray emission spectroscopy at the Yb  $L_3$  edge,” *Phys. Rev. B*, vol. 89, p. 045112, 2014.
- [76] K. Matsubayashi, T. Hirayama, T. Yamashita, S. Ohara, N. Kawamura, M. Mizumaki, N. Ishimatsu, S. Watanabe, K. Kitagawa, and Y. Uwatoko, “Pressure-induced valence crossover and novel metamagnetic behavior near the antiferromagnetic quantum phase transition of  $\text{YbNi}_3\text{Ga}_9$ ,” *Phys. Rev. Lett.*, vol. 114, p. 086401, 2015.
- [77] A. L. Cornelius, J. S. Schilling, D. Mandrus, and J. D. Thompson, “Anomalous hydrostatic pressure dependence of the curie temperature of the kondo-lattice compound  $\text{YbNi}_3\text{Ga}_9$  to 38 gpa,” *Phys. Rev. B*, vol. 52, pp. R15699–R15702, 1995.
- [78] G. Knebel, R. Boursier, E. Hassinger, G. Lapertot, P. G. Niklowitz, A. Pourret, B. Salce, J. P. Sanchez, I. Sheikin, P. Bonville, H. Harima, and J. Flouquet, “Localization of 4f state in  $\text{YbRh}_2\text{Si}_2$  under magnetic field and high pressure: Comparison with  $\text{CeRh}_2\text{Si}_2$ ,” *Journal of the Physical Society of Japan*, vol. 75, no. 11, p. 114709, 2006.

## **Part II**

# **Spin-charge excitations in cerium compounds studied by Resonant inelastic X-ray scattering**



# RIXS to probe the properties of Ce Kondo systems

## 3.1 Introduction

Original electronic properties such as the Kondo effect, intermediate valence, heavy fermion, or non-conventional superconductivity are encountered in Ce intermetallic compounds. These properties result from the interplay between very large intra-atomic Coulomb interactions in the  $f$  shell and a partial delocalization due to the hybridization of  $f$  states with the conduction electrons. They are characterized by the formation at low temperature of a correlated Fermi liquid state with heavy quasiparticles associated with an emergent low energy scale, the Kondo energy  $K_B T_K$ . This emergent Kondo energy governs the low energy physical properties which exhibit scaling law behaviors as a function of  $T/T_K$ . Valence band photoemission and inverse photoemission are powerful spectroscopic techniques to study Kondo systems and to evidence, the different energy scales of interest: the high energy scale which is related to charge excitations (Coulomb interaction  $U_{ff}$  and the energy of the localized  $f$  states  $\epsilon_f$ ), and the low energy scale related to spin excitations (the Kondo energy) [1]. However, these spectroscopies are surface sensitive and surface effects can obscure the results. We will show that resonant inelastic X-ray scattering (RIXS) is a unique technique that can directly probe the charge and spin excitations usually observed by combined photoemission (PES) and inverse photoemission spectroscopies (IPES). In section 3.2, we describe the RIXS process with the accessible experimentally and theoretically information, focusing on Ce-based materials. Section 3.3 presents a summary of the experimental as well as theoretical studies of Ce based materials with the RIXS technique reported to date. Section 3.4 describes the experimental aspects for soft x-ray RIXS measurements with peculiar attention to the SEXTANTS beamline and its spectrometer AERHA. Then in section 3.5, we will present the model and formalism (full multiplet configuration interaction) used to simulate the Ce  $M_5$ -edge XAS and RIXS spectra. In section 3.6, we will focus on the CeAgSb<sub>2</sub> Kondo material ( $T_K \sim 23$  K, with a  $f$ -state occupation of  $n_f \sim 0.99$ ) as an example to demonstrate how RIXS can yield access to the  $f^1 - f^2$  and  $f^1 - f^0$  charge excitations. We will study the

$4f$  spin-orbit excitations and evidence the symmetry of the ground state through the drastic polarization dependence of the RIXS elastic peak and the  $f^0$  structure. We will investigate the temperature dependence of the fluorescence-like structure and discuss how it might be a signature of the Kondo energy scale. Finally, in section 3.7, by tracking the spectral weight of the structures corresponding to the  $f^1 \rightarrow f^2$  and  $f^1 \rightarrow f^0$  charge excitations as well as the fluorescence-like structure, we will look at how RIXS spectra evolve with the Kondo temperature  $T_K$  in three Ce-based Kondo materials: a  $\gamma$ -like Ce compound (  $\text{CeSi}_2$ ,  $T_K \sim 50$  K), an  $\alpha$ -like Ce compound (  $\text{CeNi}_2$ ,  $T_K > 500$  K) and an intermediate  $T_K$  one (  $\text{CePd}_3$ ,  $T_K \sim 150$  K).

## 3.2 RIXS review on cerium compounds

Resonant Inelastic X-ray Scattering (RIXS) is a photon in-photon out technique that is very efficient in studying elementary excitations in a large variety of systems such as charge transfer excitations, the crystal field, spin-orbit excitations, collective magnetic excitations, and phonons [2, 3, 4, 5, 6]. The result of light-matter interaction when a photon beam is incident on a sample is generally, a scattering of a photon with a certain energy in an arbitrary direction and polarization. This scattered photon energy can be either the same as the initial incident photon energy (elastic scattering) or a different one (inelastic). In the latter case, an excitation takes place in the system since it is left in a state different from the ground state. Thanks to the use of spectrometers and synchrotron light equipped with monochromators and undulators, the emitted photon's energy  $\hbar\omega_0$  can be accurately measured in order to obtain the energy loss in the scattering process from the incident photon's energy  $\hbar\omega_i$ :  $E_{loss} = \hbar\omega_i - \hbar\omega_0$ . Moreover, the momentum conservation of the system  $q = k' - k$  provides spectra that are sensitive to different scattering geometries. Therefore, one can infer the symmetry of the excitations, and the energy/momentum dependence occurring in the sample by studying the elastic and inelastic structures of the RIXS spectra.

In particular, for photon energies across the Ce  $3d$  or Ce  $4d$  absorption edges, RIXS is a powerful probe of the  $ff$  excitations as well as the charge transfer excitation in Ce-based Kondo systems with a  $4f^0$ ,  $4f^1$ , and  $4f^2$  hybridized states. Importantly, contrary to the first-order optical process (photoemission and x-ray absorption), RIXS also yields access to the second-order  $ff$  excitations. In addition, RIXS provides bulk sensitive and site-selective information through its resonant character. Since it is a photon-in/photon-out technique, RIXS can be performed in extreme conditions by applying high-pressure, electric, or magnetic fields.

### 3.2.1 Scattering process and outstanding features of RIXS

RIXS is a second-order optical process, in which a core electron is first resonantly excited across an absorption threshold by an incident x-ray photon, and then a valence electron decays to fill the core hole by emitting an x-ray photon (see Figure 3.1). RIXS has a number of unique properties compared to other spectroscopic techniques such as inelastic neutron scattering, photoemission spectroscopy, and x-ray absorption.

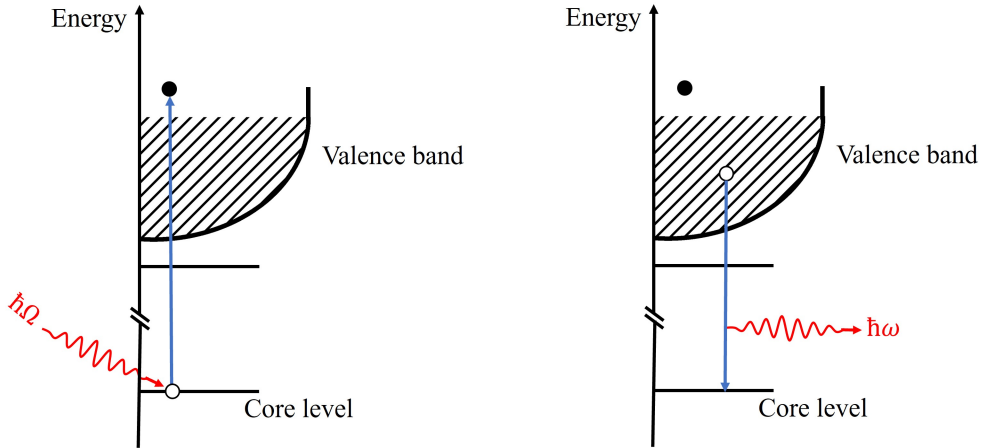


Figure 3.1: Scheme of the RIXS process. An electron from a deep-lying core level is promoted to an empty valence state above the Fermi level following the absorption of an incident photon energy  $\hbar\Omega$  (left panel). Afterward, a valence electron fills the core hole, and a photon  $\hbar\omega$  is emitted leaving behind an excitation in the system (right panel).

- **Element and chemical sensitivity:** The absorption spectrum in the x-ray range is characterized by a sharp step that corresponds to a promotion of a core electron above the Fermi level. Such a sharp step is called an absorption edge and is specific to each atomic element. Therefore, we can prioritize the scattering from a given element in the studied material by tuning the incoming photon energy on its absorption edge. In this respect, RIXS provides an element selectivity (the absorption edge energy and shape depend on the chemical state, and thus, provides chemical sensitivity). Furthermore, RIXS is also orbital-specific, and this is particularly important when one wants to focus on specific excitations such as the  $dd$  or  $ff$  excitations.
- **Bulk sensitivity:** It is well known that the x-ray penetration depth of a given material strongly depends on its energy. Typically, this depth increases from  $\sim 0.1\mu m$  in the soft x-ray regime (around 1000 eV) to  $\sim 50\mu m$  in the hard x-ray regime (around 10000 eV). RIXS technique is, therefore, non-surface sensitive, and allows us to avoid additional contributions in the spectra due to surface or modification defects. If needed, it is possible to enhance the surface contribution by measuring with a grazing incidence of the scattering geometry. However, the crystal face quality is important when investigating the features superimposed or close to the elastic peak. Indeed, the intensity of the elastic peak is strongly dependent on the roughness of the surface.
- **Charge neutral:** In contrast to photoemission and inverse photoemission where the total changes of the systems changes from  $N$  to  $N-1$  and  $N$  to  $N+1$  respectively, no electron is removed from or added to the studied sample during the RIXS process. This overall neutrality of the process is due to the fact that RIXS is a photon-in-photon-out technique. It is a fundamental characteristic to avoid charging effects, especially when

measuring insulating materials, such as many strongly correlated compounds.

- **Small sample volume:** RIXS requires only a very small sample volume compared to neutron scattering which needs massive samples to compensate for a small scattering cross-section. Indeed, thanks to the resonant character of RIXS, the signal is significantly enhanced and allows us to measure even thin films and nano-materials.
- **Photon polarization:** RIXS can exploit the variation of the incident photon polarization to characterize the symmetry of the ground state or the nature of the excitations through the scattering geometry and the use of selection rules.
- **Momentum dependence:** RIXS also provides a momentum dependence of the scattered photon in addition to its energy. This is valuable because the wavelength in the soft x-ray range is  $\approx 1 \text{ \AA}$ , which is comparable to the interatomic lattice spacing in solids. Therefore, RIXS can map the dispersion of low-energy excitations in the Brillouin zone.

### 3.2.2 Theoretical description of RIXS

In this section, we derive the expression of the RIXS cross-section by first writing the Hamiltonian of the system following the method of Ref [5]. According to quantum electrodynamics, the incident photons that interact with the electrons are described by an electromagnetic field, represented by a wave vector potential  $A(r, t)$ . In the non-relativistic case and in the limit that the potentials related to electrons and photons in the systems are small compared to twice the mass of the electron ( $e\phi/2mc^2, e|A|/2mc \ll 1$ ), the Hamiltonian for a system with  $N$  electrons interacting with an electromagnetic field is written as

$$\begin{aligned}
 H = & \sum_j^N \frac{[P_j + eA(r_j)]^2}{2m} + \sum_j^N \frac{e\hbar}{2m} \sigma_j \cdot \mathbf{B}(r_j) + \\
 & + \sum_j^N \frac{e\hbar}{2(2mc)^2} \sigma_j \cdot [\mathbf{E}(r_j) \times [p_j + eA(r_j)] - [p_j + eA(r_j)] \times \mathbf{E}(r_j)] + \\
 & + V(r_j) + \int dk \sum_{\epsilon} \hbar\omega_k \left( c_{\epsilon,k}^+ c_{\epsilon,k} + \frac{1}{2} \right), \tag{3.1}
 \end{aligned}$$

where  $P_j$ ,  $r_j$ , and  $\sigma_j$  are respectively, the momentum operator, the position operator, and the Pauli matrices of the  $j$  electron,  $A(r)$  is the vector potential,  $\mathbf{E}(r) = -\nabla\phi(r) - \partial A(r)/\partial(t)$  is the electric field and  $\mathbf{B}(r) = \nabla \times A(r)$  is the magnetic field.  $c_{\epsilon,k}^+$  and  $c_{\epsilon,k}$  respectively creates and annihilates a photon with energy  $\hbar\omega_k = c|k|$  and polarization vector  $\epsilon$  in the mode with a wave-vector  $k$ . The first term of the Hamiltonian describes the kinetic energy of the electron in presence of the electromagnetic field, the second term yields the Zeeman splitting, the third is the spin-orbit coupling, and the fourth term  $V(r_j)$  is the periodic potential. The last term gives the energy of the radiation summed on all the modes, each mode having the energy  $\hbar\omega_k$

and polarization  $\epsilon$ .

To establish the scattering cross-section, it is convenient to split the Hamiltonian  $H$  in the electronic part  $H_{el}$ , the electromagnetic field part  $H_{em}$ , and the remaining term  $H'$ , which describes the electron-photon interaction. Therefore, we can treat  $H'$  as a perturbation of  $H_0 = H_{el} + H_{em}$ . The eigenstates of  $H_0$  can be written as the product of those of  $H_{el}$  and  $H_{em}$  since  $H_0$  does not contain the electron-phonon interaction.

In order to calculate the RIXS cross-section, we consider an initial state with a single photon with momentum  $\hbar k_i$ , energy  $\hbar\omega_{k_i}$  and polarization  $\epsilon_i$ ; the latter is scattered to  $\hbar k_0$ ,  $\hbar\omega_{k_0}$  and  $\epsilon_0$ . The system changes from the initial state  $|g\rangle$  to the final  $|f\rangle$  one in the RIXS process. Therefore, the total wave functions can be written as  $|g\rangle = |g, 1_{\epsilon_i, k_i}\rangle$  and  $|f\rangle = |f, 1_{\epsilon_0, k_0}\rangle$ . Where  $|1_{\epsilon_i, k_i}\rangle$  is the one-photon wavefunction built by applying the creation operator  $c_{\epsilon, k}^+$  on the vacuum state  $|0\rangle$ .  $|g\rangle$  and  $|f\rangle$  are the eigenstates of  $H_0$  and their energies are respectively given by  $E_g = E_g + \hbar\omega_{k_i}$  and  $E_f = E_f + \hbar\omega_{k_0}$ . According to the Fermi golden rule, the transition rate  $w$  for the scattering process in the second-order perturbation theory can be written as:

$$w = \frac{2\pi}{\hbar} \sum_f \left| \langle f | H' | g \rangle + \sum_m \frac{\langle f | H' | m \rangle \langle m | H' | g \rangle}{E_g + \hbar\omega_{k_i} - E_m} \right|^2 \delta((E_f + \hbar\omega_{k_0}) - (E_g + \hbar\omega_{k_i})), \quad (3.2)$$

where  $m$  runs over the intermediate states  $|m\rangle$ , eigenstates of the unperturbed Hamiltonian  $H_0$  with energies  $E_m$ . In general, the first-order amplitude dominates the second-order amplitude. However, when the incident photon energy is set at an absorption edge in the material ( $E_g + \hbar\omega_{k_i} \approx E_m$ ) the second order becomes very large. Therefore, the second order yields a resonant scattering, whereas the first order term contains non-resonant scattering. So, in the non-relativistic and small potential limits, the resonant part of the second-order amplitude can be written as:

$$w = \frac{e^2 \hbar}{2m^2 V \epsilon_0 \sqrt{\omega_{k_i} \omega_{k_0}}} \sum_m \sum_{j, j'}^N \frac{\langle f | \epsilon_0^* \cdot p_{j'} e^{-ik_0 \cdot r_{j'}} | m \rangle \langle m | \epsilon_i \cdot p_j e^{-ik_i \cdot r_j} | g \rangle}{E_g + \hbar\omega_{k_i} - E_m + i\Gamma_m}, \quad (3.3)$$

where  $V$  is the volume of the system and the term  $\Gamma_m$  introduced in the denominator stands for the lifetime broadening of the intermediate states. It accounts for the usual core-hole lifetime. It is generally assumed that all the  $\Gamma_m$  are the same at a given edge and as a result, it can be taken to be a constant  $\Gamma_m = \Gamma$ . Let's consider now the dipole approximation. This limit consists of expanding the spatial dependence  $e^{ik \cdot r} = 1 + ik \cdot r - (k \cdot r)^2/2 + \dots$ , and to neglect the higher order quadratic terms. We, therefore neglect the spatial variation of the potential vector. Indeed, this is legitimated by the fact that the photon wavelength is much larger than the length scale of the atomic wavefunctions. So, by neglecting the first order term and considering Equation 3.2 and Equation 3.3, one obtains the Kramers-Heisenberg

expression for the RIXS cross-section:

$$\begin{aligned} & \frac{e^2\hbar}{2m^2V\epsilon_0\sqrt{\omega_{k_i}\omega_{k_0}}} \sum_m \sum_{j,j'}^N \frac{\langle f|\epsilon_0^*p_{j'}|m\rangle\langle m|\epsilon_i p_j|g\rangle}{E_g + \hbar\omega_{k_i} - E_m + i\Gamma_m} \approx \\ & \approx \frac{e^2\hbar}{2m^2V\epsilon_0} \sqrt{\omega_{k_i}\omega_{k_0}} \sum_m \sum_{j,j'}^N \frac{\langle f|\epsilon_0^*r_{j'}|m\rangle\langle m|\epsilon_i r_j|g\rangle}{E_g + \hbar\omega_{k_i} - E_m + i\Gamma_m}, \end{aligned} \quad (3.4)$$

this is obtained by substituting the operator  $p$  with the following relation of the commutator of  $im[H_0, r]/\hbar$ :  $\langle m|\epsilon_i.[H_0, r]|g\rangle = \langle m|H_0\epsilon_i.r|g\rangle - \langle m|\epsilon_i.rH_0|g\rangle = (E_m - E_g)\langle m|\epsilon_i.r|g\rangle \approx \hbar\omega_{k_i}\langle m|H_0\epsilon_i.r|g\rangle$ . Finally, we obtain the double differential cross-section by multiplying  $w$  by the density of outgoing photons states in the solid angle  $d\Omega(Vk_0^2d|k_0|d\Omega/(2\pi)^3)$  and dividing by the photon flux  $c/V$ :

$$d^2\sigma(\omega, k_i, k_0, \epsilon_i, \epsilon_0) = w \frac{V^2k_0^2d|k_0|d\Omega}{c(2\pi)^3} = w \frac{V^2\omega_{k_0}^2d\hbar\omega d\Omega}{\hbar c^4(2\pi)^3}. \quad (3.5)$$

The RIXS cross-section in the dipole approximation is :

$$\frac{d^2\sigma}{d\hbar\omega d\Omega} = r_e^2 m^2 \omega_{k_i}^2 \omega_{k_0}^3 \sum_f \left| \sum_m \sum_{j,j'}^N \frac{\langle f|\epsilon_0^*r_{j'}|m\rangle\langle m|\epsilon_i.r_j|g\rangle}{E_g + \hbar\omega_{k_i} - E_m + i\Gamma_m} \right|^2 \delta(E_g - E_f + \hbar\omega), \quad (3.6)$$

where  $r_e = e^2/(4\pi\epsilon_0 mc^2)$  stands for the classical electron radius. The energy conservation is assured by the  $\delta$  function, and as a result, the elementary excitations observed at constant energy losses are equal to the difference in the photon energies.

### 3.3 Relevant energy scales probed by Ce- $M_5$ RIXS

In this section, we discuss in detail the elementary excitations measured by RIXS, briefly outlined in the introduction. We first review the high-energy excitations, which are typically the charge transfer energies, and then describe the low-energy excitations, the spin-orbit, and crystal field excitations.

#### 3.3.1 First evidence of the charge transfer excitations

In condensed matter physics, charge transfer is described by the energy required for moving an electron from one site to another. There are two relevant energy scales for this process in strongly correlated cerium compounds. The first energy scale is associated with a hopping of an electron from the  $4f$  shell to the ligand orbital ( $f^n \rightarrow f^{n+1}\underline{L}$ ). This is known as the charge transfer energy defined as  $\Delta = E(f^1\underline{L}) - E(f^0)$ , where  $E(f^1) = \epsilon_f$  and  $E(\underline{L}) = \epsilon_{\underline{L}}$  are respectively the  $4f$ -state energy with respect to the Fermi level and the energy of a hole  $\underline{L}$  in the conduction band width. The second energy is the Coulomb repulsion  $U$  associated

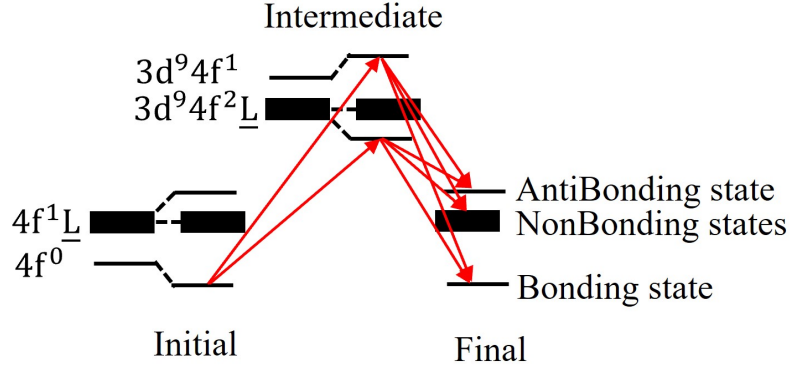


Figure 3.2: Total energy level scheme of  $3d \rightarrow 4f \rightarrow 3d$  RIXS of  $\text{CeO}_2$ . The black rectangle denotes the O  $2p$  valence band. Reproduced from Ref.[7].

with moving an  $4f$  electron from one  $f$  site  $i$  to another  $f$  site  $j$  ( $f_i^1 f_j^1 \rightarrow f_i^0 f_j^2$ ), where  $U = E(f^2 \underline{L}^2) + E(f^0) - 2E(f^1 \underline{L}^1)$ . The corresponding RIXS features of these charge transfer excitations are expected to be observed in the range between 2 and 10 eV loss energy and they could be investigated even with the low resolution of the early RIXS measurements.

The early RIXS measurements on a cerium compound were carried out in 1996 by Butorin et al. [8, 7]. They studied the strongly intermediate valence (mostly  $f^0$ )  $\text{CeO}_2$  compound at the Ce  $M_4$  and  $M_5$  edges. Following a theoretical analysis with the SIAM[7], they demonstrated that the RIXS technique is sensitive to charge excitations and that the experimental spectra could be reproduced with appropriate parameters. The schematic Ce  $3d \rightarrow 4f \rightarrow 3d$  RIXS process of  $\text{CeO}_2$  is shown in Figure 3.2. The Ce ion in  $\text{CeO}_2$  is nominally in the  $\text{Ce}^{4+}$  state ( $f^0$  system), but actually, the  $|f^0\rangle$  and  $|f^1 \underline{L}\rangle$  configurations are strongly mixed (with the f-state occupation  $n_f \sim 0.58$  eV), giving rise to a bonding ground state between the  $|f^0\rangle$  and  $|f^1 \underline{L}\rangle$  configurations ( $|\Psi_{GS}\rangle = a|f^0\rangle + b|f^1 \underline{L}\rangle$ ), a first excited nonbonding state high in energy at about 4 eV and an antibonding state located at 6 eV. The configurations of the final state are the same as the initial one. In the intermediate RIXS process, the  $3d^9 4f^1$  and  $3d^9 4f^2 \underline{L}$  are close in energy owing to the strong core-hole interaction and their hybridization also leads to bonding, nonbonding and antibonding states between the  $3d^9 4f^1$  and  $3d^9 4f^2 \underline{L}$  configurations. Figure 3.3 shows the results of the experimental and calculated Ce  $3d$  XAS and Ce  $3d \rightarrow 4f \rightarrow 3d$  RIXS. In figure 3.3a and 3.3b, the uppermost curve represents the experimental Ce  $3d$ -edge XAS spectrum characterized by two main groups of peaks due to the Ce  $3d_{3/2}$  and  $3d_{5/2}$  core-level final states. Each group exhibits a main peak B and a satellite A separated by about 5 eV, corresponding to the bonding ( $|\Psi_{GS}\rangle \rightarrow 3d^9 4f^2 \underline{L}$ ) and antibonding states ( $|\Psi_{GS}\rangle \rightarrow 3d^9 4f^1$ ). Then the RIXS spectra depicted by curves A and B respectively correspond to the incident photon energy set to XAS structures A and B. The RIXS spectra shown as a function of the emitted photon energy exhibit two main peaks whose intensity depends on the incident photon energy. When the incident photon energy is fixed at the XAS

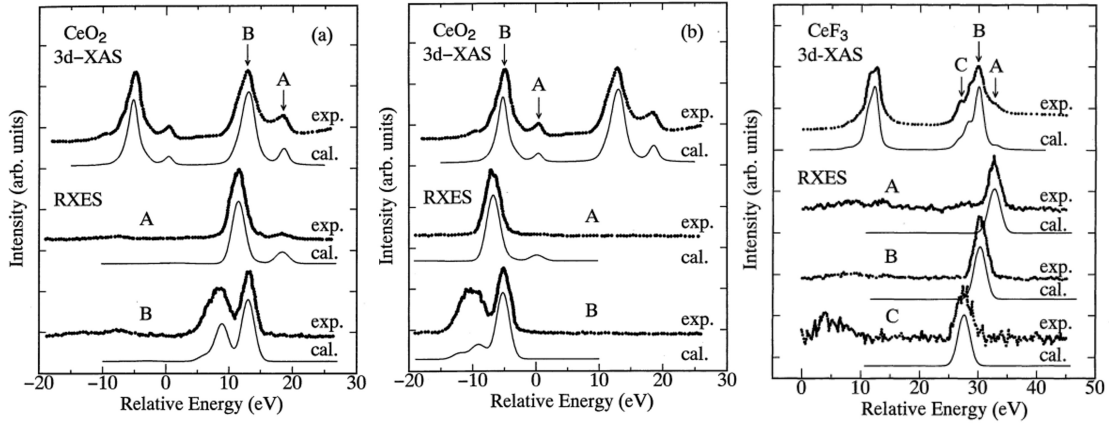


Figure 3.3: Experimental and calculated Ce  $M_5$  XAS spectra and RIXS spectra for CeO<sub>2</sub> (a), (b) and CeF<sub>3</sub> (c). A, B, and C of the XAS spectra indicate the incident photon energy tuned to obtain the RIXS spectra. Reproduced from Ref.[7]

main peak B, the bonding state is selected in the intermediate state and as a result, we have the transitions to all the final states but predominantly to the nonbonding state. Therefore, the RIXS spectrum exhibits in addition to the elastic peak a prominent structure at  $\sim 4.5$  eV broadened due to the O  $2p$  bandwidth. When the incident photon energy is tuned on the XAS satellite peak, the intermediate antibonding state is selected and we have a strong transition to the antibonding final state. It should be noted that the charge excitations originating from the  $f^2$  configuration are not important in the RIXS spectra of CeO<sub>2</sub> since the  $f^2 \underline{L}^2$  configuration lies at very high energy in the initial state.

Butorin et al. also measured the Ce 3d XAS and Ce  $M_5$ -edge RIXS spectra of the purely trivalent CeF<sub>3</sub> compound. In this case, the hybridization effect can be disregarded and the system is well described as a trivalent free Ce<sup>3+</sup> ion. The experimental and calculated spectra are shown in Figure 3.3 right panel. The Ce ion in CeF<sub>3</sub> has a Ce<sup>3+</sup> ( $4f^1$ ) configuration and the RIXS process is described by the transition  $3d^{10}4f^1 \rightarrow 3d^94f^2 \rightarrow 3d^{10}4f^1$ . By tuning the incident photon energy on A, B, and C of the XAS spectrum, the corresponding RIXS spectra always exhibit an elastic x-ray scattering single peak. Actually, the spectra should show an elastic structure corresponding to the transition to the  $f_{5/2}^1$  initial ground state, and an inelastic structure corresponding to the  $f_{7/2}^1$  excited state. However, the energy separation between  $f_{7/2}^1$  and  $f_{5/2}^1$  states (4f spin-orbit energy  $\sim 0.3$  eV) was much smaller than the experimental resolution (about  $\sim 2$  eV) [8].

In 2001, Magnuson et al [9] measured the RIXS spectra of the heavy fermion CeB<sub>6</sub> compound and calculated the RIXS spectra using the SIAM. The measurements (see Figure 3.4) were made at room temperature with  $\pi$  polarization (depolarized geometry) of the incident photon. The experimental Ce 3d-edge XAS spectrum in the top panel of Figure 3.4 exhibits the main peak and a very weak satellite separated by about 6 eV. While the XAS spectrum looks similar to that of the typical CeF<sub>3</sub> trivalent system, the corresponding RIXS spectra do



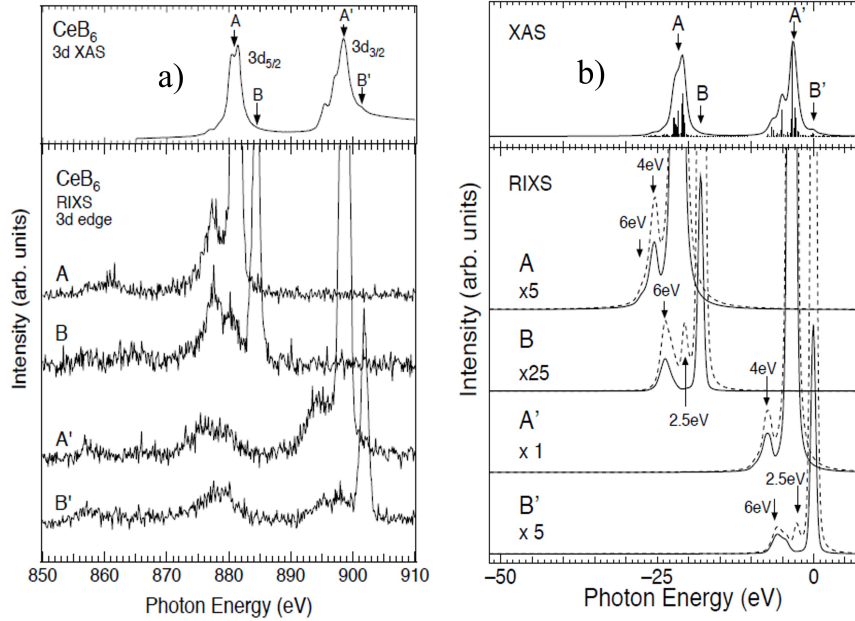


Figure 3.4: Experimental (a) and calculated (b) Ce  $M_5$ -edge XAS and RIXS spectra of the heavy fermion compound  $\text{CeB}_6$ . Reproduced from Ref. [9]

not exhibit a single peak as in  $\text{CeF}_3$ . Indeed, by tuning the incident photon energy on A, the RIXS spectrum exhibits an elastic peak and an inelastic structure located at 4 eV. The spectrum excited at the satellite structure (B) always exhibits the inelastic structure at 4 eV but with reduced intensity. However, an additional structure is observed at  $\sim 6$  eV-loss energy. This latter is not related to a fluorescence-like structure (see next section for further details). By tuning the incident photon energy on  $A'$  and  $B'$ , the spectra exhibit similar loss energy structures at 4 eV and 6 eV as those observed with excitation on A and B. However, a broad structure is observed at  $\sim 878$  eV of photon energy corresponding to a normal fluorescence ( $3d_{3/2} \rightarrow 3d_{5/2}$  emission). According to SIAM calculations which are in good agreement with the experimental spectra, the loss energy structures at 4 eV and 6 eV correspond to the  $4f^2$  final state ( $f^1 \rightarrow f^2$  charge excitations). Another interesting point is the theoretical prediction of an additional RIXS structure at 2.5 eV corresponding to the  $f^0$  final state. Indeed, this structure is only expected in  $\sigma$  polarization (polarized geometry).

Dallera et al. [10] performed Ce  $M_5$ -edge RIXS measurements with  $\sigma$  polarization of the incident photon (polarized geometry) and evidenced the  $f^0$  final state ( $f^1 \rightarrow f^0$  charge excitations) for the solid solution  $\text{Sc}(7 \text{ at.}\%)\text{:Ce}$ . This Ce system exhibits the well known  $\alpha$ - $\gamma$  transition as a function of temperature. The experimental RIXS spectra at the photon energy corresponding to the maximum of the  $M_5$ -edge XAS main structure ( $d^9 f^2$  final states), and to the  $f^1$  satellite, are shown in the left panel of Figure 3.5. The spectrum measured using a photon energy tuned to the  $f^1$  satellite exhibits, in addition to the elastic peak, a strong structure located at 2 eV with mainly  $f^0$  character. Interestingly, the relative intensity of

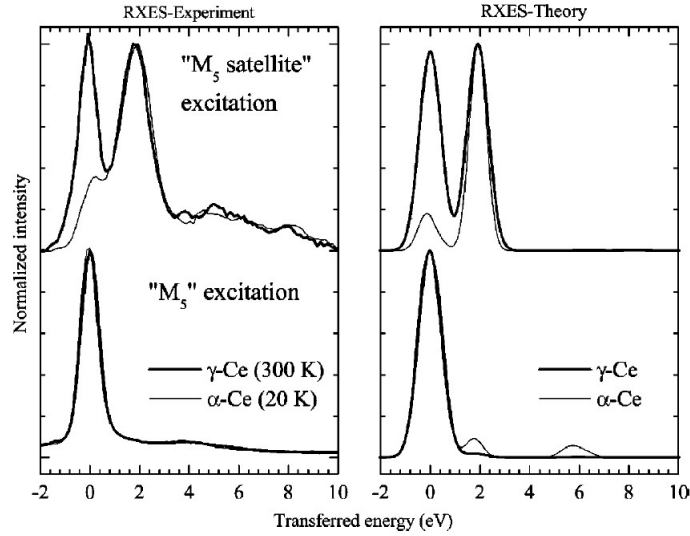


Figure 3.5: Left: Ce  $M_5$ -edge RIXS spectra measured at 20 K ( $\alpha$ -phase) and 300 K ( $\gamma$ -phase) at the maximum of the XAS main structure (bottom) and the XAS satellite (top). Right: Calculated spectra within the SIAM model.

the  $f^0$  structure with respect to the elastic peak is strongly affected by the  $\alpha$ - $\gamma$  transition, it decreases by  $\sim 4$  times in the  $\gamma$  phase. The calculated spectra shown in the right panel of Figure 3.5 are in nice agreement with the experimental ones. Indeed, this spectral change reflects the weight of the  $f^0$  configuration in the  $\alpha$  ( $1 - n_f = 0.15$ ) and  $\gamma$  ( $1 - n_f = 0.05$ ) phases. Surprisingly, they did not observe loss energy structures corresponding to the  $f^2$  final states in their experimental results. Indeed, the spectrum measured at  $M_5$  exhibits only a strong elastic peak in both  $\alpha$  and  $\gamma$  phases, while theoretical calculations predicted additional loss energy structures associated with the  $f^0$  and  $f^2$  final states in the  $\alpha$  phase. However, they clearly showed that polarization dependence is very useful for investigating the hybridization strength between the 4f and conduction states.

### 3.3.2 Spin-orbit and crystal field excitations

20 years after the early RIXS experiments, there has been a strong improvement in the energy resolution of the technique which allowed investigating the low energy excitations in cerium compounds such as the 4f spin-orbit and the local crystal electric field levels [13, 14, 15, 16]. We will focus on the typical  $\text{CeRh}_2\text{Si}_2$  heavy fermion to illustrate this recent progress in the field of RIXS studies of Ce materials. A free  $\text{Ce}^{3+}$  ion corresponding to a  $4f^1$  configuration is characterized by a  $L = 3$  angular momentum and a  $S = 1/2$  spin. This configuration is 14-fold degenerate as depicted in Figure 3.6. Nonetheless, the spin-orbit interaction breaks this degeneracy and gives rise to two different levels characterized by the total angular momentum  $J$ :  $J = |L - S| = 5/2$  and  $J = L + S = 7/2$ . The  $f$  shell being less than half-filled, the ground state is given by  $J = 5/2$  (the term symbol  $^2F_{5/2}$  6-fold degenerate), following the

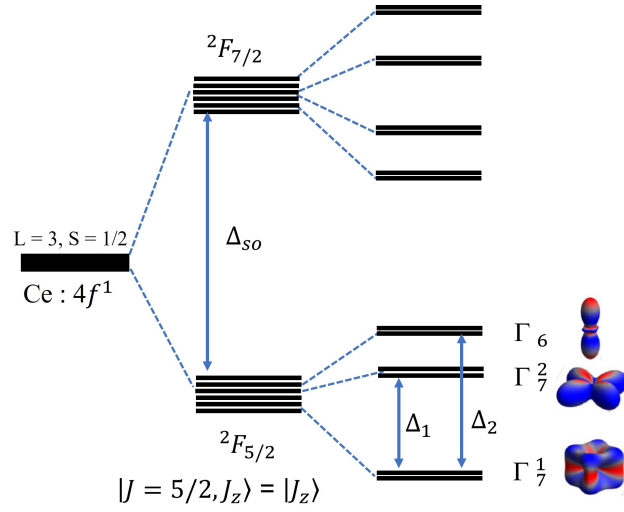


Figure 3.6: Schematic illustration of the spin-orbit and crystal electric field splitting of the 4f states in a tetragonal symmetry with the charge distribution for each Kramer's doublet arising from the  ${}^2F_{5/2}$  multiplet.

Hunds' rule. The upper state is given by  $J = 7/2$  (the term symbol  ${}^2F_{7/2}$  8-fold degenerate) and is separated from the ground state by the spin-orbit energy  $\Delta_{so} \sim 300$  meV. When the  $\text{Ce}^{3+}$  ions are in a crystal, the presence of the ions surrounding the Ce atom leads to an additional electrostatic interaction that induces a further splitting of the Hund's rule ground state. The resulting states, called the crystal electric field (CEF) states, are characterized by an anisotropy of the 4f electrons spatial distribution which affects most of the physical properties. These CEF states and their energies are described by an effective CEF model [17]. Owing to the atomic-like character of the 4f electrons (see figure 3.7), the CEF energy in rare earths ( $\sim 10 - 30$  meV) is one order of magnitude lower than the spin-orbit coupling ( $\sim 300$  meV), unlike in the transition metals. In the case of a tetragonal symmetry, the CEF states for the low-lying  $J = 5/2$  multiplet are three Kramer's doublets given by the symmetry:

$$\begin{aligned}
 \Gamma_6 &\Rightarrow |\pm 1/2\rangle \\
 \Gamma_7^1 &\Rightarrow a|\pm 5/2\rangle + b|\pm 3/2\rangle \\
 \Gamma_7^2 &\Rightarrow b|\pm 5/2\rangle - a|\pm 3/2\rangle
 \end{aligned} \tag{3.7}$$

with  $a^2 + b^2 = 1$ ,  $a$  and  $b$  depending on the details of the CEF Hamiltonian. So, a goal when performing RIXS experiments is to determine on the one hand, the CEF excitation  $\Delta_1$  and  $\Delta_2$  to the first and second excited CEF levels respectively, and on the other hand, the mixing parameter,  $a$ .

In figure 3.8, we show a typical example of high-resolution Ce- $M_5$  RIXS spectra of  $\text{CeRh}_2\text{Si}_2$  measured by Amorese [12] in the vicinity of the elastic peak. The corresponding incident photon energy is indicated by the black arrow in the XAS spectra, and RIXS spectra were

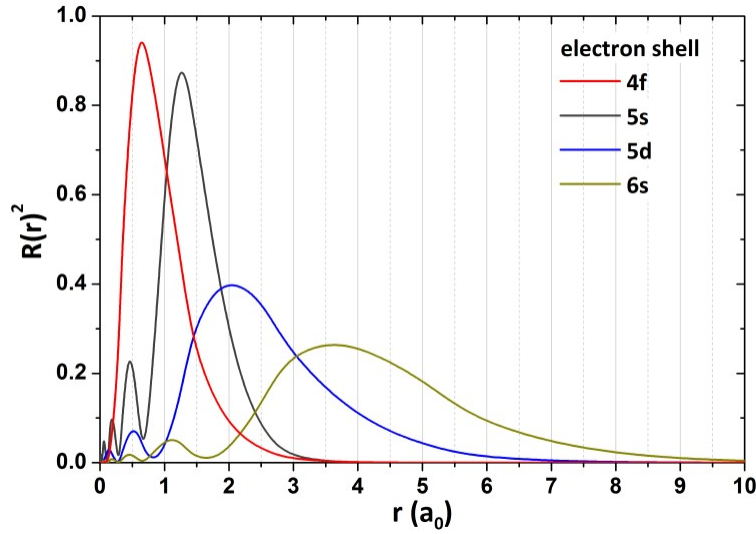


Figure 3.7: Square of the atomic radial wave functions for the  $4f$ ,  $5s$ ,  $5d$  and  $6s$  shell calculated by the Hartree Fock method for the  $Ce^{3+}$  configuration. The distance  $r$  from the nucleus on the  $x$ -axis is given in units of the Bohr radius  $a_0$ . reproduced from [11].

measured with  $\pi$  and  $\sigma$  polarization of the incident photons. A phenomenological fit of the spectra allows for getting an idea of the CEF energies. The  $4f$  level peaks are split into two groups corresponding to the  $f_{5/2}^1$  multiplet (the elastic peak and levels peaks at about 46 meV and 73 meV) and the  $f_{7/2}^1$  multiplet (4 levels in the range between 250-400 meV). For an accurate investigation of the CEF energies and identifying the arrangement of the CEF states ( $\Gamma_6$ ,  $\Gamma_7^1$ , and  $\Gamma_7^2$ ) a simulation of the spectra (see figure 3.8) is required. For the  $CeRh_2Si_2$  compound, the comparison between the experimental data and calculated spectra allows to deduce that the ground state is given by the  $\Gamma_7^1$  states, and the first and second excited states are respectively given by the  $\Gamma_6$  and  $\Gamma_7^2$  states. The corresponding mixing parameter is  $a = 0.96$ [14].

An important feature of RIXS can be stressed here. Indeed, RIXS is a second-order optical process with absorption and emission transitions. Each one is governed by the dipole selection rules. However, the total RIXS process does not follow these rules. Typically, RIXS yields access to the  $ff$  excitations as described above, unlike x-ray absorption.

### 3.3.3 Fluorescence emission

In addition to the  $ff$  and charge transfer excitations observed in the range below 10 eV, other features are visible at high energy loss in the RIXS spectra of cerium compounds. These features involved different electronic levels in the absorption and emission processes and as a result, they are not related to a RIXS process. In these kind of processes, the information on the energy of the incident photon and the intermediate state are generally lost. The energy

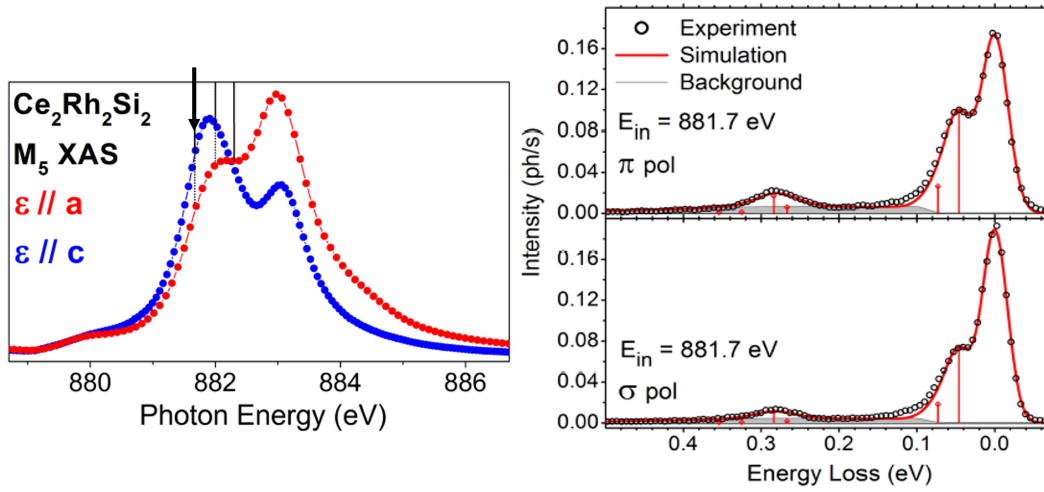


Figure 3.8: (a) Ce  $M_5$  XAS spectra of  $\text{CeRh}_2\text{Si}_2$  measured with  $\sigma$  and  $\pi$  polarization of the incident photon. The black arrow indicates the incident photon energy (881.7 eV) for the RIXS spectra. (b) Ce  $M_5$  RIXS spectra nicely fit by the simulations with a CEF splitting of 0-46-73 meV associated with  $\Gamma_7^1$ - $\Gamma_6$ - $\Gamma_7^2$  states for the  $f_{5/2}^1$  multiplet. Reproduced from Ref [12]

of the outgoing photon only depends on the energies of the levels involved in the emission process. It does not depend on the energy of the ingoing photon. This kind of feature is referred to as *fluorescence*. For Ce  $M_{4,5}$ -edge RIXS spectra,  $5p \rightarrow 3d$  transitions as depicted in Figure 3.9 can occur concurrently. A typical example is shown in figure 3.10a.

Another feature is visible in RIXS spectra, but only at the Ce- $M_4$  edge (see figure 3.10b). Indeed, the corresponding deexcitations require the presence of a  $3d_{3/2}$  hole. This process is referred to as the MMN Coster-Kronig transition (see Figure 3.9 right panel). When a  $3d_{3/2}$  is excited into the  $4f$  states, a  $3d_{5/2}$  electron deexcites in order to fill the hole, and its energy is transferred to an electron in the valence band which is photoemitted. Then in the final state, a valence electron decays to fill the  $3d_{5/2}$  left by the Coster-Kronig conversion. The emitted photon energy is about 17 eV, corresponding to energy between the  $3d_{3/2}$  and  $3d_{5/2}$  levels and can be measured as the energy separation between the main XAS structures of the  $M_4$  and  $M_5$  edges. It is worth noting that the energy loss of the structure corresponding to this process does not depend on incident photon energy and it is usually assigned to a normal  $3d_{5/2}$  fluorescence [9].

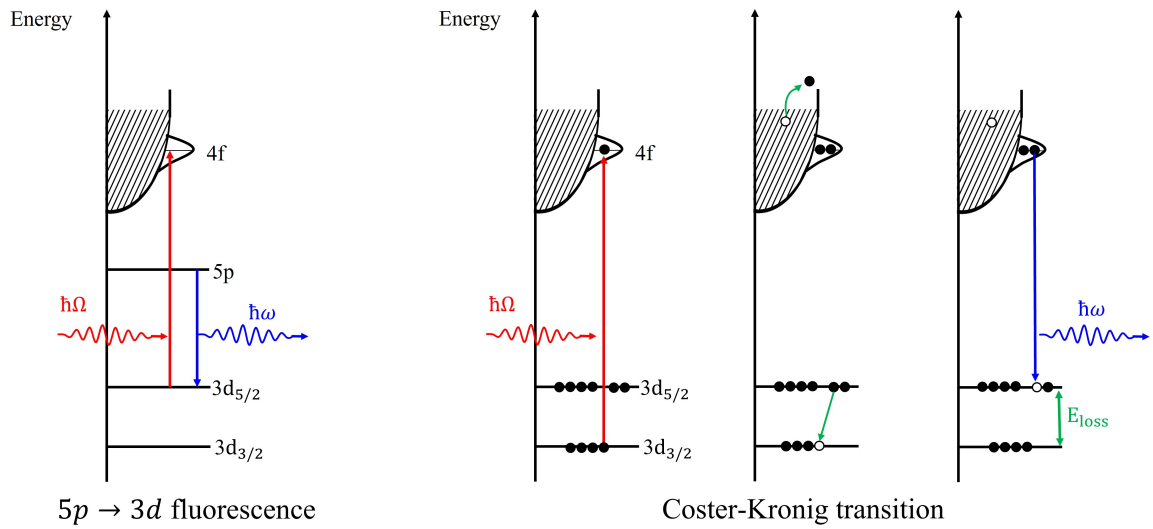


Figure 3.9:  $5p \rightarrow 3d$  and MMN Coster-Kronig fluorescence emissions who may be observed in the Ce  $M_5$ -edge RIXS spectra

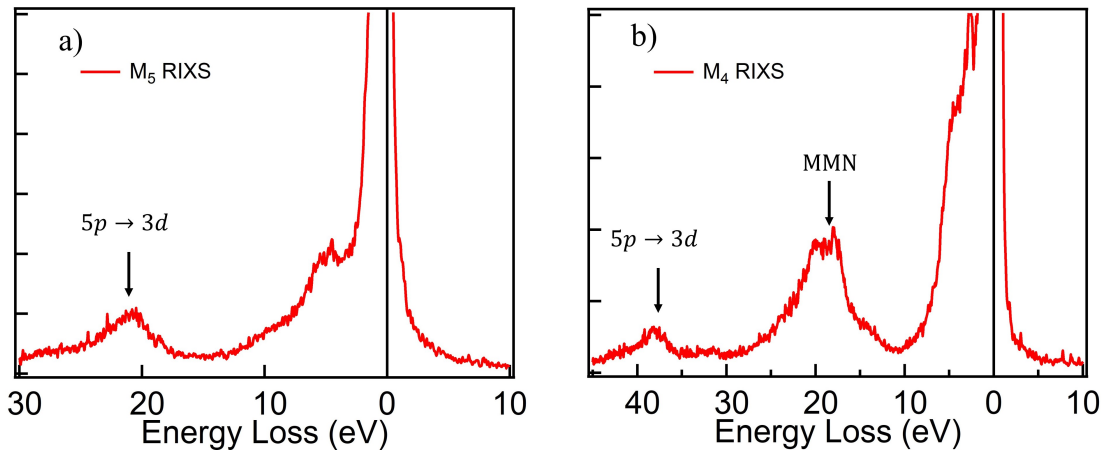


Figure 3.10:  $5p \rightarrow 3d$  and MMN Coster-Kronig fluorescence emissions in RIXS spectra measured at  $M_5$  (a) and  $M_4$  (b) edges of a CeMnSi compound we measured at SEXTANTS beamline.

## 3.4 Experimental Aspects

Three elements are important in order to carry out XAS/RIXS measurements:

- A monochromatic light from synchrotron radiation.
- A clean sample surface of the material under investigation, which requires an ultra-high vacuum environment, especially for XAS.
- A means of collecting and analyzing the energy and momentum of the emitted photons, typically through a spectrometer with a CCD detector.

The experimental works presented in this thesis have been performed on two spectrometers. The AERHA spectrometer[18] of SEXTANTS beamline[19] at synchrotron SOLEIL and the AGM-AGS spectrometer of Taiwan Light Source. We will briefly discuss the equipment of the SEXTANTS beamline.

### 3.4.1 RIXS at AERHA spectrometer at synchrotron SOLEIL

Sextants is a beamline of the Synchrotron Soleil, conceived for the investigation of electronic and magnetic properties of solids through an elastic, inelastic, and coherent scattering of soft X-ray photons. The different experimental end-stations installed at Sextants allow performing resonant inelastic x-ray scattering, x-ray resonant magnetic scattering, and coherent x-ray scattering, the last one including also imaging via Fourier transform holography. The beamline is equipped with:

- Two Apple-II undulators of 44 mm (HU44) and 80 mm (HU80) period, providing linear or circular polarization control over the whole 50-1700 eV energy range.
- A fixed-deviation monochromator based on five plane gratings and one spherical mirror. One of the two branches of the beamline delivers a  $2 \times 100 \mu\text{m}^2$  spot size to the AERHA spectrometer, to perform RIXS experiments on solid and gaseous species in the soft and ultra-soft X-ray regime. The resolving power exceeds  $10^4$ , and the maximum flux on the sample at 1000 eV is  $2.10^{23}$  ph/s/0.1% bw (photons per second per relative spectral bandwidth).
- Optics focusing down to  $2 \mu\text{m}$  in the vertical beam size, allow to achieve of high energy resolution while preserving high transmission, yielding the best compromise considering the low cross-section of the RIXS process.

The optical layout of the beamline firstly consists of pair of horizontal mirrors that deviate the beam from the undulator sources. The following optical element is the fixed-deviation monochromator. It consists of five interchangeable VLS gratings and a spherical mirror that focuses the radiation dispersed by the grating to the vertically occulting exit slit. Finally, an elliptical-cylindrical mirror refocuses the beam onto the sample chamber. The scattered photons at a fixed angle of  $90^\circ$  from the incoming beam are brought to the AERHA spectrometer

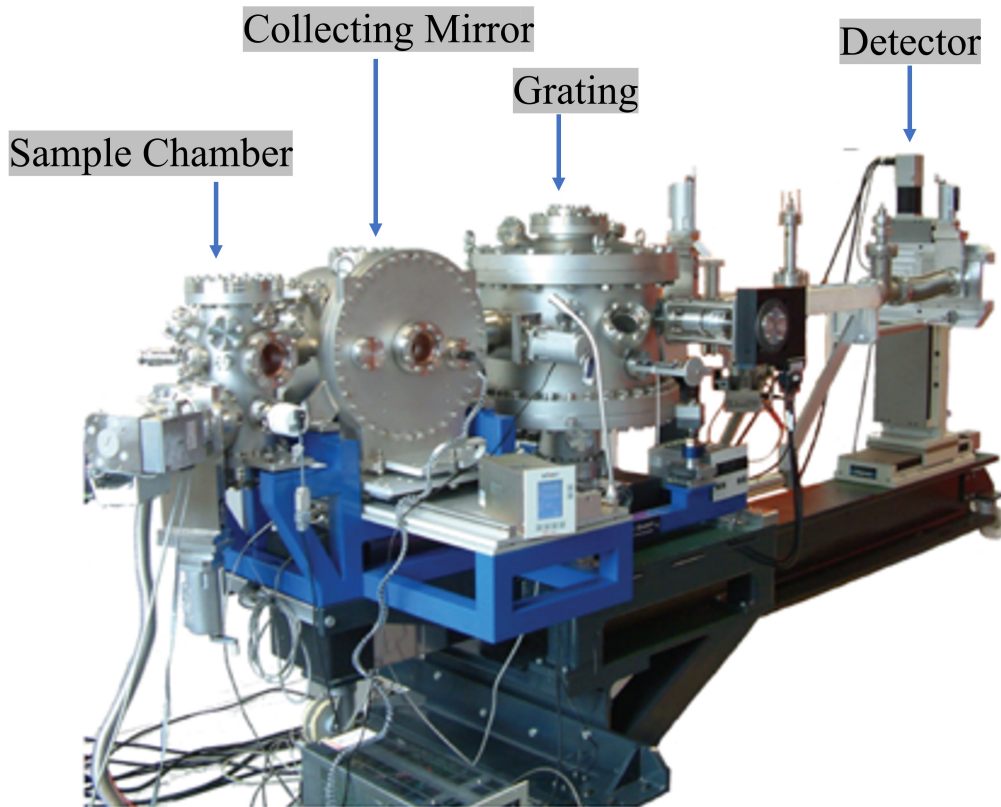


Figure 3.11: Picture of the AERHA spectrometer of SEXTANTS beamline with its main component: the sample chamber, the arm of the RIXS spectrometer together with the collecting mirror, the grating chamber and the RIXS detector.

(Adjustable Energy Resolution High Acceptance). The spectrometer collects over a certain solid angle the photons scattered by the sample and analyzes their energy. The AERHA sample chamber is equipped with a quadripolar magnet that delivers a rotatable magnetic field with a maximum strength of 0.45 T. moreover, the sample holder is equipped with 12 electrical contacts and works in the temperature range from 20 K up to 300 K. This offer the possibilities of performing temperature dependent RIXS under applied magnetic and electric field.

A picture of the AERHA spectrometer that incorporates a 3-meter-long arm is shown in figure 3.11 and its optical element scheme is shown in figure 3.12 The AERHA spectrometer is based on an elliptical mirror and a VLS grating focusing on a  $13 \mu\text{m}$  pixel charge-coupled device (CCD) detector cooled by liquid nitrogen in order to reduce the thermal noise. Figure 3.14 shows a raw image on the detector that consists in horizontal lines at different heights, each corresponding to photon energy. As shown in Figure 3.14, the data reduction process consists of the integration of the acquired images along the vertical axis of the detector (the



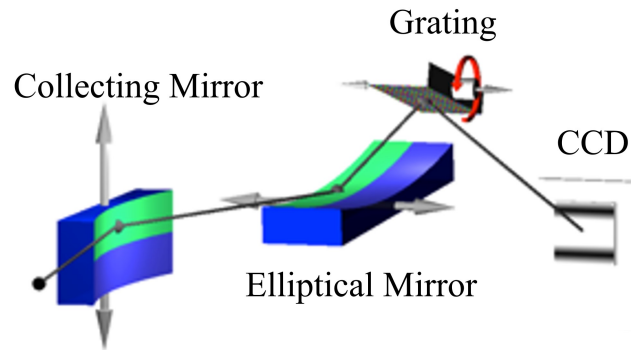


Figure 3.12: Optical element scheme of the AERHA spectrometer.

isoenergetic lines). Owing to the focussing properties of the grating (elliptical), the shape of certain photon energy is not a straight line onto the CCD, but it is a sort of arc. This can be corrected by the acquisition software with parabolic interpolation. Before the experiments, a calibration procedure is performed in order to assign the proper energy scale to the spectra, which are discretized in pixels along the vertical axis of the CCD detector. This consists in measuring the changes in the position of the elastic line (from the bottom to the top of the detector) while gradually changing the incident photon energy (see figure 3.13).

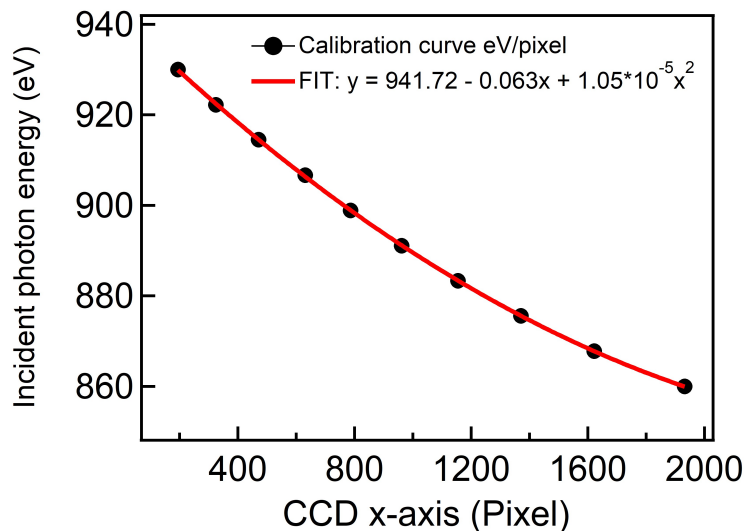


Figure 3.13: Calibration curve eV/pixel: incident photon energy versus peak position

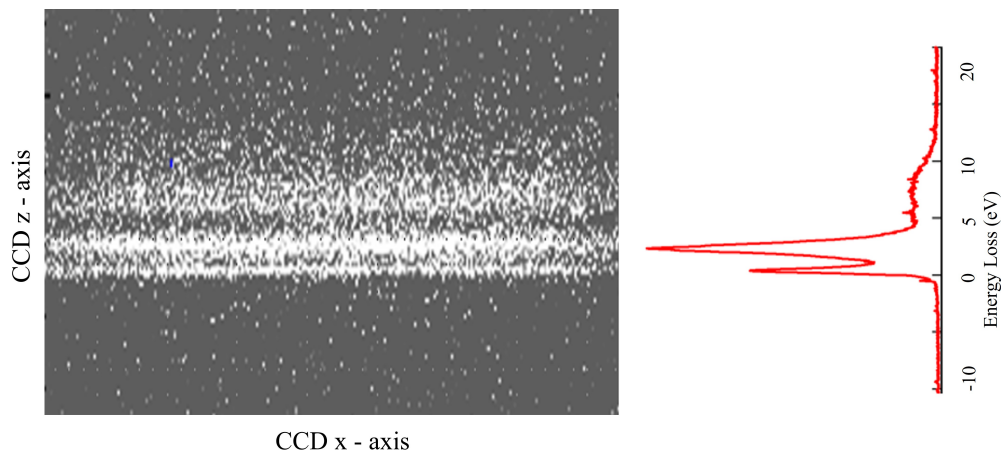


Figure 3.14: The RIXS intensity captured at the CCD detector showing in the left panel a 2D RIXS image measured on a cerium compound. Photons are scattered to the detectors as a function of energy in the z-axis and intensity in the x-axis. The right panel shows the RIXS spectrum, which is produced by integrating the CCD image along the horizontal axis.

### 3.4.2 Sample surface

The measurements we carried out at the SEXTANTS beamline dealt with the  $M_5$  edge of polycrystalline cerium compounds. The surface of such samples oxidizes heavily. Moreover, the total electron yield (TEY) detection mode of the XAS measurements is extremely sensitive to the surface. In order to obtain a clean surface and to avoid oxide contribution in the spectra, a cleaning procedure of the sample in vacuum conditions ( $\sim 10^{-8}$  mbar) by scraping the sample in the load lock has been established during our beamtime. Even for RIXS measurements, we will see that a clean sample is required to obtain spectra without oxide contribution. The comparison of XAS/RIXS measurements between a freshly scraped surface and a surface that has been exposed for more than 10 hours will be presented in section 3.7.3.

## 3.5 XAS and RIXS simulation

This section will describe the method to calculate XAS and RIXS spectra of intermediate valence compounds. For this purpose, it is crucial to combine the SIAM with the full multiplet theory. Indeed, the SIAM part [20] will allow reproducing the relative energies of the spin and charge loss structures, while the full multiplet part will allow reproducing the correct shape of the spectra and, more importantly, the polarization dependence of the spectra. The simulations were performed with the Quanty program created by M. W. Haverkort [21, 22, 23, 24] which is a suitable approach to describe the electronic wave function of the system in the many-body atomic picture (Atomic full multiplet theory). In this thesis chapter, we have combined the atomic full multiplet theory with a simplified single impurity Anderson model to calculate the XAS and RIXS spectra of intermediate valence Ce compounds, as detailed in the following. For a detailed reading of the full multiplet calculations, Refs.[25, 26, 27, 28, 29, 30] present the original formalism.

### 3.5.1 Atomic full multiplet theory

**Coulomb interaction** The Coulomb repulsion between electrons has to be considered for partially filled shells (shells with more than one electron or hole) and is the key ingredient for reproducing the complex line shape due to multiplet structures in core level spectroscopy. The Coulomb interaction Hamiltonian is given by:

$$H_C = \frac{1}{2} \sum_{i>j} \frac{e^2}{|r_i - r_j|}, \quad (3.8)$$

The Coulomb repulsion can be described as a scattering of two electrons with quantum numbers  $\tau_1$  and  $\tau_2$  following the exchange with an entity  $k$  of two entering electrons with quantum numbers  $\tau_3$  and  $\tau_4$  as depicted in Figure 3.15. It can be written in second quantization as

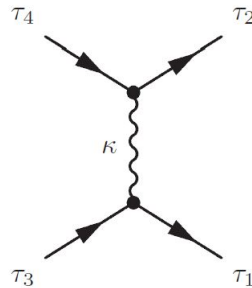


Figure 3.15: Scattering event of the Coulomb repulsion. The two electrons have respectively the quantum numbers ( $\tau_3$  and  $\tau_4$ ) and ( $\tau_1$  and  $\tau_2$ ) before and after the scattering.

$$H_C = \sum_{\tau_1 \tau_2 \tau_3 \tau_4} U_{\tau_1 \tau_2 \tau_3 \tau_4} c_{\tau_1}^+ c_{\tau_2}^+ c_{\tau_3} c_{\tau_4}, \quad (3.9)$$

with

$$U_{\tau_1 \tau_2 \tau_3 \tau_4} = \int \int \Psi_{\tau_1}^*(r_i) \Psi_{\tau_2}^*(r_j) \frac{e^2}{|r_i - r_j|} \Psi_{\tau_4}(r_i) \Psi_{\tau_3}(r_j) dr_i dr_j \quad (3.10)$$

where  $\tau_i = (n_i, l_i, m_i, \sigma_i)$  denote the set of principal quantum number  $n_i$ , the orbital angular momentum  $l_i$ , the  $z$ -component of the angular momentum  $m_i$ , and  $z$ -component of spin  $\sigma_i$ .  $c_{\tau_i}^+$  and  $c_{\tau_i}$  are respectively the creation and annihilation operators of an electron in the spin-orbital  $\Psi_i$ . In order to determine the matrix element  $U_{\tau_1 \tau_2 \tau_3 \tau_4}$ , the electron-electron interaction term can be written as the multipole expansion:

$$\frac{e^2}{|r_i - r_j|} = \sum_{k=0}^{\infty} \frac{r_{<}^k}{r_{>}^{k+1}} P_k(\cos \alpha), \quad (3.11)$$

where  $\alpha$  is the angle between  $r_i$  and  $r_j$ ,  $r_{<} = \min(r_i, r_j)$  and  $r_{>} = \max(r_i, r_j)$  denote respectively the lesser and greater value of the distance  $r_i$  and  $r_j$ . The  $P_k(\cos \alpha)$  are the Legendre polynomials which are given by:

$$P_k(\cos \alpha) = \frac{4\pi}{2k+1} \sum_{m=-k}^k Y_{-m}^{(k)}(\theta_i, \phi_i) Y_m^{(k)}(\theta_j, \phi_j), \quad (3.12)$$

Next, we consider the atomic spin-orbitals given by

$$\Psi_{\tau_i}(r, \theta, \phi) = R_{n_i l_i}(r) Y_{m_i}^{(l_i)}(\theta, \phi) \sigma_i, \quad (3.13)$$

where  $R_{n_i l_i}(r)$  are the real radial part which depends on the electronic configuration (shell and subshell), and  $Y_{m_i}^{(l_i)}(\theta, \phi)$  are the spherical harmonics which is determined by the angular degree of freedom. We then evaluate the matrix element  $U_{\tau_1 \tau_2 \tau_3 \tau_4}$  by considering Eq. 3.12 and Eq. 3.13. We first consider the angular dependence by collecting the parts of the integral dependent upon the variables  $(\theta_i, \phi_i)$  and  $(\theta_j, \phi_j)$ . This gives rise to two factors which are the so-called Gaunt coefficients expressed in Eq.3.14 and Eq.3.15:

$$\int_0^{2\pi} d\phi_i \int_{-1}^1 d \cos(\theta_i) Y_{-m_1}^{(l_1)}(\theta_i, \phi_i) Y_m^{(k)}(\theta_i, \phi_i) Y_{m_3}^{(l_3)}(\theta_i, \phi_i) \quad (3.14)$$

$$\int_0^{2\pi} d\phi_j \int_{-1}^1 d \cos(\theta_j) Y_{-m_2}^{(l_2)}(\theta_j, \phi_j) Y_m^{(k)}(\theta_j, \phi_j) Y_{m_4}^{(l_4)}(\theta_j, \phi_j) \quad (3.15)$$

By considering the  $\phi$ -dependence of  $Y_m^{(l)} = P_m^{(l)} e^{im\phi}$ , it is interesting to find that the Gaunt coefficients Eq.3.14 and Eq.3.15 are respectively different from zero only if  $m - m_1 + m_3 = 0$  and  $m - m_2 + m_4 = 0$ . Hence, by combining these two conditions, we obtain  $m_1 + m_2 = m_3 + m_4$ , which implies that the  $z$ -component of the total angular momentum  $M^z$  is conserved in the scattering process. Let us now investigate the integral over the two radial variables

$r_i$  and  $r_j$ . These integrations are more difficult, and the general expression involving four different shells in the scattering process is given by:

$$R^k(\tau_1\tau_2\tau_3\tau_4) = e^2 \int_0^\infty \int_0^\infty \frac{r_{<}^k}{r_{>}^{k+1}} R_{n_1 l_1}(r_i) R_{n_2 l_2}(r_j) R_{n_3 l_3}(r_i) R_{n_4 l_4}(r_j) dr_i dr_j. \quad (3.16)$$

So, we get the final Coulomb matrix element as

$$U_{\tau_1\tau_2\tau_3\tau_4} = \delta_{\sigma_1,\sigma_3} \delta_{\sigma_2,\sigma_4} \sum_{k=0}^{\infty} a^k(l_1 m_1, l_3 m_3) a^k(l_4 m_4, l_2 m_2) R^k(\tau_1\tau_2\tau_3\tau_4), \quad (3.17)$$

where  $\delta_{\sigma_1,\sigma_3}$  ( $\delta_{\sigma_2,\sigma_4}$ ) indicate that the spin-component of  $\tau_1$  and  $\tau_3$  ( $\tau_2$  and  $\tau_4$ ) must be the same if the integral is not to be zero. We also introduced the following short notation for Gaunt coefficients:

$$a^k(l_1 m_1, l_2 m_2) = \sqrt{\frac{4\pi}{2k+1}} \int_0^{2\pi} d\phi \int_{-1}^1 d\cos(\theta) Y_{-m_1}^{(l_1)}(\theta, \phi) Y_{m_1-m_2}^{(k)}(\theta, \phi) Y_{m_2}^{(l_2)}(\theta, \phi). \quad (3.18)$$

The  $a^k$  values depend only on the symmetries and can be solved analytically, and they are tabulated in the textbook by Condon and Shortley [28]. Following the conservation of the angular momentum,  $a^k$  values are nonzero only if  $|l_1 - l_3| \leq k \leq |l_1 + l_3|$  and  $|l_2 - l_4| \leq k \leq |l_2 + l_4|$ .

For two electrons in the same sub-shell,  $n_1 = n_2 = n_3 = n_4$  and  $l_1 = l_2 = l_3 = l_4$ , i.e. the Coulomb interaction within one single shell, one defines

$$F^k = R^k(\tau_1\tau_2\tau_3\tau_4), \quad (3.19)$$

where  $k$  runs from 0 to  $2l$  in steps of 2. So for 2 electrons in  $d$  shell only  $F^0$ ,  $F^2$ , and  $F^4$  are nonzero and we should consider  $F^0$ ,  $F^2$ ,  $F^4$  and  $F^6$  for 2 electrons in the  $f$  shell. we can thus expressed the Coulomb interaction matrix element as a function of  $F^k$  and then calculate the multiplet energies in the  $LS$  coupling. For instance, one obtains for the  $f^2$  configuration:

$$\begin{aligned} E(^1S) &= F_0 + 60F_2 + 198F_4 + 1716F_6 \\ E(^3P) &= F_0 + 45F_2 + 33F_4 - 1287F_6 \\ E(^1D) &= F_0 + 19F_2 - 998F_4 + 7156F_6 \\ E(^3F) &= F_0 - 10F_2 - 33F_4 - 286F_6 \\ E(^1J) &= F_0 - 30F_2 + 97F_4 + 78F_6 \\ E(^3H) &= F_0 - 25F_2 - 51F_4 - 13F_6 \\ E(^1I) &= F_0 + 25F_2 + 9F_4 + F_6 \end{aligned} \quad (3.20)$$

From the energies of the different spectroscopic terms (Eq. 3.20), weighted by their degeneracy  $(2L+1)(2S+1)$ , we determine the average Coulomb interaction  $U_{ff}^{av}$ , i.e. the barycenter of the spectroscopic terms with respect to the energy of the configuration  $f^2$ . One obtains:

$$U_{ff}^{av} = F_{ff}^0 - \frac{4}{195} F_{ff}^2 - \frac{2}{143} F_{ff}^4 - \frac{100}{5577} F_{ff}^6, \quad (3.21)$$

where we use reduced expression  $F_0 = F^0$ ,  $F_2 = F^2/225$ ,  $F_4 = F^4/1089$  and  $F_6 = F^6/7361.64$ , following Condon and Shortley [28].

In the presence of a core hole like in the final state of Ce-M<sub>4,5</sub> XAS with a configuration  $3d^9 4f^n$ , one has to take into account the coulomb interaction between the 3d and 4f shell. In the scattering process of Figure 3.15, the electrons can remain in the same shell ( $n_1, l_1 = n_3, l_3$  and  $n_2, l_2 = n_4, l_4$ ) which gives rise to the direct term (Eq. 3.22) of the Coulomb interaction or can exchange their shells ( $n_1, l_1 = n_4, l_4$  and  $n_2, l_2 = n_3, l_3$ ) which corresponds to the indirect or exchange term as expressed in Eq. 3.23 .

$$F^k = e^2 \int_0^\infty \int_0^\infty \frac{r_i^k}{r_i^{k+1}} R_{n_1 l_1}^2(r_i) R_{n_2 l_2}^2(r_j) r_i^2 r_j^2 dr_i dr_j, \quad (3.22)$$

$$G^k = e^2 \int_0^\infty \int_0^\infty \frac{r_i^k}{r_i^{k+1}} R_{n_1 l_1}(r_i) R_{n_2 l_2}(r_j) R_{n_2 l_2}(r_i) R_{n_1 l_1}(r_j) r_i^2 r_j^2 dr_i dr_j, \quad (3.23)$$

In Eq. 3.22,  $k$  run from 0 to  $\min(2l_1, 2l_2)$  in step of 2 and Eq. 3.23 is nonzero only if  $|l_1 - l_2| \leq k \leq |l_1 + l_2|$ . For the  $3d^9 4f^n$  configuration, these conditions give rise to the nonzero Slater integrals  $F^0, F^2, F^4, G^1, G^3, G^5$  and the corresponding multiplet energies are given by:

$$\begin{aligned} E(^1P, ^3P) &= F_0 + 24F_2 + 66F_4 \pm (G_1 + 24G_3 + 330G_5) \\ E(^1D, ^3D) &= F_0 + 6F_2 - 99F_4 \pm (3G_1 + 42G_3 - 165G_5) \\ E(^1F, ^3F) &= F_0 - 11F_2 + 66F_4 \pm (6G_1 + 19G_3 + 55G_5) \\ E(^1G, ^3G) &= F_0 - 15F_2 - 22F_4 \pm (10G_1 - 35G_3 - 11G_5) \\ E(^1H, ^3H) &= F_0 + 10F_2 + 3F_4 \pm (15G_1 + 10G_3 + G_5) \end{aligned} \quad (3.24)$$

In the same was as in Eq 3.21, the average Coulomb interaction for the  $3d^9 4f^n$  configuration is given by:

$$U_{fd}^{av} = F_{fd}^0 - \frac{3}{70}G_{fd}^1 - \frac{2}{105}G_{fd}^3 - \frac{5}{231}G_{fd}^5. \quad (3.25)$$

configuration	4f-4f			3d-4f					spin-orbit	
	$F^2$	$F^4$	$F^6$	$F^2$	$F^4$	$G^1$	$G^3$	$G^5$	$\zeta(4f)$	$\zeta(3d)$
$4f^0$	-	-	-						-	
$4f^1$	-	-	-						0.087	
$4f^2$	10.223	6.347	4.548						0.074	
$3d^9 4f^1$	-	-	-	8.189	3.748	5.652	3.309	2.285	0.119	7.442
$3d^9 4f^2$	12.628	7.940	5.717	7.486	3.384	5.073	2.968	2.048	0.107	7.442
$3d^9 4f^3$	11.383	7.1	5.096	6.719	2.998	4.470	2.613	1.803	0.095	7.450

Table 3.1: Table showing the Slater integrals values and spin-orbit coupling constant for different Ce ion configurations. The values are determined from the Hartree-Fock calculations. Taken from Crispy [31], the graphic interface of the Quanty code.

Unlike the angular dependence given by the Gaunt coefficient which can be solved analytically, the radial dependence given by the Slater integrals  $F^k$  and  $G^k$  cannot be calculated

analytically. They are determined for a free ion based on the Hartree-Fock approximation with the atomic structure code RCNK36K by R. D Cowan [30]. The Slater integrals values for different Ce ion configurations are given in table 3.1. In a solid, the Slater integrals are empirically reduced in order to take into account the further modifications in the Hamiltonian introduced by the fixed ions and screening by the free electrons. Indeed, the intra-atomic electron-electron interactions are partially screened by the presence of other charges. This result in the multiplet splitting measured experimentally to get reduced from the ionic values. A reduction factor of 80% of the Hartree-Fock values of the Slater integrals has been noticed by comparing with experimental spectra to take this screening effect into account. Furthermore, in the presence of a 3d hole, the Coulomb repulsion between the 4f electrons and the 3d hole is reduced to 60% in order to reproduce the  $CeM_{4,5}$ -edge XAS spectra.

### 3.5.2 Full multiplet configuration interaction

Combining the multiplet description with the SIAM implies that the single Coulomb repulsion term in the SIAM Hamiltonian is replaced by a summation over four 4f-orbitals  $\alpha, \alpha', \beta, \beta'$  with  $z$ -component of the spin  $\sigma$  and  $\sigma'$ . The full multiplet configuration interaction Hamiltonian is therefore given by:

$$H_{AIM}^i = \epsilon_{4f} \sum_{\alpha\sigma} f_{\alpha\sigma}^+ f_{\alpha\sigma} + \sum_{k\sigma} \epsilon_k c_{k\sigma}^+ c_{k\sigma} + V \left( \sum_{k\alpha\sigma} c_{k\sigma}^+ f_{\alpha\sigma} + H.C. \right) + \sum_{\alpha\alpha'\beta\beta'\sigma\sigma'} U_{\alpha\alpha'\beta\beta'}^{ff} f_{\alpha\sigma}^+ f_{\beta\sigma'} f_{\alpha'\sigma'}^+ f_{\beta'\sigma} + \zeta_{4f} \sum_{\alpha\alpha'} l.s f_{\alpha}^+ f_{\alpha'}, \quad (3.26)$$

where the term  $U_{\alpha\alpha'\beta\beta'}^{ff}$  correspond to the Coulomb interaction matrix element. The diagonal matrix elements are function of the Slater integral parameters  $F_{ff}^0, F_{ff}^2, F_{ff}^4$  and  $F_{ff}^6$  as discussed above. We also added the last term that describes the 4f spin-orbit coupling.

For the SIAM part, and we used a simple form with a zero bandwidth conduction band representing a fully occupied ligand state to get a singlet ground state via the hybridization with the f states. Thanks to the Quany code, we have the possibility to set the number of configurations. We thus considered three different configurations in the initial and RIXS final states  $f^0, f^1 \underline{L}, f^2 \underline{L}^2$  and  $d^9 f^1, d^9 f^2 \underline{L}, d^9 f^3 \underline{L}^2$  for the intermediate states of RIXS ( final states of XAS). The 4f energies are defined as  $\epsilon_f = E(f_{5/2}^1 \underline{L}) - E(f^0)$  and  $E(f^2 \underline{L}^2) - E(f_{5/2}^1 \underline{L}) = \epsilon_f + U_{ff}$ . It is worth noting that the Coulomb interaction between 4f electrons in the SIAM is  $U_{ff}$  is not  $F_{ff}^0$ . By taking into account the 4f spin-orbit coupling, the ground state,  $|g\rangle$  is described by a linear combination of configurations as

$$|g\rangle = w^0 |f^0\rangle + w_{5/2}^1 |f_{5/2}^1 \underline{L}\rangle + w_{7/2}^1 |f_{7/2}^1 \underline{L}\rangle + w^2 |f^2 \underline{L}^2\rangle, \quad (3.27)$$

where  $\underline{L}$  denotes a hole in the conduction band.  $|w^0|^2, |w_{5/2}^1|^2, |w_{7/2}^1|^2$  and  $|w^2|^2$  are respectively the weight of the  $|f^0\rangle, |f_{5/2}^1 \underline{L}\rangle, |f_{7/2}^1 \underline{L}\rangle$  and  $|f^2 \underline{L}^2\rangle$  configuration and their dependence as a function of the hybridization strength  $V$  are shown in figure 3.16.

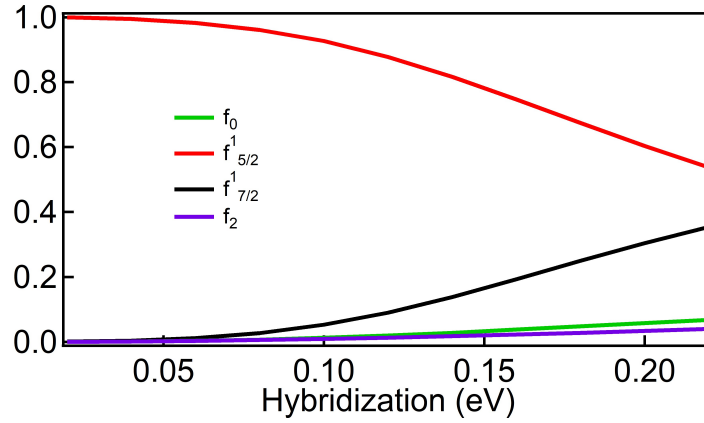


Figure 3.16: Weight of the  $f^0$ ,  $f_{5/2}^1$ ,  $f_{7/2}^1$  and  $f^2$  configurations in the initial ground state as a function of the hybridization  $V$  for  $\epsilon_f = -2.3$  eV and  $U_{ff}=7.15$  eV

In the intermediate state of RIXS ( XAS final state), there is an extra electron in the  $4f$  states in addition to a  $3d$  core hole. Therefore, the energy and occupation of the  $3d$  core hole are added in the corresponding Hamiltonian. Similar to the initial state, the multiplet effects due to the Coulomb repulsion between the core hole and the  $4f$  states are obtained by replacing the  $U_{fc}$  term with a summation over two  $4f$  and two  $3d$ -orbitals. The Hamiltonian in the intermediate state is therefore given by:

$$\begin{aligned}
H_{AIM}^f = & H_{AIM}^i + \epsilon_{3d} \sum_{\alpha\sigma} d_{\alpha\sigma}^+ d_{\alpha\sigma} \sum_{\alpha'\beta\beta'\sigma\sigma'} U_{\alpha\alpha'\beta\beta'}^{df,direct} d_{\alpha\sigma}^+ f_{\beta\sigma'} f_{\alpha'\sigma'}^+ d_{\beta'\sigma} \\
& + \sum_{\alpha\alpha'\beta\beta'\sigma\sigma'} U_{\alpha\alpha'\beta\beta'}^{df,exchange} f_{\alpha\sigma}^+ d_{\beta\sigma'} f_{\alpha'\sigma'}^+ d_{\beta'\sigma} + \zeta_{3d} \sum_{\alpha\alpha'} l.s d_{\alpha}^+ d_{\alpha'},
\end{aligned} \tag{3.28}$$

where the terms  $U_{\alpha\alpha'\beta\beta'}^{ff,direct}$  and  $U_{\alpha\alpha'\beta\beta'}^{ff,exchange}$  respectively correspond to the direct and indirect term of the Coulomb interaction matrix element described as a function of the Slater integral  $F_{df}^0$ ,  $F_{df}^2$ ,  $F_{df}^4$ ,  $G_{df}^1$ ,  $G_{df}^3$ ,  $G_{df}^5$  as discussed above. In the same way as in the initial state, the attractive Coulomb interaction between  $4f$  and  $3d$  hole in the SIAM  $U_{fd}$  is not  $F_{df}^0$ . The last term of the Hamiltonian describes the  $3d$  spin-orbit coupling.



### 3.5.3 XAS and RIXS spectral functions

For calculating the Ce  $M_5$ -edge XAS and RIXS spectra, we will use the SIAM combined with the full multiplet theory introduced in the previous section. The XAS spectral intensity is provided by the Fermi's golden rule

$$I_{XAS}(\hbar\omega) = \sum_f |\langle \phi_f | T_1 | g \rangle|^2 \delta(E_g + \hbar\omega - E_f), \quad (3.29)$$

where  $g$  and  $\phi_f$  respectively denote the initial ground state and all the XAS final states.  $T_1$  is the transition operator of the absorption process. The probability of a transition from the ground state to a given XAS final state is given by the integral  $|\langle \phi_f | T_1 | g \rangle|^2$  while the delta function ensures for the energy conservation. In order to numerically calculate an XAS spectrum, one has to first diagonalize the initial and final state Hamiltonian to find the initial ground state and all the possible final states. Then, one has to compute the transition probability between the ground state and each final state, each one corresponding to a delta peak in the spectrum. Finally, one can compare this with the experiment after broadening to account for the core-hole lifetime as well as the experimental resolution. However, this becomes less efficient typically when we have a large Hamiltonian matrix since it will require a significant computation time. The Quany code as well as most modern codes [32] calculates the spectra by using Green's functions formalism which requires less computational burden. Exploiting the fact that the matrix element  $|\langle \phi_f | T_1 | g \rangle|^2$  can be rewritten as  $\langle g | T_1^+ | \phi_f \rangle \times \langle \phi_f | T_1 | g \rangle$ , and using the identity

$$\sum_f |\phi_f \rangle \langle \phi_f| \delta(E_g + \hbar\omega - E_f) = \frac{-1}{2\pi i} (G^+ - G^-) \quad (3.30)$$

with  $G^\pm(E_g + \hbar\omega) = \frac{1}{\hbar\omega - H_{AIM}^f + E_g \pm \frac{1}{2}i\Gamma}$ ,

where  $G^+$  and  $G^-$  are Green's functions. So the XAS spectral intensity is now given by:

$$I_{XAS}(\hbar\omega) = -\text{Im} \langle g | T_1^+ \frac{1}{\hbar\omega - H_{AIM}^f + E_g + \frac{1}{2}i\Gamma} T_1 | g \rangle, \quad (3.31)$$

where "Im" stands for the imaginary part. This spectral function consists of a series of Lorentzians of width  $\Gamma$  at all the eigenvalues of the final state Hamiltonian. One only needs to calculate the inverse of the final state Hamiltonian instead of all the eigenvectors of the final state Hamiltonian. In the same way, one obtains the RIXS spectral intensity by using the Kramers-Heisenberg formula described below :

$$G_{T_1, T_2}(\omega, \Omega) = -\text{Im} \langle g | T_1^+ \frac{1}{\hbar\omega - H_{AIM}^f + i\Gamma/2} T_2^+ \frac{1}{\hbar\Omega - H_{AIM}^i + i\Gamma/2} \times \quad (3.32)$$

$$T_2 \frac{1}{\hbar\omega - H_{AIM}^f + i\Gamma/2} T_1 | g \rangle,$$

where  $T_1$  and  $T_2$  represent the optical transition operator for the absorption and emission process, respectively.  $H_{AIM}^i$  and  $H_{AIM}^f$  are the Hamiltonian in the initial and intermediate state, respectively.

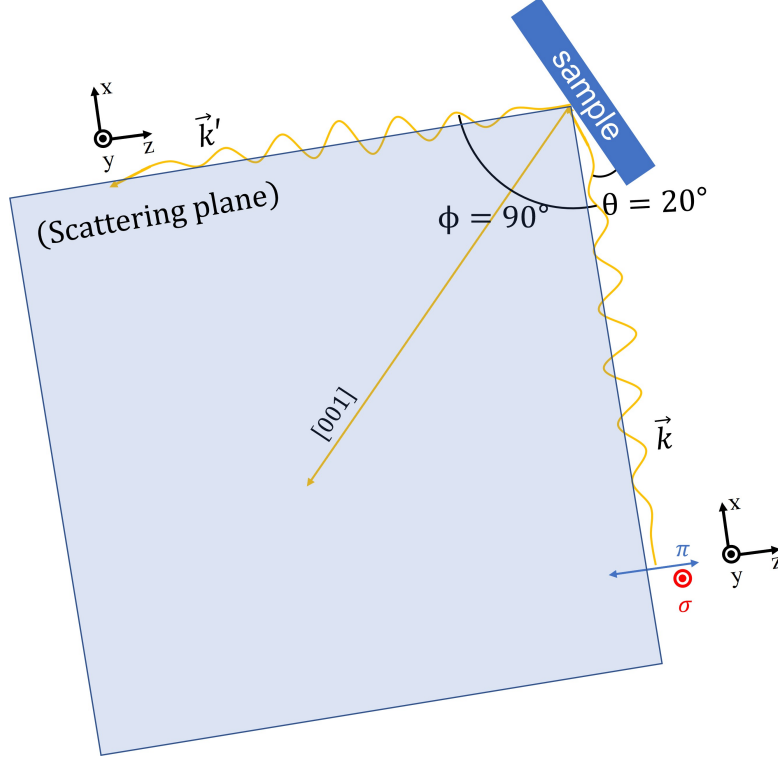


Figure 3.17: Geometry of the measurement.  $\vec{k}$  and  $\vec{k}'$  are the momenta of the incident and emitted photon respectively. The polarization vectors of the incident photon energy in depolarized geometry ( $\pi$  polarization) and polarized geometry ( $\sigma$  polarization) are respectively parallel to the z-direction and y-direction. The emitted photon energy is polarized in both the y-direction and x-direction.

Let us now take into account the scattering geometry as well as the polarization dependence. Figure 3.17 shows the two different polarization geometries used for linear polarized incident x-rays when the scattering angle is fixed to 90 degrees: Polarized geometry ( $\sigma$  polarization) where the incident x-ray is perpendicular to the scattering plane and the so-called depolarized geometry ( $\pi$  polarization) where the incident x-ray is parallel to the scattering plane. By using the polarization vector  $e = (e_x, e_y, e_z)$  and the spherical tensor operator  $C_q^{(k)}$ , the dipole transition operator  $T_1$  is expressed as:

$$T_1 = e \cdot r = r \times \left[ \frac{-1}{\sqrt{2}}(e_x - ie_y)C_1^{(1)} + \frac{1}{\sqrt{2}}(e_x + ie_y)C_{-1}^{(1)} + e_z C_0^{(1)} \right], \quad (3.33)$$

where  $C_q^{(k)}$  ( $q=-1, 0, 1$ ) are defined with the spherical harmonics  $Y_q^{(k)}$  by :

$$C_q^{(k)} = \sqrt{\frac{4\pi}{2k+1}} Y_q^{(k)}. \quad (3.34)$$

Thus, the dipole transition operator for an incident or emitted x-ray parallel to x, y and z directions are respectively given by:  $T_x = \frac{1}{\sqrt{2}}(C_{-1}^{(1)} - C_1^{(1)})$ ,  $T_y = \frac{i}{\sqrt{2}}(C_{-1}^{(1)} + C_1^{(1)})$  and  $T_z = C_0^{(1)}$ . By taking into account the fact that the polarization of the emitted x-ray is not usually detected, the RIXS spectra in  $\sigma$  and  $\pi$  polarization with  $90^\circ$  of scattering angle are respectively given by:

$$G_\sigma = G_{T_y, T_x} + G_{T_y, T_y}, \quad G_\pi = G_{T_z, T_x} + G_{T_z, T_y}. \quad (3.35)$$

### 3.5.4 RIXS spectra for a trivalent system: $\text{CeF}_3$

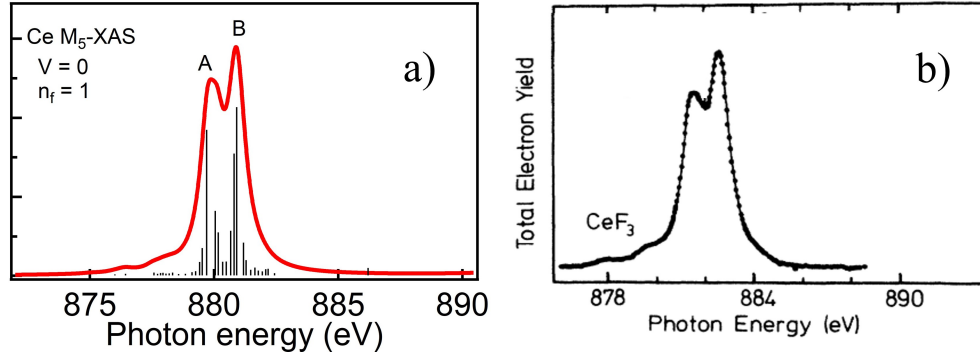


Figure 3.18: (a) Calculated Ce  $M_5$ -edge XAS spectrum for a trivalent Ce compounds. the vertical bar diagrams indicate the intensities and positions of the transition probability to the final states. (b) Experimental Ce  $M_5$ -edge XAS spectrum of  $\text{CeF}_3$  compound taken from [33].

configuration	$J$	Terms symbols	degeneracy
$4f^1$	$5/2$	$^2F$	1
	$7/2$	$^2F$	1

Table 3.2: Symmetries of  $4f^1$  electron

Figure 3.18a and 3.18b respectively show the calculated Ce  $M_5$ -edge XAS spectrum for a purely trivalent Ce compound and a typical experimental spectrum for  $\text{CeF}_3$ [33]. The calculated spectrum exhibits a prominent structure centered at 880 eV corresponding to the  $3d^{10}4f^1 \rightarrow 3d^94f^2$  transitions [34]. The complex line shape of the spectrum arises from the multiplet effects of the  $3d^94f^2$  configuration, which corresponds to  $10 \cdot \frac{14 \cdot 13}{2} = 910$  possible

configuration	$J$	Terms symbols	degeneracy
$3d^9 4f^2$	1/2	$^2D(2) ^2P(3) ^4P(2) ^4D(2) ^2S$	9
	3/2	$^2P(2) ^2D(5) ^4D(2) ^4P(3) ^4F(2)$	15
	5/2	$^2D(4) ^2F(5) ^4P(2) ^4F(3) ^4G(2) ^4D(2)$	18
	7/2	$^4F(3) ^4G(2) ^4H(2) ^2G(5) ^2F(5) ^4D(2)$	19
	9/2	$^2G(5) ^2H(4) ^4F(3) ^4G(2) ^2H(2) ^4I$	17
	11/2	$^4G(2) ^4H(2) ^4I ^4J ^2H(4) ^2I(3)$	13
	13/2	$^4H(2) ^2I(3) ^2J(2) ^4I ^4J ^2I(3)$	9
	15/2	$^4I ^4J ^2J(2) ^2K$	5
	17/2	$^4J ^4K$	2
	$\Sigma = 910$		$\Sigma = 107$

Table 3.3: Symmetries of  $3d^9 4f^2$  electrons. The different multiplet terms selected by their different  $J$  values are given. The number of representations per  $J$  value and the total number of representations, and the total number of states are given in the last column. Notations such as  $^4H(2)$  should be read as two  $^4H$  configurations. The multiplet terms depicted in red correspond to those the dipole selection rules allow.

final states. These 910 states are grouped in 107 multiplets with different  $J$  as shown in table 3.3 and imply, in principle, 107 possible final states. However, the number of transitions is significantly reduced owing to the dipole selection rule  $\Delta J = 0, \pm 1$ . It can be found from Table 3.2 that the  $4f^1$  has a ground state with  $J = 5/2$  and from Table 3.3, it can be found that within the  $3d^9 4f^2$  configuration, there are only 18 states with  $J' = 5/2$ , 15 states with  $J' = 3/2$  and 19 states with  $J' = 7/2$ . Therefore, the atomic  $4f^1$  to  $3d^9 4f^2$  transition is reduced to a total of 52 peaks. The most intense peaks in the  $M_5$ -edge labeled A and B in Figure 3.18 correspond to a  $^2F_{5/2} \rightarrow ^2G_{7/2}$  transitions.

The Ce  $M_5$  RIXS process for a trivalent Ce compound can be described by the transitions  $3d^{10} 4f^1 \rightarrow 3d^9 4f^2 \rightarrow 3d^{10} 4f^1$  (the intermediate state corresponds to the XAS final state, while the XAS final state of the RIXS process is same as the initial state). In figure 3.19, we show the calculated RIXS spectra with the incident photon energy tuned around the  $M_5$  edge of the XAS spectrum. In both polarizations, the calculated spectra exhibit an elastic peak corresponding to the  $f_{5/2}^1$  final state and another structure at 0.28 eV corresponding to the  $f_{7/2}^1$  final state. Since there was not enough experimental resolution to study the  $4f$  spin-orbit coupling when performing the early RIXS measurements, the calculated spectra were broadened in order to obtain only one structure matching the experimental one (see Figure 3.3). It is worth noting that the elastic peak associated with the  $f_{5/2}^1$  final state is present in both polarizations. However, the relative intensity of the  $f_{7/2}^1$  structure with respect to  $f_{5/2}^1$  in  $\sigma$  polarization is strongly reduced than that of  $\pi$  polarization (see section 3.5.6 for detailed explanation). It is interesting to note that when the incident photon energy is varied across the XAS main structure, the  $f_{5/2}^1$  final state exhibits two maxima separated by about 0.8 eV in both  $\pi$  and  $\sigma$  polarization. These two maxima are associated with the structures A and B in the XAS spectrum ( $E_A - E_B = 0.8$  eV).

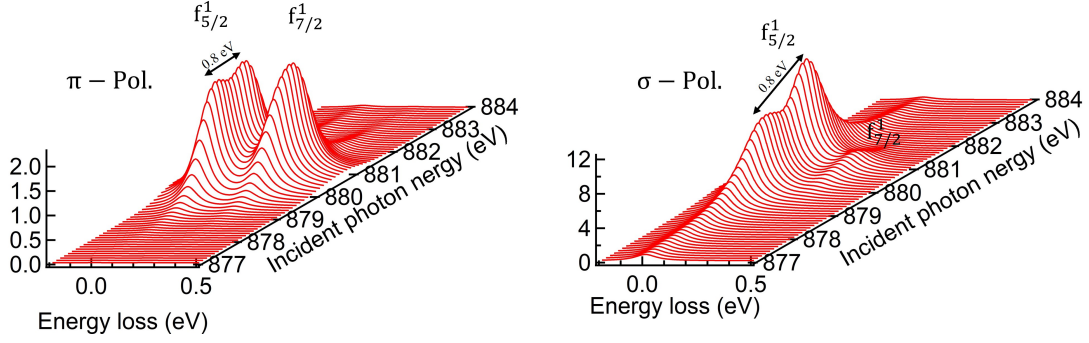


Figure 3.19: calculated result of the Ce  $M_5$  RIXS spectra of a purely trivalent system with  $\pi$  (a) and  $\sigma$  (b) polarizations of the incident photon energy.

### 3.5.5 RIXS spectra for an intermediate-valent system

In this subsection, we will present the calculated RIXS spectra for an intermediate valent system. However, at first, let us recall the energy levels for an intermediate valence Ce compound with the 4f spin-orbit splitting schematically shown in figure 3.20a. The spin-orbit coupling splits the 4f orbital into a sixfold degenerate  $J = 5/2$  level and an eightfold degenerate  $J = 7/2$  level separated by about  $\Delta \sim 280$  meV. The hybridization between 4f and conduction band states lifts these degeneracies and leads to the stabilization of two singlet states.  $\Psi_0$  is the Kondo singlet ground state with energy  $E_g$ . The first excited states  $\Psi_1$  with predominantly  $f_{5/2}^1$  character are separated from the ground state by  $T_K$ . The singlet state  $\Psi_2$  located at  $E_g + T_K + \Delta_{so} - T_{ex}$  resembles that of  $\Psi_0$  but with predominantly  $f_{7/2}^1$  character. The states  $\Psi_3$  lying at  $E_g + \Delta_{so}$  have mainly  $f_{7/2}^1$  characters. Finally, the states  $\Psi_4$  and  $\Psi_5$  located at high energy at  $\epsilon_f$  and  $2\epsilon_f + U$  have predominantly  $f^0$  and  $f^2$  character respectively.  $T_K$  and  $T_{ex}$  respectively reflect the energy gain by the singlets from the  $J = 5/2$  and  $J = 7/2$  manifolds. Bickers et al. [35] have calculated these two energy scales by using the large-N expansion approximation of the Anderson Hamiltonian, and they obtained:

$$T_K = D \exp\left(\frac{\pi\epsilon_{f_{5/2}}}{6\Gamma}\right) \left(\frac{D}{\Delta_{so} + T_K}\right)^{8/6}, \quad (3.36)$$

$$T_{ex} = D \exp\left(\frac{\pi\epsilon_{f_{7/2}}}{8\Gamma}\right) \left(\frac{D}{\Delta_{so} - T_{ex}}\right)^{6/8}, \quad (3.37)$$

where  $\Gamma = \pi N(0)V$  (given by the Fermi golden rule) is the hybridization width acquired by the f states due to the hybridization (V) with the conduction electrons at the Fermi level ( $N(0)$ ). D is the bandwidth of the conduction electrons.

In the presence of a 3d core hole (XAS final state and RIXS intermediate state), the lowest states become the  $3d^9 4f^2$  configuration which overlaps with the  $3d^9 4f^3$  configuration, and the first excited states are given by the  $3d^9 4f^1$  configurations. This reordering of the different

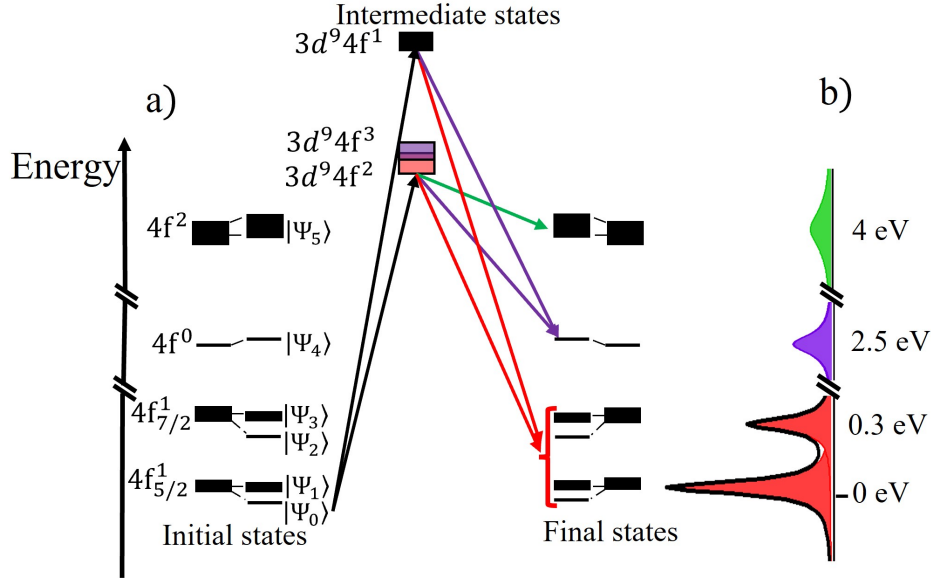


Figure 3.20: a) Total energy level scheme and RIXS transitions in cerium Kondo systems. b) Expected shape of the RIXS spectrum when measured with an experimental resolution of about  $\sim 100$  meV. The low energy  $ff$  excitations are depicted in red colors. The  $f^1 \rightarrow f^0$  and  $f^1 \rightarrow f^2$  charge excitations are respectively depicted in purple and green colors.

configurations is due to the strong core-hole interaction with the  $f$  states. Indeed, the energy of the  $3d^9 4f^n$  ( $n = 0, 1, 2, 3$ ) configuration in the intermediate state is given by:

$$E(3d^9 4f^n) = n\epsilon_f + \frac{n(n-1)}{2}U_{ff} + nU_{fc} + \epsilon_c, \quad (3.38)$$

where  $\epsilon_c$  is the binding energy of the  $3d$  hole. Let's first discuss the absorption spectrum. The calculations are performed with the following parameters:  $V = 0.13$  eV,  $\epsilon_f = -1.7$  eV,  $U_{ff} = 7$  eV and  $U_{fc} = 10.85$  eV. The number of  $4f$  electrons in the ground state calculated with these parameters is  $n_f = 0.96$ . When the incident x-ray photon excites a Ce  $3d_{5/2}$  electron to the  $4f$  state, we have the  $3d^9 4f^1$ ,  $3d^9 4f^2$  and  $3d^9 4f^3$  configurations which are mixed by the hybridization. Therefore, two main transitions are expected in the Ce  $M_5$  XAS, the first one consists of the  $3d^9 4f^2$  and  $3d^9 4f^3$  configurations which nearly overlap, and the second transition corresponds to the  $3d^9 4f^1$  configuration (see Figure 3.20)a. The calculated Ce  $M_5$  XAS spectrum in figure 3.21 exhibits, in addition to the main structure centered at 880 eV, a satellite structure which is located at about 886 eV. This latter feature reflects the intermediate valent character of the ground state, and its intensity is proportional to the hybridization between the  $f$  and conduction band states.

Figure 3.20a shows the transitions for different incident photon energies in the RIXS process. When the incident photon is tuned around the main Ce- $3d_{5/2}$  XAS structure, the intermediate states which correspond to a mixture between the  $3d^9 4f^3$  and  $3d^9 4f^2$  configurations are selected and they can decay to all possible final states, but mainly to those with  $f^2$  and  $f^1$

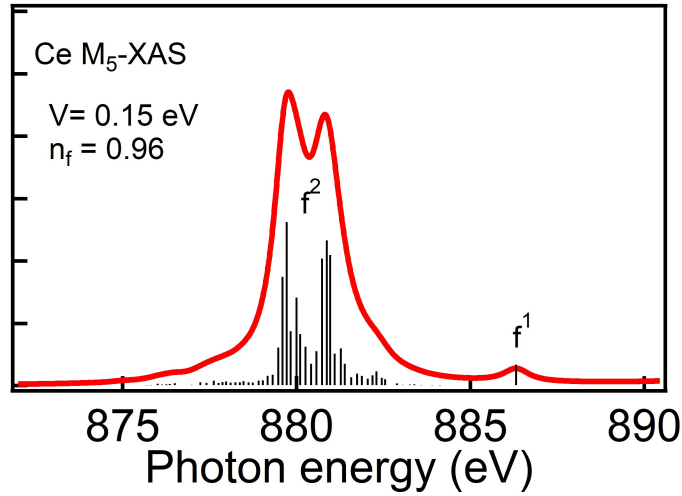


Figure 3.21: Calculated Ce  $M_5$ -edge XAS spectrum for an intermediate valence ( $n_f = 0.96$ ) Ce compounds. The calculations have been made with  $V = 0.15$  eV,  $U_{ff} = 7$  eV and  $U_{fc} = 10.85$  eV

character. Similarly, when the incident photon energy is set to the Ce- $3d_{5/2}$  XAS satellite structure, the intermediate states are dominated by  $3d^9 4f^1$  configuration and decay predominantly to the final states with  $f^0$  character. Figure 3.22a, and 3.22b show a waterfall plot of the calculated RIXS spectra as a function of the incident photon energy in  $\sigma$  and  $\pi$  polarization, respectively. A prominent structure centered at about 5 eV loss energy dominated by the multiplet effects corresponding to the  $f^2$  final state is observed in both polarizations. When the incident photon energy increases from 875 eV to 890 eV, this structure is resonantly enhanced at about 881 eV. Figure 3.22a also exhibits a single peak at about 2 eV loss energy, corresponding to the  $f^0$  final state. This latter feature is resonantly enhanced when the incident photon energy corresponds to the  $f^1$  XAS satellite at about 886 eV. Note that there is also a small amount of the  $f^0$  final state at around 881 eV. It arises from the small amount of  $f^1$  character in the  $3d^9 4f^1$  intermediate state (see purple transitions in Figure 3.20a). Moreover, it exhibits two maxima associated with the two main structures, A and B of the XAS spectrum. The calculated RIXS spectra with  $\pi$  polarization of the incident photons also exhibit  $f^2$  final states. However, the  $f^0$  final state is completely suppressed. This behavior will be discussed in more detail in the next section. Before that, let's look at the low-energy excitations.

In order to study the low energy excitations, we show in Figure 3.23 the calculated RIXS spectra in the energy loss range below 0.5 eV, obtained for the incident photon energy tuned to the main structure of the XAS spectrum. Indeed, at this energy, the intermediate state dominated by the  $3d^9 4f^2$  decays predominantly to the ground state, as mentioned above. Therefore, in addition to the elastic peak, three structures are observed corresponding to  $\Psi_1$ ,  $\Psi_2$ , and  $\Psi_3$  final states in  $\sigma$  polarization. The transitions to  $\Psi_1$  and  $\Psi_3$  final states are the two

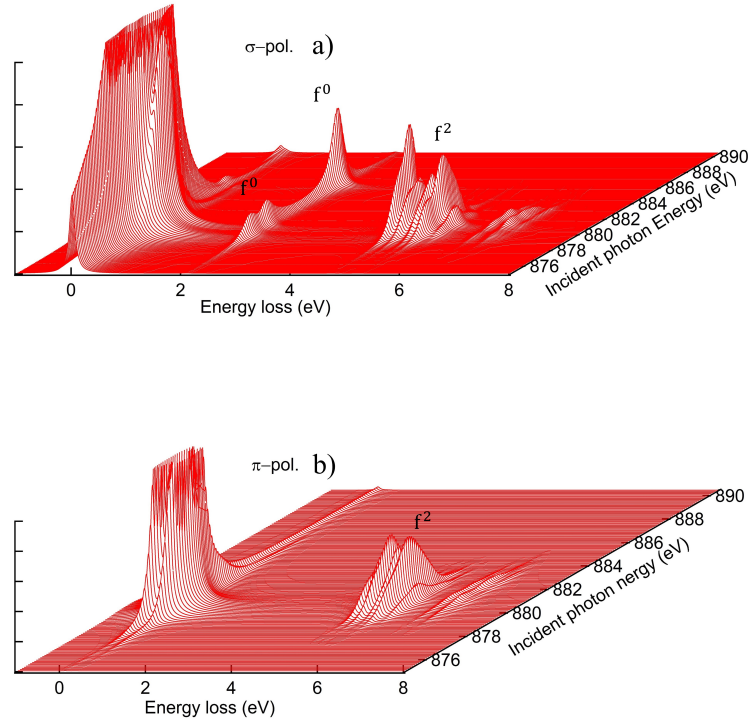


Figure 3.22: Waterfall plot showing the incident photon energy dependence of the calculated Ce  $M_5$ -edge RIXS spectra of an intermediate valence system. The spectra were calculated with  $\sigma$  (a) and  $\pi$  (b) polarization of the incident x-ray with the following parameters:  $V = 0.15$  eV,  $\epsilon_f = -1.7$  eV,  $U_{ff} = 7$  eV and  $U_{fc} = 10.85$  eV. The  $f^2$  (2 eV) and  $f^2$  (5 eV) final states resonate for different photon energies. The  $f^0$  final state is completely suppressed in  $\pi$  polarization.

Kondo resonances as expected in inverse photoemission spectroscopy [35]. In  $\pi$  polarization, only the Kondo resonance and its spin-orbit replicate are observed.

### 3.5.6 Polarization dependence: Discussion

In this subsection, we will discuss in more detail the polarization effect in RIXS spectra of purely trivalent and intermediate valence cerium compounds, obtained in the calculations discussed in the previous section.

The polarization dependence is very important to understand the symmetry of the ground state. It has been theoretically shown [36, 37] that  $f^0$ -like compounds (such as  $\text{CeO}_2$ ) exhibit a drastic polarization dependence: the  $f^0$  final state and the elastic peak are forbidden in polarized geometry. This has been confirmed experimentally by Watanabe [38]. The same drastic polarization effect was also predicted in Ce Kondo systems but was never observed.



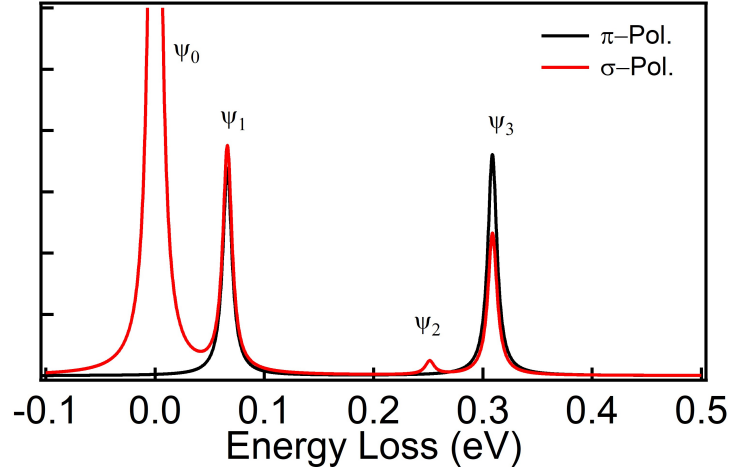


Figure 3.23: Detailed view of the calculated spectra ( $V = 0.11$  eV,  $\epsilon_f = -1.7$  eV and  $U_{ff} = 7$  eV with  $n_f = 0.98$ ) in the energy loss range below 0.5 eV in  $\sigma$  (red line) and  $\pi$  (black line) polarizations of the incident x-ray. The incident photon energy is tuned on the XAS main structure (B).

By using the Wigner-Eckhart theorem, the dipole transition matrix element can be written as a function of the 3- $j$  symbol:

$$\langle \gamma' J' M' | C_q^{(1)} | \gamma J M \rangle = (-1)^{J' - M'} \begin{pmatrix} J' & 1 & J \\ -M' & q & M \end{pmatrix} \langle \gamma' J' || C^{(1)} || \gamma J \rangle, \quad (3.39)$$

where  $\langle \gamma' J' || C^{(1)} || \gamma J \rangle$  is the reduced matrix element which is independent of  $M'$ ,  $M$  and  $q$ . Depending on the X-ray polarization,  $q$  takes the values -1, 0, or 1. Considering the case of the emission process,  $J$  and  $J'$  are the total angular momentum of the intermediate and final state, and  $M$  and  $M'$  are their  $z$ -components. Using the 3- $j$  symbol, the transition matrix element is zero, unless

$$M - M' + q = 0. \quad (3.40)$$

Therefore, the transitions in the absorption and emission process occur only if Equation 3.40 is valid.

Let's briefly discuss about the symmetry of the configurations. The  $f^0$  configuration has a total angular momentum  $J = 0$ . The  $f_{5/2}^1 \underline{L}$  ( $f_{7/2}^1 \underline{L}$ ) configuration consists of a 4f electron with angular momentum  $j = 5/2$  ( $j = 7/2$ ) and a hole in the conduction band states with angular momentum  $j_{\underline{L}} = 5/2$  ( $j_{\underline{L}} = 7/2$ ). So, the total angular momenta of the  $f_{5/2}^1 \underline{L}$  ( $f_{7/2}^1 \underline{L}$ ) configuration are  $J = 0, 1, 2, \dots, 5$  ( $J = 0, 1, 2, \dots, 7$ ) since  $|j - j_{\underline{L}}| \leq J \leq j + j_{\underline{L}}$ . Given that the hybridization term of the SIAM conserves the total angular momentum  $J$ , only its matrix elements between states with same total angular momentum are non zero. Therefore, only the states  $f_{5/2}^1 \underline{L}$  and  $f_{7/2}^1 \underline{L}$  with  $J = 0$  hybridize with the  $f^0$  ( $J = 0$ ) states and gives rise

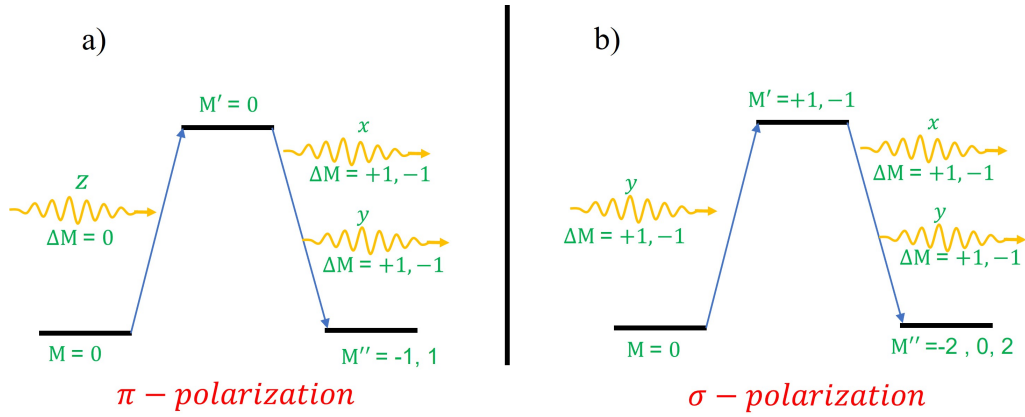


Figure 3.24: Illustration scheme of the  $\pi$ -polarization (a) and  $\sigma$ -polarization (b) dependence of the Ce  $M_5$ -edge RIXS process.

to the singlet ground state  $\Psi_0$  and its spin-orbit replicate  $\Psi_2$  with total angular momentum  $J = 0$ . The remaining non hybridized states with  $J = 1, 2 \dots 5$  and  $1, 2 \dots 7$  correspond to  $\Psi_2$  and  $\Psi_3$  respectively.

The polarization dependence in the Ce  $M_5$ -edge RIXS process is illustrated in Figure 3.24. In the absorption process, the polarization is in the  $y$ -direction for a  $\sigma$  polarization (perpendicular to the scattering plane) and it corresponds to a linear combination of  $q = 1$  and  $q = -1$  (see Equation 3.33). So, by using the 3- $j$  symbol of equation 3.39, the  $z$ -component of the total angular momenta in the intermediate state of RIXS are  $M' = 1$  and  $-1$ . Owing to the experimental geometry ( $90^\circ$  of scattering angle) the polarizations of the emitted x-ray are only in the  $x$  and  $y$ -directions and not along the  $z$ -direction. So, in the final state of RIXS, the total angular momenta  $M''$  values would be  $-2, 0$ , and  $2$ . Therefore, the elastic peak  $\Psi_0$  and all the inelastic final states mentioned above are allowed.

For the  $\pi$  polarization on the other hand, the incident x-ray polarization is in the  $z$ -direction (parallel to the scattering plane) and associated with the polarization component  $q = 0$ , so that in the intermediate state we have  $M' = M = 0$ . The polarization component of the emitted x-ray should be a linear combination of  $q = 1$  and  $q = -1$ , then the values of  $M$  in the final state of RIXS are  $-1$  and  $1$  and as a result, the transition to the singlet states ( $\Psi_0, \Psi_2$  and  $\Psi_4$ ) with  $M = 0$  are forbidden (see Figure 3.20a and 3.23).

For purely trivalent systems such as  $\text{CeF}_3$ , the total angular momentum of the ground state is nonzero ( $J = 5/2$ ). The ground state is 6-fold degenerate with different  $M$  values from  $-5/2$  to  $5/2$ . By generalizing the argument discussed above for an intermediate valence system, the transitions from the initial state ( $M$ ) to the final state ( $M''$ ) are allowed only if  $\Delta M = -1, 1$  for a  $\pi$  polarization and  $\Delta M = -2, 0, 2$  for a  $\sigma$  polarization of the incident photon. So, the elastic peak for a purely trivalent system is always allowed since the transition from the ground states ( $J = 5/2, M$ ) to the final states ( $J = 5/2, M \pm 2$ ) are possible.

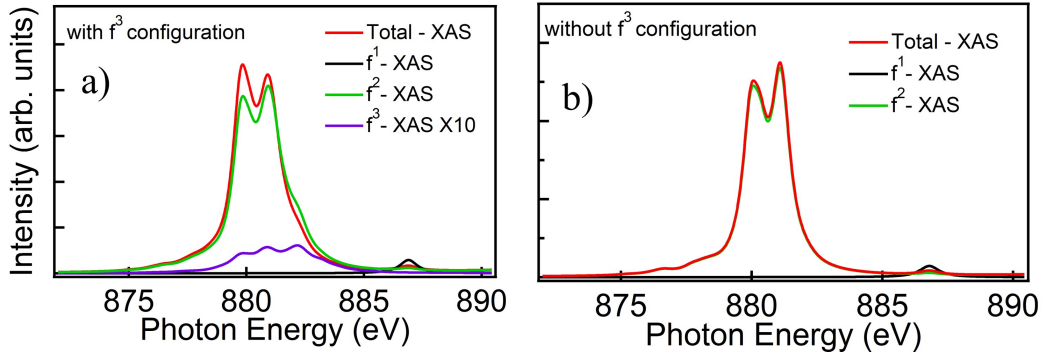


Figure 3.25: Calculated XAS spectra at Ce- $M_5$  edge and the contribution associated with the different configurations with (a) and without (b) inclusion of the  $f^3$  configuration in the initial state ( $f^2$  configuration in the ground state). It is noted that the total XAS is not the sum of  $f^1$ ,  $f^2$ , and  $f^3$  contribution due to interference effects.

### 3.5.7 Importance of the $f^2/f^3$ configuration in the initial/intermediate state

Since the ground state is a mixture of the  $f^0$ ,  $f^1$  and  $f^2$  configurations, three different contributions are expected in the Ce  $M_5$  XAS spectrum corresponding to the transitions  $3d^{10}4f^0 \rightarrow 3d^9 4f^1$ ,  $3d^{10}4f^1 \rightarrow 3d^9 4f^2$  and  $3d^{10}4f^2 \rightarrow 3d^9 4f^3$ . Following the Gunnarsson and Schönhammer [39] approach, only the  $d^9 f^1$  and  $d^9 f^2$  final states are usually identified and quantified, and regarding the  $d^9 f^3$  final state, Fuggle et al. [40, 41] mentioned that due to the large increase of the Coulomb repulsion, the  $d^9 f^3$  final state feature should be weak, and at higher energy than the  $d^9 f^2$  final state. However, while the  $d^9 f^3$  final state is expected to be weak, it is crucial for describing RIXS spectra where the 4f signal is enhanced by the resonant character. In Quanta, we have the possibility to calculate the partial excitations of these three contributions. In figure 3.25a, we show, in addition to the total calculated XAS spectrum, the contributions corresponding to the transitions from the ground state to the  $3d^9 4f^1$ ,  $3d^9 4f^2$  and  $3d^9 4f^3$  final states. We remark that the  $f^2$  and  $f^3$  structures overlap. Indeed, while the Coulomb repulsion significantly increases with the 4f occupancy, it gets compensated by the core hole interaction with the f electrons. With a zero hybridization, we have  $E(3d^9 4f^3) = 3\epsilon_f + 3U_{ff} - 3U_{fc}$  and  $E(3d^9 4f^2) = 2\epsilon_f + U_{ff} - 2U_{fc}$  which yields  $E(3d^9 4f^3) - E(3d^9 4f^2) \sim 1.5$  eV for typical parameters of cerium systems.

For comparison, we show in Figure 3.25b the calculated XAS spectrum by neglecting the  $4f^2$  configuration in the initial state and  $3d^9 4f^3$  in the final state. Consequently, the weak  $f^3$  contribution has a small influence on XAS but has a drastic effect on the RIXS spectra, which cannot exhibit the final  $f^2$  energy loss structures without the  $f^3$  configuration (see Figure 3.26). Figure 3.26 shows that without the  $3d^9 4f^3$  configuration in the XAS spectrum, the  $4f^2$  structure in the RIXS spectrum is completely missing. This result shows that an

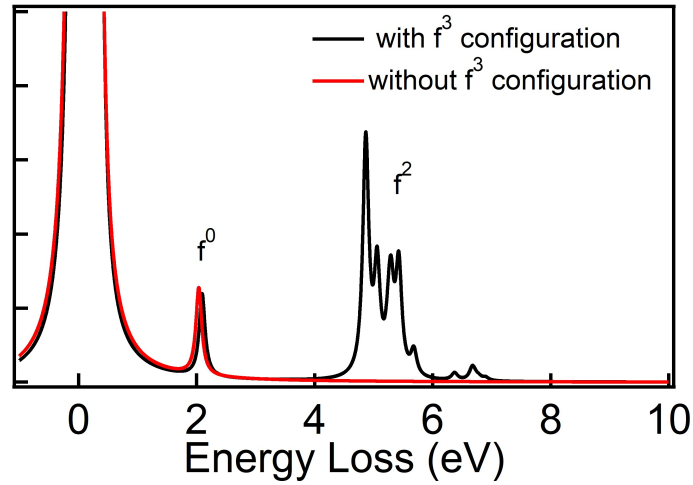


Figure 3.26: Calculated RIXS spectra with (black line) and without (red line) the  $f^2(f^3)$  configuration in the initial state(intermediate state). The incident photon energy is set on the XAS main structure with  $\sigma$  polarization.

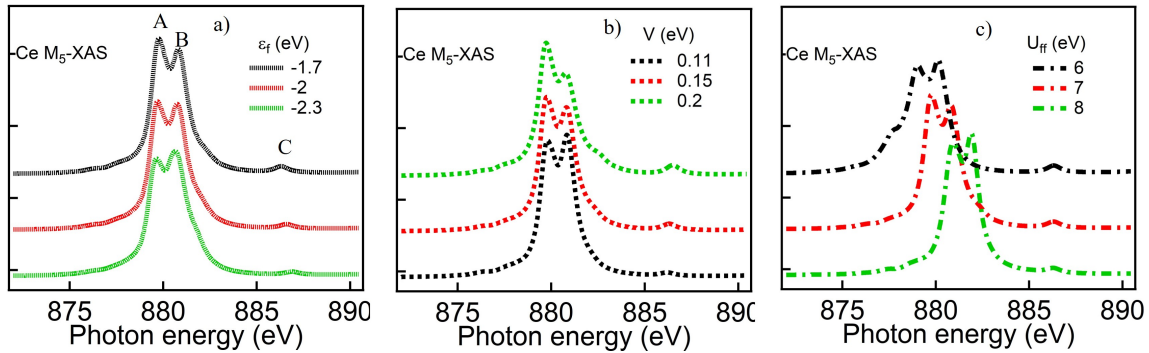


Figure 3.27: Calculated XAS spectra for various SIAM parameters. a)  $f$  state energy  $\epsilon_f$  dependence ( $V = 0.15$  eV and  $U_{ff} = 7$  eV). b) hybridization  $V$  dependence ( $\epsilon_f = -1.7$  eV and  $U_{ff} = 7$  eV). c) Coulomb repulsion  $U_{ff}$  dependence ( $\epsilon_f = -1.7$  eV and  $V = 0.15$  eV).

extended basis is necessary to simulate the different loss structures in the RIXS.

### 3.5.8 Influence of the different parameters

From the figure 3.20b, the loss energy structures are associated with the  $f^0$ ,  $f^1$  and  $f^2$  final states. Their intensities depend on the hybridization strength  $V$ , the Coulomb repulsion  $U_{ff}$ , and the  $f$ -state energy  $\epsilon_f$ . Figures 3.27a, 3.27b, and 3.27c show the overall influence of the parameters on the Ce  $M_5$ -edge XAS spectra, especially the intensities of the satellite (C) and

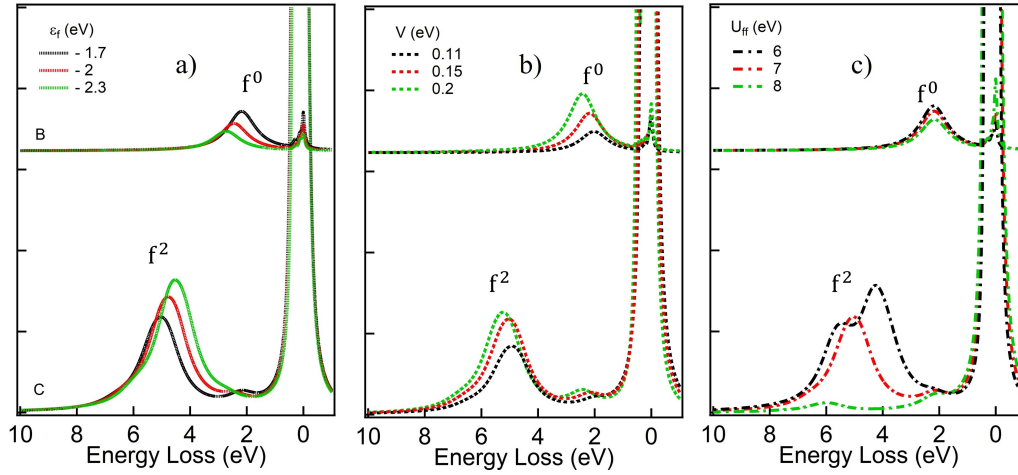


Figure 3.28: Calculated RIXS spectra with incident photon energy tuned on the main (B) and XAS satellite (C) structure for various SIAM parameters. a)  $f$  state energy  $\epsilon_f$  dependence ( $V = 0.15$  eV and  $U_{ff} = 7$  eV). b) hybridization  $V$  dependence ( $\epsilon_f = -1.7$  eV and  $U_{ff} = 7$  eV). c) Coulomb repulsion  $U_{ff}$  dependence ( $\epsilon_f = -1.7$  eV and  $V = 0.15$  eV).

the energy separation between the satellite and the main peaks (A, B). The corresponding RIXS spectral line shapes for an incident x-ray energy set to the  $f^2$  main peak (B) and the  $f^1$  satellite (C) are respectively shown in figures 3.28a, 3.28b and 3.28c. In the intermediate state of RIXS, the  $d^9 f^1$  configuration lies at high energy compared the  $d^9 f^2$  configuration and mixes quite less with the latter. Therefore, the intensity of the  $f^0$  peak depends mainly on the weight of the  $f^0$  configuration in the initial state. However, the  $d^9 f^2$  and  $d^9 f^3$  configurations overlap and are strongly mixed. Therefore, the intensity of the  $f^2$  peak depends on the weight of the  $f^2$  and  $d^9 f^3$  configurations in the initial and intermediate state, respectively. The energy separation between the  $f^0$  and elastic peak increases with increasing  $|\epsilon_f|$  and the hybridization strength  $V$ . In addition, the intensity of the  $f^0$  peak increases with the hybridization but decreases with increasing  $|\epsilon_f|$ . When the Coulomb repulsion increases, the  $f^0$  peak remains at the same energy, but its intensity slightly increases. Regarding the  $f^2$  structure, the  $f^2$  configuration lies at  $\sim |\epsilon_f + U_{ff}|$  with a zero hybridization. So, the energy separation between the elastic and  $f^2$  peak increases with increasing  $|\epsilon_f|$ ,  $U_{ff}$  and the hybridization strength  $V$ , and its intensity increases with increasing  $|\epsilon_f|$  and  $V$  but decreases with increasing  $U_{ff}$ . It is interesting to observe that the intensities of the  $f^0$  and  $f^2$  peaks evolve in the same way with increasing  $V$  whereas they evolve in the opposite way with increasing  $|\epsilon_f|$ . Indeed, the energy separation between the  $d^9 f^2$  and  $d^9 f^3$  configurations decreases with increasing  $|\epsilon_f|$  and, as a result, hybridizes more, and the weight of the  $d^9 f^3$  configuration increases. Furthermore, as mentioned above, the intensity of the  $f^0$  peak depends only on the weight of the  $f^0$  configuration, which decreases with increasing  $|\epsilon_f|$ .

## 3.6 RIXS insights into $\text{CeAgSb}_2$ Kondo system

In this section, a study of the low and high-energy excitations of the ferromagnetic  $\text{CeAgSb}_2$  compounds by means of RIXS spectroscopy is presented.

### 3.6.1 Properties of $\text{CeAgSb}_2$

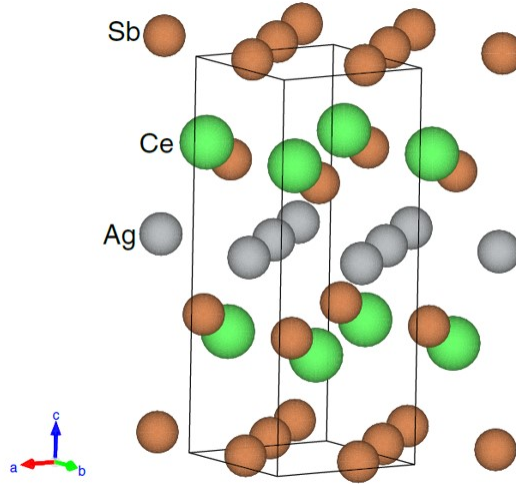


Figure 3.29: Crystal structure of  $\text{CeAgSb}_2$  compound. The lattice parameters are  $a = b = 4.363 \text{ \AA}$  and  $c = 10.699 \text{ \AA}$ .

$\text{CeAgSb}_2$  is a heavy fermion compound which crystallizes in  $\text{ZrCuSi}_2$ -type structure as shown in Figure 3.29, with the cell parameters:  $a = b = 4.363 \text{ \AA}$  and  $c = 10.699 \text{ \AA}$  [42]. Its linear coefficient of the specific heat (Sommerfeld coefficient) is moderately enhanced  $\gamma \sim 46 \text{ mJ}/(\text{mol} \cdot \text{K}^2)$ , corresponding to a mass enhancement of  $\approx 21$  with respect to its nonmagnetic La analog [43]. Its Kondo temperature has been estimated by magnetic susceptibility measurements at  $T_K \sim 65 \text{ K}$  [44]. However, inelastic neutron scattering [45], as well as spin rotation measurements [46], yields  $T_K \sim 60\text{-}80 \text{ K}$ , while a slightly lower value of  $T_K \sim 23 \text{ K}$  [44] was suggested from an analysis based on the relation between the Wilson number and the Kondo temperature.  $\text{CeAgSb}_2$  orders ferromagnetically at  $T_C \sim 9.7 \text{ K}$  [47]. This is unusual since the competition between the RKKY interaction and the Kondo effect usually gives rise to an antiferromagnetic ordering in cerium compounds. For such ferromagnetic Kondo lattices, the maximum in resistivity which is a signature of the Kondo energy scale is usually observed just above  $T_C$  [48]. In  $\text{CeAgSb}_2$ , it is seen at about  $15 \text{ K}$  allowing us to conclude that  $T_K$  is close to  $T_C$ , in the range  $10\text{-}20 \text{ K}$ . This ferromagnetic ground state is an evidence of the strong competition between the Kondo screening and the RKKY interactions. Its weak intermediate valence character ( $n_f \sim 0.99$ ) has been shown by 3d- XAS [49], as well as  $4d - 4f$  resonant photoemission spectroscopy [50]. Figure 3.30 shows the

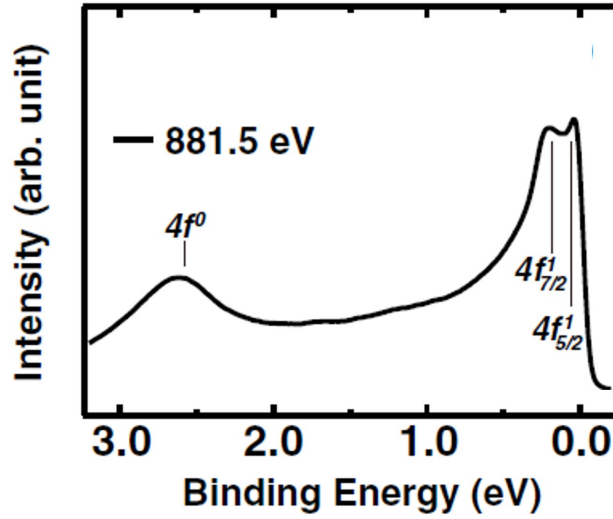


Figure 3.30: Experimental Valence band photoemission spectra of CeAgSb<sub>2</sub> measured with a photon energy of  $h\nu = 881.5$  eV (resonance at the  $M_5$  edge), taken from Ref. [49].

valence band photoemission spectrum measured at  $h\nu = 881.5$  eV. As expected in the SIAM, the peak in the vicinity of the Fermi level is associated with the  $f_{5/2}^1$  state, and the peak at about  $\sim 0.25$  eV corresponds to its spin-orbit replicate  $f_{7/2}^1$ . The structure located at about  $\sim 2.6$  eV corresponds to the  $f^0$  final state and reflects the intermediate valence character of the ground state. We will see that these final states are associated with loss structures in the RIXS spectra.

### 3.6.2 Charge transfer excitations

Figure 3.31a shows the Ce  $3d_{5/2}$  X-ray absorption spectrum at  $T = 20$  K. The spectrum exhibits a structured feature around  $E = 880$  eV corresponding to the  $3d_{5/2}^9 f^2$  multiplet states due to the strong interaction between the  $3d_{5/2}$  core hole and the Ce  $4f$  state. There is also a very weak satellite at  $E = 886$  eV which corresponds to the  $3d_{5/2}^9 f^1$  final state. The presence of this satellite in XAS spectra is an indication of the Kondo singlet ground state and its intensity reflects the  $f^0$  contribution in the ground state (this contribution is very weak since  $n_f \sim 1$ )[40].

Figure 3.31c shows a set of RIXS spectra of the CeAgSb<sub>2</sub> single crystal recorded at different incident photon energies  $h\nu$  indicated by arrows in the XAS spectrum (see Figure 3.31a) around the Ce  $M_5$  edge. All spectra were measured with  $\sigma$  polarization of the incident photons. When the incident photon energy is tuned on the main peak of the XAS (point B), the RIXS spectrum exhibits two structures: The elastic peak at zero energy loss which corresponds to the  $f^1$  final state, and a broad structure at 4.5 eV loss energy which corresponds to the  $f^2$  final states. When the incident photon energy is tuned at the weak XAS satellite (point F), in addition to the elastic peak, an inelastic structure is observed at 2.7 eV energy

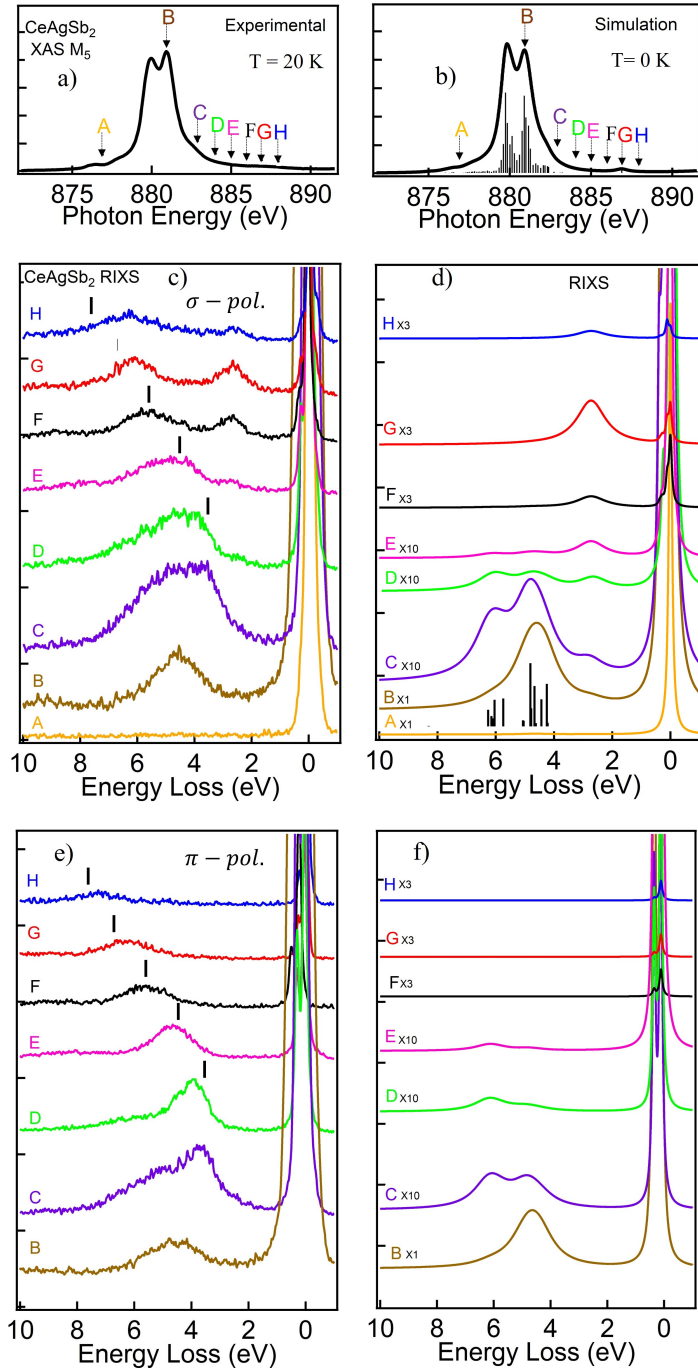


Figure 3.31: (a) Experimental ( $T = 20$  K) and (b) calculated ( $T = 0$  K) Ce- $3d_{5/2}$  X-ray absorption spectra of CeAgSb<sub>2</sub> at 20 K. A set of experimental (c, e) ( $T = 300$  K) and (d, f) calculated ( $T = 0$  K) RIXS spectra for different photon energies around the the M<sub>5</sub> edge and the satellite. The measurements were made at  $T = 20$  K with  $\sigma$  polarization.



loss which corresponds to the  $f^0$  final state. The energy loss of the  $f^0$  final state is consistent with photoemission measurements (see Figure 3.30). Moreover, it is interesting to notice that the  $f^2$  structure observed at about 4.5 eV is consistent with the inverse photoemission results [51, 52, 1, 53, 54, 55, 56]. Therefore, RIXS can evidence all the charge excitations ( $f^1 \rightarrow f^0$  and  $f^1 \rightarrow f^2$ ) usually observed in combined PES and IPES measurements. In addition to these loss energy structures, a prominent inelastic scattering peak at 6 eV energy loss appears and its energy loss increases with increasing incident photon energy. A similar structure has been observed in the RIXS spectra of  $\text{CeO}_2$  compound [38] and has been attributed to a fluorescence-like transition to discriminate it from the normal fluorescence which appears for the incident photon energy tuned well above the threshold. Indeed, this structure is due to the fact that the XAS satellite structure reflects an admixture of the f states with the continuum. The fluorescence-like structure was also observed in RIXS spectra of  $\text{CeB}_6$  Kondo systems [9]. By varying the incident photon energy from A to I, the  $f^0$  and  $f^2$  final states show a constant energy loss which is consistent with the strong localization of the f states contrary to the fluorescence-like structure which involves delocalized states.

In order to accurately describe the RIXS spectra and to determine the hybridization strength  $V$ , the f binding energy  $\epsilon_f$  and the Coulomb repulsion  $U_{ff}$  of the  $\text{CeAgSb}_2$  compound, we performed a full-multiplet configuration-interaction calculation presented in the previous section 3.5. Ce  $M_5$ -edge XAS and RIXS spectra were simulated using following parameters: The hybridization between 4f state and conduction band  $V = 0.15$  eV, the Coulomb interaction between 4f electron and core hole  $U_{fc} = 10.85$  eV, the Coulomb interaction between 4f electrons  $U_{ff} = 7.15$  eV and the f binding energy  $\epsilon_f = -2.3$  eV. These parameters result in an intermediate valent ground state ( $n_f = 0.99$ ) consisting of the  $f^0$  (3.3%),  $f^1$  (94.7%) and  $f^2$  (2%) configurations. In order to account for the experimental resolution as well as the conduction electron bandwidth, the  $f^2$  and  $f^0$  structure in RIXS spectra were convoluted with a Lorentzian of width  $\Gamma = 1.2$  eV (FWHM). Figures 3.31b and 3.31d show the results of the calculated XAS and RIXS spectra. The calculated spectra are in good agreement with the experimental ones shown in Figure 3.31b except for the fluorescence-like structure which can not be reproduced with our model. The RIXS calculations were made with  $\sigma$  polarization of the incident photons. The  $f^2$  structure exhibits a clear multiplet effect due to the strong  $4f - 4f$  interactions contrary to the  $f^0$  structure which is a single peak resonantly enhanced at the XAS satellite (incident photon energy point G). Indeed, the  $f^2$  final states consist mainly of the  $^3H$  multiplet when the incident photon energy is tuned on point B. However, the  $f^2$  final states evolve into two main multiplets namely  $^3H$  and  $^3P$ , on increasing the incident photon energy from point B to C. It should be noted that similar multiplet effects have been observed on the  $f^2$  final state of RIPES at the Ce  $N_{4,5}$  edge of cerium intermetallic compounds [57, 58, 59]. We recall that the pronounced  $f^2$  structure in RIXS spectra is due to the mixing between the,  $3d^9 4f^2$ , and  $3d^9 4f^3$  configurations in the intermediate state and that it is not possible to reproduce the  $f^2$  states in RIXS spectra without taking into account the  $3d^9 4f^3$  configuration in the intermediate state ( $f^2$  configuration in the initial state, see section 3.5.7).

The polarization dependence of the RIXS spectra with the incident photon energy  $h\nu = G$  of the XAS satellite (associated with intermediate states with a  $f^1$  character) is clearly

evidenced by comparing figure 3.31c with 3.31e. As theoretically discussed in section 3.5, the  $f^0$  final state is completely suppressed in  $\pi$  polarization and by disregarding the fluorescence-like structure, the spectra are similar to those of a purely trivalent compound. This behavior seen in the experimental data of figure 3.31e is nicely reproduced by the simulations (see Figure 3.31f) and confirms the  $^1S_0$  symmetry of the initial state.

### 3.6.3 Low energy excitations

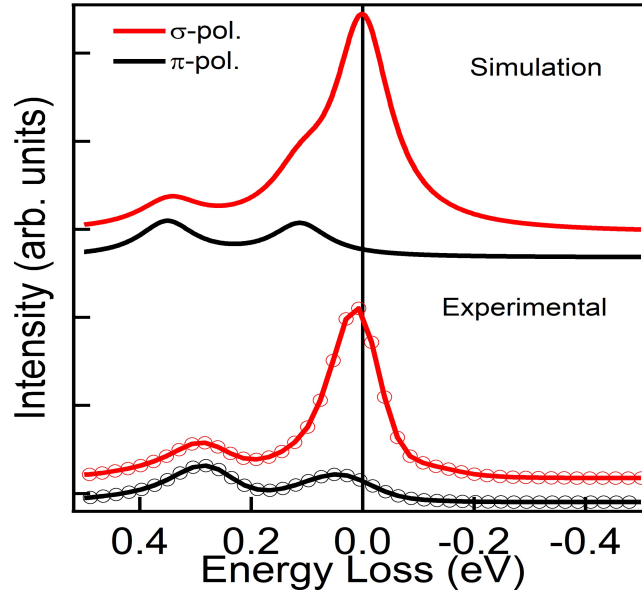


Figure 3.32: Experimental and calculated RIXS spectra of  $\text{CeAgSb}_2$  in the energy loss range below 0.5 eV. The incident photon energy is tuned on the main XAS structure (B).

Let's look at the RIXS spectra in the energy loss range below 0.5 eV. This region corresponds to the low energy excitations such as the 4f spin-orbit splitting, crystal field excitations, and the Kondo energy. The energy resolution of the AGM-AGS spectrometer [60] which is about  $\sim 100$  meV is enough to resolve the 4f spin-orbit splitting in cerium compounds which is known to be about  $280 \pm 10$  eV. However, the crystal field energies of  $\text{CeAgSb}_2$  determined from inelastic neutron measurements [45] are about  $\Delta_1 \sim 5$  meV and  $\Delta_2 \sim 5$  and their corresponding features could not be resolved with the present energy resolution. While they could not be resolved, they nonetheless contribute to the broadening of the elastic peak and its spin-orbit replicate. Finally, the Kondo resonance corresponding to the energy between the Kondo singlet ground state and the first excited magnetic states is expected above the Fermi level in the spectral function of the SIAM. To investigate these low energy excitations, RIXS spectra have been measured with the incident photon energy tuned on the main XAS structure (point B in Figure 3.31). Indeed, when the photon energy is set to the XAS main structure B, the  $3d^9 4f^2$  intermediate states are selected and decay mainly to

the final state with  $f^1$  character i.e., in the energy loss range close to the elastic peak (see Figure 3.20). As discussed in the previous section, two singlet states  $|\Psi_0\rangle$  and  $|\Psi_2\rangle$  associated with the two spin-orbit features are stabilized owing to the hybridization between the  $f$  states and conduction band states. Figure 3.32 shows the experimental RIXS spectra below 0.5 eV energy loss measured with  $\pi$  and  $\sigma$  polarizations of the incident photon. The spectrum measured in  $\sigma$  polarization exhibits a strong elastic peak and a small feature at about 280 meV. These two structures are satisfactorily reproduced by the calculation. The unresolved structures corresponding to the  $|\Psi_0\rangle$  final state and  $|\Psi_1\rangle$  manifold (Kondo resonance) are smeared into the experimental peak near the zero energy loss. The second experimental structure at 280 meV corresponds to the spin-orbit replicate  $f_{7/2}^1$  which is also composed of two contributions related to the final  $|\Psi_2\rangle$  and  $|\Psi_3\rangle$  states corresponding to the spin-orbit replicate of  $|\Psi_0\rangle$  and  $|\Psi_1\rangle$ , respectively. In the  $\pi$  polarization, the experimental spectrum exhibits two structures corresponding to the transitions to non-singlet states namely  $|\Psi_1\rangle$  and  $|\Psi_3\rangle$ . Indeed the transitions to the  $|\Psi_0\rangle$  and  $|\Psi_2\rangle$  (singlet states  $J = 0$ ) final states are forbidden as discussed in the previous section. This is evidenced by the strong reduction of the intensity of the structure close to zero energy loss. Thus in  $\pi$  polarization, the spin-orbit interaction of CeAgSb<sub>2</sub> is measured from the energy separation of these two structures with an energy  $\Delta_{so} = 280$  meV. This is comparable to high-resolution photoemission [49] measurements. The calculated spectrum in  $\pi$  polarization is shown in Figure 3.32 and is in satisfactory agreement with the experimental one. It should be noted that, unlike photoemission spectroscopy where only the singlet states (the ground state  $|\Psi_0\rangle$  and its spin-orbit replicate  $|\Psi_2\rangle$ ) can be reached, all states ( $|\Psi_0\rangle$ ,  $|\Psi_1\rangle$ ,  $|\Psi_2\rangle$  and  $|\Psi_3\rangle$ ) can be reached when we tuned the incident photon energy at the main peak of XAS with  $\sigma$  polarisation. This situation is similar to inverse photoemission spectroscopy.

### 3.6.4 Temperature dependence of the fluorescence-like structure

In this subsection, we will discuss the remaining structure indicated by the vertical bars in Figure 3.31, namely the fluorescence structure. As mentioned in the introduction, two normal fluorescences are usually observed in the RIXS spectra when the incident photon energy is tuned above the threshold. The first one appearing at 17 eV corresponds to the  $5p \rightarrow 3d$  emission and the second one at 22 eV is attributed to the MMN Coster-Kronig transition. The structure indicated by the vertical bars in figure 3.31c and 3.31e have been attributed to fluorescence-like structures in order to distinguish it from normal fluorescence. A similar fluorescence-like structure has been observed in CeO<sub>2</sub> [38] and CeB<sub>6</sub> [9], but not in CeF<sub>3</sub> [61]. Moreover, the fact that the intensity of the fluorescence-like structure has the highest intensity at the incident photon energy set on point G indicates that it is likely associated with the  $f^0$  character in the singlet ground state.

Fluorescence-like structures have been also observed in RIXS spectra at the  $L$ -edge ( $2p \rightarrow 3d \rightarrow 2p$ ) of transition metal oxides [62, 63, 64] where their analysis is used to address questions regarding the localization of charge excitations and the itinerancy of charge carriers [62, 63]. There is currently a strong debate on their origins. Bisogni et al. [65] observed a low energy fluorescence-like structure in the  $L$ -edge RIXS spectra of NdNiO<sub>3</sub> compound and

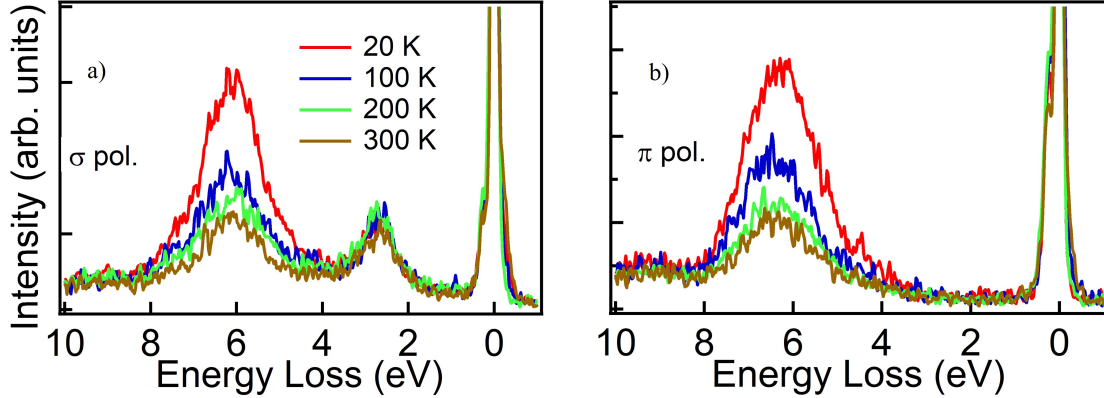


Figure 3.33: RIXS spectra at the  $M_5$  edge for several temperatures in both  $\sigma$  (a) and  $\pi$  (b). The energy loss structure at 2.7 eV corresponds to a final state of mainly  $f^0$  character whereas the one at 6 eV is a fluorescence structure whose temperature dependence directly reflects the  $T_K$  energy scale.

concluded that the gap opening at low temperature is related to the temperature dependence of the fluorescence-like structure. They proposed that this fluorescence feature reflects the unbound particle-hole pairs in the final state of RIXS. However, Pfaff et al.[63] investigated localized and delocalized Ti  $3d$  carriers in  $\text{LaAlO}_3/\text{SrTiO}_3$  with RIXS and they suggested that the fluorescence-like structure is a signature of the nature of the intermediate states of RIXS. This has been recently theoretically supported by Hariki et al. [66] using a combination of local-density approximation with dynamical mean-field theory .

Figures 3.33a and 3.33b show the temperature dependence of RIXS spectra with  $\pi$  and  $\sigma$  polarizations, respectively of the incident photon energy tuned on the XAS satellite (point G). Interestingly, the fluorescence-like structure exhibits a strong temperature dependence which is reminiscent of the temperature dependence of the Kondo resonance observed in IPES [35, 51]. What could be the physical origin of the strong temperature dependence of the fluorescence structure? In Kondo systems, the  $f$  state occupation  $n_f$  obeys a universal scaling behavior as a function of  $T/T_K$ . This scaling behavior was evidenced by photoemission, inverse photoemission, and X-ray absorption spectroscopy in many Ce Kondo systems. It is well known that the intensity of XAS satellite structure decreases with increasing temperature and exhibits also the universal scaling behavior as a function of  $T/T_K$  [67, 68]. Indeed, for  $T \ll T_K$ , the XAS spectra exhibit in addition to the  $f^2$  final states, a satellite structure that reflects the mixed-valence character. However, for  $T \gg T_K$ , the XAS spectra appear similar to those of purely trivalent compounds with only  $f^2$  final states. Furthermore, the intensity of the XAS satellite structure reflects the degree of delocalization of the  $f$  states in the ground state, and no fluorescence-like structure is observed in the RIXS spectra of the purely trivalent  $\text{CeF}_3$  compound. Moreover, with increasing  $T$ , the purely trivalent first excited states located at  $k_B T_K$  are progressively populated and no fluorescence is expected for these states similar to the  $\text{CeF}_3$  ground state. A strong  $T$ -dependence is actually observed in both  $\pi$  and  $\sigma$

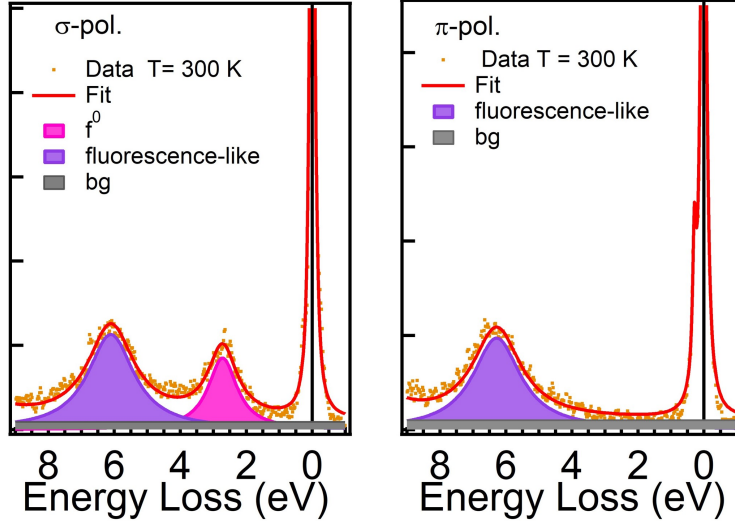


Figure 3.34: Result of fit analysis of the Ce  $M_5$ -edge RIXS spectrum at room temperature. The incident photon energy is tuned on the XAS satellite (point G) in  $\sigma$  (left panel) and  $\pi$  polarizations (right panel). The dot point represents the experimental data and the red line is the phenomenological fit to the experimental spectra. The fluorescence-like contributions are depicted in purple. We assumed a constant background depicted in gray.

polarizations leading us to conjecture that this dependence reflects the Kondo energy scale. In order to corroborate this scenario, we compared the evolution of the fluorescence-like structure intensity with temperature and the  $f^0$  weight in the ground state ( $\Delta n_f(T) = 1 - n_f(T)$ ). We performed a phenomenological fitting with a Lorentzian profile, as shown in Figure 3.34 to estimate the fluorescence-like contribution. For the  $f^0$  weight, we used the Zwicknagl, Zevin and Fulde (ZZF) approach [69, 70] with  $n_f(0) = 0.987$  and using a  $\Gamma_6$  ground state,  $\Gamma_7^1$  and  $\Gamma_7^2$  crystal-field excited states at 5 meV and 12 meV, respectively. The results shown in Figure 3.35 suggest a qualitative consistency with the T-dependent fluorescence intensity. Thus, we propose a similar mechanism to the one proposed by Kotani[71] and Hariki [66] for  $d^0$  systems. When the incident  $h\nu$  energy is tuned on the XAS  $f^0$  structure which reflects an admixture of the  $4f$  states with the continuum, a conduction electron escapes to the  $4f$  state leaving behind a hole in the conduction band. The probability of this process :

$$\Psi_0(3d^{10}4f^0) \rightarrow 3d^94f^1 \rightarrow 3d^94f^2 + \underline{L} \rightarrow 3d^{10}4f^1 + \underline{L}, \quad (3.41)$$

(with  $\underline{L}$  denoting a hole in the conduction band) increases with the hybridization strength between the  $f$  states and the conduction states. Therefore the fluorescence-like intensity probes the weight of the  $f^0$  configuration in the initial ground state and follows the same temperature dependence as the Kondo resonance in IPES.

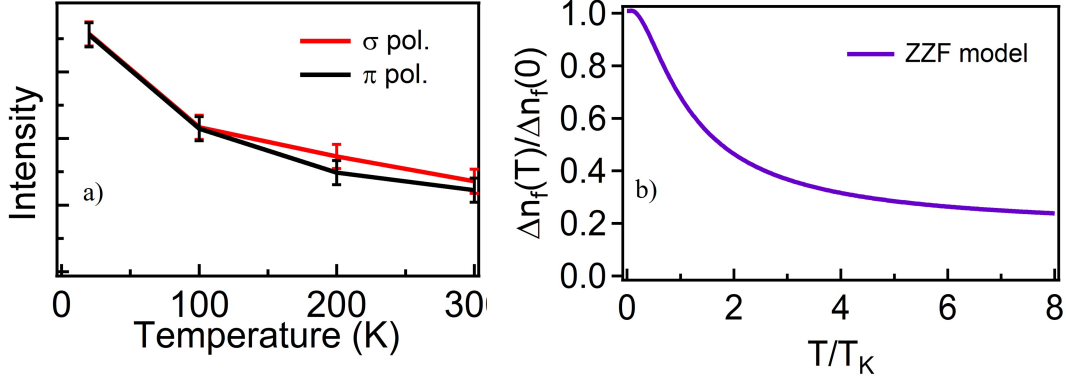


Figure 3.35: (a) Evolution of the intensity of the fluorescence-like structure in  $\sigma$  and  $\pi$  polarization with temperature. (b) Temperature dependence of  $\Delta n_f(T)/\Delta n_f(0)$  calculated using the ZZF approach.

### 3.7 RIXS in typical low- $T_K$ and high- $T_K$ Kondo systems

As mentioned in the introduction, cerium compounds attracted considerable interest due to their outstanding properties. One of them is the famous first-order isostructural (fcc  $\rightarrow$  fcc) phase transition of cerium metal (see figure 3.36) from a  $\gamma$  phase stable at ambient condition to an  $\alpha$  phase at low temperature (or high pressure). This transition is associated with a volume collapse of about 17% and a loss of magnetic moments. This transition has been explained early by a change in the electronic structure of cerium. The hybridization strength between Ce  $4f$  and conduction electron states changes due to the change of the lattice spacing with the crystal structure unchanged: In the  $\gamma$  phase, the  $f$  states are localized ( $n_f \sim 0.97$ ), while in the  $\alpha$  phase, the  $f$  states get partially delocalized (strong intermediate valence character  $n_f \sim 0.88$ ) into  $5d$  and  $5s$  conduction band states. Such behavior is observed in intermetallic cerium compounds, and they are classified into two categories:

- $\gamma$ -like Ce compounds where the cerium is nearly trivalent with a localized magnetic moment and a small Kondo temperature, and sometimes a magnetic ordering at low temperature.
- $\alpha$ -like Ce compounds where the local magnetic moment disappears due to the Kondo effect, the large hybridization yielding an intermediate valence, and a very large Kondo temperature.

In this section, we will investigate the Ce ground state electronic configuration by measuring the RIXS spectra at the Ce  $M_5$  absorption edge of three polycrystalline compounds with different Kondo temperatures: a  $\gamma$  and  $\alpha$ -like Ce compounds with low  $T_K$  (CeSi<sub>2</sub>,  $T_K \sim 50$  K) and high  $T_K$  (CeNi<sub>2</sub>,  $T_K > 1000$  K) respectively, and an intermediate  $T_K$  compound (CePd<sub>3</sub>,  $T_K \sim 150$  K - 600 K). This can be deduced by tracking the spectral weight of the

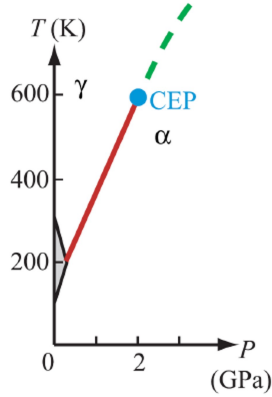


Figure 3.36: Temperature-Pressure phase diagram of Ce metal. The first-order valence transition line (red line), separates the phases and ends in a Critical End Point (CEP) at  $T = 600$  K and  $P = 2$  GPa. The dotted line represents the valence crossover. The gray area represents the parasitic  $\beta$  phase. Taken from Ref [72]

structures corresponding to the  $f^1 \rightarrow f^0$  and  $f^1 \rightarrow f^2$  charge excitations at the Ce  $M_5$  edge as well as the fluorescence-like structure. Moreover, since the intensity of the different spectral features should depend on the ground state electronic structure, we will discuss the significant change observed with increasing the Kondo energy from CeSi<sub>2</sub> to CeNi<sub>2</sub>.

The CeSi<sub>2</sub> compound exhibits characteristics thermodynamical properties of intermediate valence compounds with a Kondo temperature of  $T_K \sim 50$  K. Its magnetic susceptibility shows a liquid Fermi behavior [73] at low temperature  $T \leq 20$  K and follows a Curie-Weiss law between 200K and 600K. The linear coefficient is unusually high ( $\gamma = 87 \pm 1 \text{ mJ/K}^2$ ) compared to that of LaSi<sub>2</sub> ( $\gamma = 6 \pm 0.5 \text{ mJ/K}^2$ ) [73]. Photoemission and inverse photoemission measurements exhibit  $f$  state symmetry close to the Fermi level, which is a signature of the intermediate valence character [51, 1]. The CeNi<sub>2</sub> compound exhibits a Pauli-type paramagnetic behavior, and Spectroscopic studies even indicate a large hybridization with a very high Kondo temperature ( $T_K > 1000$  K) [1, 55]. CePd<sub>3</sub> is a dense Kondo material with  $f$ -state occupation of  $n_f \approx 0.75$  [74] determined from x-ray absorption spectroscopy, and  $T_K \sim 150$  K- 600 K [1, 6]. Moreover, in addition to the Kondo energy scale, the CePd<sub>3</sub> exhibits another low energy scale associated with the coherence, which is  $T_{coh} \sim 130$  K (from transport measurements [75]).

### 3.7.1 Overview of the RIXS results

Experiments have been carried out on the AERHA spectrometer of the SEXTANTS beamline. The overall energy resolution, estimated from the width of the elastic peak, is about 325 meV, which is a little bit larger than the  $4f_{5/2} - 4f_{7/2}$  spin-orbit energy ( $\Delta_{so} \sim 280$  meV). Figure 3.38a shows a set of RIXS spectra recorded at different excitation energies around the  $M_5$  edge with  $\sigma$  polarization. When the incident photon energy is tuned at the XAS

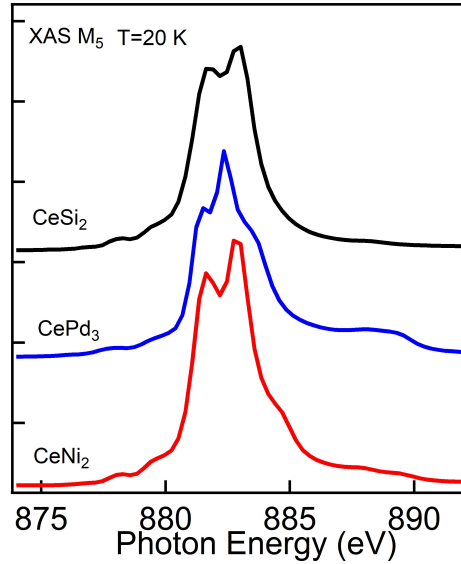


Figure 3.37: Ce  $M_5$  XAS of CeSi<sub>2</sub>, CePd<sub>3</sub> and CeNi<sub>2</sub> measured at  $T=20$  K.

main structure (see figure 3.37), the RIXS spectrum exhibits, in addition to the elastic peak, the  $f^2$  final state at  $E_{loss}=4.2$  eV ( $f^1 \rightarrow f^2$  charge excitation). Moreover, the  $f^0$  final state at  $E_{loss}=2.2$  eV ( $f^1 \rightarrow f^0$  charge excitation), is clearly observed when the incident photon energy is tuned at the XAS satellite. With increasing the incident photon energy from  $M_5 + 3$  to  $M_5 + 6$  edge, two additional inelastic structures (indicated by the star and the black circle dot) are observed, whose energy losses increase with the incident photon energy. These two structures are also well visible in  $\pi$  polarization (see figure 3.38b). The structure indicated by the star corresponds to a fluorescence-like structure similar to the one observed in the RIXS spectra of the CeAgSb<sub>2</sub> compound presented in the previous section. It is worthwhile underlining that the drastic polarization dependence of the  $f^0$  final state is well seen in RIXS spectra of CeSi<sub>2</sub> compound, even though this latter is a polycrystal, unlike the CeAgSb<sub>2</sub> compound presented above, which is a single crystal. The total suppression of the  $f^0$  final state (see figure 3.38b) is due to the scattering angle ( $90^\circ$ ), and yields access to the  $^1S_0$  symmetry of the ground state. The RIXS spectra of CeSi<sub>2</sub> are very similar to the results of CeAgSb<sub>2</sub>. Note that the Kondo temperature of CeSi<sub>2</sub> ( $T_K \sim 50$  K) is slightly higher than  $T_K$  of CeAgSb<sub>2</sub> ( $T_K \sim 10 - 20$  K). Figure 3.39a and 3.39b respectively, show the RIXS spectra of CeNi<sub>2</sub> and CePd<sub>3</sub> measured at low temperature with  $\sigma$  polarization of the incident photon energy. In addition to the  $f^0$  and  $f^2$  final states, the RIXS spectra of CeNi<sub>2</sub> exhibit several "dispersive" (fluorescence-like) features indicated by the star, the black circle dot, and the black square dot. Similarly, the RIXS spectra of the CePd<sub>3</sub> compound also exhibit several dispersive structures. Moreover, when the incident photon energy is tuned at  $M_5$ , an unexpected structure appears at 2 eV energy loss: this structure is not a  $f^0$  final state since it is not suppressed in  $\pi$  polarization. In addition, another unexpected structure



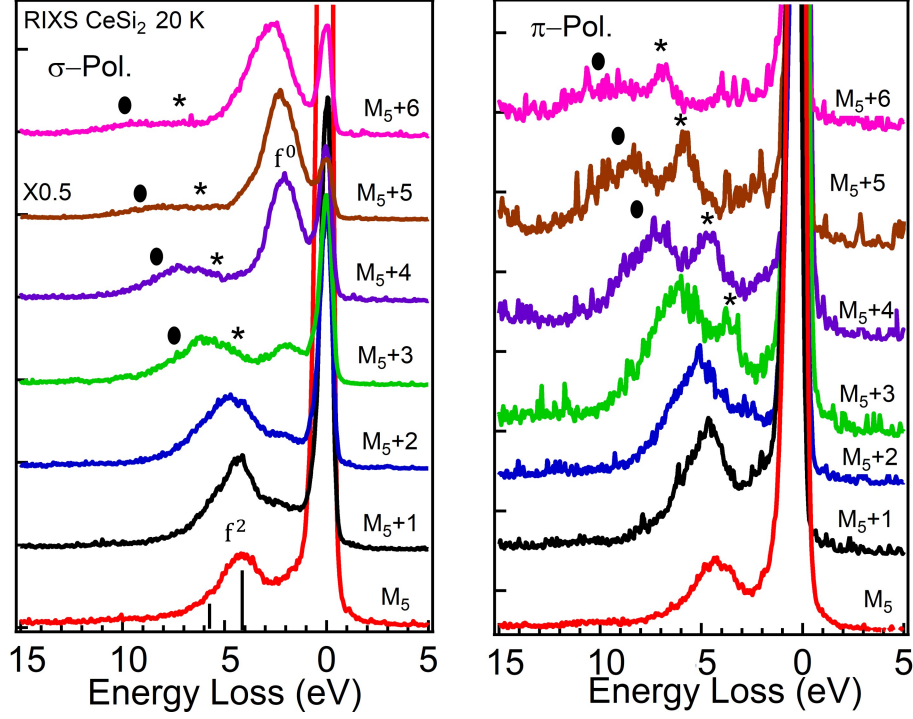


Figure 3.38: Set of RIXS spectra of  $\text{CeSi}_2$  compound measured with  $\sigma$  and  $\pi$  polarizations of the incident photon. Fluorescence-like structures are indicated by the star and the black dot.

is observed in the low energy loss range at about  $\sim 0.5$  eV (see figures 3.40b and 3.40c). Surprisingly, the RIXS spectra of high Kondo temperature compounds ( $\text{CePd}_3$ ,  $\text{CeNi}_2$ ) are more complicated than expected. Additional unknown structures compared to the low  $T_K$   $\text{CeSi}_2$  and  $\text{CeAgSb}_2$  are observed. The presence of these unknown structures complicates the analysis of the spectra with the calculation presented in section 3.5. Nevertheless, we can perform a phenomenological fit to quantitatively analyze the evolution of the RIXS spectral weight of  $\text{CeSi}_2$ ,  $\text{CeNi}_2$ , and  $\text{CePd}_3$ . For this purpose, we focus on the RIXS spectra taken at the incident photon of the XAS satellite (see figure 3.40). We introduce the quantity  $r_f$ , which stands for the intensity of the  $f^0$  structure with respect to the total  $4f$  intensity expressed as follows:

$$r_f = \frac{I(f^0)}{I(f^0) + I(f^1)}, \quad (3.42)$$

where  $I(f^0)$ , and  $I(f^1)$  represent the integrated intensity of the  $f^0$  and  $f^1$  structures, respectively.  $r_f$  reflects the delocalized character of the  $4f$  states in the systems given by the weight of the  $f^0$  component in the ground state,  $1 - n_f$ . The structures corresponding to the final state with  $4f^0$  final state (purple line in figure 3.40) are respectively observed at 2.2 eV, 2.8 eV and 3.1 eV in the RIXS spectra of  $\text{CeSi}_2$ ,  $\text{CeNi}_2$ , and  $\text{CePd}_3$ . The RIXS intensity ratio  $r_f$  expressed in Equation 3.42, is estimated in Table 3.4. The  $r_f$  value of  $\text{CeSi}_2$  is smaller

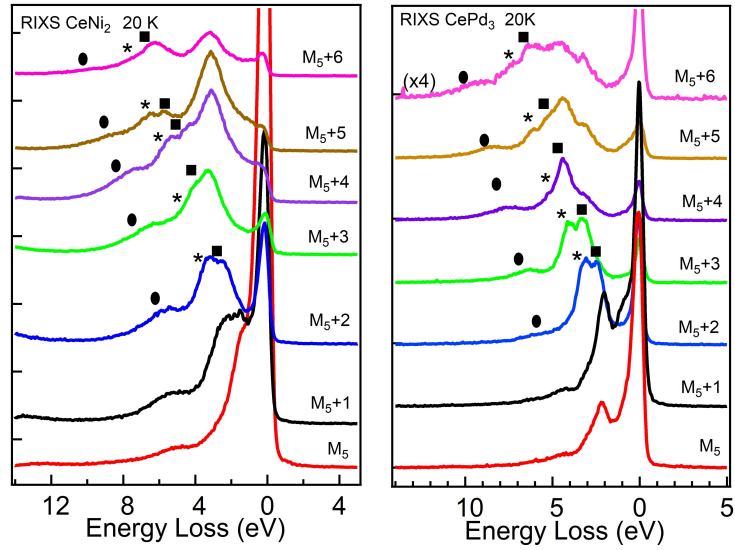


Figure 3.39: Set of RIXS spectra measured with  $\sigma$  polarization of the incident photon energy of  $\text{CeNi}_2$  and  $\text{CePd}_3$ . Fluorescence-like structures are indicated by the star, the black circle dot, and the black square dot.

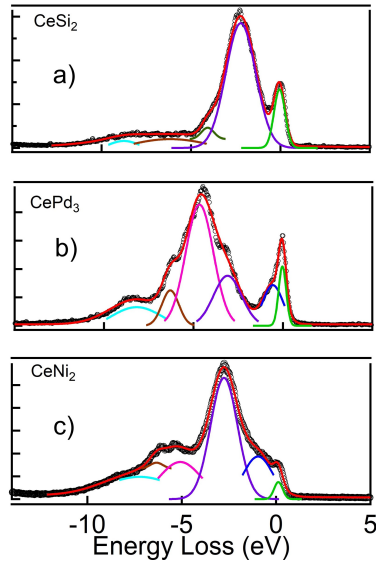


Figure 3.40: RIXS spectral line shape of  $\text{CeSi}_2$  (top panel),  $\text{CePd}_3$  (middle panel) and  $\text{CeNi}_2$  (bottom panel) measured with the incident photon energy tuned at the  $f^1$  XAS satellite ( $M_5 + 5$ ). The solid lines refer to Gaussian fits of the elastic peak (green), the  $f^0$  charge excitation (purple), the fluorescence-like structure (brown), and the  $f^2$  charge excitation (aqua). The red line refers to the sum of all the fitting contributions.

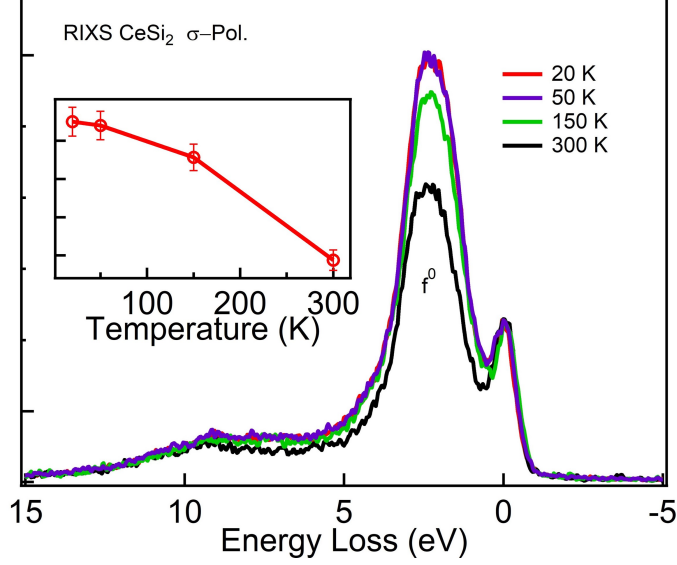


Figure 3.41: Temperature dependence of the Ce  $M_5$ -edge RIXS spectra of CeSi<sub>2</sub> taken with the incident photon energy tuned at the  $f^1$  XAS satellite. Clear temperature dependence of the  $f^0$  final state is observed. The insert shows the evolution of the integrated intensity of the  $f^0$  structure.

than that of CeNi<sub>2</sub>, which is consistent with their Kondo temperatures. However, the  $r_f$  value of CePd<sub>3</sub> is weaker than that of CeSi<sub>2</sub> while its Kondo temperature is one order of magnitude larger than that of CeSi<sub>2</sub>. Therefore, it is difficult to conclude. Indeed, we should introduce an error bar (incertitude) regarding these estimations caused by the following two reasons: one is that  $r_f$  was estimated in the spectrum measured at the incident photon energy where the  $f^0$  structure is resonantly enhanced, and then its intensity is overestimated; the second is that the intensity of the elastic peak ( $f^1$  final state), strongly depends on the roughness of the sample surface [3, 5]. So, the intensity of the elastic peak from one sample to another will increase or not depending on how they were scraped before the RIXS measurements.

	$E_{loss}(f^0)$ (eV)	$r_f$
CeSi <sub>2</sub>	2.2	0.85
CePd <sub>3</sub>	3.1	0.63
CeNi <sub>2</sub>	2.8	0.95

Table 3.4: Energy loss of the  $f^0$  and RIXS intensities ratio,  $r_f$  for the CeSi<sub>2</sub>, CeNi<sub>2</sub> and CePd<sub>3</sub> compounds.

Figure 3.41 shows the temperature dependence of the Ce  $M_5$ -edge RIXS spectra of CeSi<sub>2</sub>. The spectra have been normalized on the elastic peak. Unlike CeAgSb<sub>2</sub> presented in the previous section, a clear and systematic decrease of the  $f^0$  spectral weight is observed on in-

creasing temperature from 20 K to 300 K. This behavior well reflects the progressive thermal population of the low-lying magnetic states as expected in the Kondo scenario.

### 3.7.2 Understanding the Ce $M_5$ -edge RIXS in Ce compounds: the Ce-Sc alloy

In the previous section, we investigated the evolution of the Ce- $M_5$  edge RIXS spectra of a low  $T_K$   $\gamma$ -Ce like compound (CeSi<sub>2</sub>) and a high  $T_K$   $\alpha$ -Ce like compound (CeNi<sub>2</sub>). We succeeded in evidencing the energy loss features associated with final states  $f^0$ ,  $f^1$ , and  $f^2$ , whose intensities directly reflect the valence admixture. While some energy loss or fluorescence structures have been identified, other ones remain misunderstood in the RIXS spectra of the high  $T_K$  compounds. To understand these features, it would be interesting to study low  $T_K$  and high  $T_K$  phases in the same material. Moreover, this will allow avoiding the uncertainty regarding the intensity of the elastic peak mentioned above in the quantitative analysis. It is well known that Ce metal can exhibit these two different electronic states as a function of temperature, but, it is triggered by applying external pressure [76, 77] (see figure 3.36). However, these two states, namely, the  $\gamma$ - $\alpha$  transition, can also be tracked as a function of temperature by using chemical pressure [78] such as substituting thorium or scandium for cerium. In order to investigate the  $\gamma$ - $\alpha$  transition of Ce-Sc alloy, RIXS measurements at Ce-L<sub>3</sub> have been carried out by Rueff et al. [79], they evidenced the transition by tracking the  $f^1/f^2$  intensity ratio. At the same time, Dallera et al [10] also evidenced the  $\gamma$ - $\alpha$  transition by following the  $f^1$  intensity of the Ce- $M_{4,5}$  x-ray absorption spectroscopy spectra. Moreover, Dallera et al [10] also performed RIXS measurements at Ce- $M_5$ , but surprisingly, they did not observe the  $f^2$  structure, while it has been theoretically predicted (see section 3.3).

In this section, we will investigate the temperature dependence Ce- $M_5$  RIXS spectra of Ce<sub>0.93</sub>Sc<sub>0.07</sub> alloy, evidence the  $f^2$  final state, and identify all the unknown structures we have measured in the Ce- $M_5$  RIXS spectra of high  $T_K$  compounds. Moreover, we will stress the outstanding feature of RIXS as a powerful tool to provide detailed information on the f electronic properties of rare earth. Namely, we will deduce the  $\gamma$ - $\alpha$  transition by tracking the spectral weight of the structures corresponding to the  $f^1 \rightarrow f^0$  charge excitation as well as fluorescence-like structure.

Figure 3.42 shows the Ce  $M_5$ -edge XAS spectra of Ce<sub>0.93</sub>Sc<sub>0.07</sub> measured at 20 K ( $\alpha$ -phase) and 300 K ( $\gamma$  phase). The spectra are dominated by the  $3d^9 4f^2$  multiplets arising via the dipole transition from the  $4f^1$  contribution in the ground state. The intermediate valence of the ground state is revealed via the  $3d^9 4f^1$  satellite at  $h\nu = 888$  eV. As discussed in section 3.5, its intensity reflects the weight of the  $f^0$  component in the ground state. In the  $\gamma$ -phase, the XAS spectrum is consistent with an f-state occupation  $n_f \sim 1$  (very small satellite), while in the  $\alpha$ -phase, a significant increase of the intensity of the satellite is observed. Figure 3.43 shows the Ce  $3d \rightarrow 4f \rightarrow 3d$  RIXS spectra of Ce<sub>0.93</sub>Sc<sub>0.07</sub> taken at 20 K (3.43a, 3.43c) and 300 K (3.43c, 3.43d) in  $\sigma$  and  $\pi$  polarizations, respectively. The spectra are shown as a function of the energy loss where the incident photon energy increases in step of 1 eV from the XAS spectrum,  $M_5$  ( $h\nu = 883$  eV) up to  $M_5 + 7$  (2 eV above the  $f^1$  XAS satellite). The  $3d^9 4f^3$  multiplet states which are reached via the dipole transition from the  $4f^2$  component

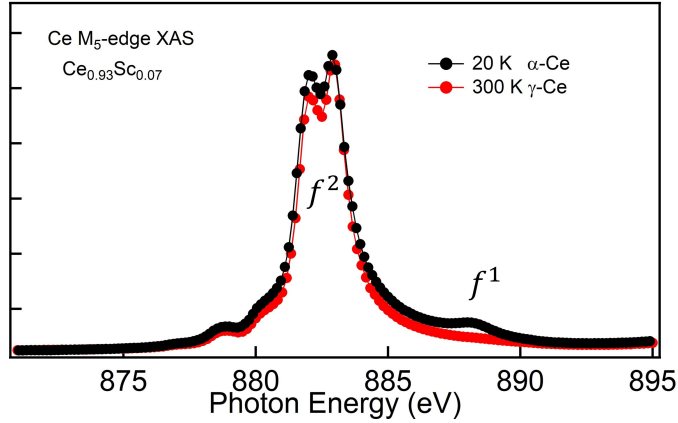


Figure 3.42: Ce  $M_5$ -edge XAS spectra of  $\text{Ce}_{0.93}\text{Sc}_{0.07}$  measured at 20 K ( $\alpha$ -phase) and 300 K ( $\gamma$  phase).

in the ground state, are hidden in the XAS spectra. As seen from figures 3.43a and 3.43b, however, when the incident photon energy is tuned at  $M_5$ , the RIXS spectrum is dominated by two structures corresponding to the  $f^1$  (elastic peak) and  $f^2$  final states. Indeed, the  $3d^94f^3$  final state is invisible in the XAS spectrum owing to the large spectral broadening and the strong overlap with the  $3d^94f^2$  which dominate the spectrum, but the  $f^2$  RIXS final state is clearly detected in these RIXS measurements, unlike those of Dallera et al. [10] (see section 3.3). When the incident photon energy is tuned at the XAS satellite structure, the RIXS spectra exhibit a structure at  $\sim 1.9$  eV corresponding to the  $f^0$  final state in both  $\alpha$ -phase and  $\gamma$ -phase. When the incident photon energy increases from  $M_5 + 5$  to  $M_5 + 7$ , the  $f^0$  structure is progressively broadening and asymmetric, indicating the presence of two different structures: The first one remains at constant energy loss (indicating by the dashed line), while the position of the other one is progressively shifted in the high energy side indicating a fluorescence regime (indicated by the vertical arrows). Similar behavior is observed in the  $f^1 \rightarrow f^2$  charge excitation region upon increases the incident photon energy from  $M_5$  to  $M_5 + 7$ . Even if the  $f^2$  final state is structured by the multiplets effects, a fluorescence-like structure (indicated by the black dot) with a linearly dispersing energy loss as a function of the incident photon energy is clearly observed, in addition to the structure at constant energy loss (indicated by the dashed line). What could be the origin of these two fluorescent structures? Indeed, similar structures have been observed in the Ni  $2p \rightarrow 3d \rightarrow 2p$  RIXS spectra of the prototype material of the charge transfer insulator NiO [80, 81].

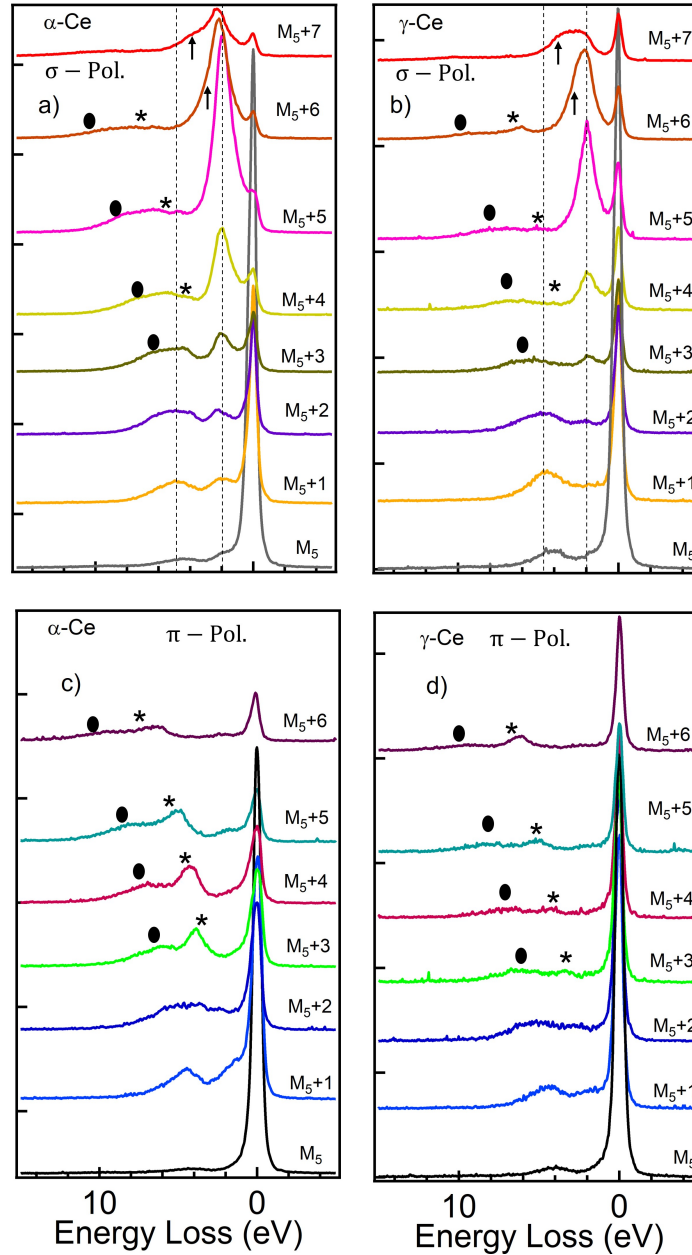


Figure 3.43:  $Ce\ 3d \rightarrow 4f \rightarrow 3d$  RIXS spectra of  $Ce_{0.93}Sc_{0.07}$  as a function of the energy loss. The measurements were performed at 20 K (a,c) and 300 K (c,d) in  $\sigma$  and  $\pi$  polarizations, respectively. The incident photon energy is tuned around the  $f^2$  XAS main structure and the  $f^1$  XAS satellite (see figure 3.42).  $M_5$  denotes the excitation energy, which coincides with the maximum of the XAS spectrum ( $h\nu = 883$  eV). The dashed lines indicate the RIXS components attributed to the mainly  $f^0$  and  $f^2$  charge excitations.

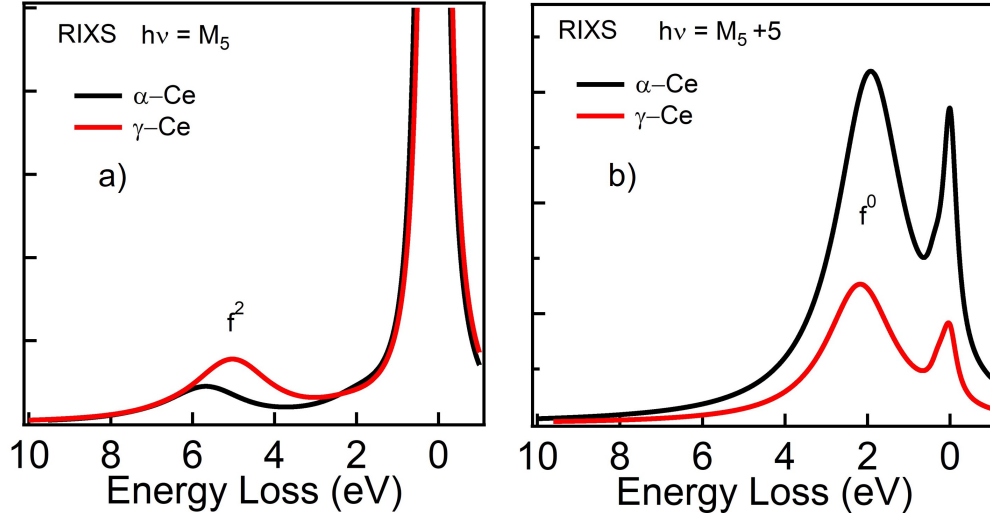


Figure 3.44: RIXS spectra of  $\alpha$ -Ce and  $\gamma$ -Ce calculated within the full-multiplet configuration interaction model at the  $M_5$  (a) XAS and the  $f^1$  satellite (b), the parameters are given in table 3.5.

Magnuson et al. [9] performed the calculations of these RIXS spectra with the SIAM, and then Butorin [82] proposed that such a charge transfer excitations which behave like fluorescence are due to the fact that the satellite in the XAS spectra has a continuous excited states owing to the finite bandwidth of the O  $2p$  valence band. Later, Matsubara et al. [83] carefully analyzed this problem with the SIAM, and they confirm the mechanism proposed by Butorin. Moreover, they pointed out that it is essential to take into account a finite width of the O  $2p$  valence band in order to reproduce all the experimental fluorescence-like excitations in RIXS. Therefore, we propose a similar mechanism for the fluorescence we observed in the RIXS spectra of  $\text{Ce}_{0.93}\text{Sc}_{0.07}$  (indicated by the vertical arrows and the black dot in figure 3.43). Typically, if we take into account of the conduction band width  $W$ , the  $4f^1\bar{L}$  and  $4f^2\bar{L}^2$  configurations in the initial and final state of RIXS will have the energy width  $W$  and  $2W$ , respectively. So, when the incident photon energy is tuned to the continuum  $3d^94f^2\bar{L}^2$  state, the transition to the continuum states ( $4f^2\bar{L}^2$  configuration) in the final state is restricted by the symmetrical condition of the hole state in the conduction band. That is to say, only the transition between the same hole state in the  $3d^94f^2\bar{L}^2$  and  $4f^2\bar{L}^2$  continuum states are allowed. Especially, only the transition to the lowest (highest) part of the continuum state in the final state is observed when the incident photon energy is tuned to the lowest (highest) part of the continuum state in the intermediate state. Therefore, the outgoing photon energy will not depend on the incident photon energy, and the corresponding  $f^2$  structure will show a fluorescence behavior.

Figure 3.44a and 3.44b shows the result of the full-multiplet configuration interaction calculation of the RIXS spectra of  $\alpha$ -Ce and  $\gamma$ -Ce. We focused on the spectra taken with the excitation energy tuned on the XAS main structure ( $M_5$ ) and its satellite ( $M_5 + 5$ ). It

	$f^0$	$f^1$	$f^2$	$n_f$	$\epsilon_f$	$U_{ff}$	$U_{fc}$	V
$\alpha$ -Ce	12.66%	85.5%	1.85%	0.89	-1.2	7	10.85	0.18
$\gamma$ -Ce	5.64%	92.7%	1.67%	0.96	-1.7	7	10.85	0.15

Table 3.5:  $f^n$  contributions and  $f$ -state occupation for  $\gamma$  and  $\alpha$  Ce. SIAM parameters used for the calculations: the  $f - f$  Coulomb exchange  $U_{ff}$ , the Coulomb interaction between  $f$  electron and  $3d$  core hole  $U_{fc}$ , the effective  $f$  binding energy  $\epsilon_f$ , and the hybridization strength V (all in eV).

should be noted that the calculations are performed at  $T = 0$ . The parameters used for  $\alpha$ -Ce and  $\gamma$ -Ce are given in table 3.5. The RIXS calculations are in satisfactory agreement with the experimental data in figure 3.43, although the fluorescence-like contributions are not included. The  $f^0$  and  $f^2$  loss energy structures are well observed respectively at  $\sim 5$  eV and  $\sim 2$  eV in both  $\alpha$  and  $\gamma$  phases. The calculations correctly reproduce the reduction of the  $f^0$  structure in the  $\gamma$  phase. This spectral weight change reflects the small hybridization and the associated  $f^0$  weight in the ground state of the  $\gamma$  phase (see table 3.5). Regarding the  $f^2$  structure, it is well known that the hybridization strength and Kondo temperature in the  $\alpha$  phase are stronger than that in the  $\gamma$  phase. Following the discussion in section 3.5, the intensity of the  $f^2$  structure increases with increasing the hybridization strength. However, in figure 3.43, the intensity of the  $f^2$  structure in the  $\gamma$ -phase is stronger than that in the  $\alpha$  phase. A way out is to decrease the  $f$ -state energy  $\epsilon_f$  in the  $\alpha$  phase with respect to the  $\gamma$  phase (see table 3.5). Nevertheless, it is worth to point out that the spectral weight of the  $f^2$  structure is underestimated in the simulated spectra, especially for high photon energies. Indeed, its intensity strongly depends on the mixing of the  $3d^9 4f^2$  and  $3d^9 4f^3$  configurations in the intermediate state (XAS final state) where the presence of an extra  $4f$  electron gives rise to an enhancement of the hybridization strength. Such a configuration dependence of the hybridization was not taken into account here.

### 3.7.3 Oxidation effect

Figure 3.45 shows a comparison between Ce  $M_5$ -edge XAS taken from a freshly scraped sample and a surface that has been exposed for more than 8 hours. The Ce  $M_5$ -edge XAS profile line shape of the oxidized surface is significantly changed compared to the clean one. Typically, a shoulder and a satellite structure arise respectively at 884 eV and 890 eV (indicated by arrows A and C, respectively). It would appear like the satellite structure of the clean sample (indicated by arrow B) has moved from 888 eV to 890 eV due to the oxidation effects, but it is not the case. Satellite B remains well at the same energy, but the spectral weight in this region is dominated by surface contributions. Indeed, shoulder A and the satellite C are respectively associated with the  $3d^9 4f^2$  and  $3d^9 4f^1$  final states, (see section 3.3) of the oxidized surface corresponding to  $\text{CeO}_2$ .

The Ce  $M_5$ -edge RIXS spectra taken at the incident photon energies  $h\nu = \text{B}$  and  $h\nu = \text{C}$  from the clean and oxidized surface are respectively shown in figure 3.46a and 3.46b. Interestingly,



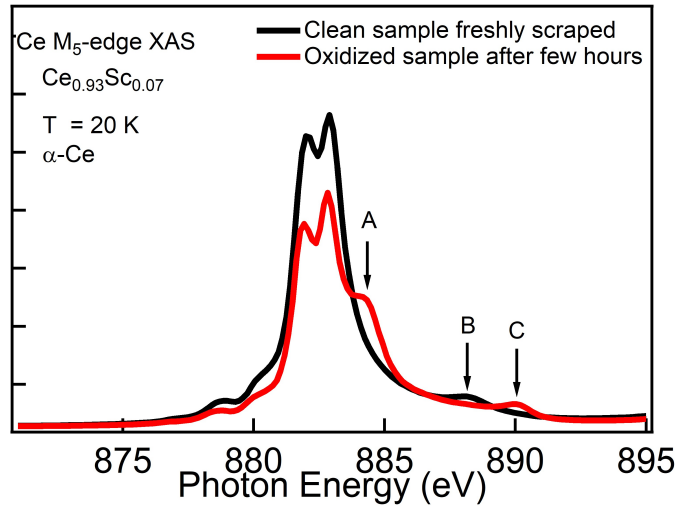


Figure 3.45: Ce  $M_5$ -edge XAS spectra of  $\text{Ce}_{0.93}\text{Sc}_{0.07}$  at  $T = 20$  K with different surface qualities. The spectrum in the black line is taken from a freshly scraped sample, and the spectrum in the red line is taken from a surface that has been exposed for more than 8 hours. Arrows A and B indicate the Considerable contributions from the oxidation effects of the aged surface.

the RIXS spectral line shape is unaffected by the oxidation effects when the incident photon energy is tuned at  $h\nu = B$  (the bulk satellite), while this satellite is almost invisible XAS spectra of the oxidized surface. However, when the incident photon energy is tuned at  $h\nu = C$  (the surface satellite), a prominent structure arises at about 6.5 eV on the spectrum measured with the oxidized surface. These two behaviors highlight two features of RIXS: Its bulk sensitivity and its chemical sensitivity. Especially, tuning the incoming photon energy on different absorption edges allows for prioritizing the scattering from a given element in the studied material. Here, the  $\text{Ce}_{0.93}\text{Sc}_{0.07}$  in the bulk, or the  $\text{CeO}_2$  of the oxidized surface.

### 3.7.4 A direct investigation of $\gamma$ - $\alpha$ phase transition by Ce $M_5$ -edge RIXS

In order to investigate the  $\gamma$ - $\alpha$  transition, we fixed the incident photon energy at the  $f^1$  XAS satellite (to make the  $f^0$  intensity of RIXS maximum), and we have followed the evolution of the RIXS spectra over a complete cycle  $20\text{ K} \rightarrow 300\text{ K} \rightarrow 20\text{ K}$ . The cooling and heating rate was about  $2\text{ K/min}$ , and each spectrum has been acquired for 40 seconds. In the RIXS color maps, we observe clear changes in the region of the  $f^0$  charge excitations upon cooling (see figure 3.47a) and heating (see figure 3.47b). For comparison, we show the RIXS spectra measured at  $20\text{ K}$  ( $\alpha$ -phase) and  $300\text{ K}$  ( $\gamma$ -phase) in figure 3.47c. It is noteworthy that the spectral lineshape is unaffected by the transition. It is obvious that the  $f^0$  structure of  $\alpha$ -Ce is much more intense than that of  $\gamma$ -Ce, however, both are located at the same energy  $\sim 1.9\text{ eV}$ . This is consistent with the XAS spectra and indicates the extremely large Kondo temperature

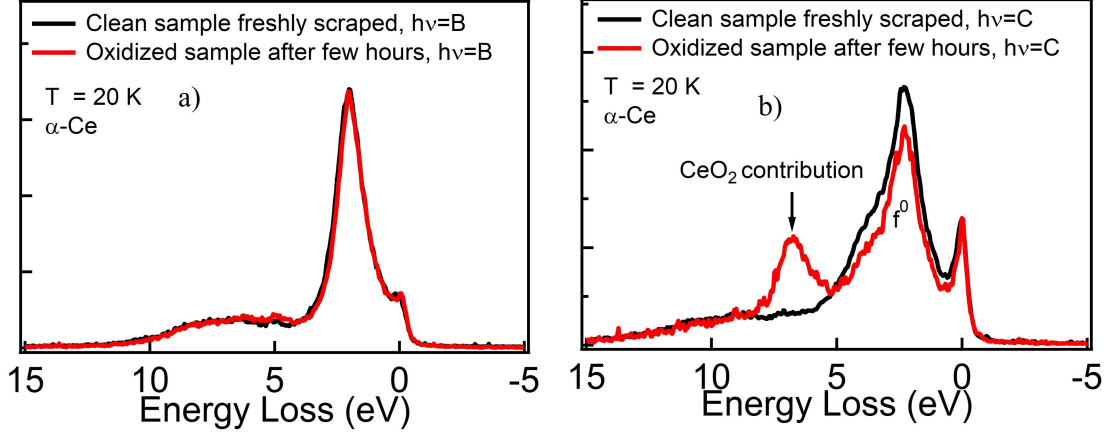


Figure 3.46: Ce  $M_5$ -edge RIXS spectra taken at the incident photon energies  $h\nu = B$  (a) and  $h\nu = C$  (b) from a freshly scraped sample and a oxidized one (see figure 3.45).

and strong delocalized character of  $4f$  states of  $\alpha$ -Ce. The RIXS intensity ratio expressed in Equation 3.42, is estimated in Table 3.6. As expected, the  $r_f$  value of  $\alpha$ -Ce is larger than that of  $\gamma$ -Ce. Moreover, it is interesting to note that these values are respectively close to those of  $\text{CeNi}_2$  and  $\text{CeSi}_2$ .

Figure 3.48 shows the temperature dependence of the integrated intensities in the region of the  $f^0$  peak at 1.9 eV extracted from the RIXS map. The onset of the phase transition is marked by a rapid decrease of the  $f^0$  intensity at 130 K on heating, and a rapid increase at 110 K on cooling. A large hysteresis is observed, comparable to what is observed in the thermoelectric power and magnetization measurements. For comparison, we measured the temperature dependence of the magnetization from the same piece of the sample used for RIXS measurements at the magnetic field  $\mu_0 H = 2$  T, shown in figure 3.48b. Interestingly, the temperature dependence of the fluorescence-like structure also exhibits a large hysteresis, similar to the one obtained from the intensity of the  $f^0$  structure (see figure 3.49). This strengthens the statement we made in the previous section. Namely, the fluorescence-like intensity probes the weight of the  $f^0$  configuration in the initial ground state and reflects the Kondo energy scale.

	$E_{loss}(f^0)$ (eV)	$r_f$
$\alpha$ -Ce	1.9	0.95
$\gamma$ -Ce	1.9	0.8

Table 3.6: Energy loss of the  $f^0$  and RIXS intensities ratio,  $r_f$  for the  $\gamma$ -Ce and  $\alpha$ -Ce.

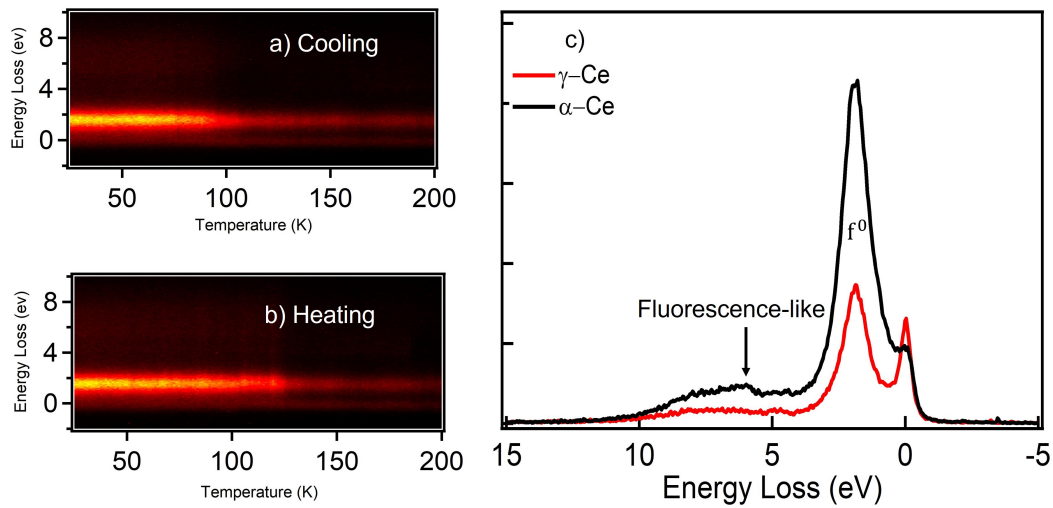


Figure 3.47: (a, b) Highlighting of the  $\gamma$ - $\alpha$  transition with the RIXS map measured as a function of the temperature. c) Comparison of the RIXS spectra measured at 20 K and 300 K. The incident photon energy in (a, b, c) was tuned at the  $f^1$  XAS satellite.

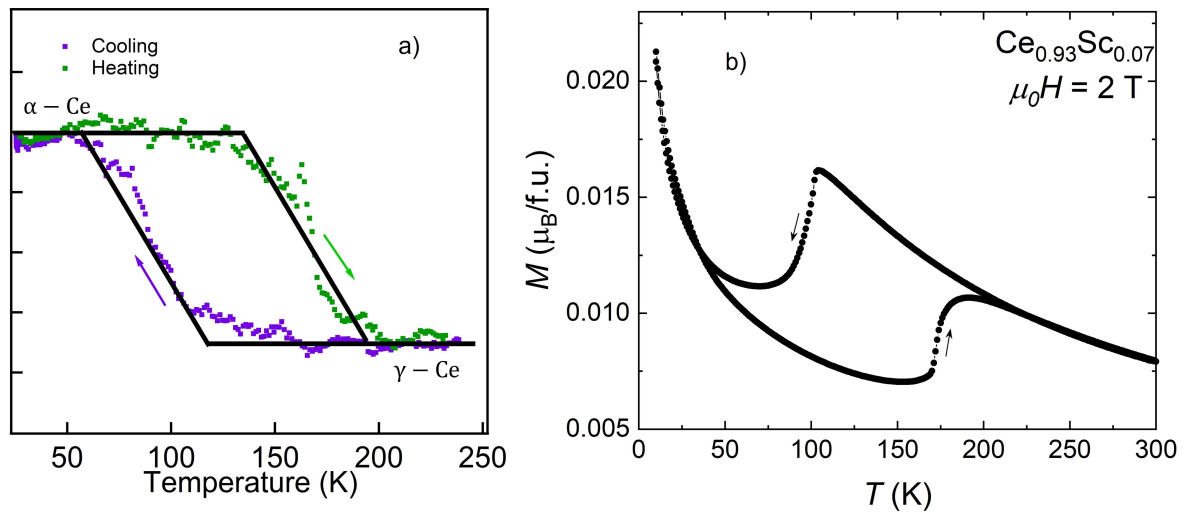


Figure 3.48: (a) Hysteresis loops derived from the integrated intensity of the  $f^0$  structure in the RIXS map of  $Ce_{0.97}Sc_{0.07}$  (see figure 3.47), the arrows indicate the circulation inside the loop. b) Temperature-dependence of the magnetization at  $\mu_0 H = 2$  T.

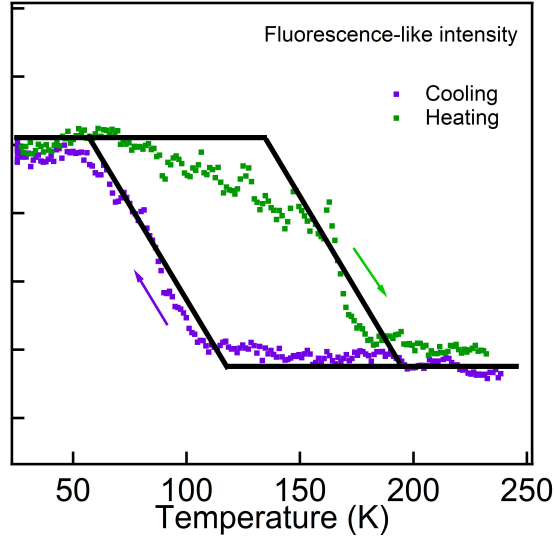


Figure 3.49: Hysteresis loops derived from the integrated intensity of the fluorescence-like structure in the RIXS map of  $\text{Ce}_{0.97}\text{Sc}_{0.07}$  (see figure 3.47).

### 3.8 Conclusion

Knowledge of the low and high energy scales, as well as the hybridization strength between  $f$  and conduction band states, are crucial for understanding the properties of strongly correlated cerium Kondo systems. In the second part of this thesis, RIXS has been presented as a powerful tool to probe these  $4f$  properties. The example of the ferromagnetic  $\text{CeAgSb}_2$  Kondo system allows us to demonstrate that RIXS probes both low energies excitation (spin-orbit excitation) and high energies excitation (Coulomb repulsion between the  $4f$  electrons and the energy of the  $4f$  level) in a Ce Kondo system by varying the incident photon energy around the main and x-ray absorption satellite structure. These energy scales are usually observed by combining photoemission and inverse spectroscopy. We used a simplified model based on the combination of the single impurity Anderson model with the full multiplet theory to analyze the experimental results. This model allows us to understand, on the one hand, all the energy loss structures and, on the other hand, to reproduce the drastic polarization dependence of the elastic peak and  $f^0$  structure and to evidence the  $^1S_0$  symmetry of the ground state. We evidenced a strong temperature dependence of the fluorescence-like structure in the RIXS spectra of  $\text{CeAgSb}_2$ , and we proposed that it is a signature of the Kondo energy scale. We investigated the evolution of the RIXS spectral line shapes of compounds with low and high Kondo temperatures, namely  $\text{CeSi}_2$ ,  $\text{CeNi}_2$ , and  $\text{CePd}_3$ , and we found that the RIXS spectra of high  $T_K$  compounds are very complex with the presence of unknown structures. In order to gain further insight into the RIXS of cerium compounds, we measured the  $\text{Ce}_{0.93}\text{Sc}_{0.07}$  alloy across the  $\gamma$ - $\alpha$  transition. The RIXS spectral weight of the  $f^0$ , as well as the fluorescence-like structure, present a sharp drop across the  $\gamma$ - $\alpha$  transition and hysteresis as a function of tem-

perature that closely resembles the magnetization loop. This allows us to conjecture that the fluorescence-like structure is correlated with the weight of the  $f^0$  configuration in the ground state and reflects the Kondo scale.

However, the temperature dependence of the  $f^0$  structure predicted by the single impurity Anderson model has been observed in the RIXS spectra of  $\text{CeSi}_2$  and across the  $\gamma$ - $\alpha$  transition of  $\text{Ce}_{0.93}\text{Sc}_{0.07}$  but not in  $\text{CeAgSb}_2$ . This unexpected temperature independent in the RIXS spectra of  $\text{CeAgSb}_2$  deserves further investigation. Moreover, we pointed out the underestimation of the  $f^2$  RIXS spectral weight in our simulation. To improve the agreement between the experimental and calculated results, it would be necessary for the future to take into account a finite width of the conduction band and to extend the SIAM model by including configurations dependent hybridization. The analysis the fluorescence-like feature shows a potential for addressing questions concerning itinerancy and localization of charge excitations and the Kondo energy scale. However, a detailed analysis of its origin is still a theoretical challenge.

## Bibliography

- [1] D. Malterre, M. Grioni, and Y. Baer, “Recent developments in high-energy spectroscopies of Kondo systems,” *Advances in Physics*, vol. 45, no. 4, pp. 299–348, 1996.
- [2] M. Matsubara, T. Uozumi, A. Kotani, Y. Harada, and S. Shin, “Polarization dependence of resonant x-ray emission spectra in early transition metal compounds,” *Journal of the Physical Society of Japan*, vol. 69, no. 5, pp. 1558–1565, 2000.
- [3] A. Kotani and S. Shin, “Resonant inelastic x-ray scattering spectra for electrons in solids,” *Rev. Mod. Phys.*, vol. 73, pp. 203–246, 2001.
- [4] G. Ghiringhelli, N. B. Brookes, E. Annese, H. Berger, C. Dallera, M. Grioni, L. Perfetti, A. Tagliaferri, and L. Braicovich, “Low energy electronic excitations in the layered cuprates studied by copper  $L_3$  resonant inelastic x-ray scattering,” *Phys. Rev. Lett.*, vol. 92, p. 117406, 2004.
- [5] L. J. P. Ament, M. van Veenendaal, T. P. Devereaux, J. P. Hill, and J. van den Brink, “Resonant inelastic x-ray scattering studies of elementary excitations,” *Rev. Mod. Phys.*, vol. 83, pp. 705–767, 2011.
- [6] Rahn, M. C. et al., “Kondo quasiparticle dynamics observed by resonant inelastic x-ray scattering,” *Nat Commun*, vol. 13, p. 6129, 2022.
- [7] M. Nakazawa, S. Tanaka, T. Uozumi, and A. Kotani, “Theory of resonant x-ray emission spectra in Ce compounds,” *Journal of the Physical Society of Japan*, vol. 65, no. 7, pp. 2303–2310, 1996.
- [8] S. M. Butorin, D. C. Mancini, J.-H. Guo, N. Wassdahl, J. Nordgren, M. Nakazawa, S. Tanaka, T. Uozumi, A. Kotani, Y. Ma, K. E. Myano, B. A. Karlin, and D. K. Shuh, “Resonant x-ray fluorescence spectroscopy of correlated systems: A probe of charge-transfer excitations,” *Phys. Rev. Lett.*, vol. 77, pp. 574–577, 1996.
- [9] M. Magnuson, S. M. Butorin, J.-H. Guo, A. Agui, J. Nordgren, H. Ogasawara, A. Kotani, T. Takahashi, and S. Kunii, “Electronic-structure investigation of  $\text{CeB}_6$  by means of soft-x-ray scattering,” *Phys. Rev. B*, vol. 63, p. 075101, 2001.
- [10] C. Dallera, M. Grioni, A. Palenzona, M. Taguchi, E. Annese, G. Ghiringhelli, A. Tagliaferri, N. B. Brookes, T. Neisius, and L. Braicovich, “ $\alpha$ - $\gamma$  transition in metallic Ce studied by resonant x-ray spectroscopies,” *Phys. Rev. B*, vol. 70, p. 085112, 2004.
- [11] F. Stigari, *Hybridization and crystal-field effects in Kondo insulators studied by means of core-level spectroscopy*. Phd thesis, Cologne, 2015.
- [12] A. Amorese, *Complete characterization of the crystal electric field in Ce Kondo lattices with resonant inelastic soft X-ray scattering*. Theses, Université Grenoble Alpes, 2017.

- [13] A. Amorese, G. Della, M. Fanciulli, S. Seiro, C. Geibel, C. Krellner, I. P. Makarova, L. Braicovich, G. Ghiringhelli, D. V. Vyalikh, N. B. Brookes, and K. Kummer, “4f excitations in Ce Kondo lattices studied by resonant inelastic x-ray scattering,” *Phys. Rev. B*, vol. 93, p. 165134, 2016.
- [14] A. Amorese, N. Caroca-Canales, S. Seiro, C. Krellner, G. Ghiringhelli, N. B. Brookes, D. V. Vyalikh, C. Geibel, and K. Kummer, “Crystal electric field in  $\text{CeRh}_2\text{Si}_2$  studied with high-resolution resonant inelastic soft x-ray scattering,” *Phys. Rev. B*, vol. 97, p. 245130, 2018.
- [15] A. Amorese, K. Kummer, N. B. Brookes, O. Stockert, D. T. Adroja, A. M. Strydom, A. Sidorenko, H. Winkler, D. A. Zocco, A. Prokofiev, S. Paschen, M. W. Haverkort, L. H. Tjeng, and A. Severing, “Determining the local low-energy excitations in the kondo semimetal  $\text{CeRu}_4\text{Sn}_6$  using resonant inelastic x-ray scattering,” *Phys. Rev. B*, vol. 98, p. 081116, 2018.
- [16] A. Amorese, D. Khalyavin, K. Kummer, N. B. Brookes, C. Ritter, O. Zaharko, C. B. Larsen, O. Pavlosiuk, A. P. Pikul, D. Kaczorowski, M. Gutmann, A. T. Boothroyd, A. Severing, and D. T. Adroja, “Metamagnetism and crystal-field splitting in pseudo-hexagonal  $\text{CeRh}_3\text{Si}_2$ ,” *Phys. Rev. B*, vol. 105, p. 125119, 2022.
- [17] P. Fulde and M. Loewenhaupt, “Magnetic excitations in crystal-field split 4f systems,” *Advances in Physics*, vol. 34, no. 5, pp. 589–661, 1985.
- [18] S. G. Chiuzbăian, C. F. Hague, A. Avila, R. Delaunay, N. Jaouen, M. Sacchi, F. Polack, M. Thomasset, B. Lagarde, A. Nicolaou, S. Brignolo, C. Baumier, J. Lüning, and J.-M. Mariot, “Design and performance of AERHA, a high acceptance high resolution soft x-ray spectrometer,” *Review of Scientific Instruments*, vol. 85, no. 4, p. 043108, 2014.
- [19] M. Sacchi, N. Jaouen, H. Popescu, R. Gaudemer, J. M. Tonnerre, S. G. Chiuzbaian, C. F. Hague, A. Delmotte, J. M. Dubuisson, G. Cauchon, B. Lagarde, and F. Polack, “The SEXTANTS beamline at SOLEIL: a new facility for elastic, inelastic and coherent scattering of soft x-rays,” *Journal of Physics: Conference Series*, vol. 425, no. 7, p. 072018, 2013.
- [20] J. Imer and E. Wuilloud, “A simple model calculation for XPS, BIS and EELS 4f-excitations in Ce and La compounds,” *Zeit. Phys. B Condensed Matter*, vol. 66, p. 153, 1987.
- [21] M. W. Haverkort, M. Zwierzycki, and O. K. Andersen, “Multiplet ligand-field theory using Wannier orbitals,” *Phys. Rev. B*, vol. 85, p. 165113, 2012.
- [22] Y. Lu, M. Höppner, O. Gunnarsson, and M. W. Haverkort, “Efficient real-frequency solver for dynamical mean-field theory,” *Phys. Rev. B*, vol. 90, p. 085102, 2014.

- [23] M. W. Haverkort, G. Sangiovanni, P. Hansmann, A. Toschi, Y. Lu, and S. Macke, “Bands, resonances, edge singularities and excitons in core level spectroscopy investigated within the dynamical mean-field theory,” *EPL (Europhysics Letters)*, vol. 108, no. 5, p. 57004, 2014.
- [24] M. W. Haverkort, “Quanty for core level spectroscopy - excitons, resonances and band excitations in time and frequency domain,” *Journal of Physics: Conference Series*, vol. 712, p. 012001, 2016.
- [25] C. J. Ballhausen, “Introduction to Ligand Field Theory,” *Mac Graw-Hill, New York*, 1962.
- [26] M. W. Haverkort, *Spin and orbital degrees of freedom in transition metal oxides and oxide thin films studied by soft x-ray absorption spectroscopy*. PhD thesis, Cologne 2005.
- [27] H. L. Schläfer and G. Gliemann, “Basic principles of ligand field theory,” *Wiley-Interscience, London*, 1969.
- [28] E. U. Condon and G. Shortley, “The theory of atomic spectra,” *Cambridge University Press, Cambridge*, 1935.
- [29] F. de Groot and A. Kotani, “Core level spectroscopy of solids,” *CRC Press, Boca Raton*, 2008.
- [30] R. D. Cowan, “The theory of atomic structure and spectra,” *Univ of California Press*, 1981.
- [31] M. Retegan, “Crispy: v0.7.3,” 2019.
- [32] F. M. de Groot et al., “2p x-ray absorption spectroscopy of 3d transition metal systems,” *Journal of Electron Spectroscopy and Related Phenomena*, vol. 249, p. 147061, 2021.
- [33] G. Kalkowski, G. Kaindl, G. Wortmann, D. Lentz, and S. Krause, “4f-ligand hybridization in  $\text{CeF}_4$  and  $\text{TbF}_4$  probed by core-level spectroscopies,” *Phys. Rev. B*, vol. 37, pp. 1376–1382, 1988.
- [34] B. T. Thole, G. van der Laan, J. C. Fuggle, G. A. Sawatzky, R. C. Karnatak, and J.-M. Esteva, “3d x-ray-absorption lines and the  $3d^9 4f^{n+1}$  multiplets of the lanthanides,” *Phys. Rev. B*, vol. 32, pp. 5107–5118, 1985.
- [35] N. B. D.L. Cox and J. Wilkins, “Self-consistent large-n expansion for normal-state properties of dilute magnetic alloys,” *Phys. Rev. B*, vol. 36, p. 2036, 1987.
- [36] M. Nakazawa, H. Ogasawara, and A. Kotani, “Theory of polarization dependence in resonant x-ray emission spectroscopy of Ce compounds,” *Journal of the Physical Society of Japan*, vol. 69, no. 12, pp. 4071–4077, 2000.



- [37] N. Sasabe, H. Tonai, and T. Uozumi, “Spectral change in 3d–4f resonant inelastic x-ray scattering of ce intermetallics across the transition between Kondo singlet and localized-spin state,” *Journal of the Physical Society of Japan*, vol. 86, no. 9, p. 093701, 2017.
- [38] M. Watanabe, Y. Harada, M. Nakazawa, Y. Ishiwata, R. Eguchi, T. Takeuchi, A. Kotani, and S. Shin, “Polarization dependence of resonant soft x-ray emission spectra in Ce compounds,” *Surface Review and Letters*, vol. 09, no. 02, pp. 983–987, 2002.
- [39] O. Gunnarsson and K. Schönhammer, “Electron spectroscopies for Ce compounds in the impurity model,” *Phys. Rev. B*, vol. 28, pp. 4315–4341, 1983.
- [40] J. C. Fuggle, F. U. Hillebrecht, J.-M. Esteva, R. C. Karnatak, O. Gunnarsson, and K. Schönhammer, “*f*-count effects in x-ray-absorption spectra of the 3*d* levels in Ce and its intermetallic compounds,” *Phys. Rev. B*, vol. 27, pp. 4637–4643, 1983.
- [41] J. C. Fuggle, F. U. Hillebrecht, Z. Zołnierek, R. Lässer, C. Freiburg, O. Gunnarsson, and K. Schönhammer, “Electronic structure of Ce and its intermetallic compounds,” *Phys. Rev. B*, vol. 27, pp. 7330–7341, 1983.
- [42] O. Sologub, H. Noël, A. Leithe-Jasper, P. Rogl, and O. Bodak, “Ternary compounds REAgSb<sub>2</sub>, RE = Y, La, Ce, Pr, Nd, Sm, Gd, Tb, Dy, Ho, Er, Tm: Magnetism and crystal structure,” *Journal of Solid State Chemistry*, vol. 115, no. 2, pp. 441–446, 1995.
- [43] Y. Inada, A. Thamizhavel, H. Yamagami, T. Takeuchi, Y. Sawai, S. Ikeda, H. Shishido, T. Okubo, M. Yamada, K. Sugiyama, N. Nakamura, T. Yamamoto, K. Kindo, T. Ebihara, A. Galatanu, E. Yamamoto, R. Settai, and Y. Onuki, “An unusual hollow cylindrical fermi surface of a quasi-two-dimensional compound CeAgSb<sub>2</sub>,” *Philosophical Magazine B*, vol. 82, no. 18, pp. 1867–1892, 2002.
- [44] E. Jobilong, J. S. Brooks, E. S. Choi, H. Lee, and Z. Fisk, “Magnetization and electrical-transport investigation of the dense Kondo system CeAgSb<sub>2</sub>,” *Phys. Rev. B*, vol. 72, p. 104428, 2005.
- [45] S. Araki, N. Metoki, A. Galatanu, E. Yamamoto, A. Thamizhavel, and Y. Onuki, “Crystal structure, magnetic ordering, and magnetic excitation in the 4*f*-localized ferromagnet CeAgSb<sub>2</sub>,” *Phys. Rev. B*, vol. 68, p. 024408, Jul 2003.
- [46] J. Dann, A. Hillier, J. Armitage, and R. Cywinski, “A  $\mu$ sr study of the magnetic properties of CeAgSb<sub>2</sub>,” *Physica B: Condensed Matter*, vol. 289-290, pp. 38–42, 2000.
- [47] T. Takeuchi, A. Thamizhavel, T. Okubo, M. Yamada, N. Nakamura, T. Yamamoto, Y. Inada, K. Sugiyama, A. Galatanu, E. Yamamoto, K. Kindo, T. Ebihara, and Y. Onuki, “Anisotropic, thermal, and magnetic properties of CeAgSb<sub>2</sub> explanation via a crystalline electric field scheme,” *Phys. Rev. B*, vol. 67, p. 064403, 2003.

- [48] D. Hafner, B. K. Rai, J. Banda, K. Kliemt, C. Krellner, J. Sichelschmidt, E. Morosan, C. Geibel, and M. Brando, “Kondo-lattice ferromagnets and their peculiar order along the magnetically hard axis determined by the crystalline electric field,” *Phys. Rev. B*, vol. 99, p. 201109, 2019.
- [49] Y. Saitoh, H. Fujiwara, T. Yamaguchi, Y. Nakatani, T. Mori, H. Fuchimoto, T. Kiss, A. Yasui, J. Miyawaki, S. Imada, H. Yamagami, T. Ebihara, and A. Sekiyama, “Electronic structures of ferromagnetic CeAgSb<sub>2</sub>: Soft x-ray absorption, magnetic circular dichroism, and angle-resolved photoemission spectroscopies,” *Journal of the Physical Society of Japan*, vol. 85, no. 11, p. 114713, 2016.
- [50] C. W. Chuang, B. T. Chiogo, D. Malterre, P.-Y. Chuang, C.-M. Cheng, T.-W. Pi., F.-H. Chang, H.-J. Lin, C.-T. Chen, C.-N. Kuo, C.-S. Lue, and A. Chainani, “Resonant photoemission spectroscopy of the ferromagnetic kondo system CeAgSb<sub>2</sub>,” *Electronic Structure*, vol. 3, p. 034001, jul 2021.
- [51] D. Malterre, M. Grioni, P. Weibel, B. Dardel, and Y. Baer, “Evidence of a kondo scale from the temperature dependence of inverse photoemission spectroscopy of CePd<sub>3</sub>,” *Phys. Rev. Lett.*, vol. 68, pp. 2656–2659, 1992.
- [52] D. Malterre, M. Grioni, P. Weibel, B. Dardel, and Y. Baer, “Temperature dependence of the 4f spectral function in the Kondo system CeSi<sub>2</sub> : Evidence of the kondo resonance smearing,” *Europhysics Letters (EPL)*, vol. 20, pp. 445–450, nov 1992.
- [53] S. Banik, A. Arya, A. Bendounan, M. Maniraj, A. Thamizhavel, I. Vobornik, S. K. Dhar, and S. K. Deb, “Estimate of the coulomb correlation energy in CeAg<sub>2</sub>Ge<sub>2</sub> from inverse photoemission and high resolution photoemission spectroscopy,” *Journal of Physics: Condensed Matter*, vol. 26, p. 335502, jul 2014.
- [54] X. Wang, H. Michor, and M. Grioni, “Probing the nature of the Ce 4f states in CeX<sub>9</sub>Si<sub>4</sub> (X = Ni, Co) by high-energy electron spectroscopies,” *Phys. Rev. B*, vol. 75, p. 035127, 2007.
- [55] M. Grioni, P. Weibel, D. Malterre, Y. Baer, and L. Du‘o, “Resonant inverse photoemission in cerium-based materials,” *Phys. Rev. B*, vol. 55, pp. 2056–2067, 1997.
- [56] F. U. Hillebrecht, J. C. Fuggle, G. A. Sawatzky, M. Campagna, O. Gunnarsson, and K. Schönhammer, “Transition to nonmagnetic f states in ce intermetallic compounds studied by bremsstrahlung isochromat spectroscopy,” *Phys. Rev. B*, vol. 30, pp. 1777–1787, 1984.
- [57] K. Kanai, Y. Tezuka, T. Terashima, Y. Muro, M. Ishikawa, T. Uozumi, A. Kotani, G. Schmerber, J. P. Kappler, J. C. Parlebas, and S. Shin, “Resonance effect on inverse-photoemission spectroscopy of CeRh<sub>3</sub>, CePd<sub>3</sub>, and CeSn<sub>3</sub>,” *Phys. Rev. B*, vol. 60, pp. 5244–5250, 1999.

- [58] T. Uozumi, K. Kanai, S. Shin, A. Kotani, G. Schmerber, J. P. Kappler, and J. C. Parlebas, “Theoretical and experimental study of surface and bulk contributions in resonant inverse photoemission of CeRh<sub>3</sub>,” *Phys. Rev. B*, vol. 65, p. 045105, 2002.
- [59] A. Tanaka and T. Jo, “Theory of resonant inverse photoemission spectroscopy in Ce compounds: Selection rule and hybridization strength,” *Journal of the Physical Society of Japan*, vol. 65, no. 2, pp. 615–621, 1996.
- [60] C. H. Lai, H. S. Fung, W. B. Wu, H. Y. Huang, H. W. Fu, S. W. Lin, S. W. Huang, C. C. Chiu, D. J. Wang, L. J. Huang, T. C. Tseng, S. C. Chung, C. T. Chen, and D. J. Huang, “Highly efficient beamline and spectrometer for inelastic soft X-ray scattering at high resolution,” *Journal of Synchrotron Radiation*, vol. 21, no. 2, pp. 325–332, 2014.
- [61] S. Butorin, D. Mancini, J.-H. Guo, N. Wassdahl, and J. Nordgren, “On the hybridization of ce 4f states in cef3 and ceo2: A near-threshold excitation x-ray fluorescence study,” *Journal of Alloys and Compounds*, vol. 225, no. 1, pp. 230–233, 1995. Proceedings of the 2nd International Conference on f-Elements.
- [62] K.-J. Zhou, M. Radovic, J. Schlappa, V. Strocov, R. Frison, J. Mesot, L. Patthey, and T. Schmitt, “Localized and delocalized Ti 3d carriers in LaAlO<sub>3</sub>/SrTiO<sub>3</sub> superlattices revealed by resonant inelastic x-ray scattering,” *Phys. Rev. B*, vol. 83, p. 201402, 2011.
- [63] F. Pfaff, H. Fujiwara, G. Berner, A. Yamasaki, H. Niwa, H. Kiuchi, A. Gloskovskii, W. Drube, J. Gabel, O. Kirilmaz, A. Sekiyama, J. Miyawaki, Y. Harada, S. Suga, M. Sing, and R. Claessen, “Raman and fluorescence contributions to the resonant inelastic soft x-ray scattering on LaAlO<sub>3</sub>/SrTiO<sub>3</sub> heterostructures,” *Phys. Rev. B*, vol. 97, p. 035110, 2018.
- [64] T. Schmitt, L.-C. Duda, M. Matsubara, M. Mattesini, M. Klemm, A. Augustsson, J.-H. Guo, T. Uozumi, S. Horn, R. Ahuja, A. Kotani, and J. Nordgren, “Electronic structure studies of V<sub>6</sub>O<sub>13</sub> by soft x-ray emission spectroscopy: Band-like and excitonic vanadium states,” *Phys. Rev. B*, vol. 69, p. 125103, 2004.
- [65] V. Bisogni, S. Catalano, R. J. Green, M. Gibert, R. Scherwitzl, Y. Huang, V. N. Strocov, P. Zubko, S. Balandeh, J.-M. Triscone, G. Sawatzky, and T. Schmitt, “Ground-state oxygen holes and the metal–insulator transition in the negative charge-transfer rare-earth nickelates,” *Nat Commun*, vol. 7, p. 13017, 2016.
- [66] A. Hariki, M. Winder, and J. Kuneš, “Continuum charge excitations in high-valence transition-metal oxides revealed by resonant inelastic x-ray scattering,” *Phys. Rev. Lett.*, vol. 121, p. 126403, 2018.
- [67] A. Delobbe, M. Finazzi, B. Buschinger, O. Trovarelli, C. Geibel, J.-P. Kappler, and G. Krill, “M<sub>4,5</sub> absorption edges in Ce-Kondo systems,” *Physica B: Condensed Matter*, vol. 259-261, pp. 1144–1146, 1999.

- [68] A. Amorese, A. Marino, M. Sundermann, K. Chen, Z. Hu, T. Willers, F. Choueikani, P. Ohresser, J. Herrero-Martin, S. Agrestini, C.-T. Chen, H.-J. L., M. W. Haverkort, S. Seiro, C. Geibel, F. Steglich, L. H. Tjeng, G. Zwicky, and A. Severing, “Possible multiorbital ground state in CeCu<sub>2</sub>Si<sub>2</sub>,” *Phys. Rev. B*, vol. 102, p. 245146, 2020.
- [69] G. Zwicky, V. Zevin, and P. Fulde, “Simple approximation scheme for the anderson impurity hamiltonian,” *Zeitschrift für Physik B Condensed Matter*, vol. 79, p. 365, 1990.
- [70] V. Zevin, G. Zwicky, and P. Fulde, “Temperature dependence of the 4f quadrupole moment of Yb in YbCu<sub>2</sub>Si<sub>2</sub>,” *Phys. Rev. Lett.*, vol. 60, pp. 2331–2334, 1988.
- [71] T. Ide and A. Kotani, “Interplay between raman and fluorescence-like components in resonant x-ray emission spectra of degenerate  $d^0$  and  $d^1$  systems,” *Journal of the Physical Society of Japan*, vol. 69, no. 6, pp. 1895–1906, 2000.
- [72] S. Watanabe and K. Miyake, “Roles of critical valence fluctuations in ce- and yb-based heavy fermion metals,” *Journal of Physics: Condensed Matter*, vol. 23, no. 9, p. 094217, 2011.
- [73] H. Yashima and T. Satoh, “Nonmagnetic-magnetic transition in CeSi system,” *Solid State Communications*, vol. 41, no. 10, pp. 723–727, 1982.
- [74] V. R. Fanelli, J. M. Lawrence, E. A. Goremychkin, R. Osborn, E. D. Bauer, K. J. McClellan, J. D. Thompson, C. H. Booth, A. D. Christianson, and P. S. Riseborough, “Q-dependence of the spin fluctuations in the intermediate valence compound CePd<sub>3</sub>,” *Journal of Physics: Condensed Matter*, vol. 26, p. 225602, may 2014.
- [75] J. M. Lawrence, J. D. Thompson, and Y. Y. Chen, “Two energy scales in CePd<sub>3</sub>,” *Phys. Rev. Lett.*, vol. 54, pp. 2537–2540, 1985.
- [76] J.-P. Rueff, J.-P. Itié, M. Taguchi, C. F. Hague, J.-M. Mariot, R. Delaunay, J.-P. Kappler, and N. Jaouen, “Probing the  $\gamma$ - $\alpha$  transition in bulk Ce under pressure: A direct investigation by resonant inelastic x-ray scattering,” *Phys. Rev. Lett.*, vol. 96, p. 237403, 2006.
- [77] Chen, Bijuan et al., “Probing cerium 4f states across the volume collapse transition by x-ray Raman scattering,” *J. Phys. Chem. Lett.*, vol. 10, pp. 7890–7897, 2019.
- [78] K. Gschneidner, R. Elliott, and R. McDonald, “Effects of alloying additions on the  $\gamma$ - $\alpha$  transformation of cerium: Part ii. effects of scandium, thorium and plutonium additions,” *Journal of Physics and Chemistry of Solids*, vol. 23, no. 9, pp. 1191–1199, 1962.
- [79] J.-P. Rueff, C. F. Hague, J.-M. Mariot, L. Journel, R. Delaunay, J.-P. Kappler, G. Schmerber, A. Derory, N. Jaouen, and G. Krill, “f-state occupancy at the  $\gamma$ - $\alpha$  phase transition of Ce-Th and Ce-Sc alloys,” *Phys. Rev. Lett.*, vol. 93, p. 067402, 2004.

- [80] H. Ishii, Y. Ishiwata, R. Eguchi, Y. Harada, M. Watanabe, A. Chainani, and S. Shin, “Resonant soft x-ray emission spectroscopy of NiO across the Ni  $L_{2,3}$  thresholds,” *Journal of the Physical Society of Japan*, vol. 70, no. 6, pp. 1813–1816, 2001.
- [81] M. Magnuson, S. M. Butorin, A. Agui, and J. Nordgren, “Resonant soft x-ray raman scattering of NiO,” *Journal of Physics: Condensed Matter*, vol. 14, p. 3669, mar 2002.
- [82] S. M. Butorin, “Resonant inelastic x-ray scattering as a probe of optical scale excitations in strongly electron-correlated systems: quasi-localized view,” *Journal of Electron Spectroscopy and Related Phenomena*, vol. 110-111, pp. 213–233, 2000. Soft X Ray Emission Spectroscopy.
- [83] M. Matsubara, T. Uozumi, A. Kotani, and J. Claude Parlebas, “Charge transfer excitation in resonant x-ray emission spectroscopy of NiO,” *Journal of the Physical Society of Japan*, vol. 74, no. 7, pp. 2052–2060, 2005.

## General conclusions and outlook

Strong electron correlations lead to numerous exotic electronic and magnetic properties such as the Kondo effect, heavy fermions, intermediate valence, charge density wave, and unconventional superconductivity... In rare-earth-based compounds (Cerium, Ytterbium), these properties are due to the very strong electron-electron interactions of the f states as well as the hybridization of the f states with the conduction electrons. One of the most direct approach to understand these systems is to study their electronic structure by spectroscopies.

This thesis aimed to investigate the fundamental electronic properties of cerium and ytterbium-based Kondo systems by using complementary spectroscopic techniques (low energy ultra-violet angle-resolved photoemission spectroscopy, hard x-ray photoemission spectroscopy, x-ray absorption spectroscopy, and resonant inelastic x-ray scattering). In particular, we investigated the spectroscopic properties of intermediate valence, which coexist and compete with long-range magnetic order or density wave order in f materials. We also carried out quantitative analysis of the spectroscopic measurements in the framework of the single impurity Anderson Model and the atomic full multiplet theory.

The material of interest in the first part of this thesis is the intermediate valence YbPd compound, which crystallizes in the cubic CsCl structure at room temperature and exhibits an antiferromagnetic phase transition at  $T_N = 1.9$  K. It undergoes an incommensurate charge density wave (CDW) characterized by the wave vector  $(0.07\ 0.07\ 1/2)$  at  $T_1 = 130$  K and a commensurate transition  $(0\ 0\ 1/2)$  at  $T_2 = 105$  K. Below 105 K, magnetic  $\text{Yb}^{3+}$  and non-magnetic  $\text{Yb}^{2.6+}$  arranged alternatively along the c axis, in a tetragonal structure exhibiting valence order. This valence order is very intriguing since YbPd shows metallic electrical resistivity in all temperature ranges. We have investigated the core-level electronic structure of YbPd by means of Hard X-ray Photoemission Spectroscopy (HAXPES). We developed a code in the framework of SIAM following the approach introduced by Gunnarsson et Schönhammer to quantify the electronic parameters. Core level Yb-3d<sub>5/2</sub> spectra reveal

temperature-independent single-Yb site mixed-valence above  $T_1$  and a clear temperature-dependent valence change of the two crystallographic Yb sites in the CDW phase. The Kondo energy gain is shown to be the driving mechanism of the CDW transition. The evolution of Kondo temperatures in the CDW phase tracks the lattice parameter changes, thus showing an interplay between the Kondo effect and the structural changes giving rise to the zero thermal expansion in the CDW phase. We propose a conjecture that Kondo mechanism could be the driving force of the CDW phase. Additional studies should be carry out to justify this original idea.

Knowledge of elementary excitations is crucial for understanding the electronic and thermodynamic properties of strongly correlated cerium-based Kondo systems. By making use of the high-energy spectroscopic techniques, the aim of the second part of this thesis was to provide a reliable and quantitative investigation of the low and high-energy excitation as well as an  $f$ -state occupation in Ce Kondo systems. Especially, standard techniques for studying the elementary excitations in Kondo systems like magnetic susceptibility, valence band photoemission, and inverse photoemission spectroscopy yield limited information about the energy scales. Typically, thermodynamic measurements only yield access to low-energy excitations (crystal field energy and Kondo energy), and PES and IPES are surface sensitive, which sometimes affects the results. Here, Resonant inelastic x-ray scattering (soft x-ray) comes into play, which was established as a new tool to probe the elementary excitations in a large variety of systems. The information that can be retrieved from Ce  $M_5$ -edge RIXS spectra has been shown by using the typical example of the ferromagnetic CeAgSb<sub>2</sub> Kondo systems. In particular, we have shown that all the charge excitations usually observed in combined PES/IPES measurements can be evidenced in RIXS. In order to accurately reproduce the experimental XAS and RIXS spectra, and deduced the  $f$ -state occupation,  $n_f$ , the hybridization strength  $V$ , the  $f$ -state energy  $\epsilon_f$ , and the Coulomb repulsion between  $f$  electrons, we combined the full multiplet calculations with the single impurity Anderson model. We have shown that an extended basis is necessary to simulate the different loss structures in the RIXS. While the  $f^3$  contribution is sometimes neglected in the Ce  $M_5$ -edge XAS spectra, it drastically affects the RIXS spectra. Typically, without the  $3d^9 4f^3$  configuration in the XAS spectrum, the  $4f^2$  structure in the RIXS spectrum is completely missing. Thanks to the scattering geometry of the measurement combined with the dipole selection rules, the  $^1S_0$  symmetry of the ground state is reflected through the drastic polarization dependence of the  $f^0$  and elastic peaks in the RIXS spectra. We evidenced a strong temperature dependence of the fluorescence-like structure, and we proposed that it is a signature of the Kondo energy scale. We investigated the evolution of the RIXS spectral line shapes of compounds with low and high Kondo temperatures, and we found that the RIXS spectra of high  $T_K$  compounds are very complex with the presence of several unknown structures. Typically, the structure observed at 2 eV in the RIXS spectra CePd<sub>3</sub> as well as the unexpected fluorescence-like structure observed in the RIXS spectra of high  $T_K$  compounds (CeNi<sub>2</sub> and CePd<sub>3</sub>) deserve further

investigations. we measured the  $\text{Ce}_{0.93}\text{Sc}_{0.07}$  alloy across the  $\gamma$ - $\alpha$  transition. The RIXS spectral weight of the  $f^0$  as well as the fluorescence-like structure present a sharp drop across the  $\gamma$ - $\alpha$  transition and hysteresis as a function of temperature that closely resemble the magnetization loop. This allows us to conjecture that the fluorescence-like structure is correlated with the weight of the  $f^0$  configuration in the ground state and reflect the Kondo scale. RIXS seems to be a powerful technique to study Kondo systems. High resolution RIXS close to the elastic peak gives information about the low energy excitations (Kondo scale, crystal electric field and spin orbit) whereas the energy loss at high energy give information about the  $f - f$  charge excitations. However, the fluorescence structures have to be understand because their intensity seems to reflect the Kondo physics.



# CURRICULUM VITAE



## Ph.D. Student

Name: **TEGOMO CHIOGO BODRY**

Affiliation : **Institut Jean Lamour UMR 7198**

**University of Lorraine, Nancy France**

Position: **Ph.D. student, 25 years old**

PO.BOX: **54000 NANCY**

Phone: **+33752709645**

Email: **bodry.tegomo-chiogo@univ-lorraine.fr**  
**tegomobodry@gmail.com**

## Training

**Since September 2019:** PhD in Physics: Institut Jean Lamour, France. spectroscopic studies of cerium and ytterbium-based Kondo systems: experiments and simulations. under the supervision of Prof. Daniel Malterre and Dr Ashish Chainani.

**2018-2019:** Master 2 in condensed matter and nanomaterial at university of Lorraine with 15,75. 5-month internship with Daniel Malterre: Simulation of x-ray absorption, photoemission, and resonant inelastic x-ray scattering spectra in the Anderson model.

### University of Dschang-Cameroon:

- 1- 2017-2018: Master 1 in condensed matter with 16,33
- 2- 2014-2017: Bachelor's degree in condensed matter with 13.88

## Experience in Laboratory

- 1- **Vacuum techniques:** Daily use and knowledge of the ultra-high vacuum environment
- 2- **Spectroscopy techniques :**
  - Photoemission spectroscopy
  - Resonant inelastic x-ray scattering spectroscopy
  - X-ray absorption spectroscopy
- 3- **Experience on synchrotron radiation :**
  - Soleil synchrotron (France) : Cassiopee, Ode and Sextants beamlines
  - NSRRC synchrotron (Taiwan): Dragon and BL21B beamlines

## Transversal skills

- 1- Common software: Word, Excel, PowerPoint, Latex
- 2- Scientific software: Igor Pro, Python, Mathematica, Crispy and Quany code
- 3- Languages: French, English (level B2)

## Awards

2021 - Prize of best poster presentation of the Track **05 - Kondo effect and valence fluctuations** at the SCES 2020 - International Conference on Strongly Correlated Electron Systems

## Publication

- 1- C. W. Chuang, **B. Tegomo Chiogo**, et al., Resonant photoemission spectroscopy of the ferromagnetic Kondo system  $\text{CeAgSb}_2$ , 2021 Electron. Struct. **3**, 034001
- 2- Y.F. Liao, **B. Tegomo Chiogo**, et al., Dual Kondo effect charge ordering and zero thermal expansion in a correlated intermetallic. Commun Mater **3**, 23 (2022).
- 3- **B. Tegomo Chiogo** et al. Resonant inelastic x-ray scattering of Spin-Charge excitations in a Kondo system, Phys. Rev. B **106**, 075141 (2022).
- 4- **B. Tegomo Chiogo** et al. Temperature and pressure dependence of the Yb valence state in  $\text{YbMn}_{\sim 0.17}\text{Si}_{\sim 1.89}$ , Journal of Applied Physics **132**, 205902 (2022).
- 5- **B. Tegomo Chiogo** et al. Kondo scale revealed by the fluorescence-like feature of Resonant inelastic x-ray scattering of  $\text{Ce}_{0.93}\text{Sc}_{0.07}$ , in preparation.

## Distraction

- ❖ Internet
- ❖ Reading, cinema, travels
- ❖ Football and Basketball

## References

- 1- Prof MALTERRE DANIEL, University of Lorraine / Institut Jean Lamour  
daniel.malterre@univ-lorraine.fr / + 33 6 11 47 03 21
- 2- Dr CHAINANI ASHISH, National Synchrotron Radiation Research Center.  
chainani.ash@nsrrc.org.tw
- 3- Prof. YANNICK FAGOT-REVURAT, University of Lorraine / Institut Jean Lamour  
yannick.fagot@univ-lorraine.fr / +33 6 78 67 51 95

# Abstract

Cerium and ytterbium compounds are systems that exhibit outstanding magnetic, electronic, and thermodynamic properties at low temperatures, such as the Kondo effect, heavy fermions, intermediate valence, and charge density waves. These properties are due to the very strong electron-electron interactions of the  $f$  states and the hybridization of the  $f$  states with the conduction electrons. In the first part of this thesis work, we investigate the temperature-dependent electronic structure of YbPd, a Kondo mixed-valent cubic compound at high temperature, which exhibits incommensurate and commensurate charge-density-wave(CDW) ordering below  $T_1 = 130$  K and  $T_2 = 105$  K, respectively. Below 105 K, magnetic  $\text{Yb}^{3+}$  and nonmagnetic  $\text{Yb}^{2.6+}$  are arranged alternatively along the  $c$  axis, in a tetragonal structure exhibiting valence order. Hard x-ray photoemission spectroscopy of Yb  $3d$  states show temperature-independent  $\text{Yb}^{2+}$  and  $\text{Yb}^{3+}$  features indicating single-Yb site dynamic valence fluctuations above  $T_1$ , and a clear temperature dependent valence change of the two crystallographic Yb sites in the CDW phase. Simplified single-impurity Anderson model calculations of the Yb  $3d$  states show good agreement with the temperature-dependent valency change and provide site-dependent Kondo temperatures. The results indicate an evolution from dynamic mixed-valence in the cubic phase to long-range static CDW order in the tetragonal phase, which is driven by the difference in Kondo energies of the two phases.

Resonant inelastic x-ray scattering (RIXS) is a very efficient technique to study elementary excitations in a large variety of systems, such as charge transfer excitations, the crystal field, and spin-orbit excitations. In the second part of this work, we investigated cerium compounds with different Kondo temperatures using RIXS at Ce  $M_5$ -edge combined with simulation using the full multiplet theory and the single impurity Anderson model. We demonstrated that all the charge excitations observed in combined photoemission and inverse photoemission can be evidenced by RIXS spectroscopy just by varying the incident photon energy around the Ce  $M_5$ -edge. We also discuss the drastic polarization dependence of the  $f^0$  structure in RIXS spectra and the strong temperature dependence of the fluorescence-like structure, which is reminiscent of the temperature dependence of the Kondo resonance.

# Résumé

Les composés de cérium et d'ytterbium sont des systèmes qui présentent des propriétés magnétiques, électroniques et thermodynamiques exceptionnelles à basse température, tels que l'effet Kondo, les fermions lourds, la valence intermédiaire et des ondes de densité de charge. Ces propriétés sont dues aux interactions électron-électron très fortes des états  $f$  et à l'hybridation des états  $f$  avec les électrons de conduction. Dans la première partie de ce travail de thèse, nous étudions la structure électronique de l'YbPd, un composé cubique à haute température, qui présente des ondes de densité de charge (CDW) incommensurable et commensurable en dessous de  $T_1 = 130$  K et  $T_2 = 105$  K, respectivement. En dessous de 105 K, les sites magnétique Yb<sup>3+</sup> et non magnétique Yb<sup>2.6+</sup> sont disposés alternativement le long de l'axe  $c$ , en une structure tétragonale présentant un ordre de valence. La spectroscopie de photoémission de rayons X durs (HAXPES) des états 3d de l'Yb montre des caractéristiques Yb<sup>2+</sup> et Yb<sup>3+</sup> indépendantes de la température au-dessus de  $T_1$ , et un changement de valence des deux sites cristallographiques d'Yb dans la phase CDW. Des calculs des spectres HAXPES au seuil 3d de l'Yb avec un modèle à une impureté d'Anderson simplifié montrent un bon accord avec la dépendance en température de la valence et fournissent les températures de Kondo des deux sites d'Yb. Les résultats indiquent une évolution de la valence intermédiaire dans la phase cubique à un ordre CDW statique à longue portée dans la phase tétragonale. Nous proposons que le mécanisme Kondo est à l'origine de l'onde de densité de charge.

La diffusion inélastique résonante des rayons x est une technique très efficace pour étudier les excitations élémentaire dans une large variété de système tels que les excitations de transfert de charge, les excitations de champ cristallin et de spin-orbite. Dans la deuxième partie de ce travail, le RIXS combiné avec des simulations à base du modèle à une impureté d'Anderson et la théorie des multiplets a été utilisé pour l'étude des composés de cérium avec différentes températures de Kondo  $T_K$ . Nous avons démontré que toutes les excitations de charge observées en les spectres de photoémission et photoémission inverse combinés peuvent être mises en évidence par la spectroscopie RIXS simplement en faisant varier l'énergie du photon incident autour du seuil  $M_5$  du cérium. Nous discutons également de la dépendance drastique de la structure  $f^0$  dans les spectres RIXS en fonction de la polarisation et de la forte dépendance en température de la structure de type fluorescence, qui rappelle la dépendance à la température de la résonance de Kondo.